GRAN SASSO SCIENCE INSTITUTE
SCUOLA INTERNAZIONALE SUPERIORE DI STUDI AVANZATI

Ph.D. thesis

The CUORE experiment: detector optimization and modelling and CPT conservation limit

PhD Candidate
Irene Nutini

Advisors

Dr. Carlo Bucci
INFN, Laboratori Nazionali del Gran Sasso

Dr. Oliviero Cremonesi
INFN, Sezione di Milano Bicocca

A thesis submitted in fulfillment of the requirements
for the degree of Doctor of Philosophy in Astroparticle Physics

October 31, 2018

Gran Sasso Science Institute
XXXI Cycle – A.Y. 2015-2018

Ai miei nonni

Contents

Introduction

The CUORE (Cryogenic Underground Observatory for Rare Events) experiment, hosted at Gran Sasso National Laboratories in Italy, is a ton-scale cryogenic experiment designed for the search for neutrino-less double beta decay ($0\nu\beta\beta$) of ^{130}Te. The CUORE detector consists of an array of 988 TeO_2 crystals operated as cryogenic bolometers at $\sim$10 mK. The total mass of TeO_2 is 742 kg, corresponding to 206 kg of ^{130}Te.

The first part of the Thesis introduces the physics of interest for CUORE and the experimental aspects.
In Chapter 1, a general overview of the double beta decay processes ($0\nu\beta\beta$ and $2\nu\beta\beta$) is presented. A description of the $0\nu\beta\beta$ process and of its importance in the search for physics beyond the Standard Model will be provided. The Standard Model (SM) predictions for $2\nu\beta\beta$ decay and the current measurements will be reported. Moreover a section will be dedicated to the effect of a possible CPT symmetry violation on the $2\nu\beta\beta$ decay, as predicted by the Standard Model Extensions (SME).
Chapter 2 fully describes the CUORE experiment, including the structure of the detector, the experimental setup and the data collection organization.
A wide and detailed overview of the thermal detectors is presented in Chapter 3. The bolometer principle of operation will be described, focusing on all the fundamental elements of this detector (energy absorber and phonon sensor). The bolometric technique will be illustrated in the case of interest for the CUORE detectors.

The second part of the Thesis is devoted to a description of the latest phase of the CUORE commissioning phase and the start of data taking in 2017. It was the first time that such a large number of bolometric detectors were simultaneously operated in a completely new and unique cryogenic system; characterization and optimization of the detectors and overall system performance were needed.
Chapter 4 will be mostly devoted to the description of the activities and analyses performed during the CUORE system optimization campaigns. The characterization of the detectors and the tuning of their operating parameters as well as the noise reduction are necessary in order to improve the energy resolution. Moreover the acquisition of the first CUORE physics data and the performance of the detector will be briefly commented.

The last part of the thesis reports the analysis procedures and the first results obtained by analyzing the CUORE data acquired in 2017.
The CUORE processing and analysis sequences used to extract useful information from recorded events will be described in details in Chapter 5. The Monte Carlo software used for the production of simulated data and the bayesian analysis tool utilized for the reconstruction of CUORE background will be described as well.
Chapter 6 reviews the first CUORE results obtained from the analysis of the physics data acquired in 2017. The first CUORE $0\nu\beta\beta$ results and the preliminary $2\nu\beta\beta$ and background model analysis will be reported.

The search for a possible CPT violation signature in the $2\nu\beta\beta$ decay will be the topic of Chapter 7; the analysis procedure, which consists in including the $2\nu\beta\beta$ decay CPT violating term in the bayesian fit of the background spectra, will be described. A study of the sensitivity of CUORE to a possible CPT symmetry violating term in the $2\nu\beta\beta$ decay of ^{130}Te and a preliminary limit on the CPTV parameter obtained from the analysis of the CUORE 2017 data will be reported.

The two appendices of this work, Appendix A and B, are devoted to the studies for the comprehension of the CUORE bolometers response, both in static conditions and for the pulse generation after an energy deposition. This a crucial topic which can contribute to the identification of the physical parameters which are affecting the bolometers energy resolution.

Chapter 1

Double beta decay

1.1 Neutrino masses

Neutrinos are the least understood particles among the building blocks of the Standard Model. Like quarks and charged leptons, neutrinos are spin-1/2 fermions, but they are electrically neutral and they interact with other particles only through weak interaction mediated by the $W^{\pm}$ charged bosons and the Z^0 neutral boson.
There are three neutrino "flavors": ν_e, ν_μ, ν_τ. Each of these is coupled via the weak interaction to the charged lepton of the same flavor: e, μ,τ.

The basic properties of neutrinos, no electric charge and little mass, were at first hypothesized by W.Pauli in 1930 to explain the apparent loss of energy in the process of radioactive beta-decay.[1]
E. Fermi in 1934 elaborated the theory of beta decay and gave the particle its name. According to Fermi theory, an electron-neutrino is emitted with a positron in positive beta decay, while an electron-antineutrino is emitted with an electron in negative beta decay.[2]

Given the Fermi theory, predicting very weak interactions for the neutrinos with matter and the experimental challenges in observing those processes, neutrinos were not detected experimentally for more than 20 years.

The first evidence of neutrino was given in 1956 from the Cowan and Reines experiment [3], where they discovered the electron-antineutrino ($\overline{\nu_e}$) via the reaction: $\overline{\nu_e}$ + p $\longrightarrow e^+$ + n

Identification of ν_μ as distinct from ν_e was accomplished in 1962 by L.Lederman, M.Schwartz and J.Steinberger at Brookhaven National Laboratories. [4]
The discovery of the tau neutrino ν_τ was announced in 2000 by the DONUT experiment, at Fermilab, which was built specifically to detect that kind of neutrino. [5]

In 1998, the experimental observation of neutrino flavor oscillations led to the discovery that neutrinos have non-zero mass.
The model to describe neutrino flavor oscillations was first proposed in 1957 by Bruno Pontecorvo [6] and developed by Maki, Nakagawa, and Sakata in 1962 [7].
A neutrino can spontaneously change from one flavor to another; this phenomenon can happen because neutrinos of definite flavor are not mass eigenstates, but a coherent superposition of them:

$$\nu_l = \Sigma V_{li} \nu_i \tag{1.1}$$

where ν_i (i=1,2,3) are neutrino mass eigenstates and ν_l (l= e,μ, τ) are neutrino flavor eigenstates. V is the Pontecorvo-Maki-Nakagawa-Sakata (PMNS) neutrino mixing

matrix (the analogous of the CKM matrix for quarks). In the case of 3 neutrino flavors and 3 massive neutrinos, V is a unitary 3×3 matrix, which can be parametrized by 3 Euler angles (3 mixing angles θ_{12}, θ_{13}, θ_{23}) and 6 phases. If the massive neutrinos are Dirac particles, there is just one CP violating phase in V, which is usually called "the Dirac CP violating phase", δ. If, however, the massive neutrinos are Majorana fermions there are altogether 3 CP violation phases - one Dirac (δ) and two Majorana (α and β).
By the neutrino oscillation phenomenon, it is possible to measure the quadratic mass differences, $\Delta m^2_{ij} \equiv m^2_i - m^2_j$, where m_i,m_j are the neutrino mass eigenstates.
So far neutrino mass is manifested only through oscillation, while experiments that aim to a direct measurement of it did not reach yet the sufficient sensitivity [8].

In the (Minimal) Standard Model (SM) neutrinos are massless. Observations of neutrino masses therefore call for an extension of the model. The Standard Model can be extended making Dirac neutrinos gaining their mass from the linear coupling between the particle and a new Higgs boson field, but it still leaves open questions about the strong mass difference among neutrinos and all charged leptons and quarks. Another theory is that neutrinos can have Majorana masses, which mix a particle with its antiparticle, while charged leptons and quarks cannot have them. The neutrino mass smallness could then be also explained by the “see-saw” mechanism which couple light neutrinos to highly massive neutrinos, which practically do not interact with matter.

In summary, it has been discovered that neutrinos have finite masses but still their absolute mass values are missing. Furthermore, it is not yet known if neutrinos are Majorana fermions or Dirac particles like all the charged building blocks of the standard model.

1.2 Double beta decay

Double beta decay is a second-order weak decay where a nucleus, (A, Z) undergoes two beta decays to its isobar (A, Z+2) in a single step, emitting two electrons in the process. See Fig.1.1.

According to the SM, the process observes lepton number conservation and two electron anti-neutrinos are simultaneously emitted ($2\nu\beta\beta$). The SM extensions that accomodate for a Majorana neutrino nature predict a lepton-number violating neutrinoless double beta decay channel in which only the two electrons are emitted ($0\nu\beta\beta$). More exotic SM extensions which include Lorentz violating operators, give predictions that can be tested in physical processes that involve neutrino phase-space properties (e.g. $2\nu\beta\beta$ CPT violating).

Suitable nuclei for double-beta decay are ^{48}Ca, ^{76}Ge, ^{82}Se, ^{100}Mo, ^{116}Cd, $^{130,128}Te$, ^{136}Xe..., which are all even-even nuclei. Indeed, given the trend of the nuclear masses, in those isotopes the single beta decay is energetically forbidden. See Fig.1.2.

The double beta decay is a very rare process. For the $2\nu\beta\beta$ decay, several measurements of the half-lives have been made for the isotopes listed above. At the same time, there are several experiments hunting for $0\nu\beta\beta$ process, but no evidence for it has been uncovered yet; thus only lower limits on lifetime of $0\nu\beta\beta$ are provided.

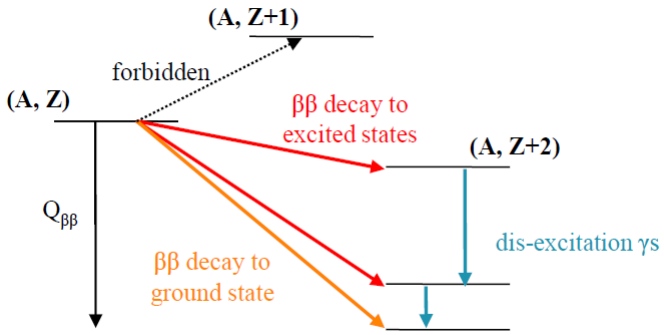

FIGURE 1.1: Scheme of possible $\beta\beta$ nuclear transitions. The initial nucleus (A, Z) can decay into the ground state or excited states of its isobar (A, Z+2), skipping the single beta decay channel which is forbidden by energy conservation. The vertical energy axis is implicit in the figure, leading to higher energies at the top.

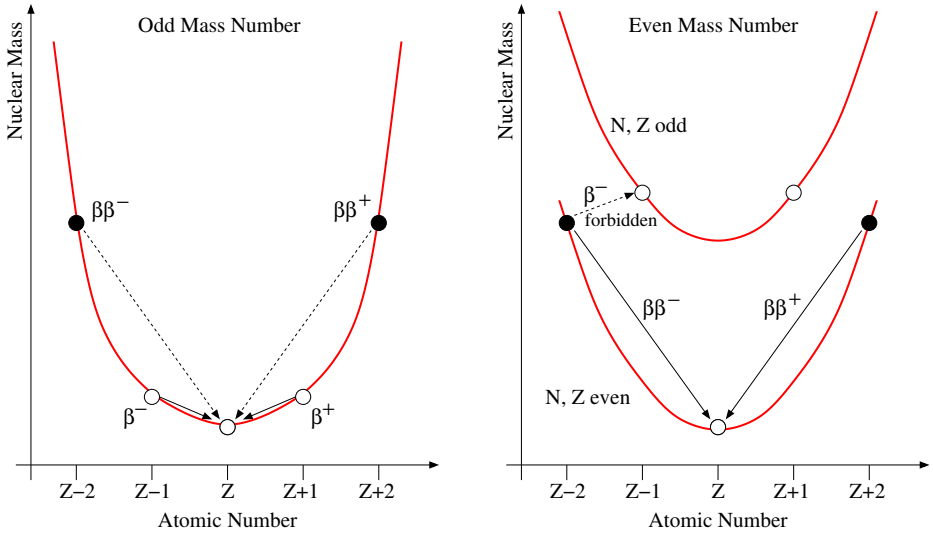

FIGURE 1.2: Nuclear mass as function of the proton number and general energy level configuration for double-beta decay emitters. [Left] For odd mass number, $\beta\beta$ decay is competing with the β decay; due to the lower rate of the $\beta\beta$ decay process, its signal is then much weaker than then the equivalent sequence of two β decays, which represents an important background. [Right] For even mass number, β decay is forbidden for certain even-even nuclei, a very attractive condition from the experimental point of view for the observation of $\beta\beta$ decay.

1.2.1 Two neutrino double beta decay

The $2\nu\beta\beta$ decay was first proposed in 1935 by Maria Goeppert-Mayer [9]. In this process, an even-even nucleus decays to its isobar by emitting two electrons; the lepton number is conserved since also two electron anti-neutrinos are produced in the decay.

$$2\nu\beta\beta : (A, Z) \longrightarrow (A, Z+2) + 2e^- + 2\overline{\nu}_e \tag{1.2}$$

Because of the heavy suppression due to the fact that this is a second-order weak process, the half-lives $T^{1/2}_{2\nu\beta\beta}$ for these decays are in the range 10^{18}-10^{24} yr and are

actually the slowest processes ever measured. See Tab.1.1.

Nuclide	Half-life $T^{1/2}_{2\nu\beta\beta}$ [10^{21} yr]	Experiment
^{48}Ca	$0.064\ ^{+0.007}_{-0.006}$(stat) $^{+0.012}_{-0.009}$ (sys)	NEMO-3 [10]
^{76}Ge	1.926 ± 0.094	GERDA [8]
^{78}Kr	$9.5\ ^{+5.5}_{-2.6} \pm 1.3$	BAKSAN [8]
^{82}Se	$0.096 \pm 0.003 \pm 0.010$	NEMO-3 [8]
^{96}Zr	$0.0235 \pm 0.0014 \pm 0.0016$	NEMO-3 [8]
^{100}Mo	$0.00690 \pm 0.00015 \pm 0.00037$	CUPID-Mo [8]
^{116}Cd	$0.029\ ^{+0.004}_{-0.003}$	$^{116}CdWO_4$ scint [8]
^{128}Te	7200 ± 400	*geochemical* [8]
^{130}Te	$0.79 \pm 0.01 \pm 0.02$	CUORE [11]
^{136}Xe	$2.165 \pm 0.016 \pm 0.059$	EXO-200 [8]
^{150}Nd	$0.00934 \pm 0.00022\ ^{+0.00062}_{-0.00060}$	NEMO-3 [8]
^{238}U	2.0 ± 0.6	*radiochemical* [8]

TABLE 1.1: Isotopes for which $2\nu\beta\beta$ decay half-life has been measured.

From an experimental point of view, the only measurable quantity in a double beta decay is typically the kinetic energy of the electrons produced in the decay, since the neutrinos rarely interact within the detector. The total kinetic energy of the electrons ($T = T_1 + T_2$) produces a broad energy spectrum that extends from 0 keV (neutrinos carrying away all the energy) up to the endpoint energy (neutrinos produced practically at rest).

The differential decay rate for the process can be derived from the Fermi rule, for 2^{nd} order processes [12], [13]:

$$d\Gamma = 2\pi\delta(E_0 - \sum_f E_f)\Big|\sum_{n,\beta}\frac{\langle f|H_\beta|m_n\rangle\langle m_n|H^\beta|i\rangle}{E_i - E_n - q_\nu - E_e}\Big|^2 \tag{1.3}$$

where E_0 is the transition energy ($Q_{\beta\beta} + 2m_e$). $Q_{\beta\beta}$ is the Q-value of the reaction; it corresponds to the difference of masses of parent and daughter nuclides, $Q_{\beta\beta} = (m(A,Z) - m(A,Z+2))c^2$. Moreover, in Eq.1.3, E_i is the initial energy, E_n is the energy of the nuclear intermediate states, E_f is the final energy of each constituent of the final state, q_ν and E_e are the energies of the emitted neutrino and electron. In this equation the neutrino is treated as mass-less, considering only its momentum q_ν, assuming the value of its mass negligible compared to the energies of the other constituents.

The Hamiltonian H is the product of the hadronic and the leptonic currents.

$$H_{cc} = (H_1 H_2)_{lept} \times (H_1 H_2)_{hadr} \tag{1.4}$$

$$\langle H_{cc}\rangle = \frac{g^4}{M_W^2}[\langle J^{\mu,\dagger}_{lept,1} J^{\nu,\dagger}_{lept,2}\rangle] \times [\langle J^{\mu}_{hadr,1} J^{\nu}_{hadr,2}\rangle] \tag{1.5}$$

By several approximations, it is possible to factorize Eq.1.3 by an atomic part (phase-space factor), a nuclear part (nuclear matrix element) and a particle term (effective neutrino mass). The nuclear matrix element can be rewritten in terms of an effective nuclear hamiltonian $H(q)$, which accounts for the whole hadronic part in the interaction and depends on q, the momentum transferred from hadrons to leptons. The

Nuclear Matrix Element (NME) $M_{\beta\beta}$ can then be defined.

$$M_{\beta\beta} = \langle f|H(q)|i\rangle \tag{1.6}$$

where $|i\rangle$ is the initial nuclear state, $|f\rangle$ is the final one; 2 neutrons are converted into 2 protons from $|i\rangle$ to $|f\rangle$.

The $2\nu\beta\beta$ differential decay rate can be derived from Eq.1.3 with few approximations [14], [15]:

- The nuclear matrix elements, that come from the hadronic current, are evaluated in the long-wavelength approximation; the De Broglie wavelength of the electrons is larger than the nuclear size, $\lambda_e \gg a$, electrons are produced in S-states. The hadronic current is reduced to non-relativistic limit (Fermi and Gamov-Teller operators).
- Only transitions from initial 0^+ (the ground state of the $\beta\beta$ emitter isotopes) to final 0^+ state, via intermediate 1^+ and 2^+ states, are considered ($\Delta l = 0$, orbital angular momentum conservation).
- The sum over the virtual intermediate nuclear states is completed via closure approximation, by replacing E_n by some average value $\langle E_n\rangle$. ($\langle E_n\rangle$ -E_i) $\approx$ 10 MeV for medium mass nuclei and $E_0 \approx 3$ MeV, assuming an average $Q_{\beta\beta}$ of 2 MeV.
- The Coulomb distortions of the outgoing electron wave functions are considered by means of the Fermi functions

The resulting differential rate is thus reported in Eq.1.7.

$$\frac{d\Gamma}{dp_1 dp_2 dcos\theta} \propto F(Z,\epsilon_1)F(Z,\epsilon_2)p_1^2 p_2^2(1-\vec{\beta_1}\cdot\vec{\beta_2})(Q_{\beta\beta}-T_1-T_2)^5 \tag{1.7}$$

where p_1, p_2 are the electrons momenta, ϵ_1, ϵ_2 are the electrons energies and T_1,T_2 are the kinetic energies, $\epsilon_i = T_i + m_e c^2$.
The term $(1-\vec{\beta_1}\cdot\vec{\beta_2}) = (1-\beta_1\beta_2 cos\theta)$ is the opening angle distribution of the emitted electrons; $\beta_1 = \frac{p_1}{\epsilon_1}$, $\beta_2 = \frac{p_2}{\epsilon_2}$.
$F(Z,\epsilon_1)$ and $F(Z,\epsilon_2)$ are the Coulomb correction functions for the electrons [14].
The non-relativistic Coulomb correction for electrons utilizes the Rosen-Primakoff approximation ($\beta = 1$):

$$F_{NR}(Z,\epsilon) = \frac{1}{\beta}\frac{2\pi\alpha Z}{(1-e^{-2\pi\alpha Z/\beta})} \tag{1.8}$$

$$F_{NR,PR}(Z) = \frac{2\pi\alpha Z}{1-e^{-2\pi\alpha Z}} \quad \text{for } \beta = 1 \tag{1.9}$$

where Z is the atomic number of the daughter nucleus and α is the fine structure constant.
The general form of the Coulomb correction is a solution of the Dirac equation for an extended nuclear charge; see Eq.1.11.

$$F(Z,\epsilon) = F_R(Z,\epsilon)L_0 \tag{1.10}$$

$$F_R(Z,\epsilon) = 2(1+\gamma)(2pR_0)^{2(\gamma-1)}e^{\pi\eta}\left|\frac{\Gamma(\gamma-i\eta)}{\Gamma(2\gamma+1)}\right|^2 \tag{1.11}$$

In case of the nuclei of interest for the $\beta\beta$ decay the correction factor L_0, which takes into account the electronic screening and a finite nuclear charge distribution, is approximately 1. R_0 is the nuclear radius, p is the electron momentum; $\gamma = [1-(\alpha Z)^2]^{1/2}$, $\eta = \frac{\alpha Z}{\beta}$, $\Gamma(z)$ is the Gamma function defined on the complex plane.

In Fig.1.3 it is reported a comparison of the $2\nu\beta\beta$ electron sum energy spectra for the ^{130}Te isotope in TeO_2 CUORE-like absorbers. The spectra have been obtained utilizing the general form and the non-relativistic approximation for the Coulomb correction functions for the electrons. In case of the non-relativistic approximation, the maximum of the spectrum is shifted to the right. In case of the ^{130}Te isotope, the non-relativistic approximation for the electrons is probably too strict. In fact, utilizing the general form of the Coulomb correction, from Eq.1.11, for the $\beta\beta$ transition rate in Eq.1.7 produces an energy spectrum which is more consistent with the spectrum obtained with complete numerical calculations of the transition rate considering all the nuclear states, performed by F.Iachello and J.Kotila [16], [17].

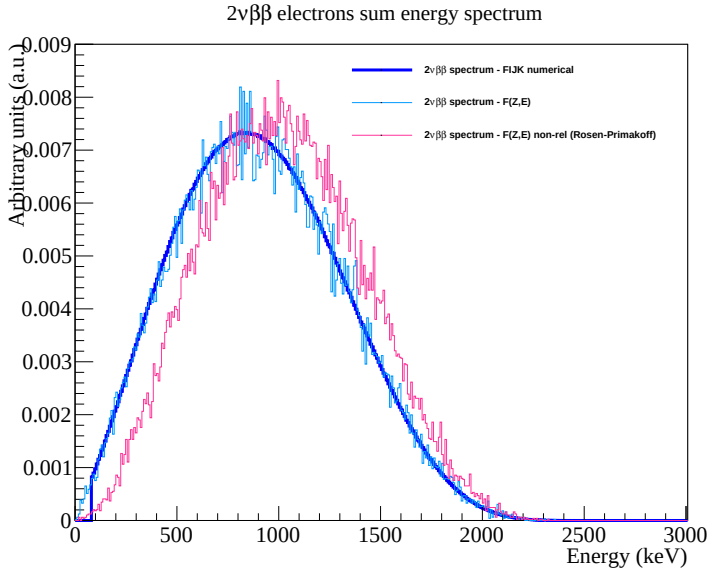

FIGURE 1.3: $2\nu\beta\beta$ electron sum energy spectra obtained utilizing different forms for the $\beta\beta$ transition rate. The spectrum labeled as "$2\nu\beta\beta$ spectrum - FIJK numerical" utilizes the numerical calculation of the transition rate, considering all the nuclear aspects, by F.Iachello and J.Kotila [16], [17]. The spectrum labeled as "$2\nu\beta\beta$ spectrum - F(Z,E)" is produced utilizing the transition rate in Eq.1.7 and the general form of the Coulomb correction from Eq.1.11. The spectrum labeled as "$2\nu\beta\beta$ spectrum - F(Z,E) non-rel" is produced utilizing the transition rate in Eq.1.7 and the non-relativistic form of the Coulomb correction, in the Rosen-Primakoff approximation, from Eq.1.9. The spectra reported in the figure, have been produced with the CUORE Monte Carlo simulation software for the $\beta\beta$ decay of the ^{130}Te isotope.

1.2.2 Neutrinoless double beta decay

Neutrinoless double-beta ($0\nu\beta\beta$) decay is a speculated lepton number violating process that can occur only if neutrinos are massive Majorana fermions [18]–[21].

In this process, two electrons are emitted without being accompanied by neutrinos. This process implies the violation of the lepton number by two units ($\Delta L = 2$)

and can be a signature for new physics beyond the SM.

$$0\nu\beta\beta : (A, Z) \longrightarrow (A, Z+2) + 2e^- \tag{1.12}$$

The experimental signature of $0\nu\beta\beta$ decay is a peak in the summed energy spectrum of the final state electrons at the $Q_{\beta\beta}$ of the decay. See Fig.1.4.

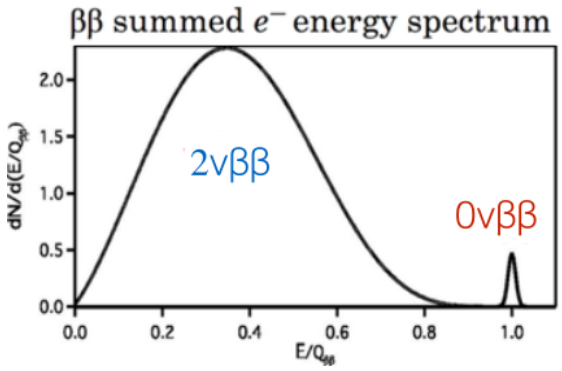

FIGURE 1.4: Schematic view of the $2\nu\beta\beta$ and the $0\nu\beta\beta$ total electron energy spectra.

There is worldwide effort to search for this decay, since its discovery would demonstrate that lepton number is not a symmetry of nature and that neutrinos are massive Majorana particles; additionally, it would be possible to constrain the absolute neutrino mass hierarchy and scale [22] .
The Schechter-Valle (Black Box) theorem [21] states that a positive observation of neutrinoless double-beta decays implies a finite Majorana mass term for neutrinos. In fact, any double beta diagram can be rearranged in order to build a neutrino mass, like in Fig.1.5, so neutrinoless double beta decay induces a non-zero effective Majorana mass for the electron neutrino, no matter which is the underlying mechanism of the decay. The Black Box is a 6 fermions effective operator (dimension 5) for the decay which arises from some underlying New Physics [23].

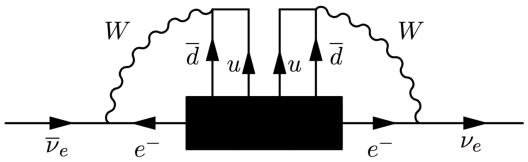

FIGURE 1.5: Contribution of the Black Box operator to the Majorana neutrino mass in the $0\nu\beta\beta$ process [21].

From an experimental point of view, the quantity that could be actually measured is the $0\nu\beta\beta$ decay rate, $\Gamma_{0\nu\beta\beta}$.
With the approximations mentioned above, the factorization of the atomic, nuclear and subnuclear terms can be expressed as Eq.1.13, where $f_{0\nu}$ is a parameter depending on the underlying mechanism responsible for the decay, $G_{0\nu}(Q_{\beta\beta}, Z)$ is the phase-space factor and $|M_{0\nu\beta\beta}|^2$ is the nuclear matrix element.

$$\frac{\Gamma_{0\nu\beta\beta}}{\ln 2} = G_{0\nu}(Q_{\beta\beta}, Z)|M_{0\nu\beta\beta}|^2|f_{0\nu}|^2 \quad \rightarrow T^{1/2}_{0\nu\beta\beta} = \frac{\ln 2}{\Gamma_{0\nu\beta\beta}} \tag{1.13}$$

The half-life of the $0\nu\beta\beta$ process, $T^{1/2}_{0\nu\beta\beta}$, can be expressed as a function of the neutrino mass. In fact, the $|f_{0\nu}|^2$ term in Eq.1.13 is related to the neutrino mass, depending on the neutrino exchange mechanisms that can be involved in the $\beta\beta$ decay.

- *Light Majorana neutrino exchange*: $f_{0\nu} = \frac{\langle m_\nu \rangle}{m_e}$
  This is the most favorable way to obtain $0\nu\beta\beta$ decay in $SU(2)_L \times U(1)_Y$ models. The minimal extension of the SM to account for neutrino mass is to add an effective Lagrangian, corresponding to a non-renormalizable operator of dimension 5 (Weinberg effective theory). In this effective theory the left-handed neutrino ν_L gets a Majorana mass.

  $$\mathcal{L} = \mathcal{L}_{\mathcal{SM}} + m_\nu \nu_L^t C^{-1} \nu_L$$

  In the $0\nu\beta\beta$ process, a light Majorana neutrino would be exchanged, therefore the neutrino Majorana mass term would give a contribution to the process, implying the lepton number violation. In this case the relation $m_\nu \ll q$ holds. $q \approx 100$ MeV, is the transferred momentum to the leptonic part of the interaction hamiltonian.

  $$[T^{1/2}_{0\nu\beta\beta}]^{-1} = G_{0\nu} |M_{0\nu\beta\beta}|^2 \left| \frac{\langle m_\nu \rangle}{m_e} \right|^2 \tag{1.14}$$

  The term related to the neutrino mass contribution $\langle m_\nu \rangle$, is usually referred as the "effective Majorana mass" in the decay:

  $$\langle m_\nu \rangle = \sum_m m^\nu_m \lambda_m U^2_{em} = \tag{1.15}$$

  $$|U_{e1}|^2 m_1 + |U_{e2}|^2 m_2 e^{i2\alpha} + |U_{e3}|^2 m_3 e^{i2\beta} \tag{1.16}$$

  where α and β are the two physical Majorana phases. (1.17)

- *Heavy Majorana neutrino exchange*: $f_{0\nu} = \frac{m_p}{\langle M_\nu \rangle}$
  Another way to obtain $0\nu\beta\beta$ decay is the heavy right handed Majorana neutrino exchange. The massive right-handed neutrino is added to the three SM left-handed light ones in order to develop a renormalizable completion of the SM (3+1 scenario - See-Saw I mechanism). The neutrino mass term in the Lagrangian, here corresponds to an effective operator of dimension 5.
  In case of the $0\nu\beta\beta$ process, $M_\nu \gg q$, where M_ν is the mass of the right-handed neutrino and q is the transferred momentum to the leptonic part. m_p is the proton mass.

  $$[T^{1/2}_{0\nu\beta\beta}]^{-1} = G_{0\nu} |M_{0\nu\beta\beta}|^2 \left| \frac{m_p}{\langle M_\nu \rangle} \right|^2 \tag{1.18}$$

  $$\langle M_\nu \rangle = |U_{e1}|^2 m_1 + |U_{e2}|^2 m_2 e^{i2\alpha} + |U_{e3}|^2 m_3 e^{i2\beta} + |U_{e4}|^2 m_4 e^{i2\phi} \tag{1.19}$$

  $$\approx |U_{e4}|^2 m_4 e^{i2\phi} \tag{1.20}$$

  m_4 is the mass eigenstate of the sterile - heavy neutrino. (1.21)

The kinematic factor $G_{0\nu}(Q, Z)$, in Eq.1.13, describes the available phase space for the decay and it is integrated over the leptonic momenta. In most models, this

factor is only weakly dependent on the details of the decay and can be calculated with great precision. Generally, this factor scales as $Q^5_{\beta\beta}$ for the $0\nu\beta\beta$.

The nuclear matrix element, $|M_{0\nu\beta\beta}|^2$ (NME), in Eq.1.13, describes the transition from the initial nuclear state to the final state (see Eq.1.6). Several techniques have been developed to compute numerically the NME. They make different approximations in modeling the complicated structure of the nucleus [16], [17], [24]–[27].

- The most common approaches in the literature are the quasiparticle random phase approximation (QRPA), which sums many possible energy states of the nucleus but only in a limited number of shell configurations. It describes collective states, but does not give details of dominantly few-particle states.
- The interacting shell model (ISM), sums over all possible shell configurations but only over a limited number of state energies. All configurations of valence nucleons are included and it describes well the properties of low-lying nuclear states. It is technically difficult, thus only calculations for lighter $\beta\beta$ emitters have been performed.
- The interacting boson model (IBM-II) pairs nucleons in shells and treats them as interacting bosons. The NME calculations, for several processes, can be done at the same time, by changing the neutrino "potential", and thus eliminating possible sources of systematic and accidental error.

Typically, the NME term evaluation carries significant theoretical uncertainties since the calculations discussed above can differ significantly. See Fig.1.6.
Following the conventional parametrization [28], the NME is written by explicitly factorizing out the axial coupling term g_A^2: $M_{0\nu\beta\beta} = g_A^2 M^{(0\nu)}$. In the literature, usually the free neutron axial coupling $g_A = 1.269$ is used for calculating the complete NME elements [29], [30]. Observed discrepancies between the calculated NME and observed rates for single beta, electron capture and $2\nu\beta\beta$ could be explained in terms of a quenching of the axial coupling constant, due to correlations with the other nucleons. The details of the $0\nu\beta\beta$ decay are however much different from the processes cited above (e.g the transferred momentum in the $0\nu\beta\beta$ decay is of the order of 100 MeV, higher than in the other mentioned processes) and there is still a strong debate about how the interpretation in terms of g_A coupling is appropriate in this case [31], [32].

Experimental search for $0\nu\beta\beta$

An experiment hunting for $0\nu\beta\beta$ decay, in general, measures the decay spectrum of the candidate $\beta\beta$ isotope and searches for an excess of events at $Q_{\beta\beta}$, which sits at the endpoint of the $2\nu\beta\beta$ spectrum (see Fig. 1.4).

The experimental sensitivity to $0\nu\beta\beta$ can be obtained by considering the half-lifetime corresponding to the maximum signal compatible with the background fluctuations at a given confidence level (n_σ) . In the case of a finite number of observed background counts ($N_B = M \cdot T \cdot B \cdot \Delta > 1$), and assuming a Poisson statistics, this is simply given by the square root of the background counts and the sensitivity can be expressed as:

$$S^{0\nu}(n_\sigma) = \ln 2 \frac{\epsilon x \eta N_A}{n_\sigma M_A} \sqrt{\frac{MT}{B\Delta}} \tag{1.22}$$

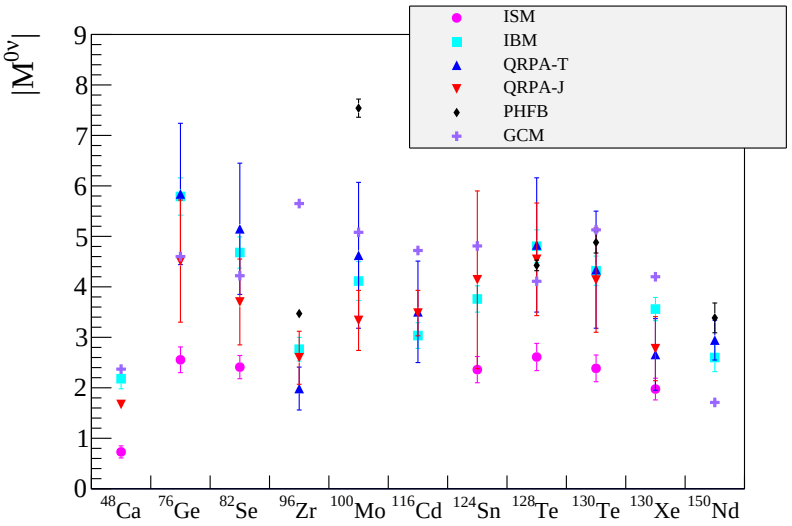

FIGURE 1.6: Distribution of $|M_{0\nu\beta\beta}|$ values for various isotopes using a variety of models for NMEs calculations, assuming the baseline light Majorana neutrino exchange model. The bars represent the minimum and maximum of the range of NMEs and the markers represents the central values. [16], [17], [24]–[27]

where M is total detector mass (kg), T is the measure time (yr), B is the background index in counts/(keV · kg · yr), Δ is the energy resolution (keV), N_A the Avogadro number, x the stoichiometric multiplicity of the element containing the $\beta\beta$ isotope, η the isotopic abundance of $\beta\beta$ isotope, ϵ the detection efficiency, and M_A the molecular mass of the detector compound.

Despite its simplicity, Eq.1.22 outlines all the relevant experimental parameters and is a guideline for the design of any $0\nu\beta\beta$ experiment. In particular, in order to maximize the sensitivity any experiment must have a low background rate (B) near $Q_{\beta\beta}$, a good energy resolution (Δ) and a large isotopic mass (M · η).

When the expected number of background counts near $Q_{\beta\beta}$ along the measurement time is lower than 1, the most probable value for B is zero and therefore no background fluctuations need to be taken into account. We enter the improperly called "zero background" regime and the sensitivity becomes:

$$S^{0\nu}_{ZB}(n_\sigma) = \ln 2 \frac{\epsilon x \eta N_A M T}{N_\sigma M_A} \tag{1.23}$$

where N_σ is a constant term depending only on the selected confidence level n_σ; it corresponds to the maximum number of counts compatible, at a given Confidence Level (C.L.) with no counts observed. This is a very coveted condition since in this regime the sensitivity scales linearly with time and is independent of the background rate and the energy resolution. Most next generation experiments aim for these conditions.

Many recent experimental efforts have focused on discovering $0\nu\beta\beta$ decay, but at present this process has not been yet observed. Therefore several R&Ds are ongoing and aiming at next generation experiments, characterized by improved sensitivities. The experimental challenge takes into account several factors, as stated above, for improving the sensitivity. The main quantities of interest, depending on the choice of the candidate isotope, are: the value of $Q_{\beta\beta}$ and the isotopic abundance of the

chosen nuclide (see Fig.1.7 and Fig.1.8).
The Q-value of the decay, $Q_{\beta\beta}$, correlates with the background counting rate that is expected in the energy region of interest. Experiments using isotopes with $Q_{\beta\beta}$ lower than 2615 keV (the ^{208}Tl γ-line which characterizes the cutoff energy for gamma natural radioactivity), have to employ active background rejection techniques, since the background induced by natural radioactivity is not negligible in the region of interest. Above 2615 keV, the background becomes much lower, and mainly due to $2\nu\beta\beta$ decays, degraded alphas and cosmic rays. When possible, the alpha backgrounds can be discriminated and rejected. Moreover a good energy resolution of the detector helps to disentangle the $2\nu\beta\beta$ background in the region of interest for the $0\nu\beta\beta$ peak.
The choice of the isotope has an obvious impact on the effective active mass for the search: isotopes characterized by large natural isotopic abundances are of course favored, but when the latter is too low, it is possible to enrich the source material in the required isotope. However, this is a procedure that can be extremely expensive and potentially introduce additional radioactive contaminants in the material, increasing the background counting rate.
The currently available most stringent limits on the half-lives, $T^{1/2}_{0\nu\beta\beta}$, for different isotopes from several experiments, are in the range $10^{24} - 10^{26}$ yr and are shown in details in Tab. 1.2.

The half-life limits can be used to extract corresponding limits (at 90% C.L.) on the effective Majorana neutrino mass ($m_{\beta\beta} = \langle m_\nu \rangle$, from Eq.1.15) in case of decays mediated by a light Majorana neutrino exchange, via Eq.1.14. For each isotope the proper phase-space factor $G(Q_{\beta\beta}, Z)$ and the nuclear matrix elements $M_{0\nu\beta\beta}$ can be obtained from a broad range of recent calculations [16], [17], [24]–[27]. In Fig.1.9 the current experimental limits on $m_{\beta\beta}$ obtained by several experiments searching for $0\nu\beta\beta$, with different isotopes and technologies, are reported. The allowed neutrino mass regions for normal and inverted mass hierarchy are the red and green bands; these are two exclusive scenarios. The band width depends on the uncertainties on the neutrino oscillation parameters, mainly on the δ CP phase and on the Majorana phases (α and β). The horizontal bands indicate the most stringent upper limits on $m_{\beta\beta}$ coming from the experimental searches of $0\nu\beta\beta$; their width is due to the uncertainties in the NMEs calculations.

Nuclide	$T^{1/2}_{0\nu\beta\beta}$ Limits [yr]	$m_{\beta\beta}$ [meV]	Experiment
^{76}Ge	$> 8.0 \times 10^{25}$ yr	< 120-260 meV	GERDA - phase II [33]
^{130}Te	$> 1.5 \times 10^{25}$ yr	< 110-520 meV	CUORE + CUORE-0 + Cuoricino [34]
^{136}Xe	$> 1.1 \times 10^{26}$ yr	< 61-165 meV	KamLAND-Zen [35]
^{82}Se	$> 2.4 \times 10^{24}$ yr	< 376-770 meV	CUPID-0 [36]
^{100}Mo	$> 1.1 \times 10^{24}$ yr	< 300-900 meV	NEMO-3 [37]

TABLE 1.2: Current $0\nu\beta\beta$ decay half-life best limits and upper bounds on $m_{\beta\beta}$ from several experiments utilizing different $\beta\beta$ isotopes.

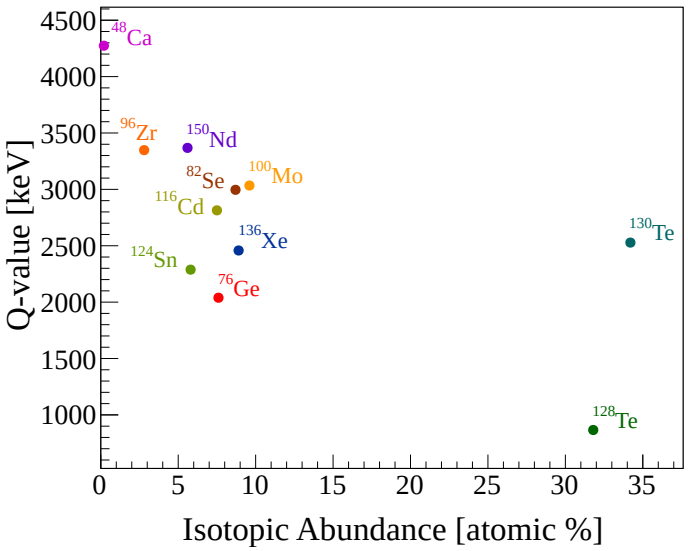

FIGURE 1.7: Isotopic abundance η and Q-value $Q_{\beta\beta}$ for the $0\nu\beta\beta$ candidate isotopes.

$\beta\beta$ Decay Reaction	Isotopic Abundance [atomic %]	Q-value [keV]
^{48}Ca$\rightarrow^{48}$Ti	0.2	4274
^{76}Ge$\rightarrow^{76}$Se	7.6	2039
^{82}Se$\rightarrow^{82}$Kr	8.7	2996
^{96}Zr$\rightarrow^{96}$Mo	2.8	3348
^{100}Mo$\rightarrow^{100}$Ru	9.6	3034
^{116}Cd$\rightarrow^{116}$Sn	7.5	2814
^{124}Sn$\rightarrow^{124}$Te	5.8	2288
^{128}Te$\rightarrow^{128}$Xe	31.8	866
^{130}Te$\rightarrow^{130}$Xe	34.2	2528
^{136}Xe$\rightarrow^{136}$Ba	8.9	2458
^{150}Nd$\rightarrow^{150}$Sm	5.6	3368

FIGURE 1.8: Table of isotopic abundance η and Q-value $Q_{\beta\beta}$ for the $0\nu\beta\beta$ candidate isotopes.

1.2.3 Lorentz violating two-neutrino double-beta decay

The double-beta decay process can be investigated also to test SM extensions other than those accommodating for the Majorana nature of the neutrino.

The Standard Model of particle physics (SM) assumes complete invariance under Lorentz transformations which leads to invariance under CPT transformations. The observation of the violation of either of these symmetries would imply the existence of new physics beyond the SM [38]–[40].

The Standard-Model Extension theory (SME) [41]–[44] includes Lorentz-violating operators and it reduces to the SM at the scale of present experimental observations. A subset of the Lorentz-violating operators also break CPT invariance. The

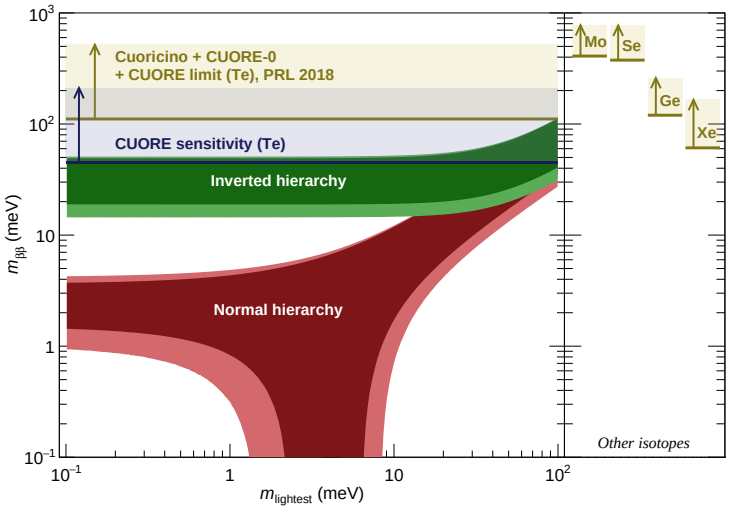

FIGURE 1.9: Experimental limits on $m_{\beta\beta}$. The regions of $m_{\beta\beta}$ allowed by oscillations are shown both for inverted and normal hierarchies of neutrino mass. The horizontal bands with arrows indicate the most stringent upper limits on $m_{\beta\beta}$ coming from the experimental searches of $0\nu\beta\beta$ with several isotopes, including the new results for ^{130}Te from CUORE combined with CUORE-0 and Cuoricino; moreover the CUORE sensitivity on $m_{\beta\beta}$ for 5 years of data taking is shown.

Lagrangian of the SME consists of the Standard Model Lagrangian with additional terms, which take into account the interaction between SM particles, with uniform and constant tensor fields permeating all of spacetime. The SME coefficients characterize the coupling between SM particles and these background tensor fields and control the size of the breakdown of Lorentz symmetry. The determination and classification of these coefficients is possible through the experimental observation of the effect of the tensor field in particle interactions. Experimental limits on hundreds of SME coefficients have been set from analyses from many sectors of physics [45].

Neutrinos are good candidates as probes for this kind of unconventional physics [46]–[49].

In the SME Hamiltonian, the coefficients for Lorentz violation in the neutrino sector act like fixed background fields that trigger observable effects when the neutrino experiment is rotated and boosted. In general, for an experiment, with the source and the detector on the Earth's surface, the neutrino-beam rotates with sidereal frequency $\omega_{\oplus} \simeq 2\,\pi/(23\text{ h }56\text{ min})$ with respect to the background fields, assuming the Sun-centered equatorial frame.

The SME operators that couple to neutrinos in SME can be classified in two types: the ones mixing the neutrino flavors, thus affecting the oscillation properties [50]–[52], and the 'oscillation free' ones. The 'oscillation-free' operators change all neutrino flavors and energies equally, thus leaving the oscillations unaffected. These operators would affect the kinematical properties of the neutrinos, like neutrino velocity or phase space. However 'oscillation-free' operators of dimension 3 do not affect the neutrino velocity; these are examples of 'countershaded Lorentz violations'.

The '**countershaded operator**' is momentum-independent, it has mass dimension three and also breaks CPT. The effect of this operator can be observed through modifications of the phase-space properties, such as in particle weak decays involving neutrinos. The corresponding countershaded coefficient can be written using a

spherical decomposition and it has four components, one time-like $(a_{of}^{(3)})_{00}$ and three space-like $(a_{of}^{(3)})_{1m}$, with m = -1,0,1 [1]. A non-zero value of $(a_{of}^{(3)})_{00}$ would produce small deviations in the shape of the energy spectrum for single or double beta decay, which can be searched for experimentally. A non-null effect of the SME countershaded operator on weak decays energy spectra would allow experimental probes of the space-time symmetries in the neutrino sector, utilizing a different approach with respect to the neutrino oscillation interferometric studies and the neutrino time of flight studies [49].

The coupling of a neutrino to the countershaded operator alters the neutrino momentum:

$$q^{\alpha} = (\omega, \mathbf{q}) \longrightarrow q^{\alpha} = (\omega, \mathbf{q} + \mathbf{a}_{of}^{(3)} - \dot{a}_{of}^{(3)}\hat{\mathbf{q}}) \tag{1.24}$$

In case of the double beta decay $2\nu\beta\beta$ transition [53], the SME countershaded component to the neutrino momentum has to be added. This deviation in the neutrino momentum modifies the form of the decay spectrum. In this case, since the two antineutrinos are not measured, the integration over all the neutrino orientations leaves only the isotropic coefficient $\dot{a}_{of}^{(3)}$ and the neutrino phase space takes the form: $d^3q = 4\pi(\omega^2 + 2\omega\dot{a}_{of}^{(3)})d\omega$.
The $2\nu\beta\beta$ differential decay rate can be then written as in Eq.1.25.

$$\frac{d\Gamma}{dp_1 dp_2 dcos\theta} = \zeta F(Z,\epsilon_1)F(Z,\epsilon_2)p_1^2 p_2^2(1-\vec{\beta_1}\cdot\vec{\beta_2})[(Q_{\beta\beta}-T_1-T_2)^5 + 10\dot{a}_{of}^{(3)}(Q_{\beta\beta}-T_1-T_2)^4] \tag{1.25}$$

The variables in Eq.1.25 are the same as the ones described for Eq.1.7, apart for the $\dot{a}_{of}^{(3)}$ coefficient.
The coefficient $\dot{a}_{of}^{(3)}$ is the parameter of interest in the search, related to the time-like component of the countershaded operator coefficient by:

$$\dot{a}_{of}^{(3)} = \frac{(a_{of}^{(3)})_{00}}{\sqrt{4\pi}} \tag{1.26}$$

From Eq.1.25, the total decay rate can be therefore expressed as a sum of the standard SM decay rate and a CPT violation-related perturbation:

$$\frac{d\Gamma}{dp_1 dp_2 dcos\theta} = \frac{d\Gamma_0}{dp_1 dp_2 dcos\theta} + \frac{d\delta\Gamma}{dp_1 dp_2 dcos\theta} \tag{1.27}$$

where $\frac{d\Gamma_0}{dp_1 dp_2 dcos\theta}$ corresponds to Eq.1.7 and $\frac{d\delta\Gamma}{dp_1 dp_2 dcos\theta}$ contains all the new Lorentz-violating information. The spectral shapes for both parts of the differential decay rate are shown in Fig.1.10.

Current limits on $\dot{a}_{of}^{(3)}$

The Troitsk and Mainz experiments by studying the endpoint of the tritium single beta decay energy spectrum had set conservative constraints on $|(a_{of}^{(3)})_{00}| < 2 \times 10^{-8}$

[1] The index m is related to the sidereal phase $\omega_{\oplus}T_{\oplus}$. This time dependence is due to the change of the neutrino-beam orientation in the Sun centered frame due to Earth's rotation.

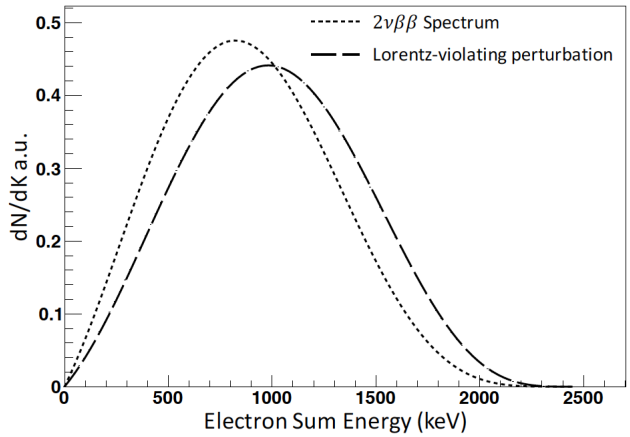

FIGURE 1.10: The electron sum spectra for $2\nu\beta\beta$ decay: SM $2\nu\beta\beta$ process (dotted line) and perturbation due to Lorentz-violating effects, LV (dashed line). Both spectra are normalized to one. [54]

GeV [41]. Studies of threshold effects in pion and kaon decay yield constraints on $\dot{a}^{(3)}_{of} < 1.9 \times 10^{-7}$ GeV [52].

Two double-beta decay measurements have been analyzed to evaluate the $\dot{a}^{(3)}_{of}$ coefficient.
The EXO-200 collaboration utilized a frequentist approach and performed a maximum likelihood fit of the physics data energy spectrum adding the Lorentz-violating double beta decay component to the standard $2\nu\beta\beta$ spectrum and to the background sources. They obtained a limit at the 90% C.L on the coefficient, $\dot{a}^{(3)}_{of} < 7.6 \times 10^{-6}$ GeV [54]. The GERDA experiment utilized a bayesian approach, adding to their minimal background reconstruction, the new spectrum shape with the $\dot{a}^{(3)}_{of}$ coefficient as the fitted parameter. Given the GERDA reconstructed background model, an upper limit of the parameter, comprising the systematic uncertainties, was computed: $\dot{a}^{(3)}_{of} < 7.5 \times 10^{-8}$ GeV (90% C.I.)[55].
In both cases the measurement was characterized by a good collected exposure , a good energy resolution and a low γ background contribution.

- EXO-200 - Exposure: 100 $kg \cdot yr$, Resolution: σ/E=1.23% [54]
- GERDA - Exposure: 19.74 $kg \cdot yr$ (BEGes) + 16.22 $kg \cdot yr$ (enriched coaxials)), Resolution: FWHM/E =0.2% [55]

The CUORE experiment, given the large active mass and excellent energy resolution, has in principle an excellent sensitivity to investigate the CPT violation on the $2\nu\beta\beta$ decay of ^{130}Te.

- CUORE 2017 data - Exposure: 86.3 $kg \cdot yr$, Resolution: FWHM/E $\approx$ 0.3% [34]

Chapter 2

CUORE

2.1 Introduction to the CUORE experiment

The CUORE (Cryogenic Underground Observatory for Rare Events) Experiment is a ton-scale cryogenic experiment based at the Gran Sasso National Laboratories of INFN in central Italy. The goal of the experiment is to investigate the $0\nu\beta\beta$ decay of ^{130}Te[56].
The CUORE detector consists of an array of 988 TeO_2 crystals operated as cryogenic bolometers at $\sim$10 mK. The total mass of TeO_2 is 742 kg, corresponding to 206 kg of ^{130}Te.
The CUORE goal is a sensitivity for limit setting of $S^{0\nu} \sim 9 \times 10^{25}$ y (90% C.L.) in 5 years of data taking [57]. CUORE has been constructed aiming at background index of $10^{-2}\ c/(keV \cdot kg \cdot yr)$ and an energy resolution of 5 keV FWHM in the Region Of Interest (ROI), around $Q_{\beta\beta}$. This requires CUORE to be operated a low radioactivity [58] and low vibration environment.

In this chapter the CUORE detector and the experimental setup will be described.

2.2 TeO_2 bolometric detectors

The CUORE choice of using the ^{130}Te isotope to search of the $0\nu\beta\beta$ process has been driven by several factors. This isotope has large transition energy, $Q_{\beta\beta}(^{130}Te)$ = 2527.518 keV, and this helps in order to have a reduced background from natural radioactivity in the region of interest. It has also the highest natural isotopic abundance, η = 33.8%, among the $\beta\beta$ emitters (see Fig.1.7). This avoids the need for a costly and time-consuming isotopic enrichment.

2.2.1 TeO_2 absorbers

The CUORE experiment employs a bolometric energy detection method, and thus operates at temperatures of the order of $\sim$ 10 mK.
The use of bolometers as single particle interaction detectors was proposed in the 1980s for several applications in , nuclear physics, astrophysics and neutrino physics, like for the search of $0\nu\beta\beta$ decay. The bolometric method is characterized by an extremely good energy resolution. It is therefore possible to consider a narrower ROI, and fewer background events will contend with the $0\nu\beta\beta$ signal. However it has to be taken into account the technical difficulty of cooling a large mass bolometric detector to such a low temperature. See Chap.3 for more details about the bolometric technique.

Bolometers made of materials containing $\beta\beta$-emitters, were developed by the group of E.Fiorini [59], that mainly focused on the search for the $0\nu\beta\beta$ of ^{130}Te using

TeO_2 crystals.
The Tellurium dioxide (TeO_2) has been found suitable for the use in cryogenic particle detectors for its thermodynamic characteristics:

- TeO_2 crystals are both dielectric and diamagnetic.
- TeO_2 has low heat capacity at cryogenic temperatures, due to the high Debye temperature (Θ_D = (232 $\pm$ 7) K) [60]. For a given energy release, this induces large temperature variations, which improves the bolometer performance (resolution, $\Delta E \sim 0.1$ % at $Q_{\beta\beta}$).
- The TeO_2 in para-tellurite form (α-TeO_2, colorless tetragonal) is commercially produced at industrial scale.
- The TeO_2 crystals are characterized by low spurious contaminations in the lattice and therefore have a good radiopurity

The mechanical characteristics of these crystals match the requirements for the application in the $0\nu\beta\beta$ search. The techniques for growing the crystals have improved with time and allowed the production of almost perfect crystals (bubble-free, crack-free, ...). Moreover dedicated production lines for the preparation of the TeO_2 powder, the crystal growth and the surface contamination polishing made the crystals compliant with the radiopurity constraints to allow an acceptable background rate in a tonne-scale detector. [61]–[65]

The CUORE TeO_2 crystals are $5\times5\times5$ cm^3 each and weigh an average of 750 g (see Fig.2.1). They are made with ^{nat}Te; each crystal contains 208 g of ^{130}Te. The crystals were grown by The Shanghai Institute Of Ceramics, Chinese Academy of Sciences (SICCAS) [63].

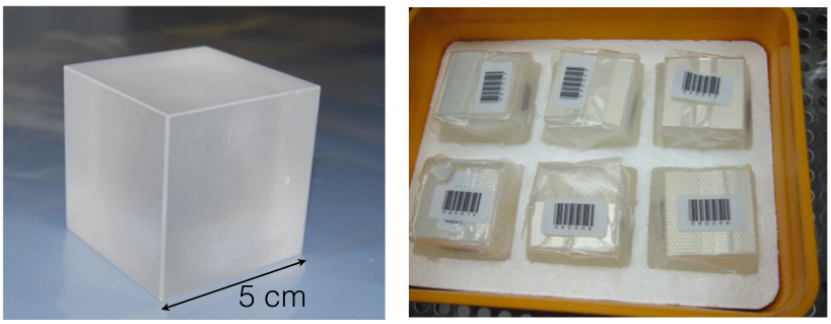

FIGURE 2.1: [Left] Picture of a CUORE TeO_2 crystal. [Right] Six TeO_2 crystals packed in vacuum for transportation and storage, before the detector was assembled. [66]

In conclusion, using TeO_2 crystals allows to have the ^{130}Te source within the detector absorber itself, increasing the detection efficiency. The technology for the growth of TeO_2 crystals makes possible to produce a large number of high quality detectors, therefore ensuring the possibility to increase the active mass. When the TeO_2 crystals are operated as bolometers at very low temperatures [59], [67], they can reach an excellent energy resolution, and this reduces the irreducible background around $Q_{\beta\beta}$ due to the $2\nu\beta\beta$ decay.

2.2.2 Bolometer Instrumentation

A bolometric detector consists generally of a (massive) single crystal (absorber), a supporting structure and a proper temperature sensor. The sense wires and the supporting structure provide the thermal conductance to a heat sink.

Each TeO_2 crystal is instrumented with a Neutron Transmutation Doped germanium (NTD-Ge) thermistor [1] and a silicon heater to monitor the response stability [66].
The NTD-Ge acts as a voltage transducer. The thermal phonons, produced by the energy release in the TeO_2 crystals, are converted into a voltage pulse at the thermistor ends. Wafers of ultra-pure germanium were produced at LBNL in Berkeley. These were irradiated with thermal neutrons at MIT Nuclear Reactor Laboratory. The neutrons are able to penetrate the bulk of the Ge wafers and this produces an uniform doping in Ga, As and Se across the entire wafer. After a waiting period of approximately 6 months, to make the short-lived isotopes decay away, the wafers were diced into $3\times3\times1$ mm^3 chips. At LBNL, gold plated electrodes were deposited along the sides of the chips; these wrap slightly around to the top of the NTD covering two small, parallel regions of area 0.2×3.0 mm^2. This wrap-around sensor design allowed for bonding on the top of the thermistors; therefore they could be bonded with gold-wires in-situ after being attached to the bolometer. See Fig.2.2.

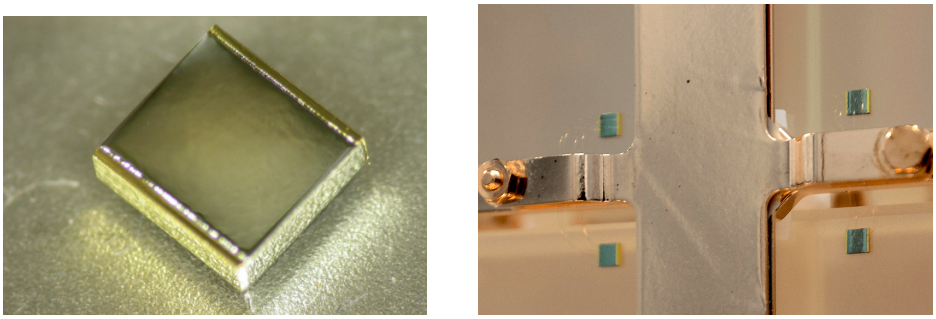

FIGURE 2.2: [Left] Picture of a CUORE NTD chip [66]. [Right] CUORE NTDs glued on the crystals and bonded to the read-out strips through gold wires.

Each crystal absorber is also instrumented with a Joule heater, which is designed to periodically provide a fixed amount of energy in the detector for gain stabilization purposes. It is a custom-designed high purity $2.33 \times 2.40 \times 0.52$ mm^3 Si semiconductor chip. On the chips, a heavily doped meander was fabricated through the standard silicon planar process. The doping results in a typical resistance of 300 $k\Omega$ for the chips. They were manufactured at Istituto per la ricerca scientifica e tecnologica (IRST), presently Fondazione Bruno Kessler (FBK) company in Trento, Italy. See Fig.2.3.

The NTDs and the heaters are glued on each crystal by means of a fixed number of epoxy glue spots to provide mechanical and thermal coupling. The choice of distributing the glue in arrays of dots (nine-dot matrix for thermistors and five-dot matrix for heaters, see Fig.2.4) rather than a continuous film, was taken in order to provide a good thermal coupling and a lower risk of temperature-induced stress fractures or detachment. The glue spots were deposited by a mechanic arm,

[1] See Chap.3.4.1 for details about the NTD phonon sensors which are coupled to the bolometer crystals.

a semi-automated system which was developed to achieve precise, uniform and reproducible chip-absorber couplings. The Araldit Rapid Epoxy glue is utilized since it guarantees a low failure rate during the cool-down and low radioactivity.

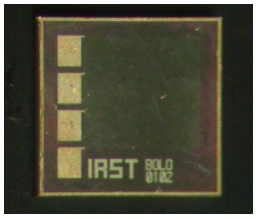

FIGURE 2.3: Picture of a CUORE Si-heater chip [66].

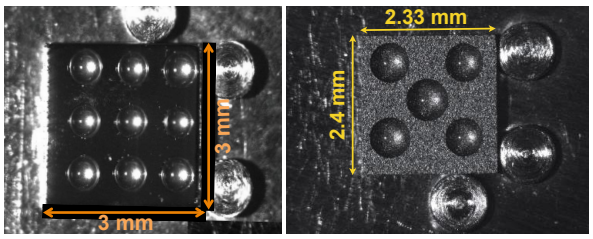

FIGURE 2.4: Glue-spot arrays deposited on a NTD thermistor [left] and on a Si-heater [right]. [66]

The signal readout is accomplished through Cu-PEN cables which are connected to the NTD and heaters by 25 μm ball bonded gold wires (Fig.2.5).
Each NTD is separately biased by means of a dedicated circuit maintained at room temperature and characterized by a differential low noise read-out and two large load resistors.
Calibration pulses from high precision pulser boards are sent periodically to the heaters to correct for possible thermal instabilities of the system [68].

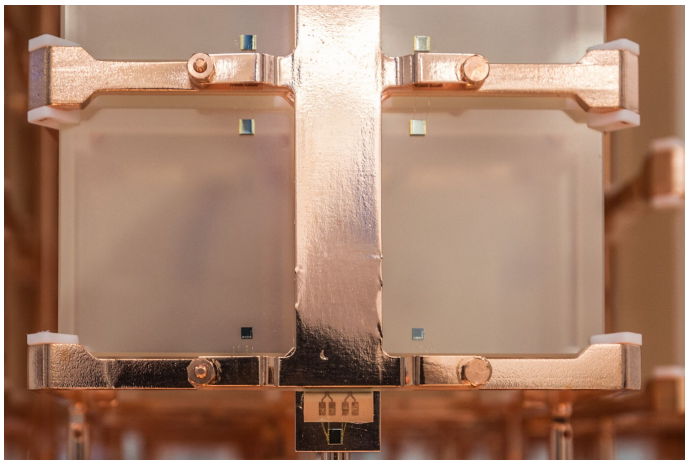

FIGURE 2.5: Picture of the CUORE instrumented bolometers. Focusing on the two crystals in foreground: the smaller black chip at the bottom is the silicon heater and the NTD is the chip on the upper part of the crystals.

More details about the CUORE detector assembly will be given in Sec.2.3.3.

2.3 Experimental setup

2.3.1 Underground location

The CUORE experiment is hosted in the Hall A of the Laboratori Nazionali del Gran Sasso (LNGS, Assergi (AQ), Italy) of the Istituto Nazionale di Fisica Nucleare (INFN). A deep underground location, in which the cosmic ray direct and induced backgrounds are reduced, is fundamental for rare event physics experiments, such as the search for $0\nu\beta\beta$.
The Gran Sasso mountain provides the detector with an overburden of 1400 m of rock (3600 meters of water equivalent), mostly calcareous [69]. The cosmic ray rate is reduced by 6 orders of magnitude relative to the surface, this strongly reduces the related background due to spallation products and cosmogenic activation. The measured muon and neutron fluxes at LNGS are about $3 \cdot 10^{-8}\ cm^{-2}s^{-1}$ and $4 \cdot 10^{-6}\ cm^{-2}s^{-1}$ respectively. [70]–[72]

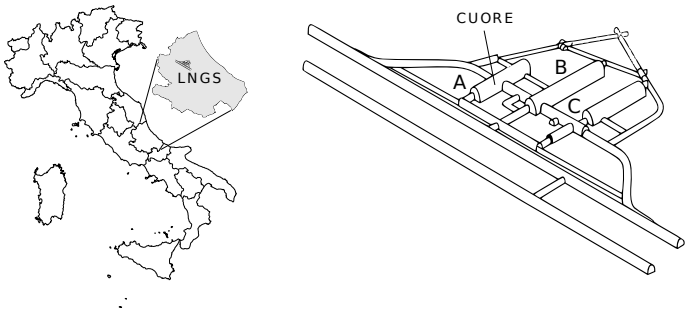

FIGURE 2.6: [Left] Map of Italy with the location of LNGS in the Abruzzo region. [Right] Map of the underground laboratories. The CUORE experiment position in the Hall A is indicated.

2.3.2 The CUORE cryogenic infrastructure

The CUORE TeO_2 crystals have to be operated at a temperature of $\sim$ 10 mK in order to behave as bolometers. The CUORE cryostat has been designed to house the ton-scale bolometric detector. Moreover, to avoid radioactive background, only a few construction materials were acceptable and lead shields were integrated in the structure (more details on the lead shields in Sec.2.3.4).

A specific cryogenic system was designed for CUORE in order to cool down the TeO_2 detectors, the cryostat components and the Pb shields and to maintain the detector volume stably at a temperature around 10 mK for at least 5 years [73]. The cooling of the detector is accomplished by a cryogen free refrigerator consisting of three subsystems: the Fast Cooling System (FCS), five Pulse Tube cryocoolers (PTs), and a powerful custom $^3He/^4He$ dilution refrigerator (DU).

Cryostat

The thermal isolation of the detector volume from the environment is crucial to maintain the very low temperature over long periods of time. This is obtained

through a multi-stage custom cryostat, consisting of six coaxial nested copper vessels, each with a corresponding top plate and flange which defines six nested independent volumes. The six vessels act mainly as thermal shields. They are maintained at temperatures of 300 K, 40 K, 4K, 600 mK (Still), 50mK (Heat Exchanger - HEX) and 10 mK (Mixing Chamber) [2], respectively [74].

The 300K and the 4K vessels are vacuum tight and define two separated volumes, Outer and Inner Vacuum Chamber (OVC and IVC).

The vessels and plates are made of high purity copper produced by Aurubis company. This choice of material was made to fulfill the requirements on the radioactivity content of the various components [3], given that the background coming from the cryogenic apparatus had to be compatible with the CUORE sensitivity goal. Only electron beam welding has been used for the construction of the cryostat vessels in order to avoid any possible contamination from carry-over of the welding electrodes.
For the 40 K, the 4 K, the Still and the HEX vessels and flanges it was used the Oxygen-Free Electrolytic copper (Cu-OFE), which is the highest purity copper commercially available (99.99%). The 300K vessel is also mostly made of Cu OFE. However the 300K plate and the upper flange are made of stainless steel, for better vacuum tightness and for sustaining the mechanical stress of all the mass that is connected to those.
Super-insulations layers are applied on the external surfaces of the 40 K and 4 K vessels, in order to limit the thermal radiation coming from higher temperature vessels. Each super-insulation foil consists of a double high reflectivity aluminized mylar interleaved with low thermal conductivity polyester layers.
The 10mK plate, flange and vessel are made of ETP1 copper alloy (Electronic Tough Pitch, also called Cu NOSV by Aurubis), having a low radioactive content and a low hydrogen content [4]. The Tower Support Plate (TSP) is inside the 10mK stage and it is made in Cu NOSV, as well. This plate supports the CUORE detector and is vibrationally decoupled from the cryostat structure. Indeed, in order to minimize the transmission of vibrations from the supporting structure, the cryostat is anchored from above to a structure called Main Support Plate (MSP), while the detectors array is suspended on the TSP, inside the 10mK vessel, by means of an independent damping suspensions.

A rendering of the CUORE cryostat is shown in Fig.2.7.

Pulse Tubes and Fast Cooling System

A two-stage PT system maintains at 35 K and 3.5 K respectively 980 kg and 7400 kg of material, mainly the cryostat plates and vessels and the inner lead shielding.

The cool-down procedure is performed in subsequent stages.
The first phase of the cool down is a pre-cooling of the whole system to a temperature of 30-40K. This procedure is initially driven by the FCS [75]. The fast cooling system

[2] These values are referred to nominal temperatures for the stages, but the actual temperature of each stage could be slightly different.

[3] Mainly Th and U bulk contaminations in copper have to be reduced. Moreover the amount of radiogenic ^{60}Co in a normal copper stored at ground level, is not compliant with the requirements for reaching the CUORE nominal background.

[4] The presence of H_2 molecules at the bolometers operating temperatures, $\sim$ mK, can affect the temperature stability. In fact, the esothermic conversion of ortho-H_2 into para-H_2 produces an heat release over long times.

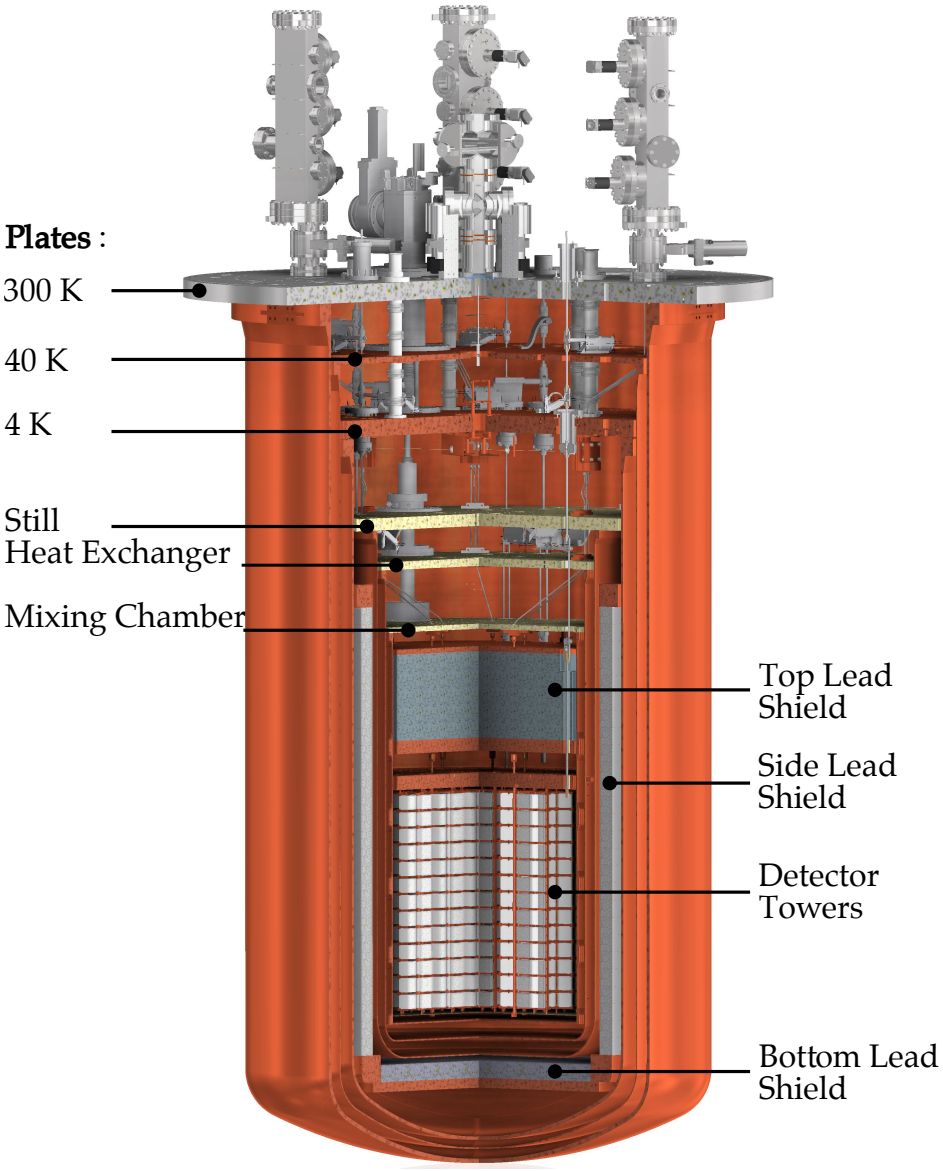

FIGURE 2.7: Representation of the the CUORE cryostat: the plates and vessels corresponding to the different thermal stages and the lead shieldings.

has, in fact, been designed and realized to provide a fast cool-down of the inner cryostat mass (IVC volume) from room temperature to $\sim$ 50 K and consequently to boost the initial cooling phase. This is based on a flow of cold helium ^4He gas through the cryostat chambers. The He is cooled down by means of an external cryostat powered by three Gifford-McMahon (GM) cold heads and the gas is injected into the IVC through a proper combination of dedicated PolyTetraFluoroEthylene (PTFE) tubes and then circulated back into the external cryostat.
The PTs are turned on a few days after the FCS is in operation, when the IVC temperatures are close to 200 K. With this configuration, the cryostat reaches 50K in approximately two weeks; the FCS is then switched off and only the PTs remain active.

The second phase of the cool down takes the mass inside the IVC at $\sim$ 4 K.

The PTs provide the basic cooling power to the system in order to reach a temperature close to 4K, by bringing and maintaining the corresponding stages of the cryostat at their design temperature.
A Pulse Tube is a cryocooler whose cooling power is provided by means of ^4He gas iso-enthalpic expansions [76]. The use of PTs increases the total duty cycle of the experiment with respect to the conventional LHe bath, due to the absence of cryogens to refill. A possible disadvantage of PTs is the increase of noise contributions due to vibrations. However, these cryocoolers do not have any moving parts at low temperatures; this increases the reliability, reduces the magnetic interferences and the intensity of vibrational noise generated with respect to other cryocoolers.
The cooling effect in a PT is obtained by a periodic pressure variation and a displacement of the working gas (He) inside one or more thin-walled tubes (the actual "pulse tubes"), which contain a large heat capacity regenerator and with heat exchangers at both ends. The pressure cycles are provided by a rotating valve (working at room temperature, moved by a DC stepper motor), that alternatively connects the PT to the high and low pressure sides of a compressor sending in the He gas. The valve makes 0.7 revolutions per second. This results in pressure waves with a frequency that depends on the PT model and which is 1.4 Hz for the CUORE PTs.
Small residual mechanical vibrations still occur in a PT due to the elastic deformation caused by pressure oscillations in the He gas inside them, thus care must be taken to minimize the impact of these residual mechanical vibrations on the detectors. In CUORE, a series of passive countermeasures have been utilized to minimize the vibrational noise coupled from the PTs into the detector system. Custom made rigid lines and commercial flex lines, after coming out from the He compressors, enter a sand box filled with non-hygroscopic quartz powder and then reach the PT motor-heads avoiding any contact with the cryostat. A remote motor option has been chosen for the PTs, meaning that the rotating valves are separated from the PT heads by means of flexible Stainless steel swan-neck outlets. The gas inlet/outlet high-pressure lines, the rotating valves and the expansion vessels are suspended to the room ceiling by means of elastic bands to further absorb the vibrations. Beside the several passive precautions, an active system to reduce PT induced noise has been developed (see Chap.4.2.1,[77]).

The CUORE experiment mounts five PTs (PT415-RM) by Cryomech [78]. These are characterized by two stages at 40 K and 4 K. Each one has a nominal cooling power of 1.2 W at 4.2K and 32 W at 45 K. Figure 2.8 shows a rendering of one of the CUORE PTs.
The large number of PTs installed in CUORE cryogenic system is determined by the significant heat load in this large system. The cooling power provided by 4 PTs is sufficient to operate the CUORE dilution unit (DU, see following section for details). The fifth PT is kept as a spare. The CUORE PTs are arranged on a circumference with a radius of $\sim 2/3$ of the top cryostat plate (300 K plate) , see Fig.2.9.

Dilution Unit

The cooldown to a base temperature below 10 mK is provided by a continuous-cycle ^{3}He-^{4}He Dilution Refrigerator (or Dilution Unit, DU), designed and built by Leiden Cryogenics for CUORE. It is a DRS-CF3000 Joule-Thomson Dilution Refrigerator; the nominal cooling power is 3μW at 12 mK (2 mW at 120 mK). The lowest temperature reached in the CUORE cryostat at full load is around 7 mK.

The working principle of a continuous-cycle DU is based on the phase diagram of the ^{3}He-^{4}He mixture a low temperatures. The dilution refrigerator is filled with a

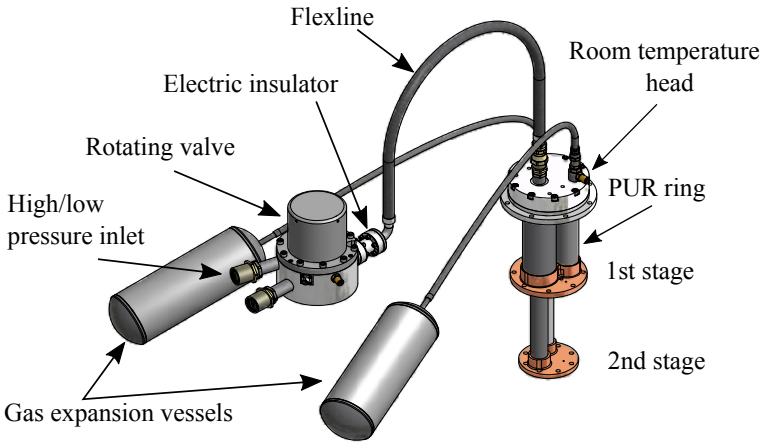

FIGURE 2.8: Rendering of a CUORE PT.

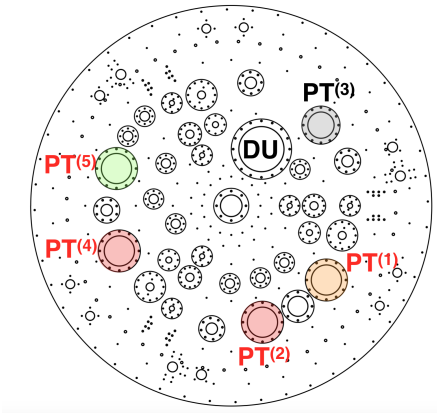

FIGURE 2.9: Top view of the 300 K plate of the CUORE cryostat. The positions of the five PTs and of the Dilution Unit (DU) are highlighted.

mixture of ^3He (17%) and ^4He, which is pre-cooled to 4 K (by the PTs system). The He liquid mixture is homogeneous at that stage. The temperature of the mixture is lowered by pumping on its surface with a vacuum pump which works at room temperature (300 K).Below 0.87 K the ^{3}He-^{4}He mixture separates into two phases: an ^3He rich phase (RHS, an almost pure ^3He Fermi liquid) and a ^3He dilute phase/^4He rich phase (LHS, an ^4He Bose liquid with a small concentration of ^3He). At first, as a consequence of its lower density, there is only LHS mixture in the Mixing Chamber (MC) and the ^3He is floating into the Still. The enthalpy of the ^3He in LHS is larger than the one of ^3He in RHS. ^3He atoms are drawn from the RHS phase across the phase interface to the LHS, to reach the thermal equilibrium. This is an endothermic reaction, which subtracts energy from the environment (walls of the MC). This mechanism generates the cooling power of the dilution refrigeration. A continuous cooling power is obtained by keeping the LHS out of equilibrium by extracting its ^3He content with a powerful pump and injecting it back into the circuit. The cooling proceeds until the heat extraction rate is balanced by the sum of the various heat inputs.

The CUORE ^{3}He-^{4}He mixture recirculation system is very complex. Since no cryogenic pump is located inside the CUORE cryostat, the ^3He gas has to be extracted out of the cryostat and then injected back without creating instabilities on the cryostat temperature. Before re-entering the cryostat, the ^3He gas is cleaned in

LN_2 traps. There are 2 condensing lines for the incoming mixture to the DU, which are thermalized between the two cold thermal stages of the PTs. This configuration allows to continue the run in case one of the lines becomes unusable. Along the condensing lines, the ^3He condenses by passing through a series of counterflow heat exchangers (HEXs) and then is injected back into the MC.

A schematic representation of the DU working principle and of the CUORE DU system is reported in Fig.2.10.

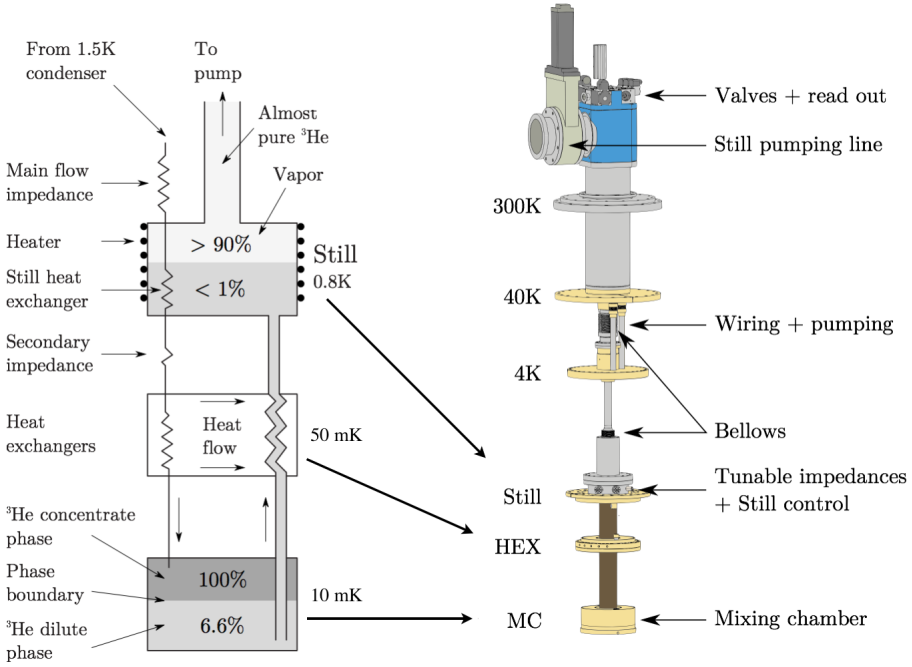

FIGURE 2.10: [Left] Functioning scheme of the DU system. [Right] Rendering of the CUORE DU from the room temperature stage to the MC (10 mK).

Thermometry

The CUORE cryostat is monitored, in all its temperature stages, by tens of thermometers. Different thermal sensors are necessary since the temperature spans over a very broad interval of values, from room temperature (300K) to detector base temperature ($\sim$ 10 mK).
Silicon diodes resistance thermometers are used to measure temperatures > 4 K. Ruthenium oxide (RuO_2) resistors are mounted on the Still and on the stages thermalized at 50 mK; these devices are utilized to measure temperatures from < 1 K to $\sim$ 50 mK.

The absolute temperature of the MC, down to few mK, is monitored by a Noise Thermometer (NT). Its calibration has been cross-checked by using as a reference a superconductive Fixed Point Device (FPD). The NT used in CUORE is a Magnetic Field Fluctuations Noise Thermometer (MFFT-1 NT) by Magnicon. The NT technology is based on the statistical thermal motion of the conduction electrons in resistive materials (e.g. copper foils). The mean square of the voltage fluctuations is correlated with the temperature, considering the Johnson noise of the resistor. The voltage fluctuations are usually amplified by the use of SQUIDs, which detect the magnetic-field fluctuations across the resistor surface (Thermal Magnetic Flux Noise), induced

by the thermal noise currents inside the copper body. The MFFT-1 software returns a temperature value as output with a relative error of less than 1% at a few mK.

Due to the strong radioactivity constraints for devices in the innermost part of the cryostat, only NTDs, of the same type used for the TeO_2 detectors, are used for the temperature monitoring on the 10 mK plate and on the TSP.
Two NTDs on the TSP (ch 1017, ch 1018) and two NTDs on the MC plate (ch 1019, ch 1020) are continuously acquired; channel 1019 is used as the input for the MC temperature stabilization system (see Chap.4.2.3). The NTDs on the two different plates were utilized also to monitor the differences of the vibrational power spectra for the two mechanically decoupled stages. There are also several NTDs attached along the CUORE detector copper frame, to monitor the temperature stability and the vibrations of regions closer to the CUORE bolometers.

2.3.3 The CUORE detector

The CUORE detector consists of an array of 988 bolometric TeO_2 crystals arranged into 19 identical structures called "towers". Each tower hosts 52 bolometers arranged in 13 floors, each containing 4 crystals. See Fig.2.11. Given that each crystal has a mass of 750 g, the total mass is 742 kg of TeO_2, or 206 kg of ^{130}Te.

FIGURE 2.11: The complete CUORE detector: the 19 towers modules hosting the 988 TeO_2 crystal.

Several TeO_2 arrays with increasing mass were constructed and tested over many years [79]–[81]; thus a lot of experience was accumulated and that helped the design and the development of the ton-scale CUORE detector. See Fig.2.12.
The CUORICINO experiment ran from 2003 to 2008 in Hall A at LNGS. The detector consisted in a tower containing 62 TeO_2 crystals, for a total mass of 40.7 kg ($\sim$ 11 kg of ^{130}Te). The CUORICINO tower included crystals of different sizes, including CUORE-sized crystals ($5 \times 5 \times 5\ cm^3$) and smaller ones ($3 \times 3 \times 6\ cm^3$), enriched in ^{130}Te. [82]

The CUORE-0 experiment consisted of 52 CUORE-sized bolometers arranged in a single tower, with a total active mass of $\sim$ 39 kg. The structure of the CUORE-0 tower was identical to the towers currently used for CUORE. The detector was housed in the same cryostat used for the CUORICINO array; it ran from 2013 to 2015. The main purposes of CUORE-0 experiment were: testing the CUORE towers assembly line and verifying the effectiveness of the improved material cleaning techniques employed after CUORICINO to reduce the radioactive background. [66]

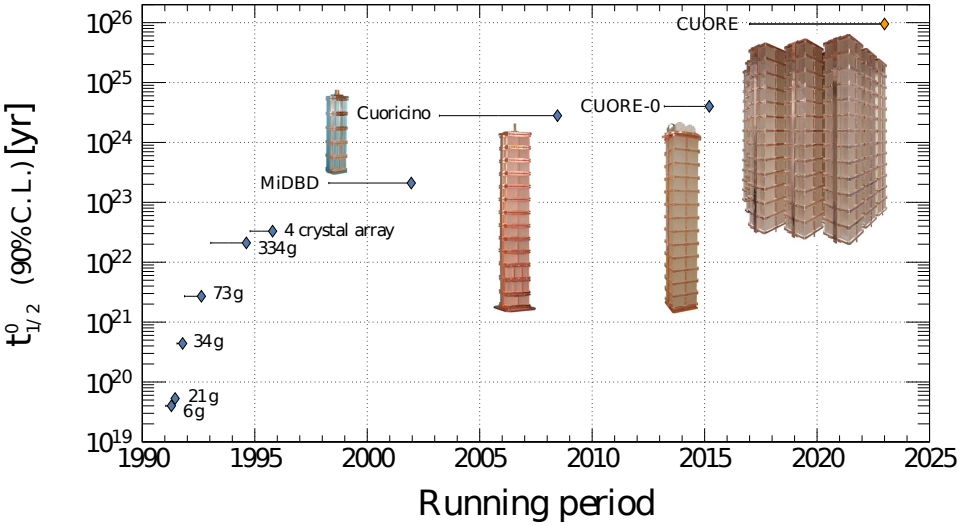

FIGURE 2.12: Time evolution of TeO_2bolometric experiments hunting for $0\nu\beta\beta$ decay of ^{130}Te, and corresponding half-lives sensitivities. [83]

CUORE towers assembly

The CUORE TeO_2 crystals, which act at the same time as source and detectors of $0\nu\beta\beta$ decays, are held in the tower structure by means of Cu frames and PFTE holders (Fig.2.13).
The copper structure is designed to reduce the amount of material near the detector to a minimum, given the mechanical and thermal constraint for the structure of a tower. However, since the frames are facing the detector directly, they are made out of Cu-NOSV alloy. The copper offers a high thermal conductivity and it acts as heat sink at the base temperature of about 10 mK.
Eight PTFE holders, one on each corner of the TeO_2 cube, support the crystals inside the copper frame. In this way, the crystals are not directly in contact with the copper structure; the PTFE spacers act as mechanical supports and a weak thermal link to the heat sink (i.e. the frame itself).

The CUORE crystals, were mounted in the tower structures by means of a dedicate *towers assembly line* [84]. This consisted in three steps: crystal gluing, tower assembly, and tower wiring. Each of them was performed in a specially designed glove box (Fig.2.14). In the glove boxes, the detector parts were kept under constant N_2 flux and out of contact with any of the rest of the environment of the clean room. Moreover strict radio-purity controls on materials and assembly tools have been performed during this procedure.

The CUORE towers were assembled from September 2012 to July 2014. In the meantime, the commissioning of the cryogenic system was performed. The towers

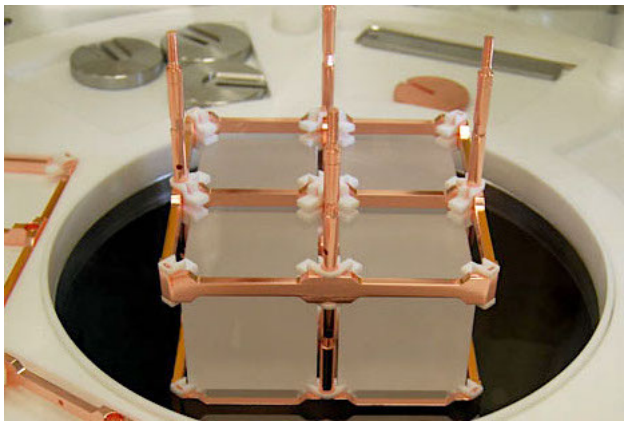

FIGURE 2.13: CUORE tower mechanical assembly: TeO_2crystals held inside the Cu structure by means of the white PTFE holders.

FIGURE 2.14: The CUORE towers were assembled in specially designed glove boxes under N_2 flux.

were stored into the clean room, in the CUORE hut, in containers with continuous clean N_2 flushing (Fig.2.15 [left]), to prevent any contamination from Rn. The towers installation in the cryostat structure was performed in summer 2016. Since it was not possible to perform this manual operation under N_2 flux, a dedicated clean room flushed with radon-free air was built around the cryostat [85]. In this controlled clean room environment, the air was passed through a Rn filter and monitoring system (Fig.2.15 [right]).

Read-out chain

The CUORE electronics chain provides the bias current to the NTDs and the read-out for the bolometer signals. It is composed by three components: Front End boards (FE), which power the NTDs and amplify the signal, Bessel filters, and Pulser boards. The electronics chain and the DAQ boards (see Sec.2.4.1 for details about the data acquisition) sit at room temperature.

The front-end (FE) electronics were specially designed for CUORE [86].
The FE racks are situated on dedicated supports overlying the cryostat suspension structure. Each rack has two crates; a FE crate hosts 13 FE boards. On the back panel of each crate, there are 6 cables arriving from the cryostat. Each cable contains the wires of 13 bolometers (one column of a tower). Therefore each crate collects the

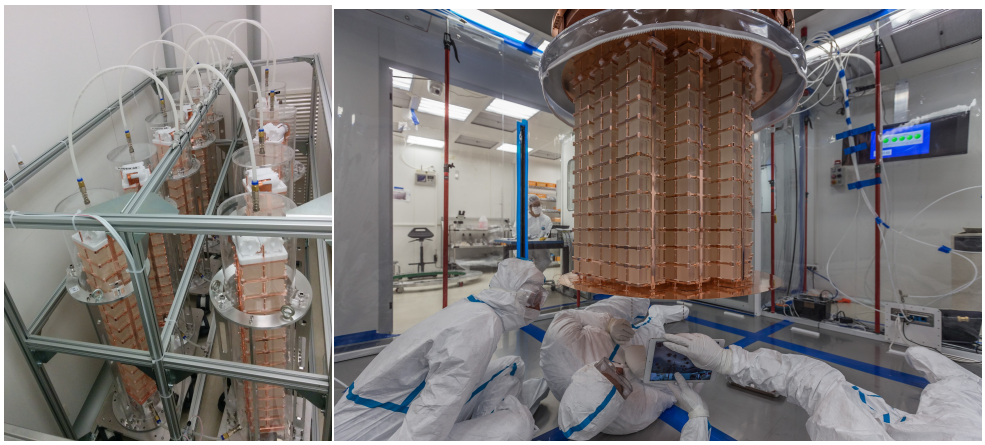

FIGURE 2.15: [Left] CUORE towers stored into N_2 flushed containers before being mounted in the cryostat. [Right] CUORE towers installation.

signal from 78 channels (1 tower and 1/2 tower); each FE board reads 6 channels. Every FE board provides a stable low-noise DC bias voltage ($I_{Bias} \sim 100$ pA), adds an adjustable offset to the NTDs voltage output (V_{bol}) to maintain the output at the end of the readout chain within the digitizers dynamic range, and passes the voltage signal through a two-stage amplifier. For example, given that the NTD pulses are quite small, like $\sim$ 200 μV/MeV, with an amplification gain of 5000, the voltage signal is increased to $\sim$1 V/MeV. The FE parameters like gain, bias, offset and load resistance are remotely programmable and channel dependent values can be set [5]. The signals are read in direct current mode (DC); in this way, the baseline value (i.e. the output voltage value read just before a pulse) can be used as temperature reference for the particle energy reconstruction. In order to suppress the common mode noise, such as cross-talk between two adjacent channels, the thermistor signal is not referenced to ground but is acquired in differential mode.

Signals coming from the FE boards are grouped and sent to the Bessel boards before being digitized. Every filter board handles 12 channels.
The filtering boards are custom made, anti-aliasing active low-pass filters of Bessel-Thomson type (six-poles filter). The filter provides an attenuation of 120 dB/decade and its cutoff frequency can be remotely set to 15, 35, 100 or 120 Hz.

The CUORE electronics also includes the Pulser boards. These are used to send electric pulses to the Joule heaters on the crystals, then releasing a constant energy on the absorber which mimics a particle interaction. Each Pulser board can send a square signal, into four separate channels, by means of a set of relays; every channel is connected to a detector column (13 channels) so a Pulser board accounts for a detector tower. The heater chips of bolometers belonging to the same column of a given tower, are connected in parallel. The amplitude, the duration and the periodicity of the pulser signal can be remotely adjusted. In order to create a pulse as similar as possible to a real particle interaction, the duration has been found to be $\sim$ 400 μs.

Figure 2.16 shows the scheme of the electronics system.

[5] The effective gain is a combination of two amplifiers, a DVP Amplifier (Pre) and a Programmable Gain Amplifier (Pga): Gain = PreGain $\times$ PgaGain; the PreGain can be either 206 or 29 V/V, the PgaGain can be any integer from 1 to 50 V/V. The bias can be set between 0 and 30 V; the offset can be set from -10 V to 10 V. The accuracy on setting and reading the bias and the offset values is $\sim$ 10 mV. The load resistance, R_{load}, can be chosen between 10 and 60 GΩ.

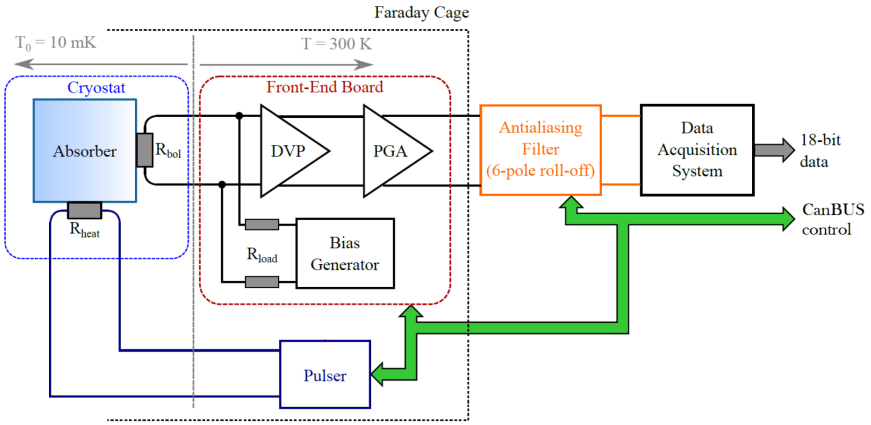

FIGURE 2.16: Schematic of the CUORE bolometer electronics chain. [66]

2.3.4 The CUORE auxiliary systems

Cryostat support structure and detector suspension system

The CUORE experiment, which utilizes cryogenic calorimeters, needs to reduce every source of noise induced on the detectors, like vibrations which transfer heat to the crystals due to vibrations. Therefore, all possible sources of vibration need to be kept under control and the detector needs to be isolated.

The cryostat support structure has been designed to accomplish two main functions: mechanical support of all the cryostat parts and isolation of the cryostat from the surrounding environment. The cryostat is anchored from above to a structure called *Main Support Plate* (MSP), represented in red in the rendering of Fig.2.17. The MSP structure is placed on the upper flanges of four tubular 4.25 m tall sand-filled columns. The columns stand on a reinforced concrete structure. Four custom designed seismic elastomeric dampers are positioned at the basement of the concrete structure, in order to mechanically isolate the cryogenic structure from the floor and thus attenuate the effects of earthquakes or the vibrations induced by activities in the underground laboratories.

Moreover the detector is decoupled from the cryogenic apparatus by means of the *detector suspension system* [87]. While the cryostat is rigidly connected to the MSP, the detector suspension system is held by a Y-shaped support structure (Y-beam), that is mounted on the MSP on top of three mechanical insulators build by Minus-K Technology. The three arms of the Y-beam form an angle of 120° among each other and have a length of 1.2 m. The Y-beam structure can be seen in the rendering in Fig.2.17. The Minus-K insulators are an arrangement of springs which simulate the behavior of a negative K-elastic system. They can thus tolerate heavy loads while behaving as soft springs. These kind of insulators allow for a very low eigenfrequency for the spring-mass system, resulting in an effective cut-off of the transferred vibration spectrum. The Minus-K insulators are designed to have an eigenfrequency around 0.5 Hz, which can be adjusted according to the amount of suspended mass. In the CUORE setup, the total mass of the detector, suspension, detector support structure and Y-beam is ∼1400 kg. Three identical vertical supports (Detector Suspensions, DS) start from the Y-beam and run into the cryostat down to the Tower Support Plate (TSP), passing through several thermalization stages and regions of different vacuum levels. The DS supports have a composite structure, since they

have to guarantee a very low thermal load, attenuation of residual vibrations from the Y-beam and being made of radio-pure materials since they arrive in proximity of the detector.

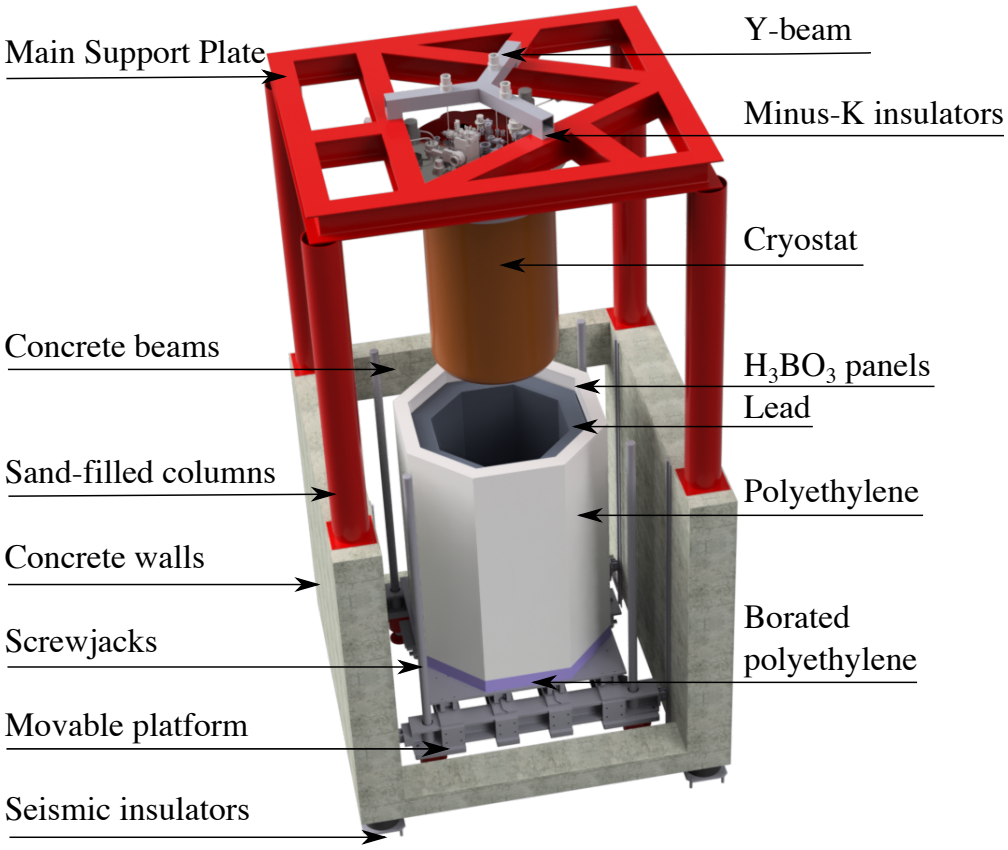

FIGURE 2.17: Rendering of the CUORE experiment support structure

Shieldings

The detector is shielded from environmental radioactivity and radioactive contaminations of the cryostat elements by means of several shields.

- External Lead Shield (ELS): A massive shield external to the cryostat, is composed by 25 cm of modern lead against environmental gamma radioactivity, and 10 cm of polyethylene and a layer of H_3BO_3 to get rid of environmental neutrons. The shield is mounted on a movable platform which lifts the structure around the cryostat during operation;
- Top Lead Shield: A thick (30 cm) modern lead disk is suspended on top of the detector (below the 10 mK plate) and maintained at 50 mK. It is meant to shield the towers from the radioactivity of the above cryostat elements. With a radius of about 45 cm, it accounts for more than 2 tons of lead.
- Inner Lead Shield (ILS): A 6 cm layer of ancient (roman) lead is put on the side and bottom of the detector and maintained at a temperature of 4 K. The total

weight of the Roman lead shield inside the cryostat is around 5 tons and it is suspended from the 600mK plate and thermalized to that.
The Roman lead is dated I century B.C. and it was extracted from ingots found on a roman ship sunk off the coasts of Oristano (Sardinia, Italy). This archaeological lead has the peculiarity of having an extremely low radioactivity and of being depleted of ^{210}Pb [88]. This isotope of lead represents an important component of environmental radioactivity. ^{210}Pb comes from ^{238}U chain. ^{210}Pb has an half-life of 22.3 yr and a 63.5 keV transition energy; its β-decay is followed by the β-decay of ^{210}Bi to ^{210}Po (with an half-life of 5.013 d and Q = 1162.7 keV) and by the α-decay of the Po isotope to the stable lead isotope, ^{206}Pb, with half-life of 138.376 d and Q= 5407.46 keV. Therefore the background rate of experiments hunting for rare events can be strongly affected by the presence of ^{210}Pb close to the detector sensitive volume.
The lead is usually extracted from galena rocks (lead sulfide mineral, PbS). The typical specimen of galena is about 86.6% lead and 13.4% sulfur by weight. However, some specimens of galena contain up to a few percent silver by weight. The ancient Romans were able to separate silver from lead; the Roman lead ingots were inscribed with "Ex Arg" (or "Ex Argento") to signify that the silver had been removed from the lead. When the silver was extracted from the galena rocks, most of the ^{222}Rn and ^{226}Ra contaminations coming from the uranium chain were concentrating in the silver, therefore the lead samples were left almost free from sources which could decay into ^{210}Pb.
The contamination of ^{210}Pb in the roman lead is then expected to be absent, since the ingots have been produced more than 21 centuries ago and all the nuclei of that isotope had decayed. Moreover that isotope couldn't be produced again inside the ingots themselves by the presence of residual contaminant sources. It could be also considered that the ingots spent such long time under 30 m of water, which protected the lead from cosmic rays, hence from further cosmogenic activation.
In Fig.2.18, there are a picture of the recovery of the lead ingots from the shipwreck [left] and the ILS mounted in the CUORE cryostat [right].

Detector calibration system

The cryostat has been equipped with a custom *Detector Calibration System (DCS)* to guarantee an uniform illumination of all the detectors, minimizing the self-shielding. The DCS is designed to calibrate the detector response over the energy full range up to the region of interest for $0\nu\beta\beta$ [89]. It is composed by 12 kevlar strings, each one equipped with 25 ^{232}Th γ-ray 'sources'. Each 'source' consists of a thoriated tungsten capsule: a copper capsule containing a ^{232}Th source and covered by a PTFE layer. The source activities have been optimized by GEANT4 Monte Carlo simulations and their positioning inside the cryostat has been decided in order to achieve an equilibrated illumination of the detector. The 6 strings deployed among the towers have 3.5 Bq of activity each, while the other 6 (external) strings deployed outside the 50mK vessel have an higher activity of 19.4 Bq. See Fig.2.19.
Generally, the sources are stored in dedicated vacuum containers (Motion Boxes) sitting on the top of the cryostat at room temperature. When a detector calibration is needed, the DCS system deploys carefully the strings into the detector volume; the strings are continuously thermalized along their path down to the detector. The overall deployment procedure takes approximately 2 days, which is a compromise

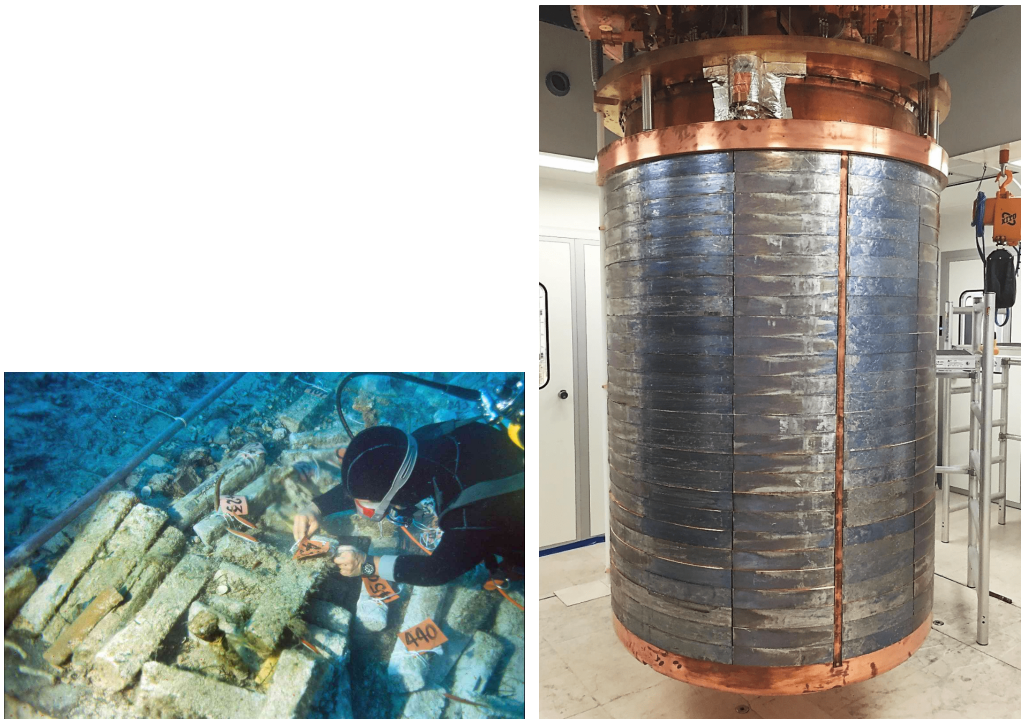

FIGURE 2.18: [Left] Recovery of the roman lead ingots. [Right] Lateral and bottom roman ILC mounted in the CUORE cryostat; the lead ingots were casted into circular sectors to build the shield structure.

between reducing the perturbation induced on the cryostat, which causes a non-negligible rise in the bolometers temperature, and the duration of the process itself. Nevertheless few hours are needed after the deployment completion to make the system stabilize back to the base temperature and then start acquiring calibration data.

An auxiliary calibration system has been installed for CUORE in early 2018. This is an *external calibration setup*; it was designed in order to provide a calibration system which could be less invasive in terms of thermal effects on the bolometers and could allow to perform faster measurements. The sources are lowered down between the 300 K vessel and the external shield, passing inside PVC pipes. The system consists in 8 strings 1 m long, which contain several electrodes from thoriated welding rods (which act as ^{232}Th source). 16 strings have been prepared: 8 dense strings (D - 28 capsules) and 8 sparse strings (S - 10 capsules). Three possible configurations of the external strings can then be utilized: strong configuration - 8 D strings ($\sim$ 100 mHz total rate, given a total activity of 80 kBq), weak configuration - 8 S strings ($\sim$ 30 mHz total rate), intermediate configuration - 4 D + 4 S strings ($\sim$ 70 mHz total rate). External DCS calibration can provide reasonable intensities for just 511 and 2615 keV lines, due to the external and towers self-shielding. It is already under study the possibility to add other sources (like ^{60}Co, or ^{88}Yb, or ^{26}Al, ...) in the external calibration strings, in order to provide multiple gamma lines also in the energy region around 1 MeV.

The deployment of the external strings is a less invasive and faster operation, since the strings do not need to be thermalized to any stage of the cryostat and the overall system works at room temperature. This system can be possibly used to perform subsequent checks of the stability of the detector response (e.g. stability of the calibration coefficients) during the data taking, with no need to deploy the internal DCS

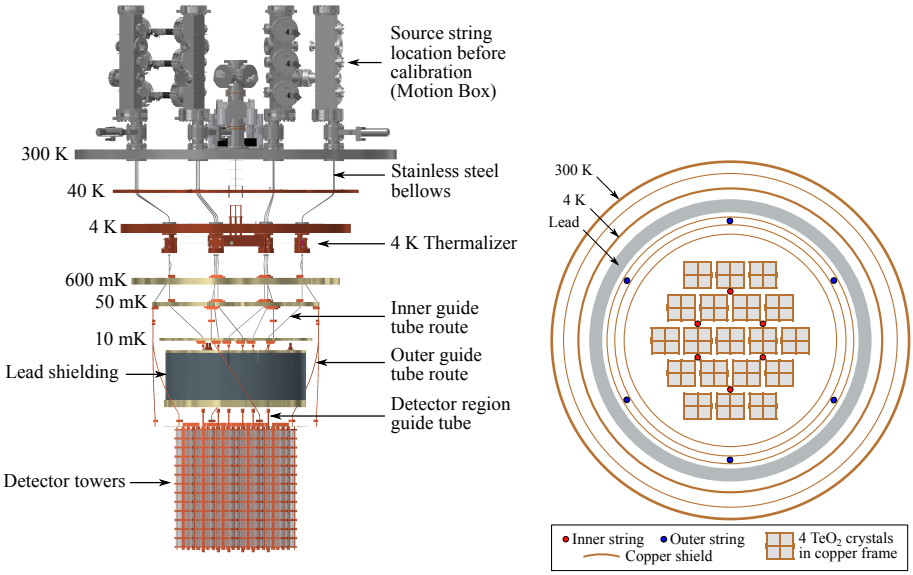

FIGURE 2.19: Rendering of the CUORE DCS system. [Left] Detailed view of the DCS components integrated in the cryostat [89]. [Right] Horizontal section of the detector and the cryostat where the position of the DCS strings is visible: 6 strings are within the towers and other 6 are outside the 50mK vessel, just before the roman lead shield.

sources, which is a more delicate and long operation.
In Fig.2.20, a representation of an horizontal section of the detector and the cryostat is shown and the position of the external calibration strings out of the 300 K vessel, is visible.

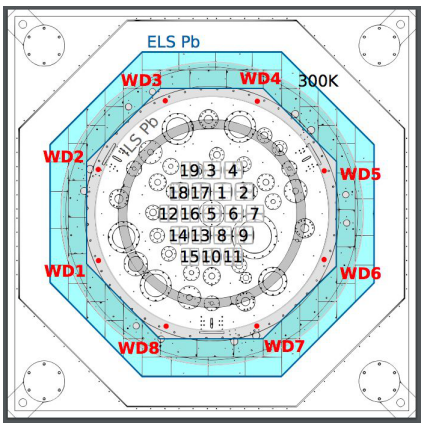

FIGURE 2.20: Schematic of the CUORE external calibration system (and strings positioning)

2.4 CUORE Data collection

The CUORE Data Acquisition System inherited its main structure from the Cuoricino and CUORE-0 experiments. However several upgrades were done in order to accommodate the increase in the number of channels.
The main purposes of the acquisition system are: digitizing $\sim$ 1000 analog signals,

performing an online triggering of the data, and storing the data and the related sensible informations. Moreover the system can send the pulses to the heaters attached to the bolometers and manage the electronics configuration.

In this section an overview of the acquisition system and the procedures for the data taking will be described.

2.4.1 Data acquisition

The CUORE DAQ [90] hardware is composed of digitizing modules by National Instruments. The digitized data are collected by six computers called *Data Readers*. Another computer, the *Event Builder*, takes the stream of data from the Readers and it is used for the event construction to save the triggered data files (*Raw Data*). Each event consists in the trigger timestamp (t_0) and the basic event information belonging to the waveform present in a window taken from the start of the data stream at the time t_0. In CUORE, the length of the window was chosen to be 10 s, of which 3 s precede the signal rise (called pre-trigger) and 7 s contain the signal waveform (post-trigger). The sampling frequency utilized for the CUORE data taking is 1 kHz. Besides saving triggered pulses (corresponding to particle pulses), the DAQ also saves continuously the detectors' waveforms (*Continuous Data*), making them accessible to the offline analysis.
Apollo is the acquisition software, which is a custom C++ code based on the ROOT package. The interface with the digitizers is guaranteed by National Instruments drivers. Apollo consists in a collection of processes running independently on the computers. Each process performs a specific task: reading the samples acquired by the digitizers; applying the trigger algorithm and writing the samples to disk for offline analysis. Specific tools have also been developed to interact with the the electronics boards and the pulser boards.
The readout maps for every analog channel and the configuration of the DAQ, trigger and pulser , as well as the run informations and the geometrical distribution of the detectors, are stored in a PostgreSQL database.

Triggering the data

In CUORE, three different kinds of triggers are implemented:

- "IsSignal": identifying particle pulses
- "IsNoise": identifying noise events
- "IsPulser": associated to pulses injected on the heaters

Particle pulses are identified by two software triggers with channel-dependent thresholds; the different trigger algorithms are identified by the variable "Trigger type".
The main signal trigger algorithm is a *derivative trigger* (DT) which fires whenever the derivative of the waveform calculated on a given distance from the start (average) exceeds a threshold for a certain number of samples (debounce). This implementation of the trigger acts only on the rise time of the pulse, requiring the pulse slope to be always above threshold. There is also a dead time for the trigger, establishing a minimum time length between a trigger and the next one. Ideally, the average and debounce should be set to a fraction of the rise time, the dead time as a fraction of the decay time of the pulse and the threshold slightly above the baseline noise in

order to identify also low energy events. The average, threshold and debounce parameters can be tuned for each channel in order to accommodate their wide range of behaviors. (See Chap.4.2.4). The DT flags are assigned with "Trigger type" = 1.
Another trigger algorithm has been developed, the *optimum trigger* (OT) [91]. This algorithm is based on the matched filter technique. The buffer of the data stream is divided into slices, each one filtered with an Optimum Filter (OF) [6] in the frequency domain. The OF transfer function is built in order to maximize the Signal to Noise Ratio, see Eq.5.7. For each channel, an average pulse built on particle pulses is used as the signal template and the noise spectral density is evaluated by averaging over several noise events. The resolution of the OF (ch_res) is evaluated by integrating the filtered noise power spectrum. Since the signal has a relatively narrow bandwidth at low frequencies, the acquired data are passed through a low-pass filter and then down-sampled from 1 kHz to 125 Hz. After that, each slice of the data stream is filtered by the OF transfer function and then the algorithm looks for triggers. The trigger threshold for identifying particle pulses for each channel is set to $3 \times ch\_res$. The filtered waveforms are less noisy than the original waveforms, and baseline fluctuations are reduced. This allows to trigger on the filtered trace in the time domain with thresholds possibly as low as < 10 keV. Furthermore, the filter is sensitive to the shape of the expected signal, suppressing trigger on spurious noise-induced pulses. The OT has been so far used for an offline re-triggering of the CUORE 2017 data, both for debugging purposes and for checking the energy threshold that can be obtained. This algorithm is currently being tested for the online triggering during the 2018 data taking. The OT flags are assigned with "Trigger type" = 3.

To monitor the detector stability and characterize the noise behavior on a run-by-run basis, waveforms are randomly collected and analyzed. To this end, a simple *random trigger*, that fires with a given probability per unit of time [7], is utilized. After discarding accidentally triggered signals, the waveforms are treated as noise events ("IsNoise").
The noise trigger and the signal trigger algorithms run in parallel during the data acquisition.

In addition to triggered pulses and noise waveforms, every few minutes each heater is injected with a voltage pulse to generate tagged reference events with fixed thermal energy. These events are identified by the Builder with the "IsPulser" flag. In case heater pulses of multiple amplitudes are injected, it is possible to choose the one to be used for the offline amplitude stabilization and these pulses will be flagged as "IsStabPulser".

Data collection organization

The CUORE data collection is organized in runs of about one day of duration. The CUORE runs are grouped in datasets. Each dataset is bracketed by an initial and a final calibration set of runs and contains about one month of physics data (the data collected for the $0\nu\beta\beta$ search) [8].
The initial calibration runs (typically 3-4 days of live time) are utilized to extract the energy calibration coefficients. These calibration coefficients are used during the background data taking of the dataset to build the energy spectrum. The final

[6] The Optimum Filter technique is described in details in Chap.5.1.2

[7] In CUORE, the random triggers are set every $\sim$ 80 s for each channel. Moreover the dead time of the random trigger is tower dependent: dead time random trg = 80000+1000*T ms where T is the tower number.

[8] In general, we refer to the runs in which we acquire physics data, as *background runs*

calibration runs have three main goals: check the stability of the energy scale of the detector across the dataset; increase the statistics on the calibration peaks to get a better estimation of the calibration coefficients; increase the statistics on the 2615 keV ^{208}Tl line which is utilized to estimate the detector response function.
Each crystal has a typical event rate of $\sim$ 6 mHz in the physics runs and $\sim$ 50 mHz in the calibration.

2.4.2 Run monitoring

The CUORE Online Run Check (CORC) is a web interface intended for the online check of the status of the data-taking, both the data quality from the bolometers and the cryogenic system monitoring.
During the data taking, in addition to the Apollo processes, some basics quantities from the bolometers, such as the trigger rate, the pulser rate, the baseline average value, the baseline RMS, etc are evaluated and are written to a database which is accessible in real time through CORC. Moreover, the Slow Monitor section of the CORC interface, shows the informations read from several devices used for the cryogenic system monitoring (e.g. detector base temperature from the Noise Thermometer, Pulse Tubes pressures and phases, circulation and flux and of the Mixture in the DU, ...).

Bad intervals

After a run has been stopped and before starting the data processing, it is necessary to check through CORC online interface if any issues have affected the run quality (eg. earthquakes, baseline instabilities, missing pulsers,...).
Periods of time in which a channel is misbehaving are flagged with "bad intervals"; this information is stored in a dedicated table in the database, *bad_channels* table. The majority of the bad intervals set in the data production are due to either noisy intervals, which mark an elevated baseline RMS, or baseline instability. Bad intervals can also be inserted into the DB to remove periods of equipment malfunction, periods when the DAQ saturates, and earthquakes. Bad interval setting is not a cut on individual events, but rather a cut on trends that negatively effect averages measured over the entire dataset.
The bad intervals in *bad_channels* table are set through CORC online for the run. The bad intervals are then written in the database.

For example, in case an earthquake happens nearby or its intensity is high enough to be detected by the detector, an abrupt change in the baseline of the channels can be identified. One channel can be selected on the towers maps in the CORC Run Info page and the plot of the baseline during the run can be displayed. After having identified and selected the time interval in which there is the spike in the baseline due to the earthquake, it is possible to set the bad interval. The time interval can be adjusted, the type of bad interval (bad status) can be chosen [9] and many channels can be selected to be flagged with that same bad interval. An example of bad intervals set on a channel, due to earthquakes, is shown in Fig.2.21.

[9] The bad status is an important feature because it allows to associate to each bad interval the problem that makes that period of data unusable for the following analysis. Many different bad statuses are available: saturated, baseline_instability, noisy, data_all_bad,...). Each bad status is handled differently by the data processing sequences.

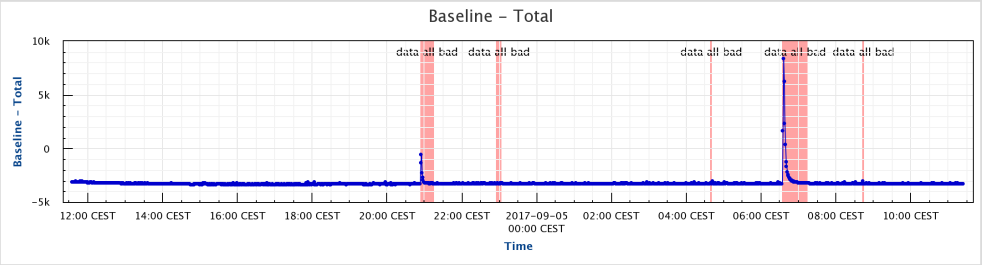

FIGURE 2.21: Example of a bad interval set and visualized via CORC online. Run 301519, channel 107: bad intervals ('data all bad') set due to earthquakes which had induced spikes in the channel's baseline. For example, the second spike in the baseline corresponds to an earthquake happened on 2017-09-05 at 06:34:21 of magnitude Mw = 3.7, at 4 km W Campotosto (AQ).

Chapter 3

Bolometric technique

A "bolometer" is a Low Temperature Detector (LTD) in which the energy deposited by a particle in a crystal is converted into thermal phonons (heat) and measured via temperature variation. The basic operation principles of the bolometers will be described in this chapter

3.1 Low temperature detectors

Most of the conventional detector techniques are based on the detection of the energy released by a particle in the form of ionization and/or excitation of the detector's atoms or molecules. Besides the advantages of being well-known processes and detection technologies, they generally have limited intrinsic energy resolution. In fact, the amount of energy lost in unobserved channels (e.g. dis-excitation with no emission of photons or with no ionization, creation of lattice defects, emission of un-detected photons,...)is quite large. Moreover the general amount of energy necessary for an atom excitation or ionization, is high, therefore a small number of carriers is produced for each energy release.

Thermal detectors are calorimeters in which the deposited energy by an interacting particle is converted into phonons and measured via temperature variation. In order to get measurable temperature variations, this kind of detectors have to be operated at cryogenic temperatures of about 10 or few tens of mK. Measuring the phonon component, which is excited by the energy release in the absorber, guarantees an excellent energy resolution. The excitation energy for phonons is lower when compared with ionization and electrons excitation energies. The intrinsic energy resolution is driven by the thermodynamic energy fluctuation, which depend only on the temperature of the absorber, while the number of phonon modes does not fluctuate for a given detector.

The use of low temperature detectors to study nuclear phenomena was suggested back in 1935 by F.Simon [92]. During the following decades, the field of bolometric detectors has been growing and reaching many areas of research. In fact, this kind of detectors features excellent energy resolution, sensitivity to all kind of particles, low energy threshold and a wide choice of construction materials. Therefore they are suitable for many different applications: solar neutrino spectroscopy, X ray spectroscopy, material contamination analysis, dark matter detection and rare processes search (such as $0\nu\beta\beta$ decay, ...). The use of large bolometric detectors for rare events physics was first suggested by Fiorini and Niinikoski in 1983 [59]. This technique has been found to be very powerful in all these applications and it is continuously under development.

3.2 Bolometer principle of operation

Bolometers are low temperature detectors sensitive to *phonons*. Therefore these devices are referred as Phonon Mediated particle Detectors.
Bolometers consist of two main components: an *energy absorber*, where the particle deposits the energy, and a *temperature sensor*, which converts the excitation phonons produced by the particle into a measurable signal. See Fig.3.1.

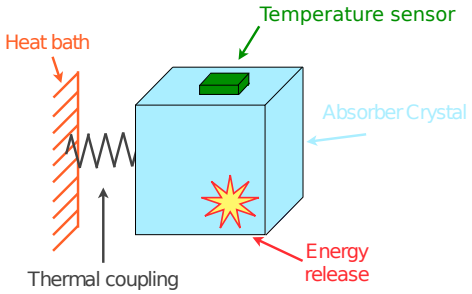

FIGURE 3.1: Scheme of a bolometric detector

3.2.1 Simplified thermal model

In a simplified thermal model, a bolometer can be schematized as a calorimeter with heat capacity C connected to a heat bath at constant temperature T_0 by a thermal conductance G; see Fig.3.2. The capacity C is an equivalent heat capacity, which takes into account all the different elements composing the detector. The conductance G represents the thermal link between the detector and the heat bath and its heat capacity is considered negligible.

When a particle releases some energy in the absorber, phonons out of the thermodynamic equilibrium are produced (athermal phonons). These phonons degrade their energy via several interactions and reach a new thermal equilibrium distribution [1]. This results in a temporary temperature variation of the absorber, which is measured by the sensor. Assuming that, for a given absorber temperature $T(t)$ at time t, $\Delta T = |T(t) - T_0| \ll T_0 \; \forall \; t$, C and G can be treated as constant quantities. The temperature variation can be described by the time evolution:

$$\Delta T(t) = \frac{E}{C} e^{-t/\tau} \quad \text{with} \quad \tau \equiv \frac{C}{G} \tag{3.1}$$

where τ is the decay time of the thermal signal and E is the deposited energy. The characteristic time τ of the thermal pulse can vary from ms up to a few seconds, depending on the values of C and G. The heat capacity C at temperature T is given by $C(T) = c(T) \cdot n$, where $c(T)$ is the (molar) specific heat and n is the number of moles in the absorber.
The maximum of the thermal pulse is reached at $\Delta T(t)_{max}$ and is proportional to $\frac{E}{C}$. A lower heat capacity C is preferred in order to have a larger signal amplitude. In order to reduce C, the detectors have to be operated at very low temperatures and a suitable material for the absorber has to be chosen.

Bolometric detectors sensitive to athermal phonons are characterized by response times of the order of μs ('fast' detectors). Instead, if the temperature sensor response

[1] See section 3.3.1, for the description of the phonon thermalization processes.

time is higher than the phonons thermalization time, it will detect mainly the thermalized phonons, thus measuring the actual temperature of the absorber; in this case the device is a 'slow' detector and it acts as an ideal calorimeter.

Experimentally, a real bolometer is more complex than the simplified detector described: the quantities C and G should be considered as a sum of many contributions, and the contribution of the phonon sensor to the signal development should not be neglected. However the simplified model described above is meant to give a qualitative idea of the principle of operation of a bolometer.

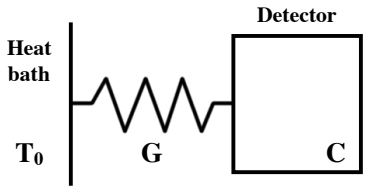

FIGURE 3.2: Simplified bolometer thermal model. *Monolithic model*: the detector is modeled as an unique system weakly coupled to the heat bath.

3.3 Energy absorber

Assuming the bolometer operates as a perfect calorimeter, the main parameter characterizing the absorber is its heat capacity C, that has to be small to achieve large and fast thermal signals. There is a wide choice of energy absorbers materials that have small heat capacity at low temperatures.

The specific heat $c(T)$ of a crystal at low temperatures can be expressed as:

$$c(T) = c_l(T) + c_e(T) \tag{3.2}$$

where $c_l(T)$ is the the lattice contribution to the specific heat, while $c_e(T)$ is the one related to electrons.
For dielectric and diamagnetic[2] materials, only the lattice term is contributing to the specific heat. At low temperatures, the lattice contribution is proportional to the cube of the temperature over the Debye temperature (*Debye law*):

$$c_l(T) = \frac{12}{5}\pi^4 k_B N_A \left(\frac{T}{\Theta_D}\right)^3 \quad T < \Theta_D \tag{3.3}$$

where k_B, N_A and Θ_D are the Boltzmann constant, the Avogadro number and the Debye temperature respectively. In terms of heat capacity, the expression becomes:

$$C(T) = \beta \frac{m}{M}\left(\frac{T}{\Theta_D}\right)^3 \tag{3.4}$$

where β = 1944 $JK^{-1}mol^{-1}$, m is the absorber mass and M is the molecular weight.
In metals, the specific heat at low temperatures is dominated by the electronic term, that is proportional to T:

$$c_e(T) = \frac{\pi^2}{\Theta_D} ZR \frac{T}{\Theta_F} \tag{3.5}$$

[2]Diamagnetic materials are usually utilized as energy absorbers, in order to avoid the dangerous paramagnetic contributions to the heat capacity.

where Z, R and Θ_F are the conduction electron number for each atom, the gas constant and the Fermi temperature respectively. If the metal is in a superconductive state, the electron contribution to the specific heat at $T \ll T_c$ (T_c is the superconductivity critical temperature) becomes:

$$c_e(T) = K_s e^{-2(\frac{T_c}{T})} \tag{3.6}$$

where K_s is a constant depending on the material characteristics.

The above considerations lead to prefer dielectric or superconductor (with T_c higher than the working temperature) materials as energy absorbers.
In case of dieletric and diamagnetic materials, the ones with high Debye temperature would be preferable. The Debye temperature is a property of the material and it scales approximately as $\Theta_D \propto A^{-1/3}\rho^{-1/6}$ [93], where A and ρ are the mass number and the material density respectively; therefore materials with low mass number and density, would ensure an higher Debye temperature. [3]
The absorber dimensions usually depend on the type of the bolometers applications (from $\sim \mu g$ in X-ray spectroscopy [94] to $\sim kg$ in case of Gamma-ray spectroscopy, $0\nu\beta\beta$ and Dark Matter searches).

3.3.1 Thermalization of phonons

The processes that allow the conversion of the deposited particle energy into thermal phonons are quite complex.

The main thermalization processes occur through the nuclear and electronic channels [95], [96]. Particles can interact with the absorber by scattering on nuclei or electrons, in both cases the energy is converted into phonons.
Nuclear channel. The particle scatters on the nuclei in the crystal lattice. The released energy produces vibrational excitations (phonons), but may also produce structural damages of the lattice, where the energy can be stored. If this energy is not converted into phonons, the statistical fluctuation of the number of produced defects can worsen the energy resolution.
Electronic channel. The particle scatters on the electrons in the crystal; it then slows down and stops ($\sim \mu m$ for heavy particles, $\sim mm$ for electrons). Along the track, electron-hole ($e-h$) pairs are produced having at the beginning very high spatial density and energy; the $e-h$ charge carriers interact with each other and diffuse quickly inside the crystal. When a quasi-equilibrium situation is reached, the $e-h$ pairs undergo their final energy degradation via direct interaction with the lattice sites: these interactions produce phonons. During this step undesirable processes can take place, a fraction of the pair energy can leave the crystal (e.g. scintillation,...) or can be stored in stable or metastable states instead of going into the crystal lattice. However most of the initial energy is transferred to the lattice as vibrational excitations, through different mechanisms depending on the $e-h$ pair density and on their energy.

The nuclear and electronic processes lead to a population of phonons having energy much higher than the energy of thermal phonons at the bolometer working temperature. These are athermal phonons which sit on the *optical branch* of the phonons dispersion curve. The optical phonons decay in the *longitudinal acoustic* (LA) branch in a very short time ($\sim$ 10-100 ps), producing two phonons with half

[3] Besides the thermal considerations, the efficiency in detecting the different particles, in the possible absorber materials has to be considered. Materials with high Z have a larger efficiency in detecting electrons and the ones with larger Z/A ratio are better γ absorbers.

of the energy of the initial optical phonon and opposite momentum. Therefore the final result is a phonon system, mainly belonging to the LA branch, and having the energy of the order of $\hbar\omega_D$ (where $\omega_D = 2\pi\nu_D$, and where ν_D is the Debye cut-off frequency of the crystal). This energy is much higher than the average energy of thermal phonons at the bolometer working temperature (for example, at T= 10 mK, the average energy is $\sim \mu eV$). At this point new phenomena of phonon energy degradation can occur, so that phonons become thermal phonons. The conversion towards low energies is a very slow process, and it is difficult to make a quantitative estimation due to the complication of the involved mechanisms (phonon-phonon interaction, scattering on impurities, and reflection on crystal surfaces). After a certain number of the phonons decay, the mean free path of the phonons becomes larger than crystal dimensions. At this point in pure crystals, the phonons start to propagate until reflection at the crystal surface becomes the only thermalization process (ballistic phonons).
The thermodynamic equilibrium between the absorber and the heat bath is hold by a continuum exchange of phonons through the conductance G.

A representation of the athermal phonons thermalization process, along a mono-dimensional projection of the phonon dispersion curve, is shown in Fig.3.3.

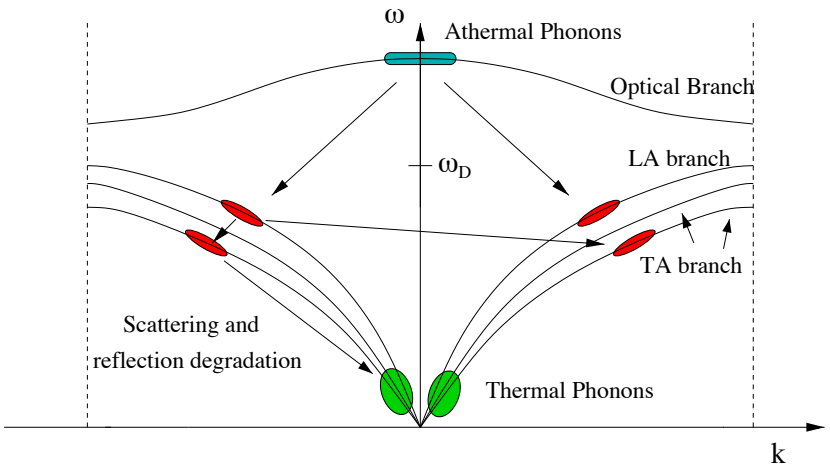

FIGURE 3.3: Athermal phonon thermalization model.

3.3.2 Intrinsic energy resolution

The intrinsic energy resolution of a bolometer is limited by the thermodynamic energy fluctuations in the absorber [97], [98]. An estimate of this noise can be obtained by the following simplified argument.
The effective number of phonon modes in the absorber at thermal equilibrium is: $N = \frac{C(T)}{k_B}$, where C(T) is the heat capacity. The energy of each phonon is $\epsilon = k_B T$. For an isothermal system, there is a spontaneous random energy flow into and out of the bolometer, due to the random propagation of the carriers. This induces a thermodynamic energy fluctuation in the detector, which is proportional to the number of phonon modes and to their mean energy:

$$\langle \Delta U^2 \rangle = (k_B T)^2 \cdot N = k_B \cdot T^2 \cdot C(T) \tag{3.7}$$

The fluctuations of the internal energy of the absorber, or phonon noise, are therefore the origin of the bolometer intrinsic energy resolution.

The thermodynamic fluctuations give a negligible contribution to the overall bolometer energy resolution. Using typical values of CUORE-like bolometers (750 g TeO_2), a resolution of $\sim$ (20-100) eV is predicted, that is well below the measured resolution (few keV). The thermodynamic limit can be obtained only when the statistical fluctuations of the physical processes coming before the thermalization are negligible, when the temperature of the heat sink is constant enough, and when the noise of the detector is minimized. This will be discussed in more details in section 3.5.1.

3.4 Phonon sensor

The phonon sensor is a device that collects the phonons produced in the absorber and in turns generates an electrical signal proportional to the energy of the collected phonons.
A simple realization consists in the use of a a thermistor, a resistive device that converts temperature variations into resistance variations. There are two main types of thermistors:

- Transition Edge Thermistors (TES): superconductive films deposited on the absorber crystal. The films are kept around the material critical temperature T_c; therefore these devices can be operated only in a narrow range of temperatures. However, these are 'fast' sensors ($\sim \mu s$) which can detect athermal phonons.
- Semiconductor Thermistors (ST): Si or Ge chips doped by thermal neutrons. These are 'slow' sensors, having a response time ($\sim ms$) of the order of the phonons thermalization time in the absorber; they are only sensitive to thermalized phonons, thus acting as ideal thermometers.

A parameter characterizing the phonon sensors is their "logarithmic sensitivity" η, defined as:

$$\eta = \left| \frac{d \log R(T)}{d \log T} \right| \tag{3.8}$$

The former expression implies that:

$$\frac{dR}{R} = \eta \frac{dT}{T} \tag{3.9}$$

Therefore, the larger is η the higher is the expected response of the device. Typical values of η are 1-10 for ST and 100-1000 for TES devices.
Despite the lower sensitivity, ST have been preferred for CUORE bolometers because of their wider range of operating temperatures and the simpler readout circuit.

The following section will be focused on the operating principles of semiconductor thermistors.

3.4.1 Semiconductor thermistors

Semiconductors are covalent solids that behave as insulators because the valence band is full and the conduction band is empty. However, the energy gap between valence and conduction band is smaller than 2 eV (1.14 eV for silicon, 0.67 eV for germanium).
The conduction happens when the activation energy is greater than the energy gap. In a pure semiconductor, at room temperature, the average electrons thermal energy

is $k_B T \simeq 0.025$ eV, lower than the energy gap. Therefore the conduction can only happen at higher temperatures.
If impurities are added into the semiconductor lattice (extrinsic or doped semiconductors), new energy levels are introduced slightly above the valence band or below the conduction band, depending on the type of atoms inserted. It is therefore possible to have electronic conduction also at lower temperatures. The dopant concentration determines the behavior of the solid. A critical concentration, N_c, characterizes the transition from metal to insulator, the region near this concentration is named *metal-insulator transition region* (MIT) [99]. In the MIT regime, the material resistivity exhibits a strong dependence on the temperature.
At temperatures lower than 10 K the conduction is driven by the migration of the charge carries between impurity sites. In this situation electrons are not localized and the conduction happens when an electron jumps from a donor site to another, without using the conduction band (*hopping mechanism*). The migration is due to quantum-mechanical tunnelling through the potential barrier separating the two dopant sites and it is activated by phonons. See Fig.3.4.
At even lower temperature and if the doping atom concentration is slightly lower than N_c, the energy of the phonons that are activating the hopping conduction mechanism is low and the charge carriers can migrate to far impurity sites if their energy levels are located in a narrow range around the Fermi energy. This conduction regime is called *Variable Range Hopping* (VRH) [100]. In the VRH conduction regime the semiconductor resistivity dependence on temperature is described by the law:

$$\rho(T) = \rho_0 \exp\left(\frac{T_0}{T}\right)^{\gamma} \tag{3.10}$$

where ρ_0, T_0 depend on the doping concentration and $\gamma = 1/2$.
The expression of the logarithmic sensitivity from Eq.3.9 can be easily derived:

$$\eta = \gamma\left(\frac{T_0}{T}\right)^{\gamma} \tag{3.11}$$

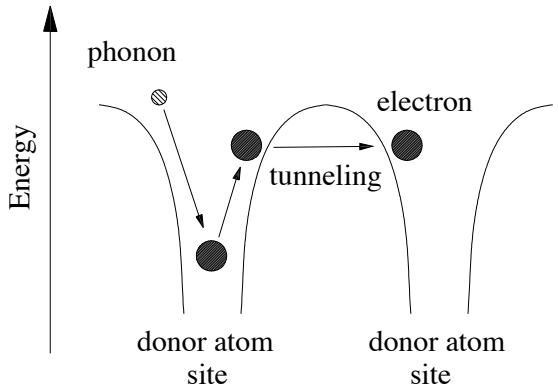

FIGURE 3.4: Schematic representation of the hopping conduction mechanism.

Semiconductor thermistors consist normally of Ge or Si small crystals with a doped region. A very useful technique to produce uniform doping of large volumes is Neutron Transmutation Doping (NTD) [101]: Ge/Si wafers are bombarded with thermal neutron beams that, inducing nuclear reactions, create donor and acceptor impurities. The dopant concentration determines the sensor performance. The wafers are then cut into pieces, each of them is a thermistor and its resistance can be

expressed as:

$$R(T) = R_0 \exp\left(\frac{T_0}{T}\right)^{\gamma} \tag{3.12}$$

where R_0 depends on the sensor geometry and is roughly $R_0 \simeq \rho_0 \frac{l}{S}$, where l and S are the length and the section of the piece, respectively; ρ_0 is the electric resistivity described by Eq.3.10. The parameters R_0, T_0 and γ are determined experimentally. The parameter γ is approximately γ=0.5 in the MIT region and at a working temperature lower than 1 K.

For the CUORE TeO_2 bolometers, NTD-Ge thermistors, working in the Variable Range Hopping (VRH) conduction regime with Coulomb gap, have been chosen as temperature sensors.

3.5 Detector operation

The thermistor converts thermal pulses into electrical signals, by means of a resistance variation. To measure the resistance and its variation, the sensor is biased with the circuit in Fig.3.5 [left]. A bias voltage V_B, produced by a voltage generator, is closed on a load resistor R_L [4] which is in series with the thermistor. If the R_L is chosen much higher than the thermistor resistance R ($R_L \gg R$), the current I in the circuit can be assumed as constant. The voltage across the thermistor, V_{bol} is then:

$$V_{bol} = I \cdot R(T) \tag{3.13}$$

The current produces a power dissipation $P = IV_{bol}$, that increases the temperature and acts back on the resistance, decreasing its value. This phenomenon is called *electro-thermal feedback*.
In static conditions the thermistor temperature T_s is:

$$T_s = T_0 + \frac{P}{G} \tag{3.14}$$

where T_0 is the temperature of the heat sink and G is the conductance between the absorber and the heat bath. The R-P dependence is reported in Fig.3.5 [right].
The electro-thermal feedback makes the I-V relation deviate from linearity and leads to a non-ohmic behavior. The static resistance is the ratio: $R_s = \frac{V}{I}$. The dynamic resistance R_{dyn} is the tangent to the I-V curve. Increasing the bias current the slope of the curve increases until it crosses the 'inversion point' (IP), where R_{dyn} vanishes and then becomes negative and decreases. The I-V curve for semiconductor thermistors is usually referred as a **load curve** and it is shown in Fig.3.6 [left]. In static conditions the thermistor electric and thermal parameters are described by a point on the load curve. The intersection of the 'load line' with equation $V_{bol} = V_B - IR_L$ and the load curve I=I(V), determines the **working point** (WP) of the sensor. In general, the working point is referred as the bias voltage V_B that has to be set to the sensor to reach the desired working condition along its load curve.

[4] The load resistor R_L is splitted into two resistors $R_L/2$ in series in the thermistor bias circuit of the CUORE electronics, as shown in Fig.3.5 [left]. The NTD is biased and read-out with a differential circuit, in order to reject the common mode noise. The load resistor is divided into two $R_L/2$ and the actual bias applied to the detector is a fraction of the bias coming from the two power supplies due to the partition coming from the load resistor system. The two $R_L/2$ happen to be connected to each of the two inputs of the differential preamplifier. [86]

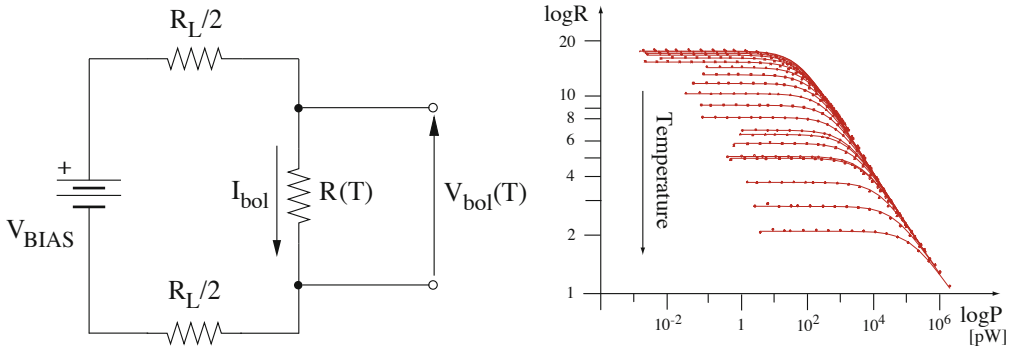

FIGURE 3.5: [Left] Electric scheme of the bias circuit for the thermistor readout. [Right] P-R curves for several values of base temperature. The dependence of the resistance on the power dissipation due to the electrothermal feedback can be observed. Moreover curves with lower resistance at P = 0 correspond to higher base temperatures. [102]

Apart from the static behavior, it has to be considered the sensor response to thermal pulses produced by an energy release in the absorber. When particles release an amount of energy E in the absorber, the voltage across the thermistor varies leading to a signal. The relationship between the maximum voltage signal ΔV, the thermistor parameters and the energy deposit, can be obtained (see Eq.3.18).
Given constant I ($R_L \gg R_s$), from Eq.3.13:

$$\frac{\Delta V}{V_{bol}} = \frac{\Delta R}{R_s} \tag{3.15}$$

Given Eq.3.9:

$$\frac{\Delta V}{V_{bol}} = \eta \frac{\Delta T}{T_s} \tag{3.16}$$

$$\Delta V = \eta \frac{\Delta T}{T_s} V_{bol} \tag{3.17}$$

Given ΔT_{max} from Eq.3.1 in the simplified thermal model, the maximum voltage signal is:

$$\Delta V \propto \eta \frac{E}{C T_s} V_{bol} \tag{3.18}$$

Looking at Eq.3.17, to increase the signal amplitude, a higher V_{bol} operation point could be chosen. However it has to be taken into account that the increase of the applied voltages determines higher temperatures T_s and so lower $\Delta T / T_s$ ratios.

In general, the working point is chosen in order to optimize the sensor response to particles energy deposition (**optimal working point**), maximizing the signal-to-noise ratio. Since all the sensor parameters are not known 'a-priori', the optimal working point is determined experimentally. The procedure consists in scanning the amplitude of a pulse of fixed energy varying the bias current, and finding the point where the signal is maximum (see Fig.3.6 [right]). Moreover the noise level variation for each bias current is analyzed. The optimal working point consists in a compromise between high pulse amplitude, low noise and stable response. The procedure for acquiring the load curves to characterize the CUORE NTDs response and to find the optimal working points, will be described in Chap.4.2.2.

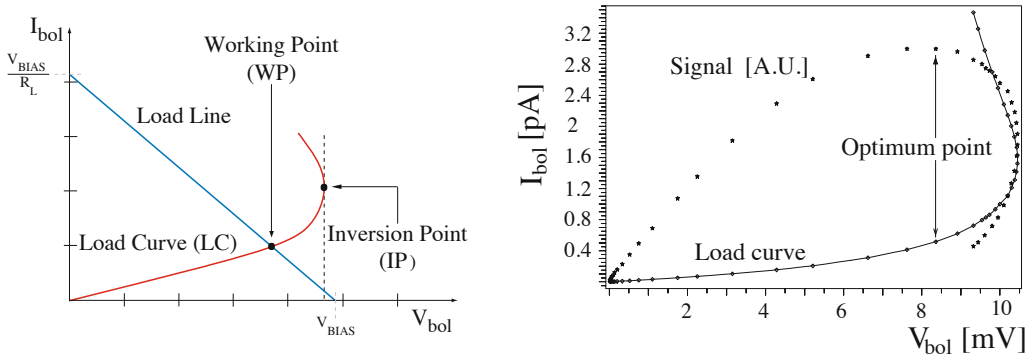

FIGURE 3.6: [Left] Load curve of a semiconductor thermistor, considering only its static behavior. [Right] The load curve (I-V) is shown together with the corresponding signal amplitude curve (Signal-V). [102]

3.5.1 Detector noise

The principal noise sources of a bolometric detector using a ST sensor can be classified as generating intrinsic and extrinsic noise.

- **Intrinsic Noise sources**. These sources depend on the detector parameters and they have to be carefully analyzed to achieve the optimal experimental configuration.
  Thermodynamic noise. In the case of complete energy thermalization, the intrinsic energy resolution is limited by the thermodynamic fluctuations of the number of thermal phonons exchanged with the heat bath (see Sec.3.3.2). In practical applications, this noise gives a negligible contribution compared to the noise coming from the electronics and the cryogenic apparatus.
  Johnson Noise. Every resistance R working at temperature T, generates a white noise due to the fluctuations of the charge carriers. For the load resistors R_L, the noise spectral density can be expressed as:

$$\Delta V_L^2 = 4 k_B T_{R_L} R_L \tag{3.19}$$

  The corresponding noise spectral density on the output voltage of the bolometer becomes:

$$\Delta V_{bol}^2 \simeq 4 k_B T_{R_L} \frac{R_s^2}{R_L} \tag{3.20}$$

  The circuit with the load resistor is at room temperature (T_{R_L} = 300 K). This contribution to the noise can be reduced by choosing a large enough value for R_L.

- **Extrinsic Noise sources**. These are the noise sources not generated inside the detector. The cryogenic apparatus, electronics and read-out setups can generate this noise. In the bolometers used in the CUORE and its predecessors setups, these sources exceed the intrinsic noise, so that they determine the real limits of the energy resolution. The extrinsic noise sources are characteristic of the experimental setups.
  Preamplifier noise. The noise associated to the preamplifier stages added after the thermistor biasing circuit, is of three types: *series*, generated by the JFET resistances, *series 1/f* and the *parallel shot* noise.

Pick-up noise. Electro-magnetic radiation and grounding effects surrounding the detector can lead to spike signals and fast variations of the detector working point, thus inducing temporary fluctuations of the voltage output. To reduce this noise, the read-out electronics can be hosted in a 'faraday cage', to be shielded by external electromagnetic fields.
Vibrational noise. The dominant noise contribution comes from the vibrations of the cryogenic apparatus.
Electrical microphonic noise. Wire vibrations can change the wire-wire and wire-ground capacitances; the consequence is a variation of the static electric charge of the read-out wires. To reduce this effect, either shorter wiring or twisted cables strictly binded to the cryostat structure can be used.
Mechanical vibrations. When the vibrations of the cryogenic apparatus are transmitted to the crystals, these could generate an energy dissipation that in turn changes the temperature. These sources have a frequency spectrum similar to the thermal signal and therefore these are the most dangerous sources of noise. Quantifying the amount of vibrational noise is difficult, and it strictly depends on the cryogenic setup and on the detector assembly. These vibrations can be partially reduced mechanically decoupling the detector and the cryostat from the outer environment.

3.6 The CUORE bolometers

In this section, on overview of the characteristics of the CUORE bolometers and the thermistors will be provided. The thermal properties of the crystals and the thermistors and the general bolometers response will be described.

3.6.1 Thermal properties

A complete thermal model of the CUORE bolometers has to take into account the heat capacities of the various components of the detectors and the thermal conductance between them and the heat bath. The absorber and the thermal sensor have to be considered separately. Moreover, the power dissipated in the thermistor causes a non-ohmic effect, explained by the "Hot Electron Model", which predicts a decoupling between the electron system and the lattice one; therefore a term of electron-phonon conductance has to be considered in modeling the thermal response of the system. The thermal circuit considering all the elements listed above is shown in Fig.3.7.

The CUORE bolometers are TeO_2 crystals with dimensions $5 \times 5 \times 5\ cm^3$ and 750 g mass (as described in Chap 2.2.1). The Debye temperature of TeO_2 is Θ_D = (232 $\pm$ 7) K; its molecular weight is M = 159.6 $gmol^{-1}$.
Dedicated measurements of TeO_2 crystal specific heat were carried out at the University of Florence and confirmed the good agreement with the estimate based on the Debye Law (from Eq.3.3) [60], [103]. For the CUORE crystals, considering their mass and dimensions, the heat capacity can be expressed as:

$$C(T) = aT^3 \quad [JK^{-1}] \tag{3.21}$$

$$\text{where} \quad a = 2.29 \times 10^{-3} \quad [JK^{-4}] \tag{3.22}$$

The CUORE crystals heat capacity at 10 mK, can be evaluated:

$$C(10mK) \sim 2.3 \times 10^{-9} [JK^{-1}]$$

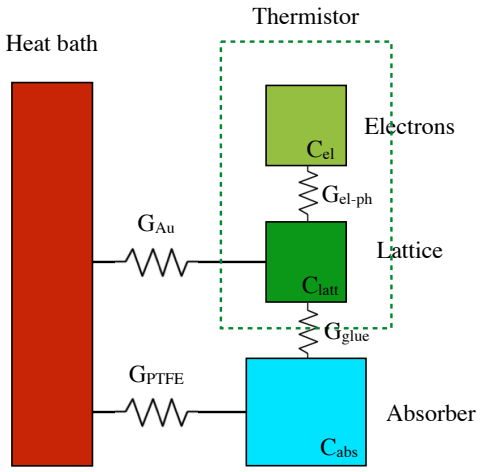

FIGURE 3.7: Scheme of a complete thermal model for a bolometric detector coupled with a thermistor.

The NTD-Ge thermistor contributes to the effective thermal capacitance by [103]:

- thermistor electrons specific heat, $C_{el}[J/(K \cdot mm^3)] = 1.1 \times 10^{-9} T[K]$
- thermistor lattice specific heat, corresponding to the Ge specific heat: $C_{latt}[J/(K \cdot mm^3)] = 3 \times 10^{-9} T[K]^3$

Several contributions to the thermal conductance G between the TeO_2 absorber and the heat bath can be considered [60]:

- thermal conductance between the crystal and the heat sink, provided by the PTFE holders, $G_{PTFE}[W/K] = 8 \times 10^{-5} T[K]^2$.
- thermal conductance of the glue spots, which connect the crystal to the thermistor, $G_{glue}[W/(K \cdot spot)] = 0.26 \times 10^{-3} T[K]^3$
- thermal conductance between the thermistor and the heat sink, due to the interface between the thermistor and the gold pads, $G_{Au}[W/(K \cdot mm^2)] = 7.91 \times 10^{-6} T[K]^{2.4}$
- electron-phonon conductance inside the thermistor itself. $G_{el-ph}[W/(K \cdot mm^3)] = 0.67 \times 10^{-1} T[K]^{4.37}$

3.6.2 NTDs characterization

The CUORE TeO_2 absorbers are coupled with NTD-Ge thermistors, as described in Chap 2.2.2. The choice of NTD-Ge sensors for the CUORE bolometers has been driven by several factors.

- The NTDs have a wide temperature range of operation.
- It is possible to achieve a (quite) uniform and stable response to temperature variations of many NTDs, since they can be produced on industrial scale with small non-homogeneities among the chips.
- The readout circuit for a NTD is relatively simple.

However, the NTDs have a slow response ($\sim$ tens of ms); they cannot stand signal rates larger than few Hz. These devices are suitable for rare events searches, with very low background rates, such as $0\nu\beta\beta$ decay. The NTDs are sensitive to thermal phonons; therefore it is not trivial to apply pulse shape discrimination, that is instead possible in the case of athermal phonons.

NTDs belonging to different (neutron implantation) batches were installed on the CUORE towers: NTD 41C, NTD 39C, NTD 39D. See Fig.3.8. Although the neutron implantation procedure was the same, the three NTD-types have slightly different characteristic parameters of their $R(T)$ curves (R_0, T_0), from Eq.3.12.

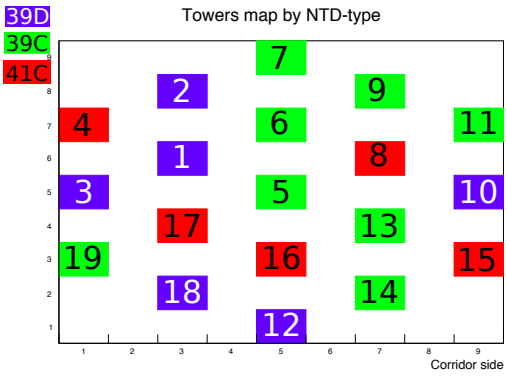

FIGURE 3.8: CUORE Towers map by NTD-type.

Several measurements on test CUORE NTDs were performed at temperatures ranging from 30 mK to 500 mK, to characterize the devices and get an estimate of the (R_0, T_0) parameters. A summary of these results is reported in Tab.3.1.
As soon as the CUORE experiment was operational, dedicated measurements were performed on all the channels at several base temperatures ($\sim$ 10-30 mK), to characterize all the NTDs and bolometers performance; this will be explained in details in Chap.4.2. The three NTD batches mounted on the CUORE crystals showed slightly different resistance values, both when small polarization was applied (*base resistance* measurement) and when a proper operating bias was applied (*working point resistance* measurement). The NTD batch 39D happens to be the most resistive one, while the 41C is the least resistive. Fig.3.9 shows the base resistance measured at several temperatures (from 15 to 27 mK) for three channels belonging to different towers, thus having different NTD-types for the readout.

	R_0 [Ω]	T_0 [K]
Orsay		
NTD 39C	$\sim$ 1.07	$\sim$ 4.26
NTD 39D	$\sim$ 1.11	$\sim$ 4.77
Berkeley		
NTD 39C	$\sim$ 1.55	$\sim$ 4.86
NTD 39D	$\sim$ 2.03	$\sim$ 5.15

TABLE 3.1: Average values of (R_0, T_0) parameters of CUORE 39C and 39D NTDs, obtained in the Orsay and Berkeley characterizations.

The working impedance of the thermistors can be very high, in the hundreds of $M\Omega$ range and up to $G\Omega$ at lower temperatures. The electrical links from the

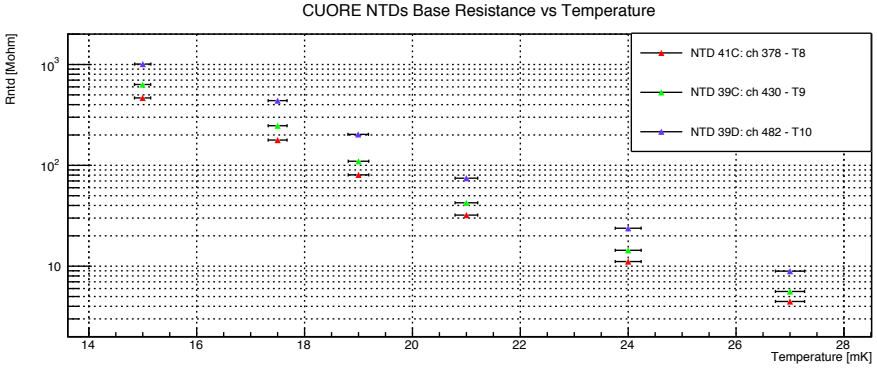

FIGURE 3.9: CUORE NTDs base resistance dependence on temperature (log-plot). Three CUORE channels have been chosen as examples: ch 378 - Tower 8 (NTD 41C), ch 430 - Tower 9 (NTD 39C), ch 482 - Tower 10 (NTD 39D). The base resistance is here measured biasing the NTDs with very low bias (100 mV). A low polarization bias should reduce the effect of the electro-thermal feedback in the NTD effective temperature, thus making possible to evaluate better the R(T) trend and possibly the (R_0, T_0) parameters.

thermistors to the input connectors of the Front-End boards (which operate at room temperature) introduces a parasitic capacitance proportional to the length of the link. Since the latter is 5 m in average, the parasitic capacitance in parallel with each pair is about $\sim$ 500 pF.

3.6.3 Thermal response and noise

Given the characteristics of the CUORE TeO_2 absorbers, NTDs and read-out chain, it is possible to quantify which is the expected bandwidth for the thermal signals. The coupling between the NTD resistance and the parasitic capacitance acts as a low pass filter limiting the signal bandwidth. For NTD *working point resistances* of the order of few hundreds $M\Omega$ and parasitic capacitances of few hundreds pF, the signal bandwidth is expected to be in the $\sim$(0-10) Hz range. The frequency spectrum of thermal signals at several temperatures is shown in Fig.3.10, for one of the CUORE channels. The temperature dependences of the amplitude and of the bandwidth are clearly visible.

Given the thermal and electrical features of the CUORE channels, it is possible to give an estimate of the noise sources contribution, discussed in Sec.3.5.1. The CUORE preamplifier and front-end boards have been designed to minimize at negligible level the corresponding noise contribution [86]. The Bessel filters help to reduce the high frequency noise contribution and with a cut-off frequency of 120 Hz (like it is used for the CUORE data-taking) they do not affect the signal bandwidth. The total input noise to the front-end circuit configuration can be summarized as the sum of *series noise* and *parallel noise*. The latter gets its contributions from: the shot noise of the preamplifier, the Johnson noise of the load resistor and non-intrinsic noise, like friction and vibration. In Eq.3.23, the noise spectral density and its several

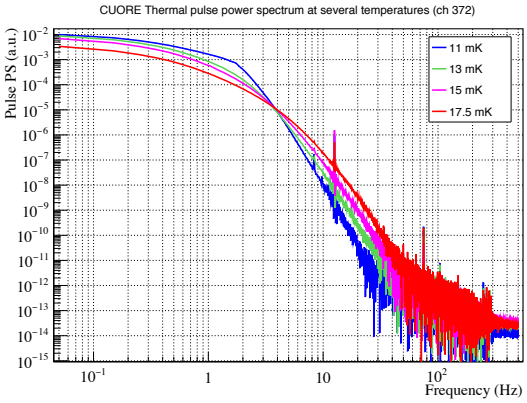

FIGURE 3.10: CUORE thermal pulse power spectrum at several temperatures (log-plot), for one of the CUORE channels (ch 372). Pulses corresponding to 2615 keV ^{208}Tl events are collected to build an 'average pulse'; the average pulse power spectrum (magnitude squared of the pulse fourier transform in the frequency domain) is shown in the plots.

contributions is reported.

$$\overline{v_i^2}(f) = 2\overline{e_A^2} + \left(\frac{\overline{i_A^2}}{2} + \frac{4K_B T_{room}}{2R_L} + \overline{i_{fri}^2}\right)\frac{R_{dyn}^2}{1+\omega^2 C_{par}^2 R_{dyn}^2} \tag{3.23}$$

$$\overline{v_i^2}(f) \approx 2\overline{e_A^2} + \left(\frac{\overline{i_A^2}}{2} + \frac{4K_B T_{room}}{2R_L} + \overline{i_{fri}^2}\right)\frac{1}{\omega^2 C_{par}^2} \tag{3.24}$$

Eq.3.24 holds in case of high resistances and frequencies less than few Hz.
In the equations above: $\overline{e_A^2}$ is the series noise of the preamplifier, $\overline{i_A^2}$ is the parallel shot noise of the preamplifier, $\overline{i_{fri}^2}$ is the non-intrinsic noise contribution, the load resistor corresponds to $2R_L$, the parasitic capacitance of the wiring is C_{par} and R_{dyn} is the thermistor dynamic impedance at the working point.
It is possible to give an estimate of the noise RMS by integrating the noise spectral density over a few Hz range, up to $f_{BW} = \frac{\pi}{2}\frac{1}{2\pi R_{dyn} C_{par}} \approx 5$ Hz. See Eq.3.25, which contains only the noise terms related to the front-end circuit.

$$V_{i,RMS}^2 \approx e_{SRMS}^2 + \left(\frac{\overline{i_A^2}}{2} + \frac{4K_B T_{room}}{2R_L}\right)\frac{1}{2\pi}\frac{R_{dyn}}{C_{par}}[V^2] \tag{3.25}$$

Using the front-end circuit specifications and the detector typical parameters for the CUORE channels, the three contributions to the noise in Eq.3.25 can be calculated. The series noise term is quantified as: $e_{SRMS}^2 \approx 2 \times 10^{-16} V^2$. Given the load resistor value of $2R_L = 60\ G\Omega$ and a preamplifier gate current $I_G = 100$ fA (and $\overline{i_A^2} = 2qI_G$), the terms in the parenthesis contributing to the parallel noise can be calculated.

$$\frac{\overline{i_A^2}}{2} = \frac{2qI_G}{2} \approx 1.6 \times 10^{-32} \quad , \quad \frac{4K_B T_{room}}{2R_L} \approx 2.6 \times 10^{-31}$$

The parallel shot noise term can be considered negligible compared to the Johnson noise of the load resistor.
Considering a parasitic capacitance $C_{par} \approx 500$ pF, the RMS due to the Johnson noise

on the load resistor can be calculated.

$$V^2_{i,RMS-Johnson} = \frac{4K_B T_{room}}{2R_L}\frac{1}{2\pi}\frac{R_{dyn}}{C_{par}} \approx 0.8 \times 10^{-22} R_{dyn} V^2 \tag{3.26}$$

The series noise term e^2_{SRMS} is negligible compared to the Johnson noise of R_L for dynamic impedances higher than few $M\Omega$. The CUORE NTDs are usually operated at working points with resistances of the order of hundreds of $M\Omega$, therefore the noise RMS in Eq.3.25 is driven mainly by the thermal Johnson noise on the load resistor.
As it will be discussed in more details in Chap.4.2.2, the average working point resistance for the CUORE channels is $R_{stat} \sim 0.8\ G\Omega$ (at 11 mK) and $0.25\ G\Omega$ (at 15 mK) and the dynamic impedance is $R_{dyn} \approx 1/3\ R_{stat}$ at the working point. The expected noise RMS due to the Johnson noise on R_L at these two temperatures can be calculated from Eq.3.26.

$$V_{i,RMS-Johnson} \approx 0.14\ \mu V \text{ (at 11 mK)}, 0.08\ \mu V \text{ (at 15 mK)}$$

Given the average conversion factors from amplitude (ADC-mV units) to energy (MeV), it is possible to give an estimate of the limit in resolution from the parallel noise of the load resistor. For an energy conversion gain of $\sim 200\ \mu V/MeV$ at 15 mK, the intrinsic resolution would be $FWHM_{Johnson} \sim 0.95$ keV; at 11 mK, where the bolometer internal gain is higher, $\sim 400\ \mu V/MeV$, the resolution would be $FWHM_{Johnson} \sim 0.80$ keV.
The effective energy resolution of the CUORE channels in the ROI for the $0\nu\beta\beta$ search (around 2.527 MeV) is few keV. [5] It is then clear that the dominant noise contribution comes from non-intrinsic sources, mainly the vibrations of the CUORE cryogenic apparatus: PT cryocoolers vibrations transmitted to the detectors, vibrations transmitted through the detector suspension system, ... The precautions and procedures applied in CUORE for the (active and passive) noise abatement will be discussed in Chap.4.2.1.

Dedicated studies to achieve advances in the CUORE bolometers thermal model understanding were started utilizing the initial CUORE data. The appendices A and B will be devoted to the initial studies and developments of the static and dynamic thermal models for the CUORE bolometers.

[5] For more details of the analysis and the CUORE results for the $0\nu\beta\beta$ decay search see Chap.6.1.

Chapter 4

CUORE Optimization and Data Taking

The CUORE experiment started taking data in 2017, after the completion of the commissioning of the cryogenic system and the installation of the detector.
A quick summary of the commissioning phase will be provided. Afterwards few details of the first CUORE cool-down at full-load with detectors installed will be given. Detector optimization campaigns were performed during 2017 in order to characterize and improve the detectors and overall system performance. This required a lot of effort since it was the first time that such a large number of bolometric detectors were simultaneously operated in a completely new and unique cryogenic system. The activities and analyses performed during the optimization campaigns will be described in details.
The first physics data collected by CUORE in 2017 (from May to June and from August to September) have been used for the $0\nu\beta\beta$ analysis; the data acquisition and the performance of the detector will be briefly commented.
Several activities for CUORE maintenance were performed in late 2017 and early 2018; the actual physics data-taking restarted in May 2018.

4.1 CUORE commissioning and cool-down

The commissioning of the CUORE cryogenic system was completed in February 2016 with a final cool-down of the system at full load (apart from the detector) [104]. Preparations for the detector installation immediately started. By the end of August 2016 the CUORE detector was hanging from the cryostat plate surrounded by protection bags. Fixing the interfaces with the cryostat asked for an additional couple of months. By the end of November 2016 the system was eventually ready for the initial cool-down.

The CUORE detector (first) cool-down started at the beginning of December 2016. During the initial phase (down to $\sim$35 K) the 5 PTs were assisted by the FCS. The cool-down progressed regularly and, after $\sim$20 days, the system reached a temperature of $\sim$3.4 K. The exchange gas was then pumped for about 3 weeks in order to reach the needed vacuum level for turning on the DR unit. By January 27, 2017 the detector reached a base temperature lower than $\sim$8 mK (Fig. 4.1).
The first CUORE pulse appeared few hours later (see Fig. 4.2), when a number of detectors were biased to check their behavior. The commissioning of the detector immediately followed.

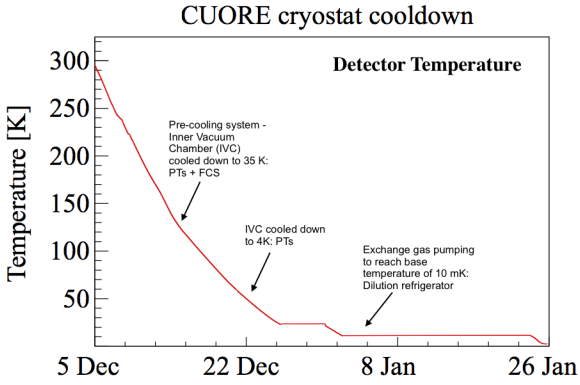

FIGURE 4.1: CUORE detector first cool-down: plot of the detector temperature decrease while each element of the multi-stage cryostat was turned on.

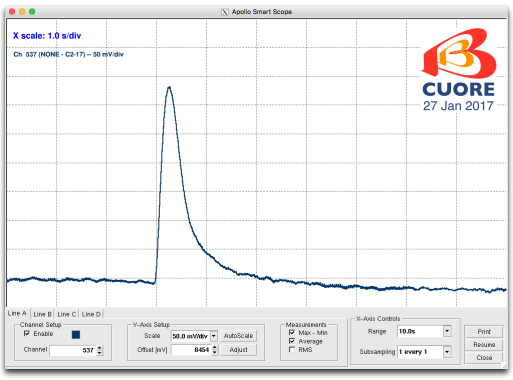

FIGURE 4.2: First CUORE pulse as seen by the Apollo Smart Scope.

4.2 CUORE Optimization

The first few months of CUORE operation in 2017 were devoted to the detector characterization. This was a necessary step in order to have a better understanding of the detector and the overall system, which were different compared to the previous experiences with smaller scale bolometer experiments, like CUORE-0.
Further characterization and optimization campaigns were performed during 2017, with the goal of improving the performance given the knowledge of the system acquired during the initial operations.

The optimization campaigns were meant to improve the sensitivity of the CUORE experiment to the $0\nu\beta\beta$ signal, which depends, among other factors, on the energy resolution and on the live time (see Eq.1.22). Therefore the environmental conditions were monitored and controlled in order to minimize the probability of having periods of unstable data taking. Moreover the detectors were characterized and their operating parameters were tuned in order to improve the energy resolution.
The CUORE detectors energy resolution is affected by several factors. The main ones which characterize the Signal to Noise Ratio (SNR) are:

- Noise sources, such as small temperature instabilities, electronic noise, ground loops, mechanical vibrations, etc.
- Detector parameters, such as the voltage chosen to bias the NTD sensors and the operational temperature, which influence the pulse amplitude and the response stability and linearity

Moreover the quality of the acquired data is influenced by the trigger thresholds and other electronics and DAQ settings.

The studies performed during the optimization campaigns, lead to a significant improvement of the CUORE data quality during 2017.

4.2.1 Noise abatement

A huge effort was devoted in reducing the transmission of vibrations by the cooling system, which immediately appeared to be the dominant noise contribution. In Fig.4.3, it is reported an Average Noise Power Spectrum for a CUORE channel, showing the spectral shape of the noise. It is a very complex spectrum, which is the sum of several contributions. It is possible to recognize few components: the high-frequency cutoff at 120 Hz due to the Bessel filters and several peaks in the spectrum. Understanding the origin of the noise peaks is of extreme importance to get rid of them or at least to reduce them. Many of them can be associated to the Pulse Tubes induced vibrations (peaks at 1.4 Hz and its harmonics, which is the frequency of the pressure waves generated by the PTs). Others are attributed to residual mechanical vibrations and oscillations related to the suspension and support structure (e.g. 0.6 Hz, 0.85 Hz, 3.3 Hz, ..).

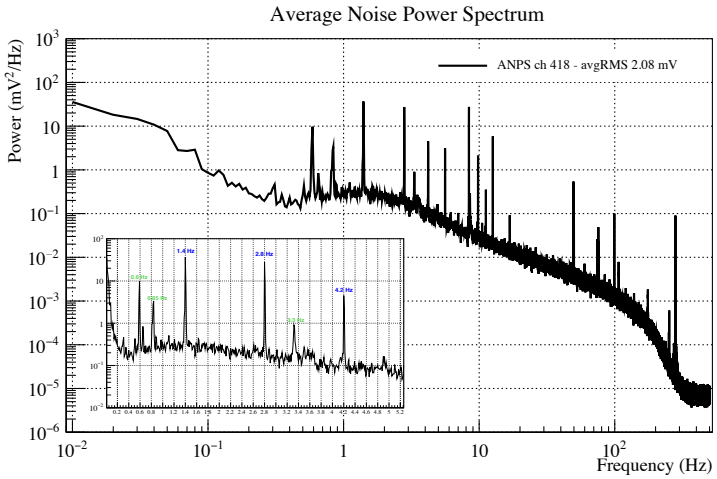

FIGURE 4.3: Average Noise Power Spectrum for a selected CUORE channel. The plot is produced averaging the power spectra of several noise events acquired during a run for a given channel; here 100 s event windows have been utilized. The inset in the plot shows a zoom with a linear scale of the ANPS in the [0,5] Hz, which is the frequency range corresponding essentially to the signal band. In the inset, the peaks related of the PT harmonics are labeled in blue and the ones related to the suspension system are labeled in green.

Mechanical vibration characterization

The detector suspension system, designed to mechanically decouple the detector structure from the structure of the cryostat, was characterized to study the residual vibrational contribution to the bolometers noise, both on the vertical and horizontal directions.

Few dedicated tests were performed in late 2017, in order to see if the acoustic noise in the environment around the top of the cryostat was transmitted to the

bolometers throughout the DS system and if this effect could be reduced.
One part of the detector suspension system is the Y-beam structure; the Y-beam has cavities from which the DS supports are hanging (see Fig.4.4). Foam rubber was utilized to wrap the parts of the DS lines entering the holes in the Y-beam, in order to test the acoustic isolation of the DS system from the outer environment. In Fig.4.5, the average noise power spectra for one CUORE channel for three subsequent test runs: 301733 - no foam, 301736 - foam on DS1 Joint hole, 301739 - foam on DS1, DS2 and DS3 Joint holes. Mainly, the noise peak at $\sim$ 0.6 Hz, related to the DS eigenfrequency, was reduced in intensity by these interventions. Moreover it can be seen that the peak at $\sim$ 150 Hz is reduced in the last configuration (run 301739); the correlation with the reduction of the intensity of this peak and the acoustic insulation of the DS system was not deeply investigated, since that frequency was far from the signal bandwidth and could be easily reduced by an offline filtering of the pulses.

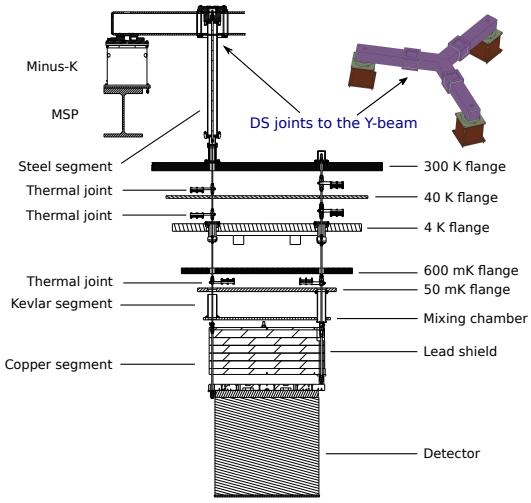

FIGURE 4.4: A cross section of the CUORE cryostat with the technical drawing the detector suspension system and the Y-beam structure (from [87]). The DS joints to the Y-beam are indicated; the holes in the Y-beam structure from which the DS is suspended were filled with foam rubber to acoustically isolate the DS system from the outer environment.

The peak around 3 Hz in the NPS of the CUORE bolometers has been associated to residual oscillations in the horizontal direction of the the cryostat support structure which is placed on the four elastomers. In mid-2017, a temporary damping system to isolate better the cryostat structure from the basement was installed. In Fig.4.6 [left], a comparison of the NPS of a CUORE channel between a test run with no dampers on the basement (301405) and one with the dampers (301410), is reported; the 3.2 - 3.3 Hz peak, which is related to the cryostat pendulum oscillation induced by transmitted vibrations from the basement along the support structure, was reduced after the dampers were installed. In Fig.4.6 [right], there is a comparison of the NPS of a channel (evaluated in approximately 2 hours of data taking) for a test run acquired in quiet and steady conditions (301756) and one acquired instead after some activities were performed on the top and on the bottom of the cryostat structure (301755); the activities perturbed the static equilibrium of the cryostat and the suspended detector, thus the 3.2 - 3.3 Hz peak in the NPS is higher for run 301755.

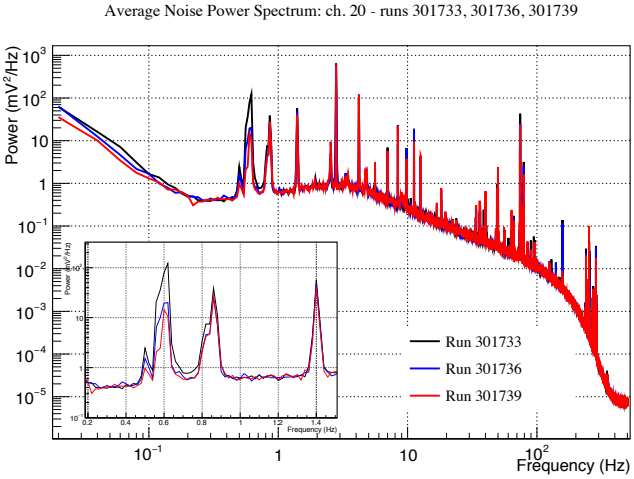

FIGURE 4.5: Average Noise Power Spectrum for a CUORE channel. Here 50 s event windows have been utilized. The inset in the plot shows a zoom with a linear scale of the ANPS in the [0.1,1.5] Hz. In the inset, the peak at $\sim$ 0.6 Hz is reduced from run 301733 to run 301739, due to the acoustic isolation of the holes for the DS joints on the Y-beam.

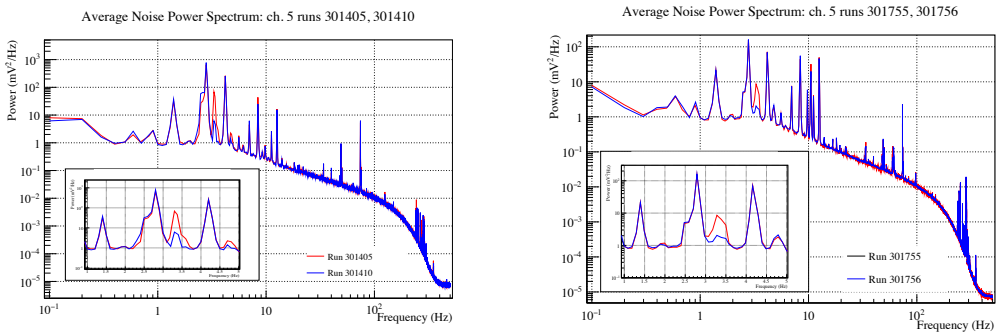

FIGURE 4.6: Average Noise Power Spectrum for a CUORE channel. Here 10 s event windows have been utilized. [Left] Comparison between a test run with no dampers on the basement (301405) and one with the dampers (301410). [Right] Comparison between a test run in quiet and steady conditions (301756) and one acquired after some activities were performed on the top of the cryostat structure (301755).

Pulse Tube active noise cancellation

In order to minimize the impact of the mechanical vibrations induced by the PT cryocoolers, a system to control the relative phases of the pressure oscillations was developed [77]. Indeed pressure oscillations induce vibrations which are transmitted to the cryostat and eventually to the detectors. By driving the relative phases of the PTs it is possible to find the configuration that maximizes the noise cancellation leveraging the interference between the PTs.

The original Cryomech stepper motor drives for the PT rotary valve have been replaced by new low-noise, linear stepper motor drives in order to have more precise and stable motion control. The model used in CUORE is a LNX Linear Series low-noise drive from Precision Motion Control; in the following it will be referred as Linear Drive (LD). The LD is a micro-stepping drive which divides the 360° angle of the PT valve into 25,600 possible positions. It allows a precise control of the rotation

frequency and reduces the vibrations produced by the rotary valve. The frequency control is an essential feature in order to be able to modify the relative phases of the pressure waves generated by the rotary valves.
The replacement of the Cryomech drives with the LDs was implemented after the CUORE cryostat had reached the base temperature. Its effect is shown in Fig. 4.7 [left]. Looking at the temperature fluctuations of the MC plate as measured by the noise thermometer (Fig. 4.7 [right]), an improvement is immediately visible in the stability of the base temperature. Besides the improved stability also a small decrease of the base temperature can be appreciated, due to the lower dissipation of energy by vibrations of the system.

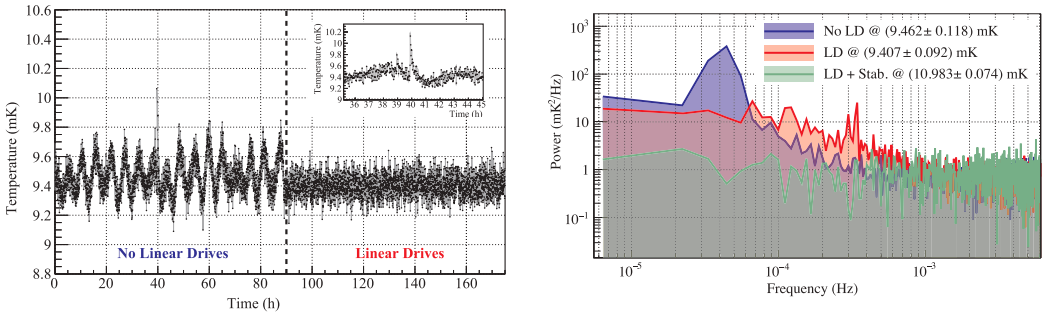

FIGURE 4.7: [Left] Effect of switching the rotary valves feed from Cryomech motors to the LDs. The plot shows the base temperature of the MC plate of the CUORE cryostat, as function of the time (hours from the beginning of the dataset). The temperature is measured by a noise thermometer that acquires 80 1-s samples at 40 kHz rate. The inset shows two small earthquakes visible in the data as two spikes approximately 40 h after the beginning of the data stream. [Right] Effect of the PT-phase stabilization process on the power spectrum of the temperature fluctuations on the MC as measured by a noise thermometer. The data have been taken at different temperatures due to the CUORE data taking constraints. The noise has been computed by averaging several 25-h windows. [77]

Given the complexity of the system, the optimal phase configuration has been obtained scanning a large number of possible phase configurations to achieve the lowest detector noise. A complete scan of the relative phases among the four active PTs has been performed to identify the noise minima and tune the system to the most convenient one.
An algorithm developed in LabView automatically scanned all the possible PT phase configurations with a given level of discretization in the parameter space.
One PT is used as a reference for the other PTs' phase calculation. Three phase shift variables are then defined (e.g. x_i = $PT^{(i)}$ - $PT^{(ref)}$ for i = 0,1,2) and break into steps of a given angular precision, resulting in n_p = $(\frac{360}{\delta})^3$ possible phase configurations. These are mapped to a scalar running from 0 to (n_p-1), called PhaseID. As an example, for δ = 20° step size, n_p = 18^3; the PhaseID mapping is obtained through the following base-18 positional notation:

$$PhaseID = \left(\frac{180^\circ + x_0}{20^\circ}\right) \cdot 18^0 + \left(\frac{180^\circ + x_1}{20^\circ}\right) \cdot 18^1 + \left(\frac{180^\circ + x_2}{20^\circ}\right) \cdot 18^2 \qquad (4.1)$$

For example, PhaseID= 3038 corresponds to the phase configuration (100°, −60°,0°).

Each PT phase configuration is maintained constant for a given time in order to allow the CUORE DAQ to acquire the corresponding detector noise. The first few

seconds are discarded in order to wait for the noise to have reached a stable conditions after each change of PT phases. In the Noise Power Spectrum (NPS), the amplitude of the 1.4 Hz noise peak and its first 10 harmonics is measured for each CUORE bolometer as a function of the PhaseID. As an example, Fig. 4.8[right] shows the intensity of the 1.4 Hz peak in the NPS of one CUORE bolometer. It is possible to identify very distinct maxima and minima in the available PhaseID space. The peak amplitudes of the first 10 PT harmonics are divided for the front-end gain of the electronics, and subsequently multiplied by the corresponding value of the signal power spectrum to weight its effect on the signal bandwidth (weigthed NPS). This suppresses the frequencies less relevant in the bolometer signal rather than assigning a uniform weight to all frequencies. As the bolometric signal is dominated by frequencies below ~ 3 Hz, the importance of the lower harmonics of the PTs (1.4 Hz, 2.8 Hz) is largely enhanced. A normalization of each weighted NPS by its integral allows comparison of channels in terms of their noise relative variations, regardless of having very different absolute noise levels. The phase optimization process was run on a subset of channels, the ones whose noise is affected the most by the PT induced vibrations. The outcome of the PT phase scan analysis is the identification of the PhaseID with the lowest detector noise; therefore the corresponding PT phases were set for the data-taking. Fig. 4.8[left] shows an example of the lowering of the PT peaks in the NPS of one of the CUORE channels when the best phase configuration was set.

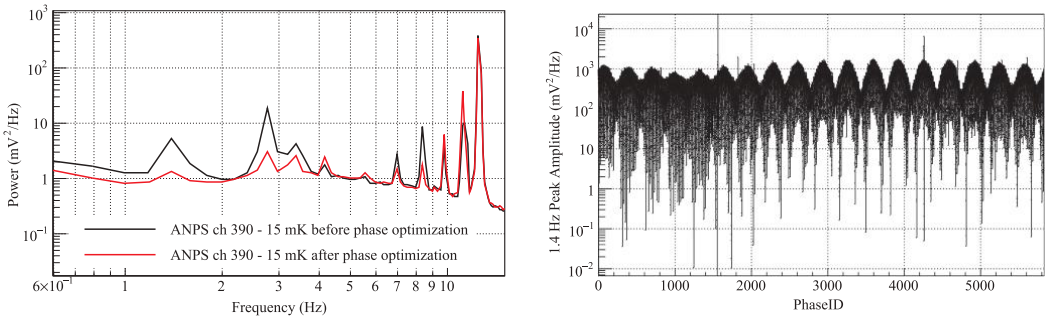

FIGURE 4.8: [Left] Average Noise Power Spectrum (ANPS) for one of the CUORE bolometer up to 15 Hz. The first ten 1.4 Hz peak harmonics are shown while using the stabilization algorithm for a non-optimized (black) high-noise PT phase configuration. The reduction of the amplitude of the lower harmonics is clearly visible after phase optimization (red). [Right] Amplitude of the 1.4 Hz peak of the NPS for a channel that is particularly sensitive to changes in PT phase configurations. The phase cconfigurations for three PTs are measured relative to a fourth, each representing a 20° increment. This results in a 3D phase space with a volume of 18^3 unique configurations. [77]

4.2.2 Setting the detectors Working Points

The choice of the correct bias voltage is crucial for the operation of the NTDs sensors. Therefore, it is necessary to acquire special runs in which the variation of the NTD resistance, signal amplitude and baseline noise are analyzed as a function of the applied voltage. The characteristic I-V curve (called "load curve") of each detector is measured and the best bias voltage, the so called "working point", is then identified along the load curve. It corresponds to the best SNR, which is defined as the ratio of the pulse amplitude and the average RMS for a given bias configuration (SNR =

$\frac{PAmp}{RMS}$). This is usually a compromise between a large signal amplitude and the lowest noise condition, while still ensuring a linear and stable behavior of the detector. [105]

The load curve measurements and the identification of the optimal working points are, in general, procedures that can be performed manually in bolometric experiments with a limited number of channels, like it was for CUORE-0. In CUORE, the number of channels to be optimized is almost one thousand, moreover the NTD thermistors have resistances values higher and with a wider spread than small-size experiments. Therefore it was necessary to develop new procedures and algorithms to automatize the load curve measurement and the working point identification.

Load Curves procedure

A dedicated sequence in the data acquisition has been developed in order to measure the characteristic **load curve** parameters of each CUORE channel. Every bolometer is slightly different from each other, therefore it is fundamental to optimize each single channel in terms of finding the bias voltage for each channel's NTD from the analysis of the *Load Curve* data.
During the load curve procedure the bias voltage V_B is varied from 0 to few Volts consequently varying the polarization voltage V_{bol} across the NTD [1].

The *Load Curve* procedure can be summarized as follows:

- Initially the actual electronics configuration is read, so that at the end of the procedure it is possible to restore it
- The preamplifier offset is usually set to 0 V, in order to have the data stream taking values in a range almost symmetric around zero
- The gain is changed to a low value G (e.g. 206 V/V) in order not to exceed the ADC dynamics along the load curve development
- The NTD is polarized, setting a total bias voltage $V_{B,1}$ to the circuit. Few hundreds of seconds of data are acquired at negative polarity, then the bias polarity is inverted and other few hundreds of seconds are acquired at positive polarity. This data correspond to one point in the detector I-V curve. The polarity is switched again to negative, a new higher value of the bias is set $V_{B,2}$ and the same steps are repeated. The procedure scans several bias voltages which are defined by a configuration file given in input.
- A fixed energy reference heater pulse is periodically fired; the pulse amplitude together with the noise RMS are then used to calculate the SNR and to identify the optimal working point
- After the scan of the response over all the bias voltages of interest is completed, the initial electronic configuration is restored for each channel

The data stream for one channel which is acquired during a Load Curve run is shown in Fig.4.9.
There is a dedicated sequence in the Apollo software which drives the data acquisition during the *Load Curve*. A different configuration ID (configuration ID > 0) is assigned to the data belonging to each electronic configuration (bias and polarity) that is scanned. The time intervals during the electronics change are flagged with a null configuration ID, and then they can be easily rejected from the further analyses.

[1] More details on the detector operation for the CUORE bolometers and NTDs are in Chap.3.5.

Given a bias voltage, the duration of the negative polarity is fixed by requiring a minimum number of heater pulses, while the positive polarity lasts a time interval which corresponds to a given minimum number of noise events. The negative polarity data are used to evaluate the reference heater pulse amplitude, while the noise events from both polarities are used to evaluate the parameters of the I-V curve.

Although the *Load Curve* procedure had already been utilized in CUORE-0, given the large number of channels in CUORE, a number of algorithms have been implemented to automatize what in CUORE-0 was done manually. Moreover a number of upgrades on the sequence for performing the *Load Curves* were implemented:

- Higher precision of the reading/writing of the bias for each step (∼10 mV), to improve to accuracy of the *Load Curve*
- Accurate choice of bias range and steps for the various NTD batches and for each temperature, in order to span all the response region but trying to avoid saturation and channels instabilities
- Developed sequences for performing bipolar and unipolar (saturated positive polarity) curves; the latter kind of runs were performed in case only the noise RMS and pulse response was to be studied, without the need to reconstruct the I-V curve

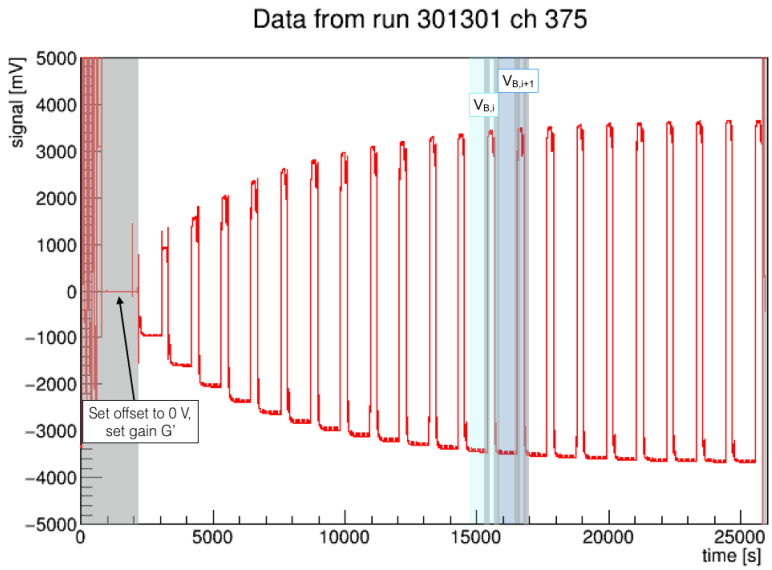

FIGURE 4.9: Example of a *Load Curve* run for one channel. The red line is the channel continuous data stream. The grey shaded areas indicate where the data are ignored by the analysis. The two regions in shaded blue correspond to two different bias voltage configurations, both negative and positive polarities; a zoom of these areas if provided in Fig.4.10.

A dedicate set of load curve runs has been taken at 15 mK before the beginning of the first CUORE dataset (late April 2017), to set the working points for the initial CUORE data taking. The procedure has been repeated after bringing the system temperature to 11 mK (late December 2017) in order to choose the correct bias for the subsequent CUORE data taking.

Load Curves data processing

Starting from the CUORE-0 load curves processing sequence, some software development was required for the processing and data quality validation of the *Load Curve* collected data in CUORE. The most relevant are:

- Optimum filter [2] and related variables were added to each point of the LC
- Dedicated modules to evaluate and save the AP and ANPS for each LC point were developed
- Custom ntuples with LC points values were created as output of the data processing
- Handling of both bipolar and unipolar curves data and correct evaluation of the load curve parameters was introduced
- Identification of saturated or unstable configurations of the load curve data was implemented

The analysis sequence of the Load Curves data takes the values of baselines[3] ($Bsl_i^{\pm}$), noise RMS, pulse amplitude, gain (G) and load resistance (R_L) for each bias configuration $V_{B,i}$ (from both negative and positive polarity data) for each channel and uses them to reconstruct the I-V curve. See Fig.4.10. The parameters of each *Load Curve* are calculated as follows:

$$\text{Baseline: } Bsl_i^{\pm} = \langle Bsl_j^{\pm} \rangle_i \text{ for } j \text{ noise triggers} \tag{4.2}$$

$$\text{Bias voltage: } V_{B,i} = \frac{V_{B,i}^{-} + V_{B,i}^{+}}{2} \tag{4.3}$$

For the I_{bol}-V_{bol} curve:

$$V_{bol,i} = \frac{Bsl_i^{+} - Bsl_i^{-}}{2G} \tag{4.4}$$

$$I_{bol,i} = \frac{V_{B,i} - V_{bol,i}}{R_L} \tag{4.5}$$

The NTD static and dynamic resistance at each bias configuration:

$$R_{bol,i}^{(stat)} = \frac{V_{bol,i}}{I_{bol,i}} \tag{4.6}$$

$$R_{bol,i}^{(dyn)} = \left(\frac{dV}{dI}\right)_i \text{ evaluated by the discrete incremental ratio} \tag{4.7}$$

The noise RMS and pulse amplitude at each bias configuration are calculated with two methods.
In the first approach, the amplitude of each pulse is calculated as the difference between the maximum and the minimum of the pulse; the amplitudes obtained at the same bias configuration are then averaged together to reduce the effect of noise, $PAmp_i$. The other method consists in averaging all the heater pulses of a same bias configuration, building an Average Pulse (AP); each point of the curve is the amplitude of the respective average pulse, $APampl_i$. In both cases events showing pileup

[2] A description of the Optimum Filter technique that is applied on the data can be found in Chap.5.1.2

[3] The term 'baseline' is referred as the voltage at the NTD output, as read after the pre-amplification stage and offset correction

or too close to the polarity inversion are discarded.
The RMS is measured on all the noise events of both polarities, eliminating those events having pulses in it or being too close to the polarity inversion. The first method consists in evaluating the standard deviation of samples of the noise events around the baseline, RMS_i; the second one uses instead the optimum filter built on all the noise and signal events of each bias configuration. In the Noise Power Spectrum (NPS) of the filtered noise events the frequencies that do not contribute to the signal events are attenuated, thus leaving mostly the low frequency components of the noise. The RMS is then evaluated as the square root of the integral of that NPS and it corresponds to the resolution of the filtered baseline, $OFRMS_i$.
Eventually, the SNR is computed using the amplitudes and the RMS calculated with both methods (SNR_i, $OFSNR_i$).

The load curve values for each channel are then used to build several curves: V_{bol} vs. I_{bol} (the I-V curve), PAmp vs. I_{bol}, RMS vs. I_{bol}, SNR vs. I_{bol} (using noise and amplitude from both standard and filtered signal). In Fig.4.11, there is an example for each of the curves built.

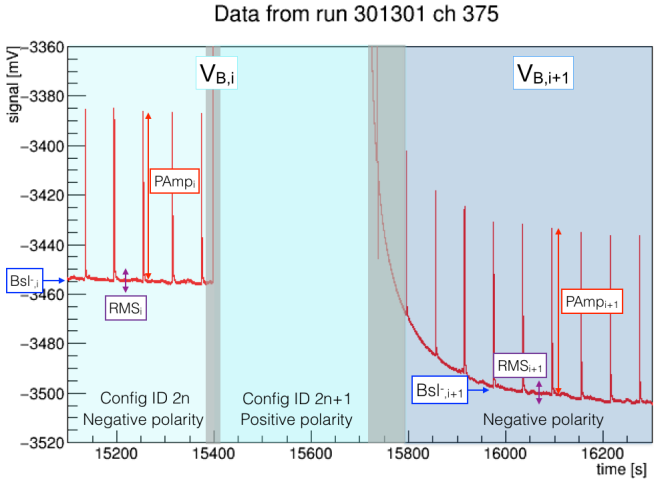

FIGURE 4.10: Example of the data stream from a *Load Curve* run for one channel (from Fig.4.9), zoomed around two regions which correspond to two different bias voltage configurations ($V_{B,i}$,$V_{B,i+1}$).

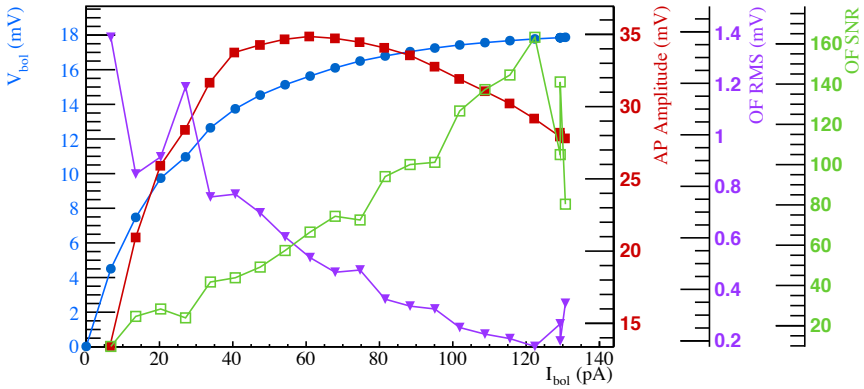

FIGURE 4.11: Example of the Load Curve Plots that are produced for each channel (here for Channel 831 Run 301018).

Load Curves analysis and WP selection

The analysis to find the working point for each channel consists in two sets of Load Curves.

A preliminary set of Load Curves is done in order to identify the correct range of bias values and find the maximum allowed bias $V_{BiasMax}$ for each channel. This is necessary because if the bias is too high and way beyond the inversion point on the V-I curve, the detector output enters an unstable region and eventually it will start oscillating (see Fig.4.12). The oscillation amplitude can be up to few Volts, influencing also channels read on the same front-end board.
Few selections on the LC data are applied to identify oscillating conditions. When the $RMS_i/G > 1$ mV, the oscillation condition is reached. Moreover a running average RMS (avgRMS) over all LC points and the standard deviation of the RMS (stdDev) of each step are evaluated, to possibly identify unstable LC points just before the oscillation; points with $|RMS_i - avgRMS| > 3$ stdDev are discarded. This procedure leads to identify the $V_{BiasMax}$ for each channel.

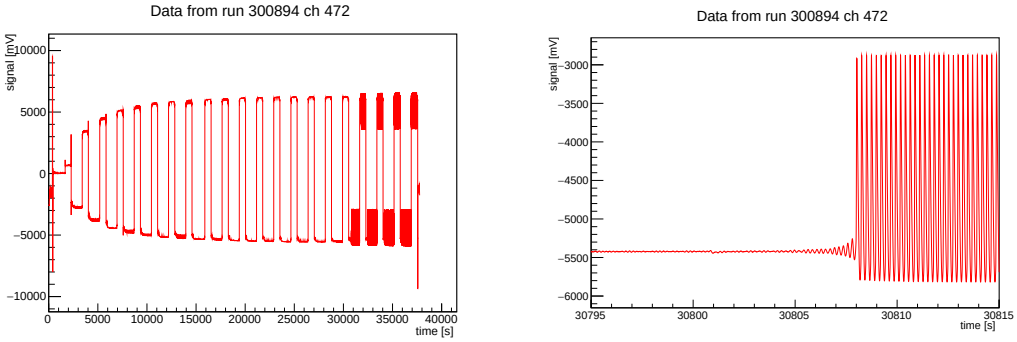

FIGURE 4.12: [Left] Example of a detector output during a Load Curve run. The channel is oscillating in the last bias configurations. [Right] Zoom in of the Load Curve on the left, around 31000s after the start of the run, in which the channel exhibits increasing instabilities up to oscillations of the order of few volts.

The final set of Load Curves consists in a finer scan of the voltages within the accepted range of V_{bias} for each channel. These runs had an average of 20-30 increasing bias values, from 0 V to the $V_{BiasMax}$ of each different channel. Each bias configuration has 20-25 heater pulses in the negative polarity and 5-10 noise triggers for the positive polarity.
The choice of the amplitude of the pulser to be used for the LC has been found to be crucial. Values of the bias too close to the inversion point enter an unstable condition during the development of the signal. This results in deformations of the pulses; the pulse deformation is energy dependent and it is less prominent at higher energies. Figure 4.13 (left) shows a channel in which the energy dependence of the pulse deformation is clearly visible. The pulser amplitude used in a LC should be chosen in order to correspond to an energy deposition close to the region of interest (ROI) for the $0\nu\beta\beta$; indeed it was found that optimizing the response at much higher energy resulted in possible deformed particle pulses at the energies of interest (< 3 MeV) at the WP set. Conversely, a proper choice of the pulser amplitude for the LC, leads to a choice of a working point bias value in a region of stability for the channel and to an improved and more uniform pulse shape at several energies, see Fig.4.13 (right).

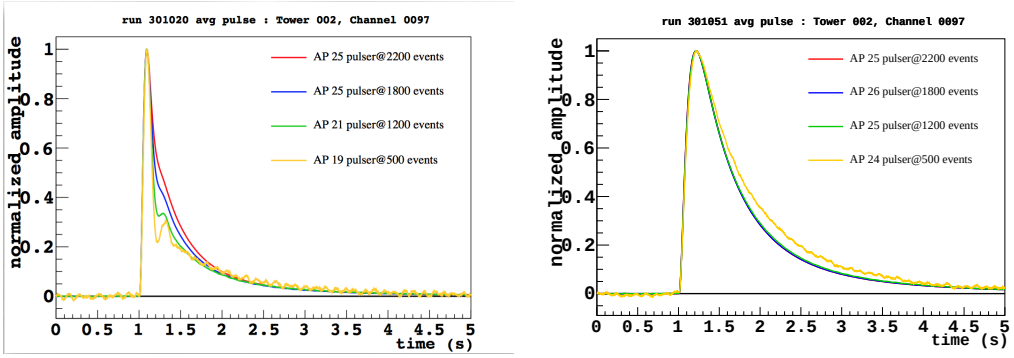

FIGURE 4.13: Example of AP at different energies of channel 97 at 15 mK. [Left] The energy dependence of the pulse deformation is clearly visible and increasing with decreasing amplitudes. Here the working point had been set to optimize the pulser@2500 ($\sim$ 7 MeV). [Right] The working point here was set to optimize the pulser@1000 ($\sim$ 1 MeV). The pulse doesn't show any deformation at lower energies.

From the Load Curves analysis, the optimal working point of the detector is chosen following some basic requirements: maximize the signal to noise ratio, stay in the region before the inversion point of the V-I curve avoiding pulse deformation.

In CUORE-0, which had only 52 channels, the procedure for choosing the working points was carried out "manually" just looking at the Load Curves Data (I_{bol} vs. V_{bol}, PAmp vs. I_{bol}, SNR vs. I_{bol}) and finding the maximum of the pulser amplitude and the maximum SNR by-eye. The V_{biasWP} was then set as an intermediate value between those corresponding to the two maxima for each channel. In CUORE an automated tool has been developed to provide the Working Point bias voltage for all the 988 channels.
The automated working point search algorithm works according to these steps for each channel:

- Get the Load Curves Data corresponding to the selected channel and build the following plots: PAmp vs. I_{bol}, RMS vs. I_{bol}, SNR vs. I_{bol} (using noise and amplitude from both standard and filtered signal), V_{bol} vs. I_{bol}
- Find the maximum of V_{bol} in the V_{bol} vs. I_{bol} curve, corresponding to the inversion point, and get the corresponding bias, $V_{bias,VbolMax}$
- Find the maximum Pulse Amplitude on PAmp as a function of I_{bol} and get the corresponding $V_{bias,PAmpMax}$
- Find the maximum Signal to Noise Ratio on SNR as a function of I_{bol} curve and get the corresponding $V_{bias,SNRMax}$.

In Fig.4.11 there is an example of all the different curves built from the Load Curve data of one of the CUORE detectors and which would be used to extract the corresponding optimal working point. In building these curves there are some additional precautions that have to be taken into account before finding the working points. A check is run on all the above curves to remove possible (still) oscillating or saturated points and outliers corresponding to an incorrect evaluation of the pulse amplitude variable (or RMS, or Vbol). These points could lead to the selection of a bad working point. An example is reported in Figure 4.14 where one point of the amplitude curve is an outlier compared to the rest of the curve; this can be caused by a physical coincident event in the same crystal or to an error in the amplitude evaluation. When

looking for the maximum of the amplitude curve, the presence of this outlier could lead to a fake maximum.
The analysis for finding the optimal WP is then performed only on the load curves points which pass these safety checks and in a bias range $[V_{bias,PAmpMax}, V_{bias,VbolMax})$.

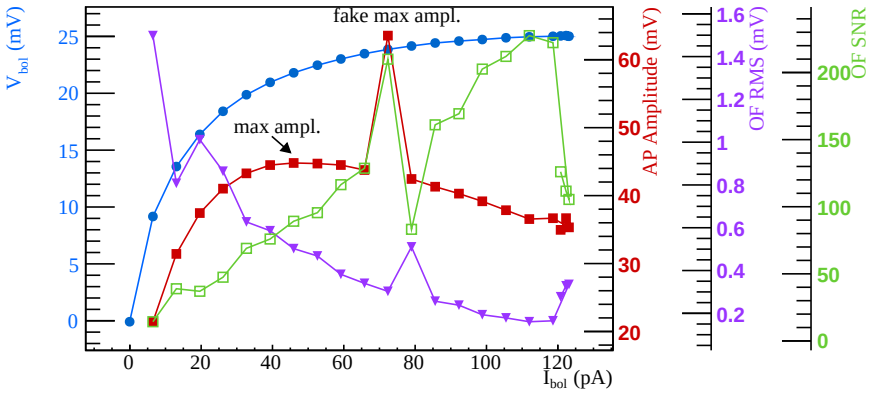

FIGURE 4.14: Example of Load Curve Plots for a channel in which a fake maximum of pulse amplitude curve is identified by the algorithm; it is therefore skipped and the real maximum of the curve is found (here for Channel 19 Run 301018).

The shape of the heater pulses at the different bias voltages has been investigated as a figure of merit for identifying instability conditions.
Sometimes the working point corresponding to the maximum of SNR is still in a region of high bias, where the pulses can be deformed due to the proximity to the inversion point (see Fig.4.15). In order to prevent pulse deformation, when setting the Working point, a check on the pulse shape at the bias voltage corresponding to the maximum of SNR is performed. If the channel is identified as having a deformed pulse, the algorithm takes iteratively the previous points on the load curve and applies the same shape checks until undeformed signals are found.
Eventually the optimal WP bias that is chosen is a compromise between avoiding deformed pulses and maximizing the SNR.

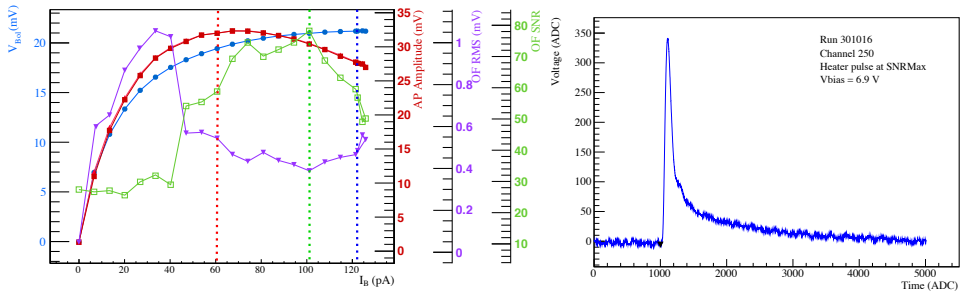

FIGURE 4.15: Example of Load Curve plots from Run 301016 channel 250. [left] The dashed red vertical line indicates the maximum of pulse amplitude, the green dashed line corresponds to the maximum of SNR curve and the blue one to the maximum of the I-V curve (inversion point). The heater pulses associated to the Vbias corresponding to the maximum of SNR curve are slightly deformed [right]; for that value of the bias (Vbias = 6.9 V), the channel is probably sitting in an unstable region of operation, close to the inversion region.

Among the 988 CUORE bolometers, there are 29 channels without a functioning heater which means that it is not possible evaluate the pulse amplitude as a function of the bias using the heater pulses. In case of heaterless channels and channels with not enough good points on the load curves (less than 4 points on the load curves)[4], a dedicated check on the Vbol-Ibol curves is performed to choose proper values for the bias voltage to be set. Eventually the algorithm provides a V_{Bias} for the working point at the conservative value a bit lower than the average bias voltages found for the other channels. In this case, the SNR could be slightly worse and the pulse amplitude lower than the other channels, but there would be no risk of having oscillating channels whose crosstalk could spoil also neighbors channels.

After setting the working points given by the algorithm, a final check of the pulses quality and the stability of the channel operating conditions is performed. This check is done with dedicated measurements, called 'Npulser runs', in which several pulsers of different amplitudes (200 keV - 2 MeV) are fired. Average pulses for all the different amplitudes are produced and compared to verify the shape stability. The efficiency of the algorithm for finding a correct WP is $\sim$ 96%; few channels showing still a bit deformed pulse shape at the WP that is set, can be found. The channels for which the algorithm doesn't provide the optimal bias voltage are usually either very noisy channels or the heater-less ones; since these would be approximately 20-50 channels, few checks and tuning of the bias voltages can be done manually.
After this tuning of the WP bias voltages, another Npulser run is taken, to perform final quality checks on the channels pulse shape, especially for those for which the bias had been changed and optimized.

Load Curves and WP at 15 mK
The first analysis to find the working point for the CUORE channels at 15 mK was performed in the second half of March 2017 and consisted in two sets of Load Curves in the following configuration: gain = 206, offset = 0 V, Bessel cutoff = 15 Hz, pulser amplitude = 2500 corresponding to a particle energy deposition of approximately 7 MeV.
The first set of Load Curves runs was done in order to find the maximum bias for each channel. The second set of Load Curves runs was done in order to find the working point for each channel.
All the working points (WP) were set in early April 2017 and the CUORE initial data taking started with a test dataset, DS3015. During dataset 3015 few problems arose, for a significant fraction of channels, that were related to values of the bias too close to the inversion point, leading therefore those channels to instability condition. The first symptom was the deformation of low energy pulses, which in its extreme forms distorts the pulse in such a way that it appears to have two maxima, mimicking a pileup event. Within the analysis chain, events with more than one pulse are usually rejected to avoid pileup, so many of these deformed pulses were rejected from the subsequent analysis. The second symptom was the impossibility to stabilize the amplitudes for those channels using the reference heater pulses, resulting in double calibration peaks and bad resolution. These problems were not noticed during the analysis of the second set of LoadCurve runs because, as it was discovered later, the pulse deformation is energy dependent and it is less prominent at high energies, at which the reference pulse was set.

[4]This can be the case for very noisy channels, in which any (or very few) event pass the selection cuts for good noise and pulse waveforms, therefore making the reconstructed LC points not reliable for the WP analysis.

A third set of LoadCurve runs was then acquired in the second half of April 2017 with the same configuration of the previous ones with the exception of the pulser whose amplitude was set to 1000, corresponding to about 800 keV.
The list of the LC runs that were used eventually to set the working points at 15 mK is:

- run 301016 (Towers 1-6) 21-04-2017
- run 301017 (Towers 7-12) 22-04-2017
- run 301018 (Towers 13-19) 23-04-2017

The Load Curve plots for these runs were built for all the channels. However due to some inaccuracy of the electronics and a not completely optimized procedure for performing the LC and analyzing the raw data, the quality of the LC reconstructed points was not optimal. This resulted in RMS and SNR curves sometimes appearing a bit jagged (see Fig.4.11).
Assuming the RMS dominated by the Johnson noise of the load resistor, then it is proportional to the NTD resistance (see Eq.3.20) which in turn depends on both the operational temperature and the V_{Bias} value. A linear robust fit of RMS vs. Rbol was performed in order to smooth the RMS curve. A range of R_{bol} covering only the stable region of operation of the NTD was selected. An example of the fit is shown in Fig.4.16 [left]. Instead of using the experimental values for the RMS, the values extrapolated from the fit were utilized. The values extrapolated for the RMS were eventually used to smooth the SNR curves as illustrated in Fig.4.16 [right].

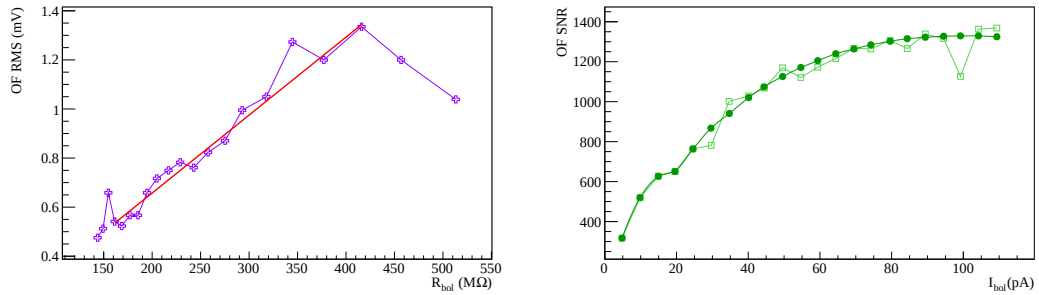

FIGURE 4.16: [Left] Example of the RMS versus Rbol linear fit. [Right] SNR curve before and after the smoothing process. The curve now is more homogeneous than before allowing the better performances of the algorithm to find the WP.

After having found the bias corresponding to the maximum SNR, the pulse shape was checked. The pulse deformation was quantified in terms of number of flexes in the pulse. Each pulse was filtered to remove high frequency noise and then sub-sampled from 1 kHz to 125 Hz, because only the deformations in the frequency range of the pulse were the ones of interest. The discrete second derivative of the subsampled and filtered pulse was evaluated and the flexes were counted on that. When the NTD was operating at 15 mK, 2-3 flexes would be identified on its signals, depending on how much the decay time constants are close to each other; deformed pulses would have more than 3 flexes. In Figure 4.17 it is shown an example of a deformed pulse and a good pulse with their second derivative on which the number of flexes is evaluated.

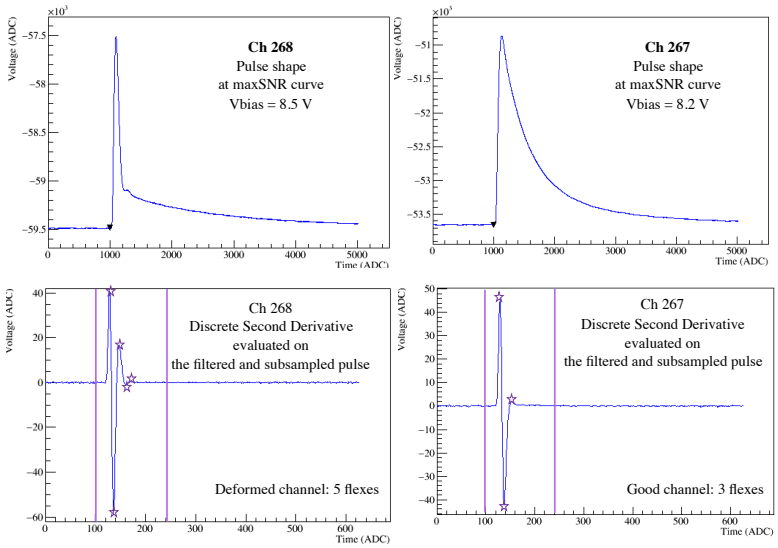

FIGURE 4.17: Example: Load Curve Run 300899, Channels 268 and 267. Pulser waveforms and their discrete second derivative for Vbias corresponding to the maximum of SNR in the Load Curve plots. The number of flexes identified on the second derivative plot allows the discrimination between stable channels (ch 267 - 3 flexes) and unstable/deformed ones (ch 268 - 5 flexes).

In conclusion, the optimal WP bias voltage for each channel was chosen, optimizing the pulse amplitude and the signal to noise ratio and avoiding pulse deformation. The bias voltage values applied to the bolometers at a base temperature of 15mK are reported in Fig. 4.18[left]. The values cluster around voltage values of 4.0 - 5.0 V [5]. This corresponds to an average WP resistance of $R_{bol,wp} \sim 0.2$ - 0.3 $G\Omega$ [6], see Fig.4.18[right].

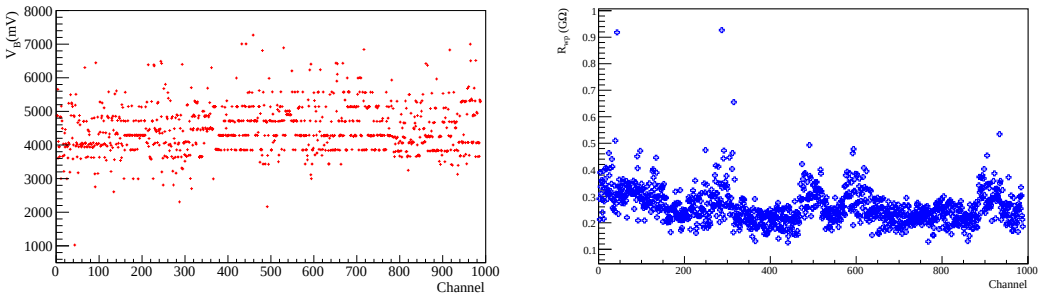

FIGURE 4.18: 15 mK base temperature. [Left] Distribution of the bias voltages applied to the NTD as a function of the channel number. [Right] Distribution of the NTD resistance at the selected WP as a function of the channel number

[5]The WP bias voltages values show a clear spacing due to the fact that the load curves at 15 mK have been acquired with a finite number of bias values, with 300 mV steps

[6]The spread of the resistance values is due to the use of the three different types of NTD with slightly different behavior, as discussed in Chap.3.6

Load Curves at 11 mK and improvements of the WP finding algorithm
The analysis to find the working point for the CUORE channels at 11 mK was performed in late December 2017 and consisted in two sets of Load Curves in the following configuration: gain = 412, Bessel cutoff = 120 Hz, pulser amplitude = 1000 - approximately 1.5 MeV, R_{load} = 60 $G\Omega$.
As usual, the first set was done in order to find the maximum bias for each channel and the second one to find the working point for each channel. In this occasion, only unipolar load curves were acquired. The gain was set to an higher value than the LC at 15 mK, in order to better exploit the ADC dynamics and improve the precision on the noise characterization.
The list of the LC runs that were used to set the working points at 11 mK is:

- run 301783 (Towers 1-6) 29-12-2017
- run 301781 (Towers 7-12) 27-12-2017
- run 301779 (Towers 13-19) 25-12-2017

With the experience gained during 2017, these load curve runs were characterized by optimized procedures for performing both the measurement and the following data processing and analysis. Therefore the LC points reconstruction quality was ameliorated.

Moreover a new approach for checking the pulse shape at each bias voltage was implemented. It made use of the parameters coming from the fit of the heater pulses with a template reproducing the main features of the thermal pulse. Main advantage of the fit is an effective and precise way to identify deformed signals, while the efficiency of the algorithm to count the pulse flexes depended on the noise RMS, the frequencies of the noise contributions and the pulse shape of each particular channel.
In the algorithm for finding the WP, the informations coming from the fit of the pulses were added and their distributions were utilized to identify the best operating conditions. The template fit function considers a transfer function for the bolometer and NTD system composed by two real poles, two complex conjugate poles and one zero. A more detailed description of the thermal response function used for the fit of the pulses and the correspondence between fit parameters and physical quantities can be found in App.B.
The LC analysis was focused on the fit results for the real and the imaginary parts of the complex conjugate poles ($Re(pole)$, $Im(pole)$), which are the ones correlated with the deformations in the pulse shape at increasing bias values. This can be explained since these poles are related with physical quantities which depend both on the electrothermal feedback induced by the bias at the given base temperature and on the RC of the circuit. The real part of the complex conjugate poles is $Re(pole) < 0$. For low bias values, the imaginary part is negligible compared to the real one. Real and imaginary parts increase in absolute value with the applied bias, until they cross and the imaginary part starts to dominate. This corresponds to the condition in which the channel operation gets unstable and the pulse deviates from the 'usual' shape, characterized by one time constant on the rising edge and two time constants on the falling edge. In Fig.4.19, it is reported the absolute value of $Re(pole)$ and $Im(pole)$ from the fit of the heater pulses in a LC for a channel at 11 mK. In Fig.4.20, it is reported the average pulse for a channel at two bias voltages, $V_{bias2} \gg V_{bias1}$, resulting in two different regions of the ($Re(pole)$, $Im(pole)$) parameter space from the fit; for a low bias, $|Re(pole)| \gg |Im(pole)|$, and the pulse shows the 'usual' shape, while at high bias, $|Im(pole)| \gg |Re(pole)|$, and the pulse shows deformations.

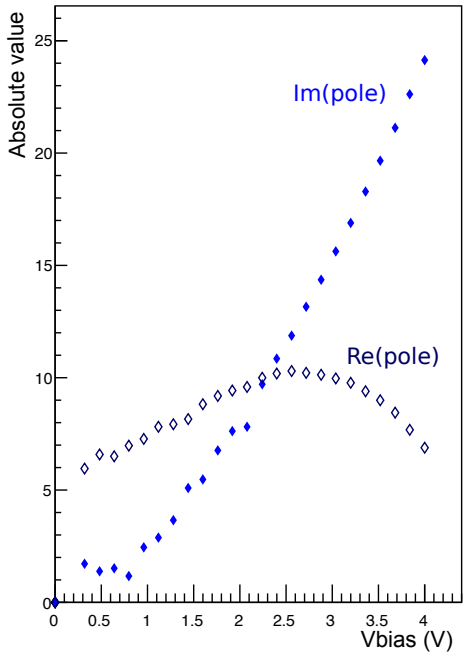

FIGURE 4.19: Absolute value of $(Re(pole), Im(pole))$ obtained from the fit of the heater pulses at the several bias voltages in a LC. Channel 350 Run 301781 at 11 mK.

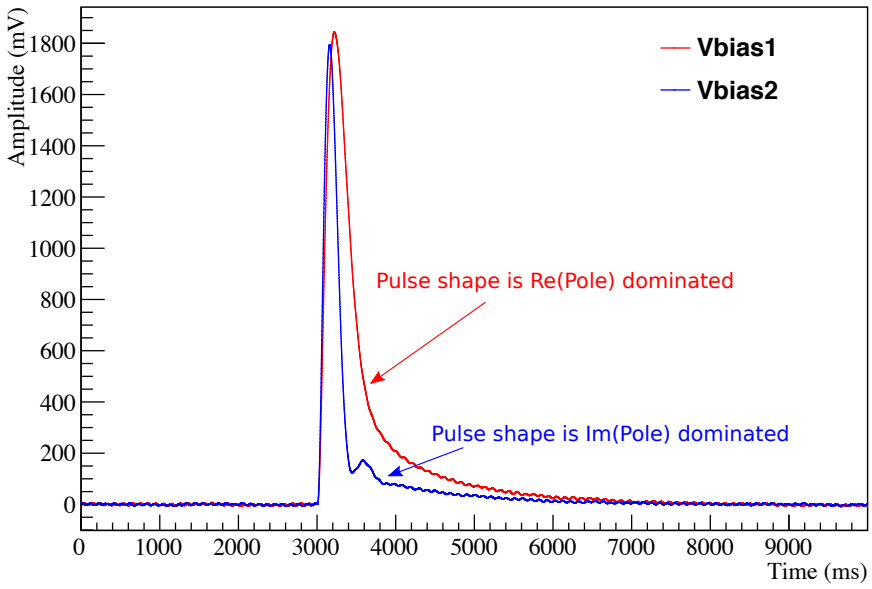

FIGURE 4.20: Shape of heater pulses in two different regions of the $(Re(pole), Im(pole))$ parameter space at 11 mK for a given channel. At low bias voltage, the pulse shape is dominated by $Re(pole)$ (red); at high bias the pulse shape is $Im(pole)$ dominated and the pulse starts showing clear deformation on its tail (blue).

Given these considerations, a check on the ($Re(pole)$, $Im(pole)$) fit parameters was added to the procedure to find the WP, ensuring the choice of stable operating conditions for the NTD. For each point of the LC, the normalized difference of the absolute values of the real and imaginary parts of the complex conjugate poles was evaluated.

$$R = \frac{|Im(pole)| - |Re(pole)|}{mod(pole)} \quad \text{with} \quad mod(pole) = \sqrt{|Im(pole)|^2 + |Re(pole)|^2}$$

A value of R_{opt} = - 0.2, was found to be a reasonable condition allowing a good SNR while avoiding deformed pulses, for 11 mK base temperature.
For each channel, the optimal working point at 11 mK was then chosen looping back on the LC points from $V_{bias,VbolMax}$ to $V_{bias,PAmpMax}$ and checking the SNR value to be maximized and the shape parameter R to satisfy $R \approx R_{opt}$ [7].
In Fig.4.21, the plot of the shape parameter R for a given channel in a LC at 11 mK is reported; the condition to find the optimal WP is illustrated. Satisfying that condition ensures to work in a $Re(pole)$ dominated region, as shown in Fig.4.22. The WP that is chosen with this updated version of the algorithm ensures a good SNR and a stable response of the channel (see Fig.4.23).

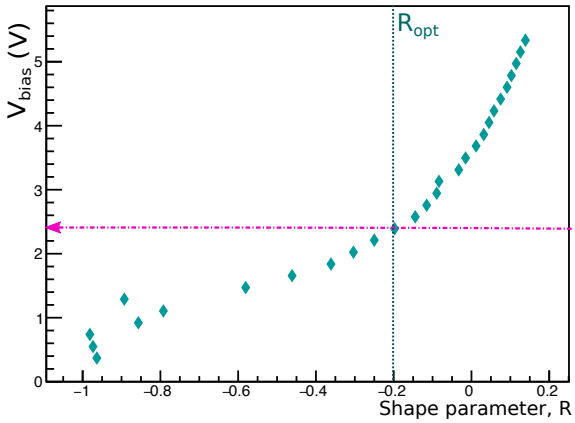

FIGURE 4.21: Channel 358 Run 301781, LC at 11 mK. Pulse shape parameter R evaluated at the several bias voltages. The dark green dashed line indicates the shape parameter optimal condition and the WP bias is found and indicated by the magenta line with the arrow.

[7] The value of precision set for the match of R with R_{opt} was 0.05, as the maximum allowed difference between R and R_{opt}

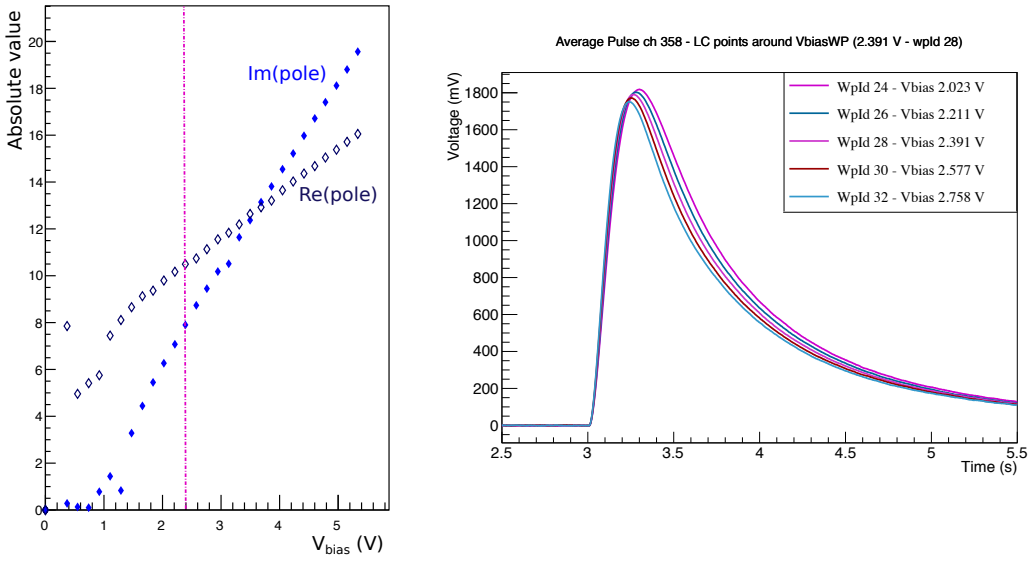

FIGURE 4.22: Channel 358 Run 301781, LC at 11 mK. [Left] Absolute value of $(Re(pole), Im(pole))$ obtained from the fit of the heater pulses at the several bias voltages in a LC. The magenta line indicates the point in the LC corresponding to the bias chosen for the WP. [Right] The heater pulses associated to the VbiasWP and to bias values for LC points around the selected one.

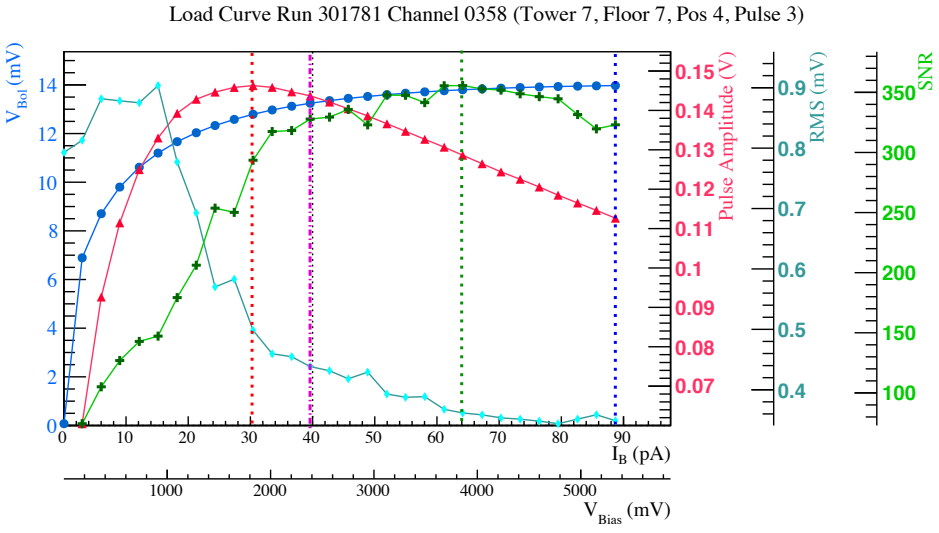

FIGURE 4.23: Example of Load Curve plots from Run 301781 channel 358 at 11 mK. The dashed red vertical line indicates the maximum of pulse amplitude, the green dashed line corresponds to the maximum of SNR curve and the blue one to the maximum of the I-V curve (inversion point). The magenta line indicates the point in the LC corresponding to the bias chosen for the WP, satisfying the high SNR and good pulse shape conditions.

The optimal WP bias voltage values applied to the bolometers at a base temperature of 11mK are reported in Fig. 4.24[left]. The values cluster around voltages of 1.5 - 2.0 V. This corresponds to an average WP resistance of $R_{bol,wp} \sim 0.6$ - 1.2 $G\Omega$, see Fig.4.24[right].

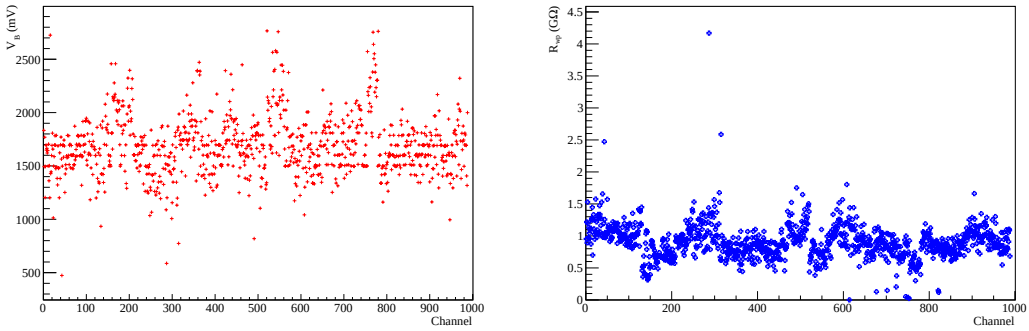

FIGURE 4.24: 11 mK base temperature. [Left] Distribution of the bias voltages applied to the NTD as a function of the channel number. [Right] Distribution of the NTD resistance at the selected WP as a function of the channel number

In conclusion, it has been developed a new procedure and algorithm to analyze the NTDs Load Curves and find the optimal WP. This is the first time that an automatic procedure is utilized for setting the WP for almost a thousand NTDs coupled with TeO_2 crystals. Furthermore, the addition of the informations related to the pulse shape dependence with the applied bias, consist in an upgrade of the standard approach of choosing WP bias voltages corresponding only to the maximum amplitude or maximum SNR. Ultimately this algorithm for finding the WP can be utilized on Load Curve data acquired at any base temperature.

Resistance measurement procedure

Given a detector operational temperature, the bias of the NTDs is set to its optimal working point (found by the Load curves analysis discussed in the previous subsections). The effective NTD resistance at the working point $R_{bol,wp}(T)$ is then measured several times during the data taking, in order to check the temperature and detectors stability.

A dedicate procedure has been implemented on the CUORE data acquisition in order to measure the **static resistance of the NTD** of each channel, which depends on the NTD itself, on the detector temperature and on the chosen bias voltage.
The procedure for a *Resistance measurement* uses the same Apollo sequence used for the *Load Curves*, with few differences:

- Only noise triggers are acquired; the pulser is not fired.
- The bias voltage of the NTD is kept at the same value.
  The bias is not changed during the procedure; only the polarity inversion is performed.
- The sleep time after the change of the electronics settings is longer (usually about 1200 s).
  Indeed, every time the electronic configuration is changed, the overall system

tends to slightly warm up[8] and it is necessary to wait the bolometers to get back to their base temperature, in order to have accurate measurements of the NTD resistance.

The *Resistance measurement* procedure can be outlined in few steps:

- Measure the baseline Bsl at gain G (gain used for the data taking, while operating at bias negative polarity)
- Change the offset in order to have baselines at $\sim$- 5000 mV (for negative polarity); change the gain to a smaller value G' (e.g. 145 V/V)
- Measure the baseline Bsl^- at gain G'
- Invert the bias polarity and measure the baseline Bsl^+ (at gain G')
- Recover the initial conditions for the offset and the gain G and measure again Bsl (at gain G), as a crosschek for the closure of the procedure

A schematic representation of the procedure described above is shown in Fig.4.25.
The Apollo sequence which drives the data acquisition assigns a different configuration ID to each electronics configuration taken; the transition periods in which the electronic parameters are changing assume a null configuration ID and they are rejected by the analysis sequence. See Fig.4.26.
The online analysis sequence takes the values of baselines, gain, bias (V_B) and load resistance (R_L) for each configuration and then calculates three values for each channel: R_{bol} (NTD static-resistance), V_{bol} (voltage drop at the NTD edges before the readout chain) and V_{offset} (the offset). See Eqs. from 4.8 to 4.10.

$$V_{bol} = \frac{Bsl^+ - Bsl^-}{2G'} \tag{4.8}$$

$$R_{bol} = \frac{R_L}{V_B/V_{bol} - 1} \tag{4.9}$$

$$V_{offset} = Bsl + G \times V_{bol} \tag{4.10}$$

The same procedure can be performed to measure the NTDs resistance when these are polarized with very low bias (e.g. $\sim$ 50 mV). This is referred as a 'base resistance measurement', $R_{bol,base}(T)$. Measuring $R_{bol,base}(T)$ at several temperatures can be utilized to have a better characterization of the thermistors and to extract the (R_0, T_0) values for the CUORE NTDs.

[8] The procedure of changing the electronics parameters on the FE boards connected to the channels actually induces some power dissipation that is transferred to the bolometers and temporarily warms them up.

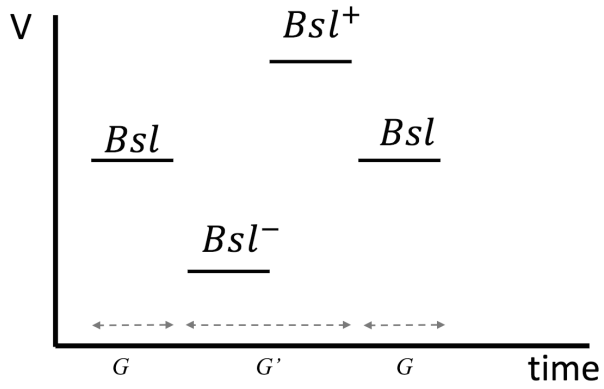

FIGURE 4.25: Schematic representation of the *Resistance Measurement* procedure. Initially the electronic configuration and the baseline are read (*G*,*Bsl*). The offset is then modified and the gain is changed to G', the baseline Bsl^- is then measured. Keeping the gain at G', the polarity is inverted and the baseline Bsl^+ is measured. The system is then restored back to the initial electronics conditions and the baseline *Bsl* is again measured and compared with the initial value.

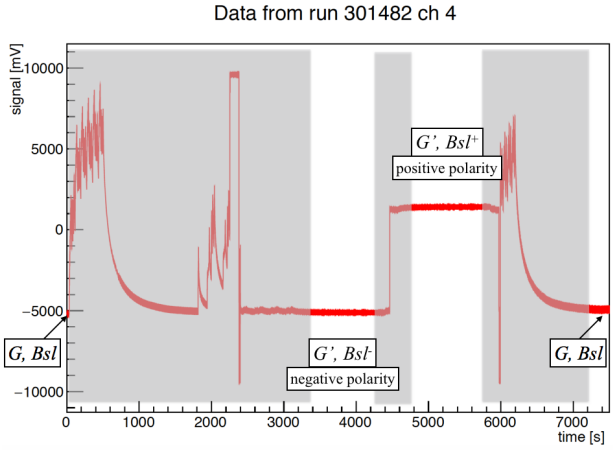

FIGURE 4.26: Example of a *Resistance Measurement* run for one channel. The red line is the channel continuous data stream. The grey shaded areas indicate where the data are ignored by the analysis.

In Figs.4.27 and 4.28, the stability of the NTD Working Point resistance for all the channels during the CUORE data taking in 2017 (15 mK) and 2018 (11 mK) is reported. Each element in the plots corresponds to the distribution of the values of $R_{bol,wp}$ for the CUORE channels, measured in dedicated runs of Working Point resistance measurement [9].
In Fig.4.29, the comparison of the base and WP resistances of the CUORE channels measured at 11 mK are reported. The average base resistance at 11 mK is $R_{bol,base} \sim$ 5 -11 $G\Omega$, while the average value at WP is $R_{bol,wp} \sim$ 0.6 - 1.2 $G\Omega$.

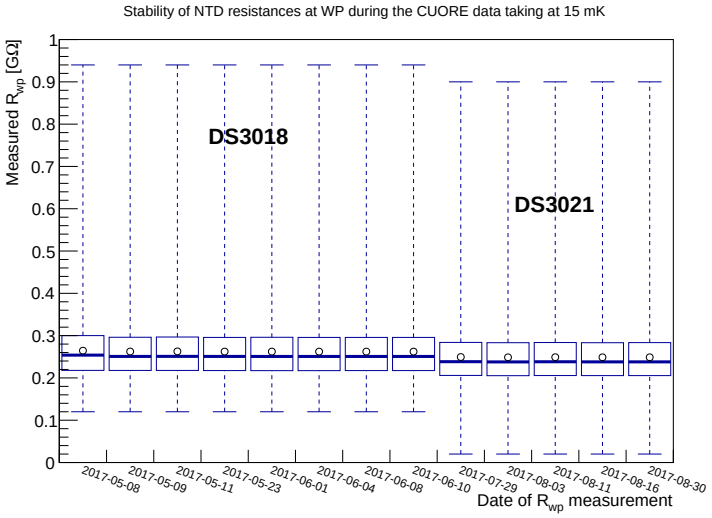

FIGURE 4.27: WP Resistance stability for all the CUORE channels during the data taking at 15 mK. The plot spans a time interval from early May 2017 to late August 2017. Two dataset are identified (DS3018 and DS3021); for each dataset the stability of the average WP resistance with time is visibile. The average WP slightly differs between the two datasets, since the base temperature (measured by the noise thermometer) of DS3018 was T_{NT} = 15.0 mK, while for DS3021 it was T_{NT} = 15.4 mK, while the applied bias voltages on the NTDs were the same for both datasets. As expected, for a fixed bias voltage, a warmer temperature leads to lower values of the NTD resistance.

[9] The plots reported are "candle plots" ("box plots"), reporting the main features of the distributions of R_{wp} measured for each run through their quartiles. The circle corresponds to the mean, the solid line to the median. The box around the median indicates the data between the upper and lower quartiles. The lines extending vertically from the boxes (whiskers) indicate the minimum and maximum values of the distribution.

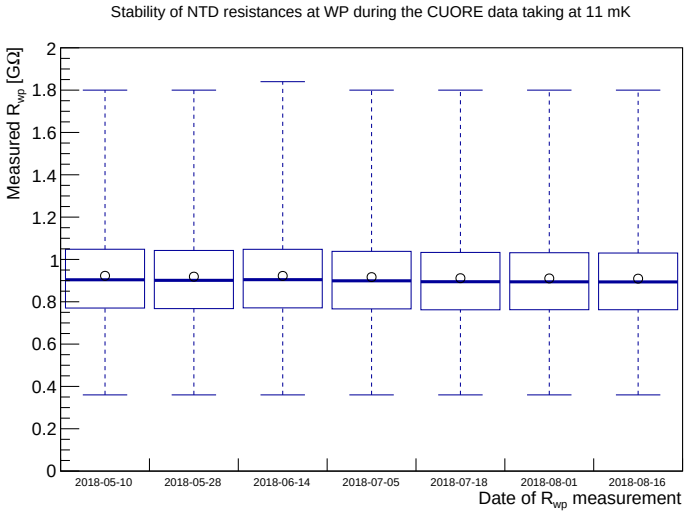

FIGURE 4.28: WP Resistance stability for all the CUORE channels during the data taking at 11 mK. The plot spans a time interval from mid May 2018 to mid August 2018. The stability of the average WP resistance with time is visibile.

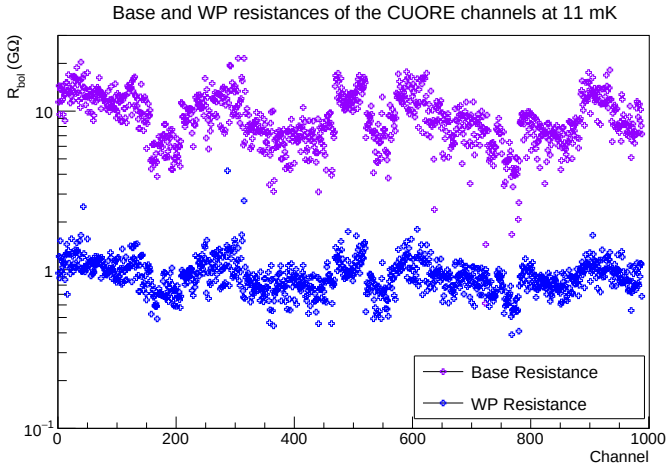

FIGURE 4.29: NTD Resistance measured for all the CUORE channels at 11 mK, at low bias ($R_{bol,base}$ - run 301763) and at the WP ($R_{bol,wp}$ - run 302043). At this temperature the base resistance is approximately one order of magnitude higher than the effective resistance at the WP that have been set for the channels. Moreover it can be seen that the procedure to find the optimal WP, sets quite uniform operating conditions for all the channels.

4.2.3 Detector operating temperature

The system temperature has to be carefully regulated in order to successfully operate a bolometric detector array like CUORE. Indeed it is crucial to identify the best operating temperature in order to achieve the highest quality readout with a good signal-to-noise ratio. Moreover it is necessary to maintain this temperature over the course of a prolonged run.

Temperature stabilization

Instabilities in the cryogenic system could cause temperature fluctuations in the detector, which can spoil the energy resolution. Therefore, a dedicate temperature control system based on a Proportional-Integral-Derivative (PID) controller has been implemented in CUORE, in order to compensate for these instabilities. The basic idea behind a PID controller is to calculate the difference between the desired working temperature and the measured one and to apply a correction accordingly. The temperature is acquired by one NTD placed on the MC-10 mK plate (channel 1019). A variable power is injected on the MC via two standard heaters ($R_h = 300\ k\Omega$) which are connected in parallel and placed on the MC-10 mK plate.

Temperature scan

Temperature scans were performed to select the best operational temperature, that together with the noise reduction, would have made CUORE reach the nominal energy resolution of 5 keV.

For each temperature, a subset of channels - 3 towers, 2 columns per each tower - were considered for the analysis. Each of the three towers carries NTDs belonging to different (neutron implantation) batches: 26 ch - NTD 41C (tower 8), 26 ch - NTD 39 C (tower 9), 26 ch - NTD 39 D (tower 10). See Fig.4.30. The choice was made in order to cover the characterization of the response of all the NTD types used for the CUORE detector.

Three temperature scans were performed: one in early March 2017 (from 9 mK to 16 mK), one in July 2017 (from 11 mK to 27 mK) and one in October 2017 (from 11 mK to 19 mK).

Towers 8-9-10 columns 1-2

Tower 8 (41C)		Tower 9 (39C)		Tower 10 (39D)	
365	378	417	430	469	482
366	379	418	431	470	483
367	380	419	432	471	484
368	381	420	433	472	485
369	382	421	434	473	486
370	383	422	435	474	487
371	384	423	436	475	488
372	385	424	437	476	489
373	386	425	438	477	490
374	387	426	439	478	491
375	388	427	440	479	492
376	389	428	441	480	493
377	390	429	442	481	494

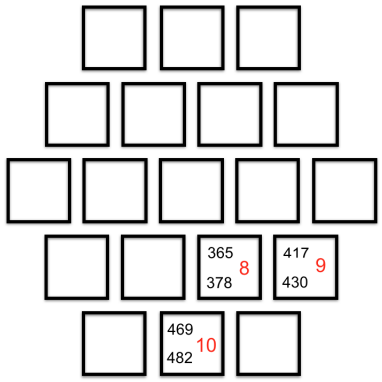

FIGURE 4.30: Towers and channels utilized to study the detector response during the temperature scans.

The first scan aimed to identify a good working temperature. The second was performed to cross-check the initial choice, after some improvement on the noise reduction, on the front-end electronics and on the data-analysis software were done.
For each temperature, a full set of load curves was performed in order to identify and set the NTD polarization bias to the optimal working point for each active channel.
Afterwards, runs with only noise triggers and heater pulses (2 pulser amplitudes: StabPulser, HighPulser) were acquired, in order to study the variation of the thermal noise and of the internal gain of the bolometers.
Several runs, belonging to the same dataset DS3021, were acquired for each temperature during the July 2017 scan:

- Run 301391 - 11 mK;
- Run 301386 - 13 mK;
- Run 301379 - 15 mK;
- Run 301369 - 17.5 mK;
- Run 301372 - 19 mK;
- Run 301375 - 21 mK;
- Run 301329 - 24 mK;
- Run 301338 - 27 mK;

The gain of the front-end was set to 5000 V/V for all channels at each temperature. For temperatures in the 11-19 mK range, 60 $G\Omega$ load resistors were used, since the values of the CUORE NTD resistances at those temperatures are around 100 $M\Omega$- 1 $G\Omega$. For the warmer temperatures 21-27 mK, the 10 $G\Omega$ load resistors were used.
The resolution of the baseline and of the pulsers, and the NTD resistance at working point (R_{NTD} at WP) were used as a proxy to choose the working temperature.
Based on the results of the first two scans, it seemed that the resolution could be improved by working at a low temperature, see Fig.4.31. However, the average NTD resistances at the working point showed values above hundreds of $M\Omega$ (see Fig.4.32), far off the designed value ($R_{wp} \sim 100\ M\Omega$), while at higher temperatures the NTD resistances decreased to the designed range. In order to find a compromise between good resolution and NTD resistances values at working point that would well match the status of the readout electronics, the working temperature was initially set at 15 mK for the CUORE initial data-taking.

During the temperature scan in March and July 2017 just the variation with temperature of detector response to pulser events was studied. Therefore it was considered the possibility to investigate the response to particle events at different temperatures.
The third temperature scan was then performed with the calibration sources deployed in order to study the resolution variation with temperature on physics events from the calibration γ lines of Tl (2615 keV) and Ac (911 keV).
One different dataset was acquired for each temperature:

- DS3030 - 11mK (approx 4 days),
- DS3039 - 13 mK (approx 6 days),

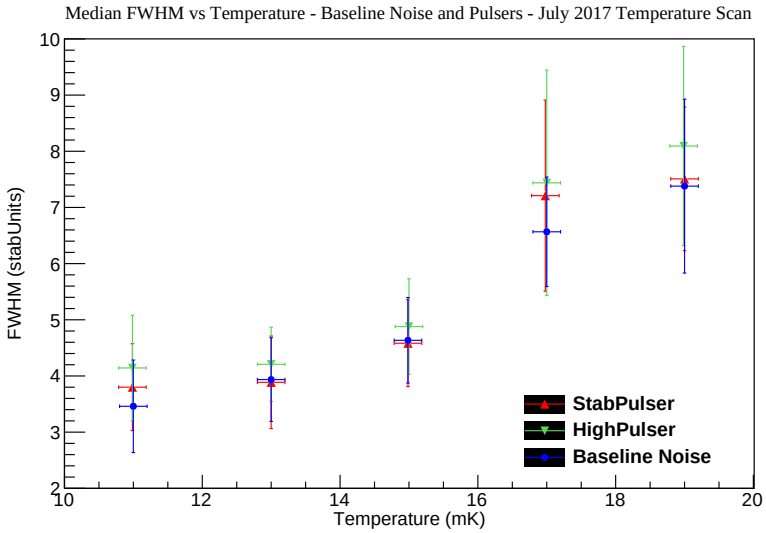

FIGURE 4.31: Pulsers and baseline resolution (median values) in 11-19 mK temperature range from July 2017 data. The FWHM is in "StabUnits", amplitude arbitrary units; it is not in keV since it was not performed the energy calibration at each T during the July 2017 temperature scan.

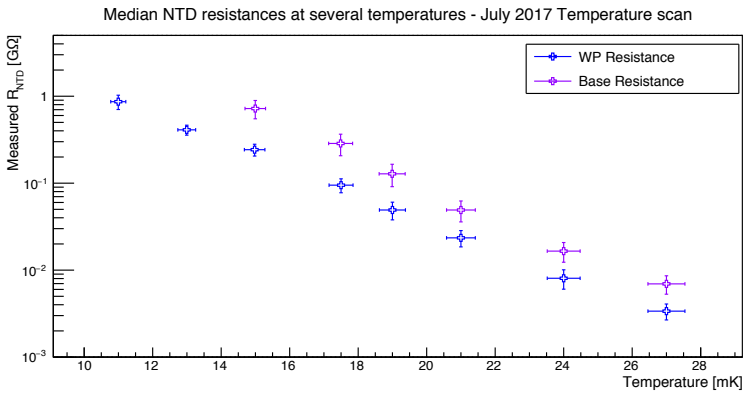

FIGURE 4.32: NTD WP and Base resistances median values at each T during the July 2017 temperature scan. The NTD resistance decreases for higher temperatures, given the thermistor response from Eq.3.12. For lower temperatures, the value of the base resistance (purple) is $\sim G\Omega$ and so the WP resistance gets to values of hundreds of $M\Omega$.

- DS3024 - 15 mK (approx 13 days - same configuration as the CUORE initial data-taking),
- DS3033 - 17.5 mK (approx 5 days),
- DS3027 - 19 mK (approx 2 days).

Like for the previous scans, only the detectors belonging to the first two columns of Tower 8-9-10 were polarized at the optimal working point and data was acquired for them. Depending on the position of the calibration strings, the three towers were differently illuminated by the sources (different average number of counts at Tl peak), as shown in Fig.4.33.

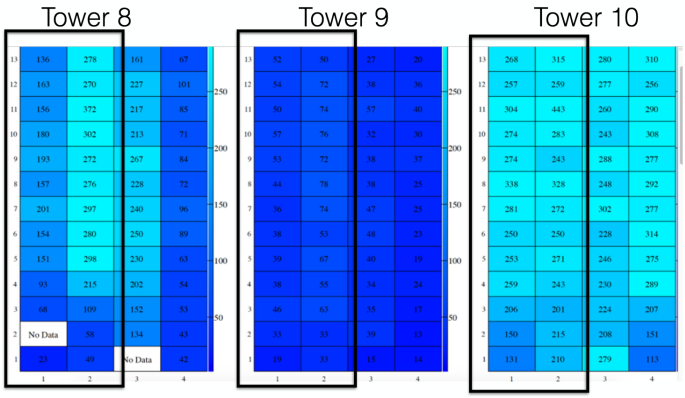

FIGURE 4.33: CUORE towers and channels utilized for the temperature scan analysis in October 2017. The number of counts at 2615 keV (over 5 days) for DS3024 - 15 mK is plotted for each channel; this value was utilized to have an estimate on how much each tower was illuminated by the calibration strings.

The working points found in the previous temperature scans, were utilized to polarize the NTDs at the desired temperatures.
Runs with signal triggers (from calibration pulses), noise triggers and heater pulses (3 pulsers with different amplitudes: StabPulser, HighPulser, LowPulser) were acquired.
The signal template for building the Optimum filter (see Chap. 5.1.2) was the average pulse (AP) built with particle signals, spanning the wide range of the calibration energy spectrum; the noise template was built using the average noise power spectrum (ANPS), in which proper selection cuts on the noise triggers were applied in order to skip events corresponding to previous pulse tails and containing small pile-up pulses. In Fig.4.34 examples of the AP and ANPS of a single channel at several temperatures are shown. From the AP, it can be seen that for lower temperatures, there is an evident increase of the intrinsic gain, resulting in higher amplitude pulses; moreover the fall time is faster, while the rise time is slower. From the ANPS, it can be seen that the low frequency continuum and therefore the average total noise is higher for lower temperatures; this might be partially related to the Johnson noise on the bolometer, which is higher for lower temperatures. In Fig.4.35 it is reported the Signal to Noise Ratio dependence on temperature evaluated as the ratio of the average amplitude of the pulses corresponding to Tl 2615 keV events and the average RMS for each channel. The SNR increases with lower temperatures; the increase in the bolometer internal gain resulting in higher amplitudes of the pulses for the same energy deposition becomes more significant in the SNR evaluation than the noise RMS, which gets slightly worse reducing the temperature.

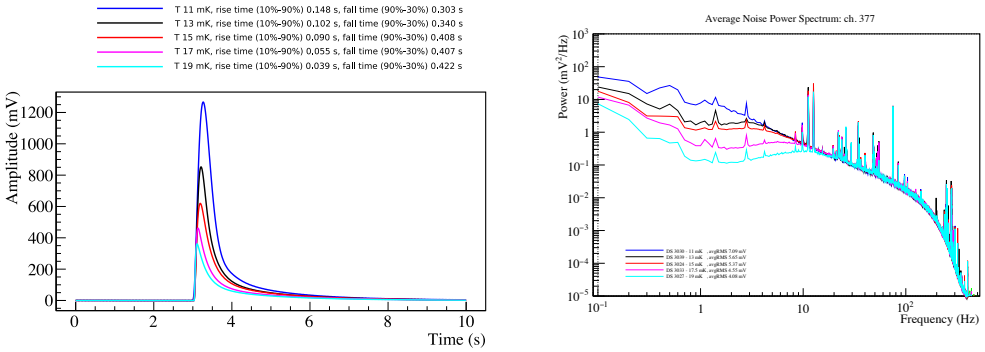

FIGURE 4.34: Example of average pulses [left] and average noise power spectra [right] at several temperatures for a given CUORE channel, eg. ch 377.

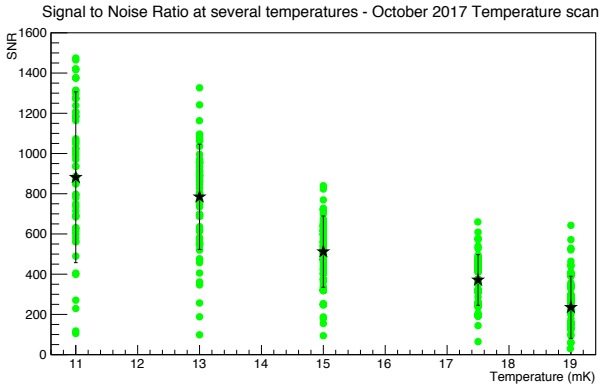

FIGURE 4.35: Signal to Noise Ratio dependence on temperature. The SNR for each channel is evaluated as the ratio of the amplitude (in mV) of the average pulse built with Tl 2615 keV events divided by its average RMS (in mV). For each temperature, the green dots correspond to the SNR for each single channel, the black star with the error bar is the median SNR.

In addition, the variation with temperature of the resolution on the baseline, on the pulsers and on particle signals was analyzed.
From Fig.4.36 (Top) it can be noticed that both the resolution of the stabPulser and of the baseline were improved at lower temperatures, which confirmed the March and July 2017 results.
From the calibration spectrum, two of the most intense peaks were analyzed for the resolution evaluation: Tl 2615 keV and Ac 911 keV γ lines. The energy resolution evaluation utilizing the calibration runs is delicate and critical, since the capability of selecting good quality particle pulses to build the energy spectrum strongly depends on the counting rate and on the pile-up rejection efficiency for each channel. For the resolution of the Tl, the peak was fitted with a single gaussian with a flat background; while for the Ac peak, it was used a single gaussian with a linear background. Fig.4.36 (Bottom) shows the spectral line resolution during calibration in the third temperature scan.
The third temperature scan confirmed that lower temperatures lead to a better energy resolution also for particle signals, with an average improvement of $\approx$ 15% from 15 mK to 11 mK.

For this reason for the data taking in 2018, it was decided to set an operational

temperature of 11 mK. Since the NTD working resistances at 11 mK would have been higher (reaching the $G\Omega$) than the nominal values proposed for CUORE, special care was taken in setting NTDs operating conditions which could ensure a stable and uniform response in a wide energy range (as described in the previous section about the WP set at 11 mK).

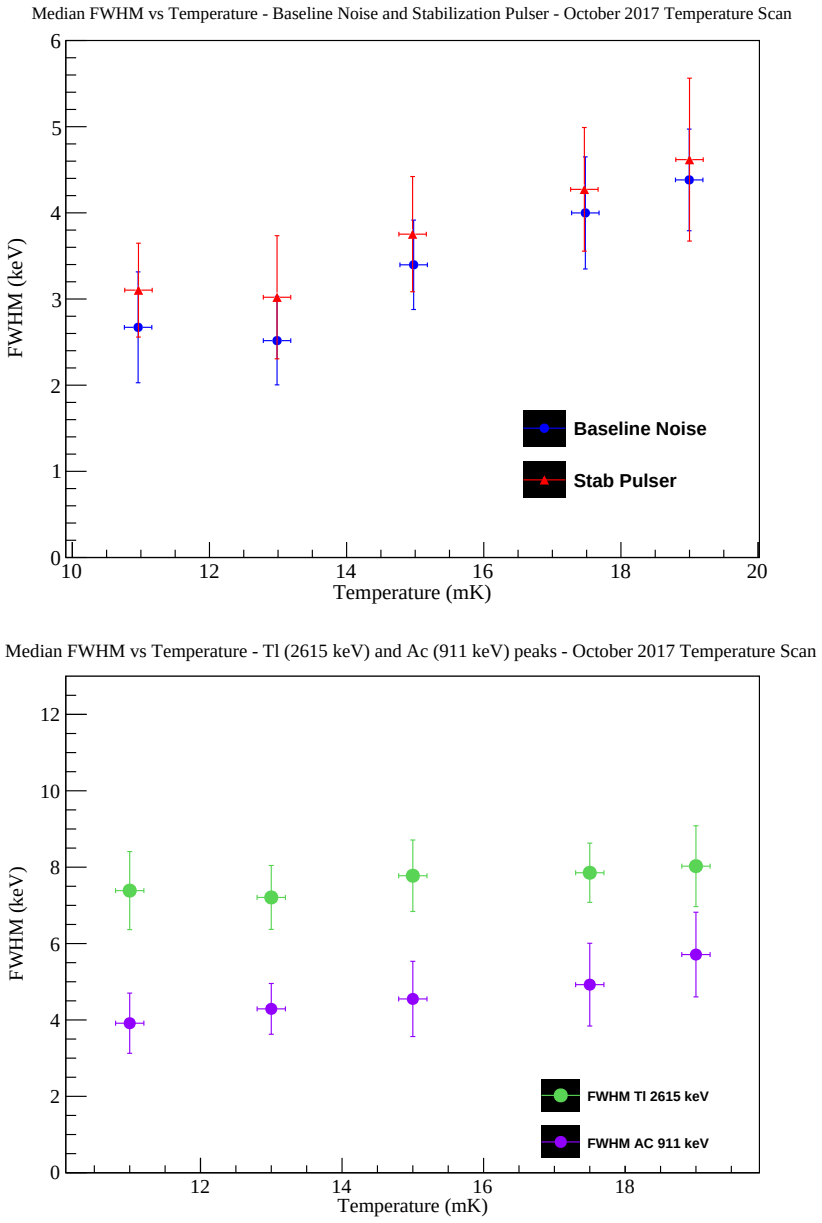

FIGURE 4.36: Resolution (FWHM in keV - median values) in 11-19 mK temperature range for pulsers and baseline [top] and for particle signals from Tl 2615 keV and Ac 911 keV γ lines [bottom] from October 2017 data.

4.2.4 Trigger thresholds

As described in Chap.2.4.1, CUORE exploits an online trigger whose role is identifying particle-induced pulses at all energies. During the 2017 data-taking only the DT was enabled, while from 2018 the CUORE data are triggered online by both the DT and OT algorithms.
Each of the CUORE bolometers behaves differently, thus their noise is often very different. The parameters of the trigger algorithm, in particular the threshold, must be tuned channel by channel with an automated procedure based on the characteristic noise of the bolometer itself. The trigger thresholds were set and optimized for each channel, before starting the physics data taking.
A few measurements were acquired after setting the DT and OT trigger parameters to measure the corresponding trigger efficiency for each channel. These runs were characterized by multiple heater pulses at different amplitudes in the low energy part of the spectrum. 8 different pulser amplitudes from few keV to about 1000 keV were utilized, each one repeated in average 12 times during the duration of the run ($\sim$ 14 hours). The energy corresponding at the 90% of the trigger efficiency has been chosen as the proxy for identifying the energy thresholds.

The distribution of all these values gives a quantitative idea of the overall level of the energy thresholds. During the CUORE 2017 data-taking, most of the channels had a DT energy threshold ranging from 20 to 100 keV. In Fig.4.37, it is shown the distribution of the ratio of the OT and DT energy thresholds evaluated from the initial CUORE runs acquired in 2018. These preliminary results of OT on CUORE data show that the DT thresholds can be strongly improved. The OT could then reach trigger thresholds of few keV, allowing several low energy analyses in CUORE.

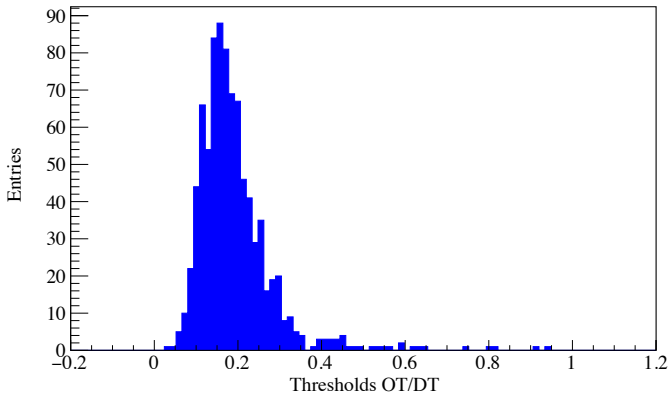

FIGURE 4.37: Distribution of the ratio of OT and DT energy thresholds at 90% of the trigger efficiency. The energy thresholds have been evaluated for all the CUORE channels using a dedicated run with pulser signals in a wide range of amplitudes. [90]

4.3 CUORE Data taking

After the initial characterization and optimization campaigns done in early 2017, CUORE acquired its first physics data for the $0\nu\beta\beta$ decay search from May to September 2017. In the following, the CUORE first science runs will be described. Afterwards the activities performed in late 2017 and the re-start of the CUORE physics data taking in 2018 will be outlined. The future perspectives for CUORE and its upgrades will be briefly discussed.

4.3.1 First physics data from CUORE

Although the detector optimization phase was still far from being completed, by the beginning of April 2017 a first CUORE science run was started at a temperature of (15.0 ± 0.1) mK.
A first short dataset was acquired in April 2017 in order to test the readiness of the data processing tools and to check the detector working points and trigger thresholds.

Two periods of science data were then acquired by CUORE in 2017:

- Dataset DS3018: $\sim$1 month from May to June 2017;
  The opening calibration lasted 5 days (from May 6^{th} to May 11^{th}), then we took physics data for about 24 days (until June 4^{th}). The dataset was closed by a second calibration which lasted 4 days, from June 6^{th} to June 10^{th}. Dataset DS3018 was initially triggered with event windows of 5 seconds each. Later it was proven that it was possible to improve the energy resolution with event windows of 10 seconds each. Therefore, the continuous data from DS3018 were re-triggered with 10 seconds windows.

- Dataset DS3021: $\sim$1 month from August to September 2017.
  After a period of optimization in July, the data taking was restarted at the end of July with the dataset DS3021. Again, the first and final days were devoted to the calibration (from July 30^{th} to August 2^{nd} and from September 4^{th} to September 9^{th}), while 27 days of physics data were collected (from August 4^{th} to August 31^{st} 2017). Given the demonstrated improvement in the resolution, the second dataset was acquired directly saving event windows of 10 seconds. In addition to the longer event windows, the improved noise situation and the lower derivative trigger thresholds resulted in a better energy resolution and higher number of channels that reached the final steps of the analysis.

Priority was first given to the search of $0\nu\beta\beta$ decay of TeO_2 with the first collected data and afterwards the analysis was focused on the evaluation of the $2\nu\beta\beta$ half-life and background model reconstruction [11], [34]. The total collected $0\nu\beta\beta$ exposure was then 86.3 kg($^{nat}TeO_2$) $\cdot$ yr. See Chap.6 for the first CUORE results.

4.3.2 CUORE: actual status

After the CUORE physics data taking in mid-2017, dedicated runs devoted to further characterization and optimization of the detector were performed in Fall 2017. PT phases scans as well as studies of the detector performance as a function of temperature were carried out. The analysis of these data led to the decision to set a new operational temperature of the system, from 15 mK to 11 mK. The month of December 2017 was then devoted to do preliminary tests of the system at the 11 mK

temperature, the noise contributions and the electronics settings; moreover Load Curves for all the channels were acquired, in order to set the new working points for the 2018 physics data taking.

Starting from January 2018, the system was warmed up at 100 K to install a new set of vacuum gate valves for the calibration system; the operation took about 2 months to complete, a reasonable time given the complexity of the CUORE cryostat and the large thermal inertia. Moreover during this period of maintenance, the external DCS was installed and other checks on the system were performed.

The CUORE experiment returned to base temperature of (11.6 ± 0.1) mK in March 2018. Firstly it was performed a scan of the pulse tubes phases to find the new optimal phase configuration. This could have been changed, given all the mechanical and electronic interventions done in early 2018. In April 2018, the new working points were set, tested and optimized and a detector calibration was performed. From the preliminary analysis of the calibration data, the estimate of the energy resolution was 7.6 keV FWHM at the Tl 2615 keV peak, close to the ROI [11]. This was not yet the designed energy resolution for the CUORE experiment of 5 keV FWHM in the ROI; still there is an ongoing work on improving the stability of the detector operation and the quality of the data analysis procedure to reach this goal. The physics data taking re-started in May 2018. Two new datasets were acquired in 2018 (DS3051 and DS3054) at 11 mK operating temperature. The acquired exposure in 2018 was $\sim$ 140 kg($^{nat}TeO_2$) $\cdot$ yr (until October 2018).

4.3.3 CUORE: sensitivity and perspectives

CUORE will be one of the most sensitive experiments for searching for $0\nu\beta\beta$ decay over the coming years. Moreover it will be possible to perform precise measurements of the $2\nu\beta\beta$ half-life of ^{130}Te.
Given its expected large exposure, CUORE allows to many other potential physics searches, like symmetry violation searches ($0\nu\beta\beta$ with Majoron emission, CPT violation in the $2\nu\beta\beta$ decay, ...), low energy searches (Dark Matter, axions, ...) and nuclear physics measurements (other $\beta\beta$ decays and decays to excited states, β^+/E.C. decays,...).

The CUORE design goals are 5 keV FWHM energy resolution in the ROI, a background index of b = 0.01 counts/(keV $\cdot$ kg $\cdot$ yr) and 5 years of live-time. In these conditions, the ultimate sensitivity for CUORE would be $S^{0\nu} \sim 9.0 \times 10^{25}$ yr for the half-life of ^{130}Te $0\nu\beta\beta$ decay. While proceeding with the physics data-taking, CUORE will keep working from the detector side for improving the energy resolution and from the analysis side to better understand the sources of background and their effect of the measured energy spectra.

Next generation of $0\nu\beta\beta$ decay experiments seek to be sensitive to the full Inverted Hierarchy region: sensitivity $S^{0\nu} \sim 10^{27}$ yr, $m_{\beta\beta} \sim 6$ - 20 meV (from Fig.1.9). CUORE's success motivates a next-generation bolometric experiment. The CUPID (CUORE Upgrade with Particle ID) project aims to build a future experiment with $\sim$ 1000 enriched light emitting bolometers mounted in the CUORE cryostat, reaching nearly zero background goal [106]. The goal of reducing the background in the ROI can be achieved by rejecting all the α events thanks to an effective particle identification; to do so, it is necessary to add the ability to read out the light emitted in a particle interaction (scintillation/Cherenkov). This will allow to combine the energy resolution of bolometers with the background discrimination of a dual channel detector. There are several ongoing CUPID R&D and demonstrator experiments (e.g. enriched TeO_2 with Cherenkov light readout, Li_2MoO_4 and $ZnSe$ scintillating

bolometers, ...). The CUPID project needs to identify the isotope, the crystal and the readout technology to be used to reach the zero background goal and to demonstrate the readiness to construct this next-generation high-sensitivity tonne-scale bolometric experiment.

Chapter 5

CUORE Data analysis and Monte Carlo

The temperature increases inside the CUORE TeO_2 bolometers due to particle interactions are transformed into electrical signals by germanium NTDs. The data are acquired in continuous stream and pulses are detected with a software trigger which operates independently on each bolometer. In this chapter the procedures for the processing and the analysis of the CUORE data will be described.
This will be followed by an overview of the Monte Carlo tools that are used to simulate particle propagation and interaction in the CUORE geometry, and to reprocess the MC data adding the detector-related features.

5.1 Data production

The CUORE first level data processing consists in all the steps that go from the recorded waveform to a calibrated energy spectrum. The data are then blinded and saved into ntuples for physics analyses. [107], [108]
The data production is done using the Diana software developed by the CUORE collaboration; this is a modular C++ software based on the ROOT package[109]. The Diana software loops through all the triggered events applying a different operation at each step of the sequence.

In this section the steps of the first-level production will be described in details.

5.1.1 Preprocessing

A preliminary processing of the raw data (pre-process) is performed in order to evaluate basic parameters of the event.
The (most relevant) parameters evaluated during the preprocess phase are listed below.

- Baseline parameters. These are evaluated for each event in the first 3/4 of the pre-trigger interval[1]. The baseline information is used to identify the detector conditions right before the particle interaction in the detector.
  - *Baseline*: output voltage (in mV) of the NTD; given a fixed offset, it can be used as a proxy for the bolometer temperature at the time of the event
  - *Baseline slope*: computed by fitting the pre-trigger fraction of each event with a linear regression; it is the coefficient of the first degree term (mV/s) in the linear function

[1] For 10 s acquisition windows with 3 s of pre-trigger, the baseline parameters are evaluated in the first 2.25 s of the event window

  - *Baseline RMS*: computed in the same way as the *Baseline slope*, it is the RMS of the deviation from the best fit of the data points; the *Baseline RMS* (mV) is a proxy for estimating the noise on the channel for each event

- Pile-up identification parameters.

  - *Single Trigger*: the *Single Trigger* variable looks for triggers which are set by the online DT on the data stream. It returns a boolean which is true if only one derivative trigger flag is found in the given event window; it is false if secondary triggers are found.
  - *Number Of Pulses*: the number of pulses is obtained by searching for peaks in the differentiated waveform which exceed a threshold in unit of the derivative RMS. Only positive pulses are counted. This algorithm is meant to compensate the inefficiency of the online derivative trigger[2] in identifying hard pile-up events or small pulses.

Fig.5.1 shows a comparison between the outcome of the *Number Of Pulses* algorithm and the *Single Trigger* variable for two events with multiple pulses in the window.

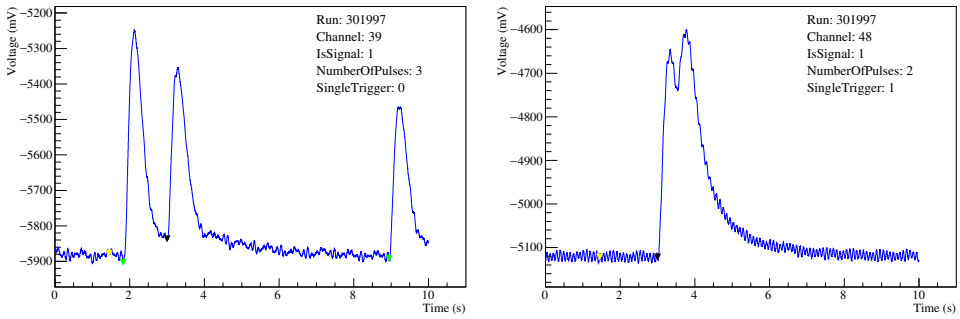

FIGURE 5.1: Example of event windows with multiple pulses and comparison between the triggers identified online (DT) and the number of pulses evaluated with the offline algorithm. [Left] An event with 3 pulses, has *Number Of Pulses* = 3 and the *Single Trigger* variable is 0, meaning that there are multiple triggers assigned to that event window. [Right] An event with 2 pulses detected very close one to each other (hard pile-up). The *Single Trigger* variable is 1 and it means the second pulse is not identified by the online DT, due the trigger inactivity period (0.8 s) after an identified pulse; however the offline algorithm instead identifies both pulses, *Number Of Pulses* = 2.

5.1.2 Amplitude

The Optimum Filter (OF) technique [110] is utilized to evaluate the amplitude of the pulses. The OF is designed to maximize the signal-to-noise ratio. It makes use of the whole pulse waveform and of the noise power spectrum. It is implemented in the data processing and it aims to mitigate the effects of the bolometric noise superimposed to the signal.

[2]See Chap.2.4.1 for details of the online trigger algorithms in CUORE.

The Optimum Filter

Let's assume the system has a response $r(t)$ to a unitary pulse and the input uncorrupted signal (no noise) is $u(t)$. The output signal $s(t)$ is then:

$$s(t) = \int_{-\infty}^{\infty} r(\tau)u(t-\tau)d\tau \tag{5.1}$$

or, in the frequency domain:

$$S(\omega) = R(\omega)U(\omega) \tag{5.2}$$

In case of a real signal, some noise contribution $n(t)$ is superimposed to the signal $s(t)$. It is possible to introduce a filter $H(\omega)$ which maximizes the signal-to-noise ratio.
The uncorrupted signal at its output is:

$$s_o(\tau_M) = \frac{1}{2\pi}\int_{-\infty}^{\infty} S(\omega)H(\omega)e^{i\omega\tau_M}d\omega \tag{5.3}$$

where τ_M is the instant corresponding to the maximum of $s(t)$.
The power dissipated by the noise at the output of the filter is:

$$< v_N^2 >= \int_{-\infty}^{\infty} |N(\omega)|^2|H(\omega)|^2 d\omega \tag{5.4}$$

where $|N(\omega)|^2$ is the noise power spectrum.
The signal-to-noise ratio squared is then η^2 (SNR^2) in Eq.5.5.

$$\eta^2 = \frac{s_o^2(\tau_M)}{< v_N^2 >} \tag{5.5}$$

Taking into account the Schwarz inequality, η^2 cannot be higher than the integral over all the frequencies of the ratio of the signal and noise power spectra:

$$\eta^2 \leq \frac{1}{2\pi}\int_{-\infty}^{\infty} \frac{|S(\omega)|^2}{|N(\omega)|^2}d\omega \tag{5.6}$$

The OF transfer function, which maximizes η, corresponds then to the equality in Eq.5.6. It can be easily shown that it is:

$$H(\omega) = k\frac{S(\omega)^\star}{|N(\omega)|^2}e^{i\omega\tau_M} \tag{5.7}$$

$$\text{where } k = 1/\Sigma\frac{|S(\omega)|^2}{|N(\omega)|^2} \tag{5.8}$$

$S(\omega)^\star$ is the complex conjugate of the Fourier transform of the ideal response s(t), $|N(\omega)|^2$ is the noise power spectrum, τ_M is the instant when the maximum of s(t) is reached. k is a proper normalization constant proportional to the actual signal amplitude.
The OF transfer function weights different Fourier components of the pulse differently depending on the noise contribution at that frequency component: frequencies that are highly influenced by noise are depressed, thus mitigating their influence on the pulse amplitude.

It can be demonstrated that the OF estimate of the amplitude will be the best (optimal) in quadratic sense.

OF Amplitude evaluation

The signal waveform $v(t)$ of each bolometer can be modeled as the sum of a detector response function, $s(t)$, and a noise term, $n(t)$:

$$v(t) = b + A \cdot s(t - t_0) + n(t) \tag{5.9}$$

where b is the baseline DC level of the detector, A is the amplitude of the signal, t_0 is the start time of the pulse within the event window. The pulse amplitude depends on several factors related to the bolometer operating conditions; on the first order, it can be decomposed in a term $a(E)$ which depends only on the energy deposited into the bolometer E, and a term $G(T)$ which represents the bolometric intrinsic gain which depends on the operating temperature of the bolometer T: $A(E,T) \approx G(T) \cdot a(E)$.

The simplest estimate of the pulse amplitude is the pulse maximum minus the baseline value: this measure is highly effected by $n(t)$. The best estimate for the signal amplitude can be obtained by filtering it with the OF transfer function.
The OF amplitude evaluation is based on the assumption that the pulse shape for particle signals does not depend on the deposited energy and therefore the detector response function $s(t)$ can be assumed as a fixed template. Moreover the stochastic noise on the bolometer has to have a stationary behavior in order to be described by a definite noise function $n(t)$.

Up to a multiplicative constant factor, the OF pulse in the frequency domain can be written as, using Eq. 5.7:

$$V^{OF}(\omega) = H(\omega)V(\omega) \propto \frac{S(\omega)^\star}{|N(\omega)|^2} e^{i\omega\tau_M} V(\omega) \tag{5.10}$$

where $V(\omega)$ and $S(\omega)$ are the Fourier transform of the signal $v(t)$ and the detector response function $s(t)$; $|N(\omega)|^2$ is the noise power spectral density; ω is the angular frequency.

Since each detector has different characteristics that in turns convert in different pulse shape and noise, in order to build the OF transfer function the detector response function $s_i(t)$ and the noise power spectrum $|N_i(\omega)|^2$ must be evaluated separately for each detector i. This can be accomplished by means of a proper averaging procedure.

Assuming a purely stochastic noise (whose mean is zero) and a proper synchronization of the recorded pulses, the time average of a sufficiently large ensemble of selected pulses (Average Pulse, $AP_i(t)$ for bolometer i) can be considered as a good approximation of the detector response:

$$AP_i(t) = \langle v_i(t) \rangle = s_i(t) \tag{5.11}$$

Given the Wiener-Khinchin theorem, the average performed over the squared modulus of Fourier transform of the noise $B_i(\omega)$ (corresponding to the autocorrelation function of the channel) can be utilized as an approximation for the noise power spectrum for each channel i. We call it Average Noise Power Spectrum $ANPS_i(\omega)$:

$$ANPS_i(\omega) = \langle |B_i(\omega)|^2 \rangle \sim |N_i(\omega)|^2 \tag{5.12}$$

Therefore, for each channel, the Average Pulse (AP) on particle signals is used as the template for the Signal and the Average Noise Power Spectrum (ANPS) for the Noise Power Spectrum.

In order to build the AP for each channel, it is necessary to identify genuine particle signals. This is obtained by a proper selection of the pulse parameters as identified by the first level analysis. First of all, particle signals are flagged by the DAQ if they pass the derivative trigger threshold ("IsSignal").
In addition they have not to belong to a a rejected time interval (bad interval). Then, an event is rejected in case there is pile-up on the main pulse. Moreover a selection on the slope of the baseline of the particle events rejects particle events in which the baseline in the pre-trigger is not flat enough and might correspond to particle triggers on previous pulses' tails. Smaller pulses are rejected, since their shape might be more affected by the noise fluctuations. The average pulse for each channel is built averaging over the selected events using the data from calibration runs.

Then it is necessary to select pure noise events, which are defined as waveforms in which no signal occurs, to build the ANPS. Noise events are acquisition windows recorded at regular intervals of time ("IsNoise").
Among all the events, the ones belonging to periods of time in which a bad interval was set (e.g. unstable baseline, malfunctioning of the channel, earthquakes, ...) are rejected, then only noise events ("IsNoise") are selected. If pulses are identified in the noise event, the event is rejected. Moreover a selection on the slope of the baseline of the noise events is present in order to reject noise events in which the baseline is not flat enough and they might correspond to noise triggers on previous pulses' tails. A range for the maximum acceptable amplitude (baseline subtracted) in terms of multiples of the *Baseline RMS* for the same event is set in order to reject events in which small pulses or spikes in the baseline are not identified by the *Number Of Pulses* variable for a given event. The Average Noise Power Spectrum for each channel is then produced averaging over these selected noise events (using the data from background runs).
In Tab.5.1, the described selections for building AP and ANPS are summarized[3].

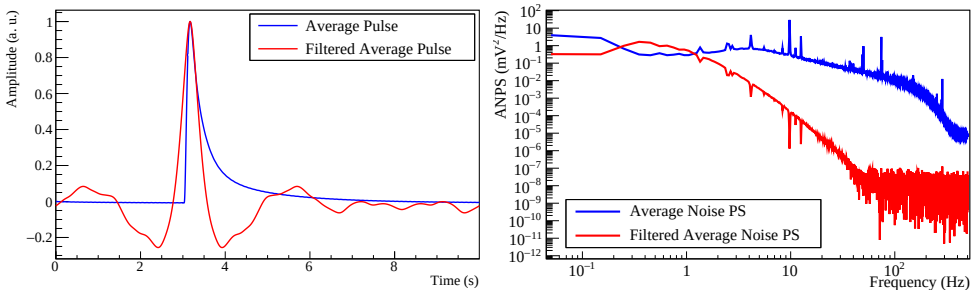

FIGURE 5.2: Channel 44, CUORE DS 3021: sample of average pulse AP (calibration runs) [left] and sample of average noise power spectrum ANPS (background runs) [right].

[3]Among the several cuts for selecting good noise and pulse events, the reported values of the thresholds on the *Baseline Slope* are the ones used for data at 15 mK. In general, the values of the baseline slope thresholds for both AP and ANPS, depend on several factors: the temperature, which partially drives the shape of the signal pulses and then can make the pulse tail time constant vary, and the mechanical and electric operating conditions, which can affect the contributions to the noise on the channels. In case of noise events for the ANPS, the selection of the baseline slope is evaluated in the whole event window (Full Window) in order not to cut events with low frequency baseline oscillations, while rejecting events with long pulse tails.

	AP	**ANPS**
Event Type	IsSignal	IsNoise
SingleTrigger	true	true
NumberOfPulses	1	0
|BaselineSlope|	< 0.005 (mV/s)	< 0.001 (mV/s) [Full Window]
Amplitude selection	$> 40 \times$ BaselineRMS	$< 10 \times$ BaselineRMS
Data kind	Calibration	Background

TABLE 5.1: List of the event selections for building AP and ANPS.

Once the AP and the ANPS are obtained, the OF transfer function for each bolometer can be built. Therefore each recorded event can thus be filtered and its optimal amplitude can be estimated with the proper transfer function. In order to reduce the discretization error of the amplitude evaluation, the amplitude of each pulse is determined by interpolating with a second order polynomial the three data points around the maximum of the filtered pulse.

5.1.3 Thermal gain stabilization

The next step in the data processing involves the pulse amplitude stabilization against thermal drifts during the data taking. Indeed, small variations of the base temperature may change the bolometer internal gain, therefore leading to a different pulse amplitude for events depositing the same energy in the crystal. The consequence of this would be a worsening of the energy resolution. A constant energy event is utilized to trace the evolution of the bolometer gain as a function of the crystal temperature. The thermal gain stabilization on the CUORE data is performed utilizing two different techniques: the heater thermal gain stabilization (heater-TGS) and the without heater thermal gain stabilization (calibration-TGS).

The first stabilization algorithm uses the constant voltage signal generated by a high precision pulser and a Si resistor (heater) to inject into each crystal a constant amount of energy, to study the trend of the gain as a function of the bolometer output voltage (baseline) which acts as a good proxy for the crystal temperature. Heater pulses of fixed amplitude are injected at regular intervals of time inside the crystals during each run. We refer to the heater pulses utilized in this procedure, as 'stabilization pulser'. The pulser amplitude is chosen in order to have reconstructed energies at approximately 3 MeV (i.e. slightly above $Q_{\beta\beta}$) and these events are flagged as "StabPulser". The reconstructed amplitude after the OF sequence for these pulses is then plotted as a function of the average value of the bolometer output just before the signal start (*Baseline*) evaluated in the pre-trigger window, $OFAmpl(V_{Base})$. In case of thermal drift, a decrease of the baseline value (cooling of the detector) corresponds to a slightly higher pulse amplitude (the bolometer internal gain increases), as shown in Fig.5.3 [left]. The amplitudes of all the recorded pulses are then corrected using the formula in Eq.5.13, after setting arbitrarily at an arbitrary value of 5000 the corrected StabPulser amplitude, see Fig.5.3 [right]. The stabilization sequence is performed on a run basis.

$$\text{StabAmplitude} = 5000 \times \frac{\text{Amplitude}(V_{Base})}{\text{StabPulser Amplitude}(V_{Base})} \tag{5.13}$$

$$\text{StabPulser Amplitude: } OFAmpl(V_{Base}) = p_0 + p_1 V_{Base}(T) \tag{5.14}$$

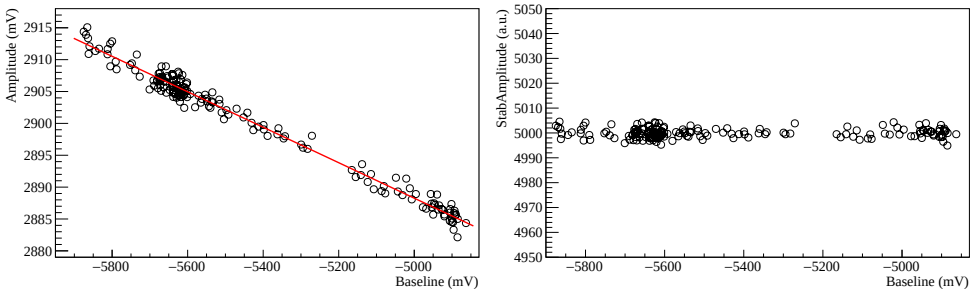

FIGURE 5.3: Channel 850, CUORE DS 3021 (run 301484): OF filtered amplitude vs Baseline [left] and stabilized amplitude vs Baseline [right] plots for the 'stabilization pulser' pulses.

The second stabilization algorithm is performed at dataset level (i.e. after all the data from a fixed number of runs have been collected). This method is based on the use of the ^{208}Tl 2615 keV line events and does not need any pulser signal. Indeed, it was developed in order to be able to stabilize the amplitude also for channels with non-functioning heater.
The dependence of the amplitude of the Tl pulses against their baseline is plotted for all the events belonging to calibration runs of the dataset, which are characterized by a larger number of 2615 keV events. The pulse baseline V_{Base} is assumed to follow the Eq.5.15, thus having a constant contribution due to the preamplifier offset V_{offset} which is set on the electronics and a term which depends on the temperature $G \times V_{bol}$.

$$V_{Base}(T) = V_{offset} - G \times V_{bol}(T) \tag{5.15}$$

In order to avoid that uncontrolled drifts of V_{offset} can fake temperature drifts, a careful check of V_{offset} is compulsory. For each detector, the offset is frequently measured and monitored during the data taking with dedicated runs (*Resistance Measurement*, see Chap. 4.2.2). The stabilization algorithm then corrects each V_{Base} value of the selected events for the closest value of the V_{offset} measured for the channel.
Eventually, for each channel the trend $OFAmpl(G \times V_{bol})$ is fitted with a quadratic function to account for non linearities in the gain temperature dependence, since this alogorithm utilizes the calibration runs which are far in time (initial and final calibration of the given dataset), and thus a much larger spread in the baseline is expected.
This relation is then used to correct the amplitudes of the events in both physics and calibration runs.
The calibration-TGS is compulsory for the amplitude stabilization of heater-less channels. Moreover this procedure can improve the resolution for channels which experience non-negligible baseline drifts during the whole dataset, which cannot be corrected via the heater-based stabilization applied at run level.

5.1.4 Energy calibration

The stabilized pulse amplitudes are converted to the corresponding energies by using the calibration runs taken at the beginning and end of each dataset. During each calibration run, kevlar strings containing sources of ^{232}Th are deployed inside the CUORE detector volume by the DCS systems in order to have an uniform illumination of the channels [89]. The mean stabilized amplitude of the six more prominent γ lines is evaluated for each channel. A calibration function expressing the relation

between the signal amplitudes at each gamma line and the corresponding energies for each channel in each dataset is built. It maps stabilized amplitudes to physical energies.

The identification of the positions of the six peaks in the thorium spectrum is the main task of the calibration module. The most intense peaks (see Table 5.2) are considered as 'primary' and must be identified for the method to work. The remaining peaks are referred as 'secondary'. The peak finding algorithm fails if less than two 'primary' peaks are located and the user intervention is needed. In these cases, the user must manually select the peaks with a GUI.

After having been identified, they are fitted with a CrystalBall function[4] plus a linear background. The best-fit value for the peak position, in units of stabilized amplitude, is used to regress the calibration function. The calibration function is a second order polynomial with no constant term:

$$\text{Energy: } E = a \cdot A_s + b \cdot A_s^2 \tag{5.16}$$

where a and b are the calibration coefficients and A_s is the stabilized amplitude. The calibration coefficients for each channel and each dataset are written to file and applied to the stabilized amplitude variable of the physics data to get the energy variable.

An example of a CUORE calibration energy spectrum reconstructed after this sequence is shown in Fig.5.4.

Energy (keV)	Peak Type	Source
239	Secondary	^{212}Pb
338	Secondary	^{228}Ac
583	Primary	^{208}Tl
911	Primary	^{228}Ac
969	Primary	^{228}Ac
2615	Primary	^{208}Tl

TABLE 5.2: γ peaks from ^{232}Th source used by the calibration algorithm

5.1.5 Coincident events

In order to discriminate among different topologies of events, it is possible to search for coincidences between different channels (i.e. events involving more than one crystal at a time). A variable called *Multiplicity* is assigned to each event. It indicates the number of detectors whose trigger fired within a narrow time window around the reference event trigger time. Moreover the coincident events are identified if the pulses are above a fixed energy threshold (e.g 150 keV for DS3021 and DS3018).

No topological information has been implemented so far in this coincidences evaluation technique, hence, for example, two events triggered on the opposite side of the detector within the same coincidence window are presently flagged as correlated, with *Multiplicity* =2. For future analysis, it's being developed a geometric cut so that the coincidences take into account also the topology of the event. This should

[4]The CrystalBall function is a probability density function commonly used to model various processes of energy loss in high-energy physics. It consists of a Gaussian core and a power-law low-end tail.

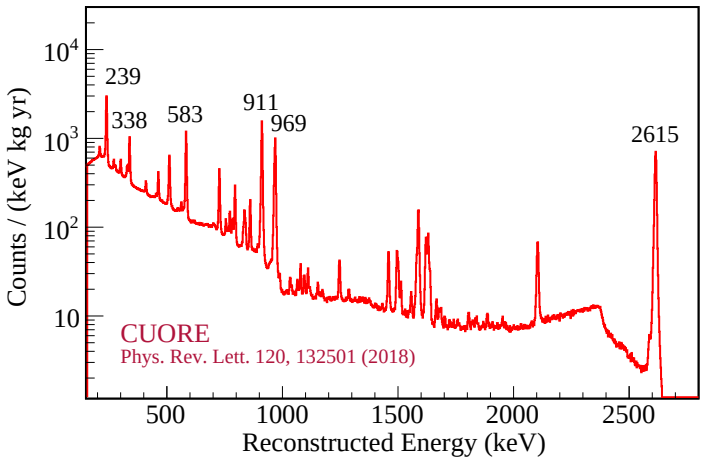

FIGURE 5.4: Log-plot of the CUORE calibration spectrum; the lines used for calibration are labeled.

increase the efficiency of anti-coincidence cuts and minimize the rejection of separate physical events happening at the same time in different regions of the detector.

Since different channels can have different time responses (e.g due to different signal shapes), this might result in misaligned triggers. Therefore coincidences with response synchronization are implemented as the standard method of calculating coincidences for the CUORE data. It allows to have a significant reduction of the rate of random coincidences, by using a shorter coincidence window, thus improving the signal selection efficiency.

First of all the *jitter* between channels has to be evaluated. This quantity corresponds to the characteristic time difference for the signals of two bolometers in case of simultaneous events. Two events whose energy sums up to 2615 keV, likely multiple Compton scatterings of the same 2615 keV γ-ray from ^{208}Tl, are identified as a true coincidence. The comparison of two truly coincident events in the same tower is shown in Fig.5.5 [left] where the difference between the two dotted lines at the pulses maxima corresponds to the jitter between the two pulses, due to difference in response of the two crystals. Jitters are then measured, given a single tower, using each couple of channels in which truly coincident events from ^{208}Tl line are found, in calibration data. The coincidence module is run for one tower at a time, with 100 ms timing windows. For the truly coincident events, the time difference for each channel, relative to a reference channel (one reference channel for each tower) is then evaluated. Afterwards the *delay* between the reference channels of the 19 towers has to be calculated. To this end, it is found by analyzing the delay of heater events, after aligning the triggers.

The jitter among channels of a single tower and the delay among the reference channels of all the towers are then combined to correct the time response of each detector and get the seeked synchronization for each channel.

At this point the system is ready for running the coincidence sequence which is applied simultaneously on all the towers at the same time (for both calibration and background data). For each channel the pulses peak time is then corrected by the overall delay, discussed above (see Fig.5.5 [right]). The recorded events are analyzed to find the ones which are within a coincidence window of 10 ms. Event multiplicities and total energy are then computed and stored.

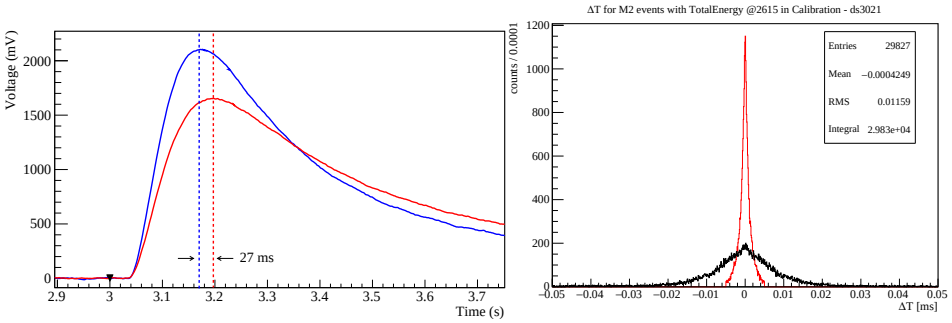

FIGURE 5.5: [Left] Two pulses, from channels of the same tower, belonging to the same true coincidence; they have different delays due the different response of the bolometer (see the different position of the maximum of each pulse - vertical dotted lines). [Right] Distribution of Δt for multiplicity-two events with total energy around 2615 keV, for the calibration runs of DS3021 without synchronization and 100 ms coincidence window (black) and with synchronization and 10 ms coincidence window (red).

5.1.6 Pulse shape discrimination

The pulse shape discrimination algorithm (PSA) was designed to distinguish between pulses originated by a particle interaction from spurious signals of other nature. For each event several pulse shape parameters are calculated with different algorithms. Pulse selection is then based on a proper combination of the parameters (cuts). These parameters measure characteristic quantities of particle pulses (eg. rise time, decay time) or the deviation of a signal from a pulse template (eg. slope of the baseline on which the pulse grows,..). Aim of PSA is the identification of noisy signals or (hard) pile-up events (see Fig.5.6) which are the most common categories of spurious events.

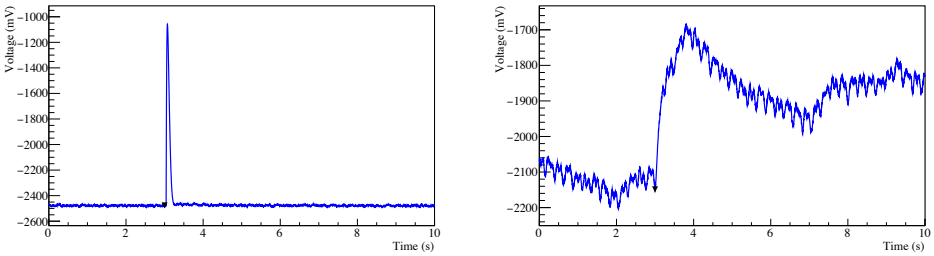

FIGURE 5.6: Example of two triggered events which can be removed utilizing the PSA variables. [Left] A noise spike with very short rise time and decay time. [Right] A very noisy event in which all the PSA variables deviates from their mean for a good pulse.

The parameters used by the PSA discrimination sequence are the following:

- *Pulse rise time*: time interval that the pulse takes to grow from 10% to 90% of its total amplitude. Noise spikes are generally characterized by a shorter rise time. On the contrary, in case of hard pile-up on the rising edge of the main pulse, this variable will be larger than the average.
- *Pulse decay time*: time interval that the pulse takes to fall from 90% to 30% of its total height. Noise spikes will have a shorter decay time; in case of small

pulses growing on the tail of the main pulse, this variable will be larger than the average.

- *Baseline slope*: it is obtained by a linear fit of a fraction (3/4) of the pre-trigger window. It is measured in mV/s. If the event is growing on the tail of a previous pulse, the baseline slope deviates strongly from zero; in this case, the baseline and pulse amplitude of the event will be badly reconstructed.

- *Peak delay*: time interval between the beginning of the event window and the pulse maximum; pulses which deviate significantly from the average peak delay for the channel, typically have poorly measured amplitudes.

- *Test Variable Left and Right (TVL, TVR)*: these parameters are the sum of the squared differences (point by point) between the filtered pulse and the filtered AP (signal template pulse), on the left and on the right side of the pulse maximum, and indicate therefore how the current pulse resembles its template.

For the initial CUORE data analysis, for all the listed parameters, apart from the *Baseline slope*, there were utilized the values calculated on the (OF) filtered pulses. For the *Baseline slope*, it was utilized the value calculated in the preprocess sequence.

All the shape parameters slightly vary with energy. Moreover, the shape parameters distributions differ from channel to channel (and from a dataset to another), although they retain the same general shape. A common feature is a broadening of the parameter distribution at low energies, due to the increasing contribution of noise.

In order to evaluate the energy dependence of the shape parameters, firstly the distribution of the pulse shape parameters for the physics data is plotted as a function of energy. Only events with *Multiplicity* = 2 are utilized to model the energy dependence of the shape parameters. This choice is made in order to build a signal-like event sample. It has been verified that the fraction of spurious coincidences is negligible and coincident events are therefore a good set of genuine events.
The energy range of interest (from 100 keV to 8 MeV) is split into fixed-width bins (50 keV wide). The central value and the width of the main distribution is then evaluated for each energy bin. To reduce the effect of events lying far away from the distribution, the central value is estimated with the median and the width with the MAD (Median Absolute Deviation). Since it hasn't yet been defined a working model for the shape of the parameter distributions, the medians and MADs are fit with phenomenological functions of the energy. These functions are different for each of the six pulse shape parameters listed above, but the same for all 988 channels.

Once the energy distribution of the median and MAD are obtained, normalized pulse shape parameters are calculated: for each data point i of energy E on channel c, and a pulse shape parameter P_i, the value of the normalized parameter P_i^{norm} is given by:

$$P_i^{norm} = \frac{P_i - f^c_{median}(E)}{f^c_{MAD}(E)} \tag{5.17}$$

where $f^c_{median}(E)$ and $f^c_{MAD}(E)$ are, respectively, the fit functions for the median and the MAD on channel c for parameter P. After the normalization procedure, the energy dependence of pulse shape parameters is strongly reduced, making box selection cuts easier to perform.

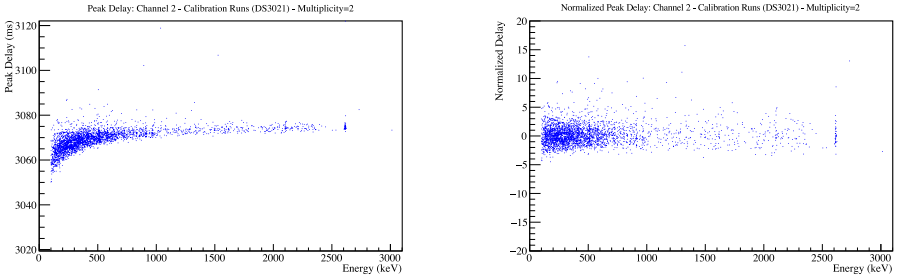

FIGURE 5.7: Example of energy distribution of the delay pulse shape variable for one channel-dataset: the energy distribution of 'peak delay' for events with *Multiplicity*=2 [left] and the 'normalized delay' distribution for the same events with *Multiplicity*=2

5.1.7 Blinding

The final step of the data processing for the $0\nu\beta\beta$ analysis is the blinding of the ROI. Main goal of the blinding procedure is to avoid any action (selection, fit, ...) that can be optimized on the ROI around $Q_{\beta\beta}$ of ^{130}Te, thus introducing a strong bias. All the selection and fit procedures are fixed while the ROI is blinded. The data blinding procedure is applied only to the background runs. The adopted blinding technique is a form of data salting. It randomly shifts the reconstructed energy of an unknown fraction of events (of the order of 40 %) within 10 keV from the ^{208}Tl peak to $Q_{\beta\beta}$, by subtracting 87 keV, and at the same time the same fraction of events is shifted from $Q_{\beta\beta}$ to the Tl 2615 keV line, by adding 87 keV. This procedure acts only on the energy of *Multiplicity* 1 events and it creates an artificial peak at $Q_{\beta\beta}$ with the shape of a true signal peak, see Fig.5.8. The true energy for each event is encrypted and stored, and only at the end of the analysis the unblinding procedure restores it to its original value.

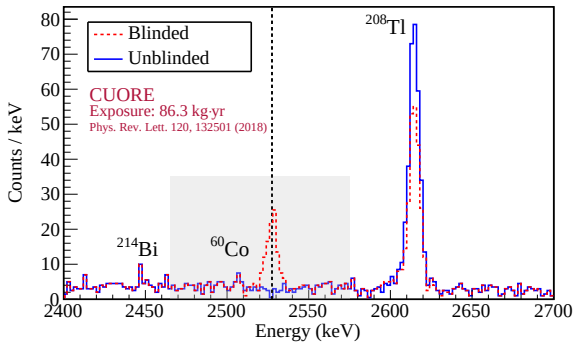

FIGURE 5.8: CUORE physics data blinded (and unblinded) spectra in and around the ROI. The grey region is the ROI, in which the artificial peak at $Q_{\beta\beta}$ due to blinding is visible, and the black dotted line indicates the position of $Q_{\beta\beta}$. Beside the ^{208}Tl line, also the ^{60}Co and the ^{214}Bi lines are visible.

5.1.8 Energy estimators

Several energy variables are produced during the processing of the CUORE data, which are based on different choices of the Optimum Filter (OF) and thermal gain

stabilization (TGS) techniques. Two energy variables are of particular interest: *Energy_OF*, which uses the standard OF and the heater-based stabilization; and *Energy_WoH*, which uses the standard OF and the calibration-based stabilization.

Only one energy variable for each channel is chosen for the physics analyses, namely the one which gives the best energy resolution. A selection technique has been developed in order to determine the best energy estimator to assign to a given channel. Both the resolution and exposure measured for a given channel can vary between energy estimators because of differences in the optimal filtering, the stabilization techniques or the operating conditions of the detector. For this reason, the estimator is optimized on a channel-dataset basis (Ch-D).

For each Ch-D, all the events which belong to the ^{208}Tl line are considered and the energy variance (from the RMS of the measured pulse amplitudes distribution) for both OF and WoH energy variables is computed, σ^2_{OF} and σ^2_{WoH}. Two quantities are defined: a figure of merit, W, which takes into account for both the energy resolution and the exposure, and a significance, Z. They are defined as follows:

$$W \equiv \frac{\sigma^2_{\mathrm{WoH}}\epsilon^2_{\mathrm{OF}}}{\sigma^2_{\mathrm{OF}}\epsilon^2_{\mathrm{WoH}}} \tag{5.18}$$

and

$$Z \equiv \frac{1-W}{\sigma_W}. \tag{5.19}$$

where ϵ_{OF} (or $\epsilon_{\mathrm{OF\_WoH}}$) is the exposure for the Ch-D, measured as the product of the detector mass and the live time.

The *Energy_OF* is the default energy estimator for most channels where it exists. Threshold values for W and Z are then set to select better alternative estimators. A value of $W < 1$ indicates a better performance of the alternative energy estimator (*Energy_WoH*), while $Z > 1$ indicates that the value of W is "significant" with respect to the width of the distribution of W (i.e., σ_W), calculated with direct propagation of errors for the specified Ch-D.
When both $W < 1$ and $Z > 1$, *Energy_WoH* is chosen as the energy estimator. Channels with non functioning heaters and channels for which the variable *Energy_OF* is invalid[5] are also assigned to use *Energy_WoH*. Channels for which both estimators are invalid were removed from the analysis. In the next sections, the energy estimator chosen for the analysis will be referred as *Energy* only.

Figure 5.9 shows the distributions of W vs Z for two physics dataset acquired by CUORE in 2017: DS3018 and DS3021.

5.2 Data selection

The selection of active channels for the CUORE physics analyses is based upon a variety of data quality criteria ranging from hardware performance to calibration stability. An analysis cut is supposed to disregard undesired events. However, cuts have a finite efficiency. Accepting bad events is usually compensated by using multiple cuts which cut the different (or independent) event populations. Throwing away good events has to be taken into account for the data analysis and cut selection efficiency evaluation is needed for this purpose.

[5]For a given channel, an energy estimator can be invalid if the data production sequence leading to that parameter evaluation, failed. This occurrence is handled in the data processing by the use of specific bad intervals (*"bad_analysis"*), which will be described in the next section, Sec.5.2.1.

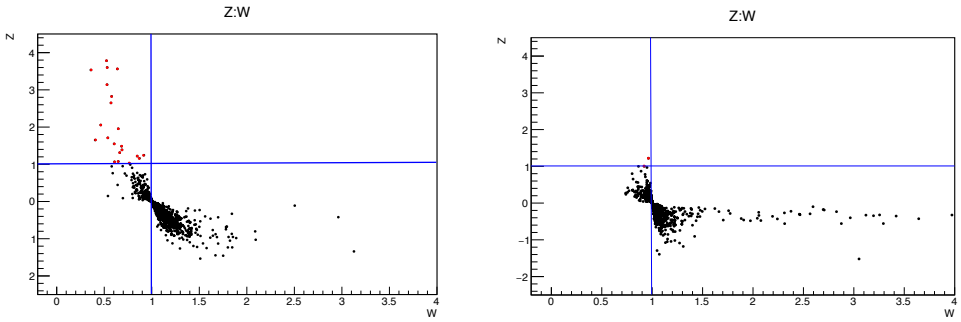

FIGURE 5.9: W versus Z for DS3018 [left] and DS3021 [right]. Channels for which *Energy_WoH* was selected are in the upper left quadrant, highlighted in red.

5.2.1 Basic data quality cuts

There are several initial selections which are applied in order to ensure basic data quality for the data processing and the subsequent analyses. Main goal of the basic data quality cut is to reject events recorded during low-quality data intervals while keeping pulses which can be signal candidates.

Bad intervals

First step is the rejection of all the recorded events whose trigger time falls within a time-based bad interval (*"bad_channels"*, see Chap.2.4.2). Whereas individual events can be cut later by pulse shape cuts, intervals of bad data need to be removed from the data processing, since that interval may not be representative of the behavior of the channel over the entire dataset. For example, a temporary high noise level can influence the amplitude estimation and thus lower the overall energy resolution of the detector.

Another kind of bad intervals (*"bad_analysis"*) are related to channels which fail any step of the analysis sequences for the data production. These bad intervals are handled in a way such that an analysis sequence in DIANA can exclude one channel's data because it depends on a previous set of analyses which have failed. Examples of bad_analysis flags are:

- *OF*: a channel fails either the average pulse or the average noise sequences, therefore the optimal filter can't be built,
- *heaterTGS*: a channel has missing heater or it fails the heater based stabilization sequence or it fails the standard calibration sequence based on heater stabilized amplitudes,
- *calibrationTGS*: a channel fails the WoH stabilization sequence or it fails the calibration sequence performed utilizing the WoH stabilized amplitudes,
- *Calibration*: a channel fails all the calibration sequences and it can't be calibrated at all,
- ...

Each one of these bad_analysis flags can also be applied to subsets of the total dataset.

The need for this second set of bad intervals is due to the presence of different processing procedures and high level analyses that can be performed in parallel to produce different energy estimators.

Bad intervals are excluded from the evaluation of the channel's live time.

Event based cuts

The CUORE physics spectrum should contain only triggered particle-induced pulses ("IsSignal"). Therefore all the events which are not triggered as signal events (noise and heater events) are not included in the physics spectrum.

Moreover in order to improve the quality of the amplitude estimation events with more than one signal trigger in the 10s event window are discarded; the selected events have the *Single Trigger* boolean true and *Number Of Pulses* variable equal to 1. See Fig.5.10.

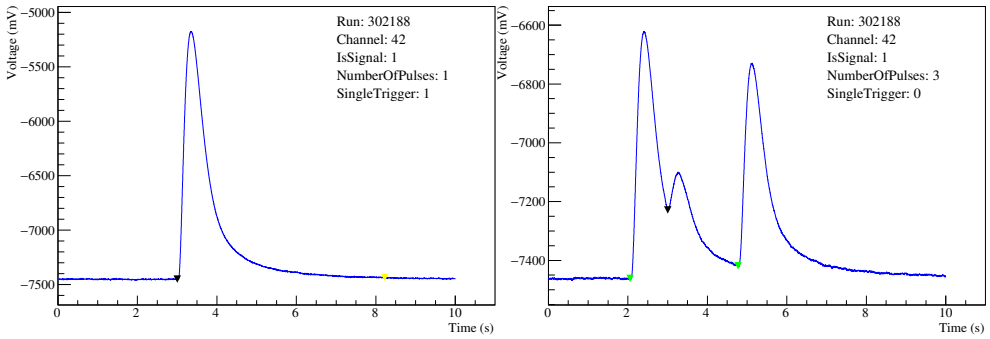

FIGURE 5.10: [Left] Example of a good pulse, which satisfies the *Single Trigger* & *Number Of Pulses*=1 condition (the black triangle identifies the primary trigger); the amplitude will be correctly reconstructed. [Right] Example of a triggered pulse (black triangle) which grows on a previous pulse tail and has itself a pile-up on the tail (secondary triggers are identified by the green triangles); this event will be rejected for the analysis, since the amplitude of this event could be mis-reconstructed.

5.2.2 Multiplicity and Pulse shape cuts

An event can be rejected by the analysis procedure also due to its multiplicity and its pulse shape.

The multiplicity cut can be different depending on the physics analysis which is pursued.

For example, $0\nu\beta\beta$ decay would have an high probability of being fully contained in one crystal; Monte Carlo simulation shows that it is contained in a single CUORE crystal with $(88.35 \pm 0.09)\%$ efficiency. Only *Multiplicity* 1 events are therefore selected for the $0\nu\beta\beta$ analysis [34]. Multiplicities are set by the coincidence sequence which identifies simultaneously hit crystals. An energy threshold of 150 keV[6] and a coincidence window of 10 ms is set by the analysis. Another example could be the

[6]Utilizing the OT algorithm, described in Chap.2.4.1, instead of the DT for identifying the pulses would allow to reach lower energy thresholds in the reconstructed spectra.

study of the $2\nu\beta\beta$ decay on excited states, for which the selection of higher multiplicity events (Multiplicity = 2, 3) would help to better identify the signature of the process and to reduce the backgrounds [111].

The other analysis cut is based on the pulse shape. It requires the shape of the pulse to be consistent with that of a reference template expressing the expected response of the system to the energy deposition by a particle interaction. This selection is important since non-physical or deformed events can randomly fill any region of the spectrum acting as a background source.
From the PSA sequence, 6 normalized pulse shape parameters are produced for each event. Given the normalized distributions of the PSA parameters, outliers corresponding to non-physical events need to be removed for building the final physics spectrum. Therefore acceptance levels on the normalized pulse shape parameters have to be set. The optimization of cuts on each single parameter is not trivial, since 12 parameters (lower and upper bounds for each PSA parameter) have to be eventually taken into account. Moreover this approach does not take into account for any possible correlation between the parameters.
To address these issues, for the CUORE analysis the Mahalanobis distance (D_M) parameter was constructed. The Mahalanobis distance is the measure of the distance of a point ($\vec{x}$) from a multidimensional distribution which has a mean $\vec{\mu}$ and the covariance matrix $\mathbf{\Sigma}$, see Eq.5.20. [112], [113]

$$D_M = \sqrt{(\vec{x} - \vec{\mu})^T \mathbf{\Sigma^{-1}} (\vec{x} - \vec{\mu})} \tag{5.20}$$

For each event, the six normalized PSA variables can be represented as a point in the parameter space. Multiplicity one events from ^{40}K and ^{60}Co gamma lines are used to evaluate the $\vec{\mu}$ and $\mathbf{\Sigma}$ for the D_M parameter calculation. The D_M variable is then calculated for each point (event) in the six-dimensional parameter space. By construction, the D_M inherently takes into account the correlations between the parameters. The pulse shape selection cut can then be optimized on the single parameter D_M, instead of 12 parameters. For example, for the $0\nu\beta\beta$ search, it was chosen the upper limit on D_M that maximized the discovery sensitivity for the process.

5.2.3 Signal efficiencies

Since analysis cuts still accept few bad events and remove few good ones, it is mandatory to estimate their efficiency. The cut efficiency is then defined as the fraction of true signals passing the analysis cut under examination.

As described in the previous sections, the event selection criteria of CUORE can be categorized as follows: basic data quality, pulse shape, and anti-coincidence (multiplicity). From the procedural point of view, the evaluation of the basic data quality cut efficiency is performed using pulser events while the efficiency of PSA and coincidence cuts are evaluated using physics pulses in the background data [114].

Efficiency of basic data quality cuts

The basic data quality selections involve the identification of pulses which have been identified by the derivative trigger ("IsSignal"), the goodness of energy reconstruction given the pulse and the rejection of events in which there is a pile-up over the main pulse.

1. *Detection efficiency*: it measures the effectiveness of the hardware trigger. Every time an heater deposits the selected amount of power chosen for the stabilization, a dedicated flag (IsStabPulser) is associated to the event. For each run and channel by channel, the efficiency is evaluated as the ratio between the number of pulses which are recognized by the derivative trigger ("IsSignal") and the total stabilization pulser events ("IsStabPulser"). A cut on the amplitude of the identified stabilization pulser signal is added, in order not to count events in which the pulser was not firing properly, since the signal detection efficiency should not depend on the pulser boards performances.

$$\epsilon_{Det} = \frac{N_{Pulser}^{Triggered}}{N_{Pulser}} \tag{5.21}$$

2. *Energy reconstruction efficiency*: this efficiency measures how many events do not belong to the expected gaussian distribution of the reconstructed energy for pulses of a given amplitude. Heater pulses are chosen to evaluate this efficiency since they ensure the same energy injection for each pulse and then the spread of the peak in the energy spectrum associated with these events is considered. For each run and channel by channel, the energy efficiency is evaluated utilizing the stabilization pulser ("IsStabPulser"). Given a channel, the stabilization pulser events are selected, an histogram of their energy is built and the mean and RMS of the pulser energy, assuming it is a gaussian distribution, is evaluated. Events which have an energy in a $\pm$ 3 σ range around the mean are identified as well reconstructed and they are compared with the number of events in a window of [mean $\pm$ 10 σ] [7]. The efficiency is then evaluated as this ratio, for each run and channel by channel.

$$\epsilon_{EnReco} = \frac{N_{Pulser}^{3\sigma}}{N_{Pulser}^{10\sigma}} \tag{5.22}$$

3. *Pile-up rejection efficiency*: it is related to the rejection of events with pile-up on the main pulse. The pile-up rejection cut utilizes both the selection on *Number Of Pulses* == 1 and *SingleTrigger* == true. To correctly evaluate this efficiency, two contributions have to be considered. The probability to have a "good signal", a particle event with no pile-up on the main pulse, is related both to the probability that given the event window there isn't a second signal and there isn't an heater pulse as well.

$$P(goodSignal) = P(no2^{nd}signal|signal) \times P(noPulser|signal) \tag{5.23}$$

The former can be evaluated utilizing the heater pulses, whose delivery time is precisely known. The latter depends on the pulser firing frequency with

[7] This window was chosen in order to avoid counting pulser events in which, due to the energy sequence failures, the energy is either reconstructed at zero or at the default value for the energy variable

respect to the event window size.

$$P(no2^{nd}signal|signal) = P(no2^{nd}signal|pulser) = \frac{N_{Pulser}^{Triggered,noPileUp}}{N_{Pulser}^{Triggered}} \quad (5.24)$$

$$P(noPulser|signal) = \frac{(T_{pulser} - window)}{T_{pulser}} \quad (5.25)$$

In $P(no2^{nd}signal|pulser)$, the $N_{Pulser}^{Triggered,noPileUp}$ variable corresponds to the number of triggered pulser events passing the selections: (*Single Trigger* && *Number Of Pulses* == 1). In $P(noPulser|signal)$, $window$ is the event window, 10s; and T_{pulser} is the pulser firing period[8].

Combining the two contributions the total pile-up rejection efficiency can be obtained:

$$\epsilon_{PileupRej} = P(goodSignal) = \frac{N_{Pulser}^{Triggered,noPileUp}}{N_{Pulser}^{Triggered}} \times \frac{(T_{pulser} - window)}{T_{pulser}} \quad (5.26)$$

The channels with non-functioning heater and the ones for which the without heater stabilization procedure was chosen, have not been used for calculating the Detection, Energy reconstruction and Pile-up rejection efficiencies, since these quantities are evaluated utilizing the heater events. It was assumed that these channels have an efficiency equal to the average of the others.
The statistical errors on the these described efficiencies are evaluated utilizing the Clopper-Pearson interval [115]. Due to the high pulser statistics, these values are way smaller than the uncertainties on the PSA and the coincidence cuts (statistics and systematics).

Efficiency of multiplicity and pulse shape cuts

The efficiencies of multiplicity and pulse shape cuts are computed directly on the signals of background data for each dataset. These cut efficiencies are averaged over all active channels.
Differently from CUORE-0 in which the cuts were tuned on 50% of the data and the efficiencies were evaluated using the other 50%, in CUORE, in order to increase the statistics on the efficiency evaluation, the cuts are tuned on one spectral line and another one is used to compute the efficiencies.

- For the PSA event selection, the tuning is performed on the ^{40}K, while the cut efficiency is calculated using the 2615 keV ^{208}Tl γ-ray peak since it offers sufficient statistics at the energy closest to the ROI.
- Regarding the multiplicity cut, it should be considered that the time jitter is found by the coincidence sequence using the ^{208}Tl γ line and moreover using

[8] The pulser firing period was: 390 s in DS3018 and 580 s in DS3021. The pulser firing period is calculated as:

$$T_{pulser} = N_t \cdot N_{col,t} \cdot \delta t_{col} + \delta t_{delay}$$

where N_t = 19 is the number of towers, $N_{col,t}$ = 4 is the number of columns for each tower, since the pulser is fired in parallel to channels of a given column. δt_{col} is the time interval for firing the pulser subsequently column-by-column, that was 5 s in DS3018 and then 7.5 s in DS3021; the choice is done in order not to have crosstalk effects on channels belonging to neighbor columns, when firing on a single column. δt_{delay} = 10 s, is the delay between each sequence of pulser firing all columns.

those events for evaluating the anti-coincidence cut (Multiplicity = 1) efficiency has limitations because they occasionally occur in coincidence with other physical events (γ lines). Therefore, the 1461 keV γ rays from ^{40}K decay, which are truly individual events are used for the evaluation of the anti-coincidence cut efficiency .

The PSA and coincidence efficiencies should quantify the effect of each single selection cut on the data; in such a way, they can be combined multiplicatively with no residual correlations. Therefore, the PSA efficiency is evaluated using only events which pass the base quality cuts. The coincidence efficiency is instead calculated on events which pass both the base quality cuts and the PSA event selection.
The technique that is used to calculate the efficiency is the same for both PSA and coincidence. Once the events from the chosen peak have been selected, the region of interest is divided into region of the peak and sidebands. The sidebands are used to evaluate the background to be subtracted from the peak region, while the signal region is chosen to be equal to 3 σ from the peak mean. In Fig. 5.11 there is an illustrative representation of the procedure, considering the ^{40}K peak: S_i is the number of events in the peak region and B_i is the number of events due to background in the peak region. The i index can be u or c representing respectively the number of entries before or after the cuts. In general, the width of the region in analysis is chosen in order to have enough statistics but still to avoid contribution of adjacent peaks. The width of the peak region plus the width of the sidebands is fixed. It is 1460 ± 35 keV for ^{40}K events and 2615 ± 60 keV for ^{208}Tl events. Consequently, an enlargement of the peak region width implies a narrowing of the sideband region.

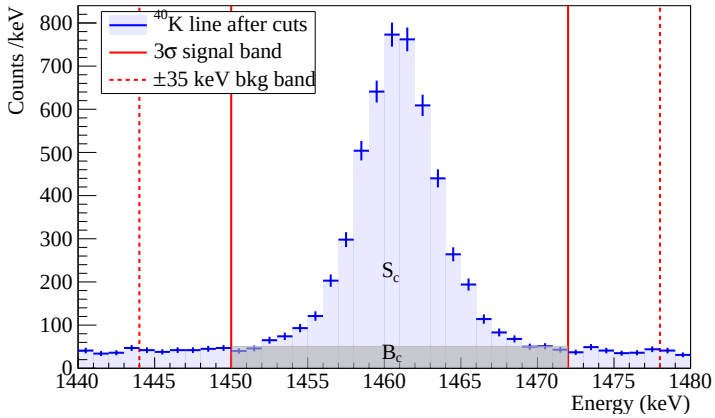

FIGURE 5.11: 1461 keV γ peak from ^{40}K decay in the background spectrum after all cuts. The plot has only an illustrative purpose showing signal and side bands used for the efficiency evaluation.

The cut efficiency $\epsilon_{PSA/coinc}$ is then defined as:

$$\epsilon_{PSA/coinc} = \frac{S_c - B_c}{S_u - B_u} \tag{5.27}$$

where the propagation of the errors follows the usual Poisson statistics.
Consistency checks are performed to ensure the choice of the peak region width does not affect the efficiency calculation, as well as its statistical error. In Figure 5.12 the plots show the variation of the efficiency as a function of the width of the peak region (in units of number of sigmas of the peak) for the first two CUORE physics

datasets. Given the region in the anti-coincidence efficiency analysis for the ^{40}K peak, it has not been possible to extend further the number of sigmas for signal calculation because in the sidebands region there would be too few events. Variations of the efficiency are well within the statistical error. The 3-σ width corresponded to the one with lower statistical error both for PSA and coincidence analysis and for both datasets.

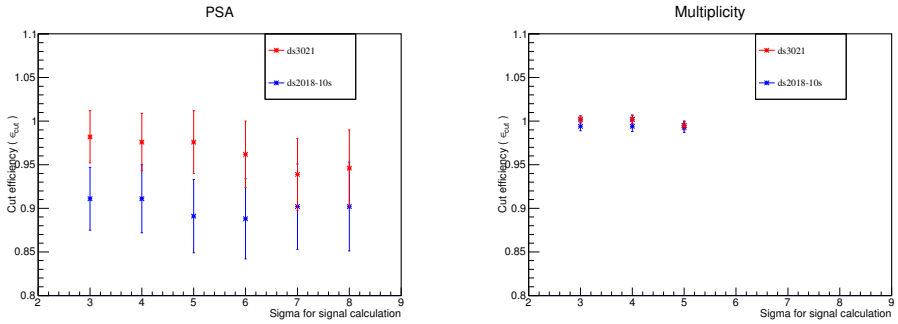

FIGURE 5.12: PSA efficiency cut [left] and anti-coincidence efficiency cut [right] as function of the width of the peak region both for ds3018 and ds3021.

5.3 Monte Carlo tools

A quick overview of the tools utilized for the Monte Carlo (MC) simulations is CUORE will be given. Two main codes are used in CUORE: *qshields*, a Geant4 based code to simulate the particles propagation and interaction in the CUORE geometry, and *g4cuore*, a tool to reprocess the Monte Carlo data adding the detector-related features.

5.3.1 Monte Carlo code: qshields

QShields is the code used for the MC simulations with the CUORE geometry, from the bolometric array up to the external shields. It simulates the effects of particle interactions in the CUORE volumes; it is written in C++ and based on Geant4, a toolkit for the simulation of the passage of particles through matter [116].
Geant4 version 4.9.6.p03 was used for the CUORE simulations that will be discussed in this work.

Given the wide availability of materials and geometries among the Geant4 classes, it was possible to include the full CUORE cryostat and detector geometry on the *qshields* simulation code, namely: the TeO_2 crystals, the copper structure holding the array, the PTFE supports, the wire trays, the NTD thermistors, the calibration sources guide tubes, the various thermal shields and other cryostat parts, the internal and external lead shields, the external polyethylene shield. See Fig.5.13.

Particles can be generated in different ways within the *qshields* code:

- Single particles (e^-, e^+, γ, μ, n, α, ...); the source can be monochromatic or with a specific energy distribution
- Single decay: a single decaying nucleus (A,Z) is generated and the particles produced during the transition from the father to the daughter nucleus are produced and propagated

- Decay chains: a concatenation of tabulated single isotopes decays is produced to correctly simulate chains of radioactive decays in secular equilibrium taking into account their specific time structures (e.g. to simulate the natural radioactivity)
- Double beta decay: various double beta decay schemes can be generated. The theoretical shape for the electrons sum energy spectrum is extracted from literature [14], [117]. It is also possible to use numerical calculations for the the $2\nu\beta\beta$ electron spectrum from Kotila-Iachello works [16], [17].

Given the particle source, its position inside the cryostat has to be set. The starting particle position (vertex) can be any volume of the CUORE geometry and the particles can come either from its full volume (bulk) or from its surface. The distribution of bulk contaminations is assumed to be uniform, while impurities on the surface are modeled assuming a diffusion process with an exponential profile.

The propagation of particles though matter can be simulated by several models in Geant4 with the possibility to activate a number of different processes and alternative models (physics lists). For the electromagnetic part for the CUORE simulations it has been used the Livermore Physics List, which appears to be the most precise at low energy. Tracking is performed in Geant4 by following each particle through a series of steps; the step size depends on particle type, energy and material. In the CUORE simulations, all primary particles and secondaries are propagated with a cut on secondary particle production optimized for the different detector volumes to balance simulation accuracy and speed (e.g. the production cut in lead is set to 1 cm for γ and 1 mm for e^-, while in copper to 1 mm for γ and 0.1 mm for e^-).

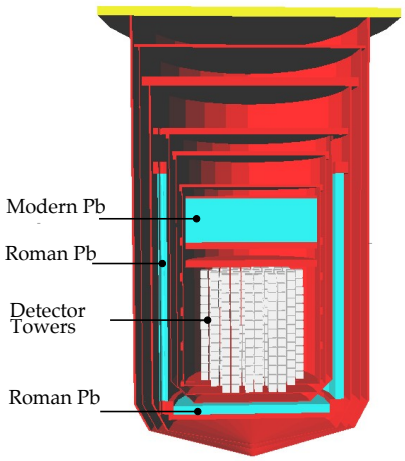

FIGURE 5.13: 3-dimensional view of the CUORE setup as implemented in the Monte Carlo simulation. [58]

5.3.2 Monte Carlo reconstruction software: g4cuore

In order to compare the Monte Carlo simulations output with the experimental CUORE data, it is necessary to take into account and model the detector time and energy response, as well as the data analysis procedures.

The *g4cuore* software is dedicated to the MC data handling, processing the raw data from *qshields* and turning them into a CUORE-like format.
The main advantage of using a separate code for the implementation of the detector

response is that any time you change any detector parameter or procedure you do not need to repeat the time consuming simulation.
G4cuore attempts to reproduce every aspect of the CUORE data. The main ones are:

- Energy resolution: the energy depositions are smeared with a Gaussian energy response function assuming the same average resolution for all the channels
- Energy threshold: each of the CUORE crystals has a different trigger threshold, depending on its noise level. The trigger threshold parameters can be modeled independently for each detector according to the experimental threshold curves. Stepwise thresholds are a possible alternative that can be applied to all the channels.
- Event time: a meaningful timing information is added to the events, in order to reproduce any possible event rate r. Several timing-related operations are performed to reproduce the detector, DAQ and analysis behavior.
  Dead time: corresponds to the derivative trigger (non-paralyzable) dead time
  Integration time: this accounts for the time structure of the physical processes which contribute to the signal formation. It corresponds to the time resolution resolution of each crystal and adds the energy depositions occurring in the same crystal within the specified time window
  Coincidence: events occurring in multiple bolometers within the coincidence window are defined as coincident

Other operations can be performed on the MC sample:

- Excluded channels: channels failing the analysis procedures in the data sample can be excluded from the MC sample as well. Dataset-dependent list of excluded channels can be provided
- PSA cut efficiency: the PSA efficiency vs energy curve for each channel, evaluated from the data, can be provided as an input. Otherwise a flat cut efficiency can be applied to all channels
- Quenching factor: *g4cuore* can modify the energy deposited by the particles of the same type by a multiplicative factor. This is used mainly for α particles, which produce slightly higher pulses than expected from the standard energy calibration performed on γ lines. [111]

5.4 Monte Carlo reconstruction of CUORE background

In this section, the techniques to build the background model and to reconstruct the CUORE physics spectrum will be briefly described.

5.4.1 Background model: sources

In rare events searches, a number of sources can produce events in the energy region of interest, including natural and artificial radioactivity, cosmogenically activated isotopes, and cosmic rays. It is common to define these contaminations as *background sources*.

The most common background sources for experiments located in underground laboratories are the radioactive contaminants of the construction materials:

- long-lived radioactive nuclei: natural decay of ^{40}K and the daughters of ^{238}U and ^{232}Th decay chains, including the surface implantation of ^{210}Pb from environmental ^{222}Rn
- cosmogenically-produced radioactive isotopes: the cosmogenic activation especially of copper and tellurium produces ^{60}Co which has a long half-life

A small contribution to the background comes from cosmic muons, environmental γs and neutrons interacting directly in the detector, which are strongly attenuated by either natural or artificial effective shields.

5.4.2 Reconstruction of background sources

The effects of the CUORE background sources are reproduced utilizing the *qshields* and *g4cuore* sequence.

A contamination source is made up by three ingredients: the physical volume which is contaminated, the responsible radioactive isotope and the geometrical distribution on the source volume (bulk, surface).
The main source volumes that are used in simulations are: TeO_2 crystals, Cu-NOSV (parts close to the detector: tower structure, tiles...), roman lead shield, top and external lead shields, 600 mK shield (representative of copper Cu-OFE shields inside the roman lead layer [9]), 4K shield (representative of shields outside the roman lead layer), cosmic μ as an external source.
The identification of contaminants in CUORE is done with the same techniques used for the CUORE-0 background model [58], [118]. Material assay measurements, estimates of cosmogenic exposure and results from the background study of the former experiment CUORE-0, were used to identify the most relevant sources of background. ^{40}K, ^{238}U and ^{232}Th are essentially everywhere in the volumes. ^{60}Co and cosmogenical activated Cu are in TeO_2 and Cu-NOSV. The cosmic μ, γs and neutron fluxes are well known, from dedicated measurements done at LNGS [119], [120].
When α decays are concerned, the distribution of contaminants inside the source volume strongly influences the shape of the measured spectrum [10]. Two possible distributions are considered: bulk and surface. The bulk contamination is uniform across the whole volume; the surface contamination is only present in a thin surface layer, with variable thickness. Surface contaminations are only simulated on crystals and close copper parts; the simulated depths of the contaminants in copper are: 0.1 μm, 1 μm and 10 μm. Every contamination outside the 10 mK shield is simulated as bulk only.

Several detector-related parameters have been implemented and utilized in the g4cuore code for converting the MC simulation output to a CUORE-like format. A gaussian response function with 10 keV width was utilized for the energy resolution for all the channels and an uniform 80 keV energy threshold was set. For associating the 'event time' to the simulated events, a small rate r was utilized, resembling the actual global rate in physics data, where the probability of accidental coincidences is very low. Given the hardware trigger settings, it was set 800 ms as the trigger dead time. Instead, from the coincidences and multiplicities analysis sequences, 10 ms for integration and coincidence time was chosen. A 95% flat cut efficiency was included, taking into account the effects of base cuts and PSA cuts on the data.

[9] Degenerate sources: sources located on different volumes, but essentially undistinguishable from each other (especially with limited statistics)

[10] Generally speaking, shallow contaminations produce peaks and deep contaminations produce tails

Moreover, a dataset dependent list of excluded was provided as input, in order to take into account the different sets of channels that could be used for the physics analysis for each acquired physics dataset.

5.4.3 Analysis technique: the bayesian approach

The background model is a fit of the CUORE observed data by a proper combination of the contributions from various radioactive sources.

Three observed spectra are used for the reconstruction: Multiplicity 1 (M1), Multiplicity 2 (M2) and Multiplicity 2 - total energy (M2Sum)[11]. Double beta decay events deposit all of their energy into a single bolometer about 90% of the time and so are primarily in the M1 spectrum, whereas many of the backgrounds deposit energy across two or more bolometers (e.g.γ-rays scattering from one crystal into another or α-decays occurring on a surface between two neighboring crystals). In addition to this, the M1 spectrum is split in two geometrical layers: outer crystals are more sensitive to contaminations on the shields (outer layer, L1), inner crystals to contaminations on towers (inner layer, L0) (see Fig.5.14). M2 and M2sum are not split, as the difference between the two layers is much less pronounced. [58]
The expected energy spectra produced by radioactive sources are reconstructed via the CUORE Monte Carlo software, as described above.

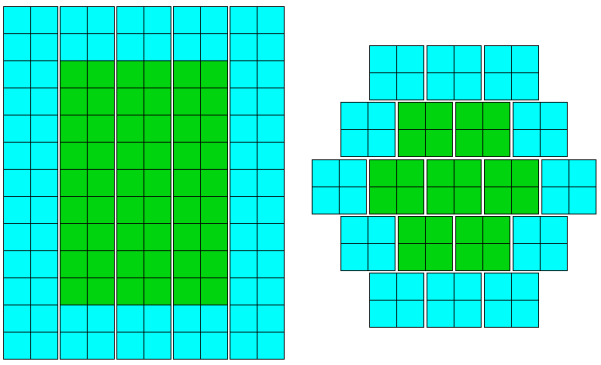

FIGURE 5.14: Side and top view of the CUORE detector with the two layers highlighted. The inner layer is labelled layer 0 (L0), the outer is layer 1 (L1).

The CUORE observed energy spectra are fitted with a linear combination of the simulated source spectra utilizing a Bayesian approach.

In general, Bayesian statistical analysis is based on the following interpretation of Bayes' theorem [121]:

$$P(theory(\theta)|data) \propto P(data|theory(\theta)) \cdot P(theory(\theta)) \tag{5.28}$$

where $P(theory(\theta))$ represents the *prior probability* that the theory is true and θ is the set of model parameters that have to be determined. $P(data|theory(\theta))$ is the *likelihood*; it is the probability, under the assumption of the theory, to observe the data which were actually obtained. The outcome of the Bayesian analysis $P(theory(\theta)|data)$

[11]The M2 spectrum is the energy spectrum of the events recorded by any of the detectors and assigned to a multiplet with multiplicity equal to 2. The M2Sum spectrum is the spectrum of the sum of the energies of the two events recorded in coincidence forming each M2 multiplet; each multiplet contributes to the spectrum with only one energy.

is the *posterior probability* that the theory is correct after seeing the result of the experiment. It is then obtained by combining the information available a priori (the prior) with the likelihood.

The combined Bayesian fit of the CUORE physics data is performed with the Just Another Gibbs Sampler (JAGS) tool [122]. It exploits Markov Chain Monte Carlo simulations to sample a *multivariate likelihood*, built utilizing the several parameters of the model.
The expectation value of the counts in the ith bin of the experimental spectrum is:

$$\langle C^{exp}_{i,\alpha} \rangle = \sum_{j=1}^{M} N_j \langle C^{MC}_{ij,\alpha} \rangle \tag{5.29}$$

where α = M1L0, M1L1, M2, M2sum. $\langle C^{MC}_{ij,\alpha} \rangle$ is the expectation value for the ith bin of the simulated spectrum of the jth source and N_j is the normalization factor related to that source (e.g the unknown activity of the jth source). M is the number of background sources utilized; for the analysis of the initial CUORE physics spectrum, M = 60 sources have been used (considering both the radioactive contaminations and the $2\nu\beta\beta$ spectrum).
The *joint posterior* probability distribution function (pdf) of the model parameters is sampled by the JAGS tool. The *marginalized posterior* pdf for each model parameter N_j is evaluated by combining the *likelihood* and the *prior* distributions, following Bayes' theorem. The data utilized to define the *likelihoods* are the observed counts in the bins of the experimental ($C^{exp}_{i,\alpha}$) and simulated ($C^{MC}_{ij,\alpha}$) spectra, both of which obey Poisson statistics. The *joint posterior* can be then build as:

$$\begin{aligned} &Posterior(N_j, \langle C^{MC}_{ij,\alpha} \rangle | C^{exp}_{i,\alpha}, C^{MC}_{ij,\alpha}) = \\ &\prod_{i,\alpha} Pois(C^{exp}_{i,\alpha} | \langle C^{exp}_{i,\alpha} \rangle) \times \prod_{j} Prior(N_j) \times \prod_{ij,\alpha} Pois(C^{MC}_{ij,\alpha} | \langle C^{MC}_{ij,\alpha} \rangle) \times Prior(\langle C^{MC}_{ij,\alpha} \rangle) \end{aligned} \tag{5.30}$$

where $Prior(N_j)$ and $Prior(\langle C^{MC}_{ij,\alpha} \rangle)$ are the priors distributions. The priors for N_j describe the available knowledge about source activities. In the case of a source with measured activity, it is used a Gaussian prior centered at the measured value with the measurement uncertainty as the width of the gaussian. In case the measured contaminations have non-negligible uncertainties or the sources are not well localized, it is used an uniform non-informative prior with an activity that ranges from 0 to an upper limit higher than the maximum activity compatible with the CUORE data. Similarly, uniform priors are used for each energy bin of the MC spectra, $\langle C^{MC}_{ij,\alpha} \rangle$.
The likelihood functions for the data and the MC spectra are defined as Poisson pdfs: $Pois(C^{exp}_{i,\alpha} | \langle C^{exp}_{i,\alpha} \rangle)$ and $Pois(C^{MC}_{ij,\alpha} | \langle C^{MC}_{ij,\alpha} \rangle)$. The normalization coefficients N_j are the unknown variables of main interest for the fit; the expectation values for all the bins of the simulated spectra for all the sources ($\langle C^{MC}_{ij,\alpha} \rangle$) are considered as 'nuisance parameters'.

A variable binning of the spectra is used to maximize the information content while minimizing the effects of statistical fluctuations and detector non-ideal behavior. As an example, all the counts belonging to the same γ and α peaks are included in a single bin, in order to avoid systematic uncertainties due to the line-shape of the energy peaks. For the background regions between γ lines and of the degraded alphas, the minimum bin size is 15 keV and bins with less than 30 counts are merged with their immediate neighbor.

The marginalized posterior distributions for the fit parameters N_j are used to evaluate the central values and the statistical uncertainties of the activities (in case of a gaussian-shaped converging posterior) or to calculate 90% upper limits for undetermined contaminations (non converging posteriors: exponential-shape, truncated gaussian-shape close to 0,...).

For a given nuclide j, given a number of MC generated decays (chains) of the isotope N^{MC}_{chain} in the volume of interest and N^{MC}_{events} events recorded in the detector sensitive geometry, the bayesian fit of the data provides the value of the normalization factor N_j for that process, which corresponds to:

$$N_j = \langle \frac{N^{exp}_{events}}{N^{MC}_{events}} \rangle \tag{5.31}$$

where N^{exp}_{events} is the number of events of the physics spectrum associated with that process. Similarly, the number of decays of nuclide j in the observed data can be reconstructed as:

$$N^{exp}_{chain} = N_j \times N^{MC}_{chain} \tag{5.32}$$

The number of observed decays N^{exp}_{chain} can be lower than the number of decays that took place during the measurement N_{decays}, due to the finite detection efficiency of the system ϵ ($\epsilon < 1$):

$$N^{exp}_{chain} = N_{decays} \times \epsilon \tag{5.33}$$

The procedure to calculate activities and lifetimes for sources utilized in the bayesian fit is reported below.

- Activity (A): number of decays per unit time of a radioactive sample.

$$A_j[Bq] = -\frac{dN}{dt} = \frac{N_{decays}}{\tau} = \frac{N^{exp}_{chain}}{\epsilon\tau} = \frac{N^{MC}_{chain}}{\epsilon\tau} N_j \tag{5.34}$$

  where N_{decays} is the number of decays that took place during the measurement and N^{exp}_{chain} is the number of observed decays;τ is the mean life-time for the decay of interest.

- Half-life ($T_{1/2}$): time taken for the activity of a given amount of a radioactive substance to decay to half of its initial value; $T_{1/2} = \tau ln(2)$

$$\frac{N_{decays}}{T_{live}} = \frac{ln(2)}{T_{1/2}} N^j \tag{5.35}$$

  where T_{live} is the live-time; N^j is the number of source atoms.
  As an example, ^{130}Te atoms in the CUORE TeO_2 crystals undergoing $2\nu\beta\beta$ decay are considered. The number of ^{130}Te source atoms, $N^j = N^{130}$, is:

$$N^{130} = \frac{M^{TeO_2}}{m.m.^{TeO_2}} \cdot N_{AV} \cdot IA^{130} \tag{5.36}$$

  where M^{TeO_2} is the total mass of the detectors, $m.m.^{TeO_2}$ is the molar mass of the TeO_2 compound, IA^{130} is the isotopic abundance of ^{130}Te in natural Te.
  The exposure is defined as:

$$Exp[kg \cdot yr] = M^{TeO_2} \cdot T_{live}$$

In this case, utilizing the fit normalization factor $N_{2\nu\beta\beta,^{130}Te}$, the half-life of the process of interest can be calculated as:

$$T_{1/2}^{2\nu\beta\beta}[yr] = \frac{ln(2) \cdot Exp \cdot \epsilon \cdot IA^{130} \cdot N_{AV}}{m.m.^{TeO_2} \cdot N_{chain}^{MC} \cdot N_{2\nu\beta\beta,^{130}Te}} \tag{5.37}$$

The preliminary results of the bayesian analysis of the CUORE data for the background model reconstruction are reported in Chap.6.2.

Chapter 6

First results from CUORE

The CUORE first science runs were carried out by mid-2017. Two physics datasets where acquired (DS3018, DS3021). Each of them was bracketed by an initial and a final calibration run and had an approximate duration of four to six weeks.
The performance of the CUORE detector during the first science runs was excellent in terms of temperature stability, noise reduction and channels livetime.
Only 4 channels over 988 were non-operational. A stable average trigger rate per bolometer of $\sim$50 mHz was observed in calibrations and $\sim$6 mHz during science runs. During the analysis [1], a fraction of the channels had to be removed for different reasons: some of the channels where too noisy, others failed during one or more analysis steps, others did not collect a sufficient number events during the calibration and so on. In the end, after removing these problematic channels, the analysis was performed on 876 channels for dataset DS3018 and on 935 channels for dataset DS3021. Accordingly the contribution from these channels was also removed from the exposure computation, yielding an exposure of TeO_2 of 37.6 kg·yr for dataset DS3018 and of 48.7 kg·yr for dataset DS3021. The total collected $0\nu\beta\beta$ exposure was then 86.3 kg($^{nat}TeO_2$) · yr, or 24.0 kg(^{130}Te) · yr, more than twice the exposure of CUORE-0.

Priority was first given to the search of $0\nu\beta\beta$ decay of TeO_2 [11], [34]. Afterwards the analysis of the $2\nu\beta\beta$ spectrum and the background model reconstruction was performed. The first CUORE $0\nu\beta\beta$ results are summarized in section 6.1; in section 6.2, the preliminary $2\nu\beta\beta$ and background model analysis will be reported.

6.1 $0\nu\beta\beta$ decay half-life limit

The main goal of the CUORE experiment is to investigate the $0\nu\beta\beta$ decay of ^{130}Te. In this section, the analysis of the first two CUORE physics datasets in order to perform the search of $0\nu\beta\beta$ decay of ^{130}Te will be described.

The physics energy spectra, in which to look for a possible $0\nu\beta\beta$ signal, were obtained after applying basic quality cuts, PSA and anti-coincidence (Multiplicity = 1) selections. The efficiencies for the selection cuts were evaluated and averaged over all channels for each dataset. The $0\nu\beta\beta$ containment efficiency was taken into account by Monte Carlo simulations of the $0\nu\beta\beta$ process in all the CUORE detectors and by evaluating the number of events contained in single crystals (Multiplicity 1). See Table 6.1.
Science data were blinded until all the selections and fit procedures had been fixed. The details of the data production and selection steps can be found in Chap.5.

[1] See Chapter 5 for details of the analysis of the CUORE data

	DS3018	DS3021
$0\nu\beta\beta$ containment	(88.345 ±0.085)%	(88.345 ±0.085)%
Detection	(99.7663 ±0.0034)%	(99.7349 ±0.0035)%
Energy reconstruction	(99.1677 ±0.0064)%	(99.218 ±0.006)%
Pileup rejection	(95.62884 ±0.0088)%	(96.6907 ±0.0084)%
PSA	(91.1±3.6)%	(98.2 ±3.0)%
Multiplicity	(99.4 ±0.5)%	(100.0 ±0.4)%
All cuts except containment	(85.67 ±3.42)%	(93.96 ±2.89)%

TABLE 6.1: Cut efficiencies as function of the dataset.

The energy resolution of each detector near $Q_{\beta\beta}$ was evaluated by considering the detector response to the 2615 keV ^{208}Tl γ line [123]. The detector response model built for each detector is the sum of five components:

- Tl PhotoPeak. As already observed in CUORE-0, the Tl photo-electric peak line shape is slightly non-Gaussian. It is modeled empirically with a primary Gaussian component centered at 2615 keV and two additional Gaussian components, one on the right and one on the left of the main peak.
- Compton continuum. The Compton edge due to scattering γs from the ^{208}Tl decay line is added to the model.
- X-Ray escape peak. In case of Te X-Ray emission following an incident 2615 keV, the Te X-Ray emission lines have energies ranging from 27 to 31 keV and, when escaping the crystal volume, the effect is a peak at about 30 keV below the 2615 keV PhotoPeak, composed by multiple adjacent X-Ray escape lines.
- Coincident Peak. In case of a coincident absorption of 2615 keV and 583 keV γs from ^{208}Tl decay, followed by pair production and subsequent escape of a 511 keV annihilation γ, a peak at energy $\sim$ [(2615+583)-511] = 2687 keV will be expected.
- Linear background. A first order polynomial is added to the model in order to take into account for coincident events with a small contribution from degraded alphas.

The line shape parameters for each bolometer are estimated with a simultaneous unbinned extended maximum likelihood (UEML) fit on a tower basis. The Tl peak line shape observed in calibrations is shown in Fig.6.1.
For Dataset 3018, the evaluated Tl peak resolution in calibration was 9.0 keV FWHM. After the optimization phase carried out during July 2017, the energy resolution observed in Dataset 3021 was improved to 7.4 keV FWHM. The cumulative average resolution at 2615 keV, exposure weighted, is 8.0 keV FWHM, in calibration runs.

The science runs were characterized by slightly better performance than the calibrations. Resolutions of (8.3 $\pm$ 0.4) and (7.4 $\pm$ 0.7) keV FWHM at the Tl peak, were observed in Dataset 3018 and 3021 respectively. A scaling factor was therefore applied to the energy resolution evaluated in calibration runs to get the correct energy resolution at $Q_{\beta\beta}$ in science runs. The exposure weighted average energy resolution at $Q_{\beta\beta}$ in the science runs is (7.7 $\pm$ 0.5) keV FWHM.
Several prominent background peaks in the physics data, with known energies between 800 and 2615 keV, are fitted with the line shape model in order to obtain an

estimate of their energy resolution for each bolometer-dataset; the resolution scaling with energy is then parametrized by a quadratic function (see Fig.6.2[left]). Moreover at each energy the fit of the peaks includes a dataset-dependent energy offset variable to parametrize energy mis-reconstruction. The energy bias corresponds to the best-fit peak position residual relative to the true energy; the residuals evaluated for the 6 peaks are fitted as a function of energy with a second order polynomial (see Fig.6.2[right]).

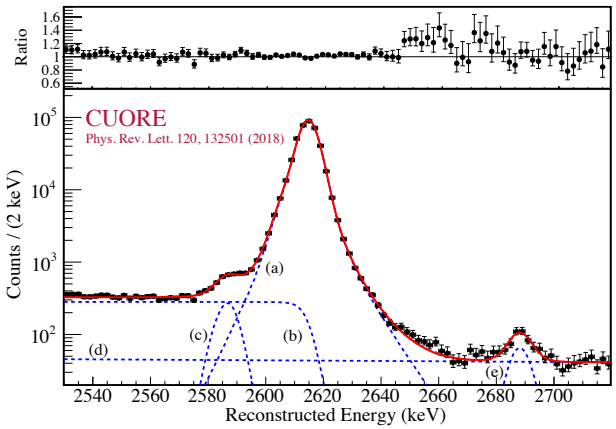

FIGURE 6.1: Cumulative result from the 19 tower-dependent fit of the Tl peak used to estimate the line shape parameters of each bolometer-dataset in calibration data. The components of best-fit model are shown by the blue dashed lines: (a) the multi-Gaussian photopeak that describes the detector response function, (b) a multiscatter-Compton contribution, (c) multiple peaks due to 27-31 keV Te X-ray escape following an incident 2615 keV γ ray, (d) a linear continuum background due to coincident events, and (e) a line due to coincident absorption of 2615 keV and 583 keV rays from the ^{208}Tl decay followed by escape of a 511 keV annihilation γ from pair production.[34]

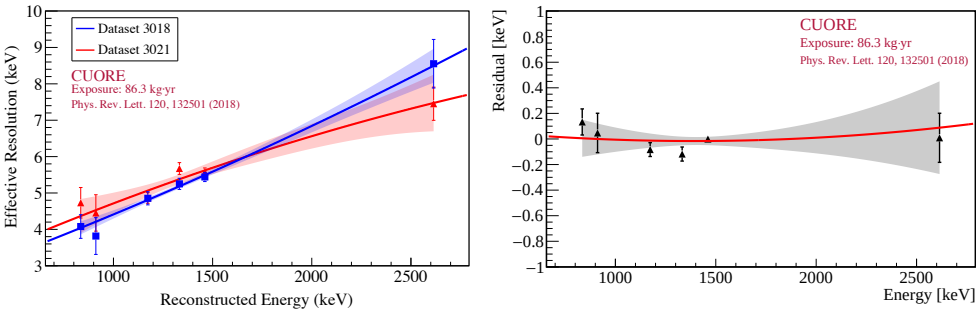

FIGURE 6.2: Resolution scaling and energy bias. [Left] Effective energy resolution of the physics lines in datasets DS3018 and DS3021. [Right] Spectral lines peak residuals relative to their true energy as a function of energy to evaluate the calibration bias in physics data. The shift at $Q_{\beta\beta}$ is (0.07 ± 0.32) keV.

A UEML fit was performed in the region of interest around $Q_{\beta\beta}$ (2465 - 2575 keV) to evaluate the TeO_2 decay rate (Fig.6.3). The fit model consists in a flat background (dataset-dependent), a sum peak for ^{60}Co coincident γ rays (1173 and 1332 keV) and a posited peak at $Q_{\beta\beta}$ (2527.515 keV)[2]. Each peak is modeled using the line shape model obtained for each channel-dataset from the detector response fit on the ^{208}Tl line on calibration data. The $0\nu\beta\beta$ decay rate, $\Gamma_{0\nu}$, is constrained to be the same for all the detectors and it was let vary freely in the fit. The position of the $0\nu\beta\beta$ peak was fixed to the reconstructed $Q_{\beta\beta}$ energy.

The best fit signal decay rate $\Gamma_{0\nu}$ is $(-1.0^{+0.4}_{-0.3}(stat.) \pm 0.1(syst.)) \times 10^{-25} yr^{-1}$. The background index in the ROI averaged over both datasets was obtained after removing the $0\nu\beta\beta$ component from the model:

$$b = (0.014 \pm 0.002)\ counts/(keV \cdot kg \cdot yr)$$

The negative value of the best fit for $\Gamma_{0\nu}$ leads to the conclusion that there is no evidence for $0\nu\beta\beta$ decay. In order to set a 90% confidence Bayesian limit on the rate of the $0\nu\beta\beta$ process, the marginalized likelihood is approximated with the profile likelihood and a flat prior for $\Gamma_{0\nu} \geq 0$ is utilized for constructing the posterior pdf for $\Gamma_{0\nu}$. An upper limit on the rate $\Gamma_{0\nu} < 0.50 \times 10^{-25}\ yr^{-1}$ (90% C.L) was then extracted by integrating the profile negative-log-likelihood (NLL) for $\Gamma_{0\nu} \geq 0$. This corresponded to a lower limit of $T^{0\nu}_{1/2}(^{130}Te) > 1.4 \times 10^{25}$ yr (90% C.L) on the half-life $T^{0\nu}_{1/2}$. The systematic uncertainties were estimated by performing a large number of pseudo-experiments with zero and non-zero signals assuming different detector line shape models and background shapes, varying the energy resolution scaling parameters within their uncertainty, and shifting the position of $Q_{\beta\beta}$ by 0.5 keV to account for the energy reconstruction uncertainty. Including the systematic uncertainties, the 90% lower limit on the half-life is $T^{0\nu}_{1/2}(^{130}Te) > 1.3 \times 10^{25}$ yr (90% C.L including syst.). A frequentist analysis, using the Rolke method [124] yields $T^{0\nu}_{1/2} > 2.1 \times 10^{25}$ yr (90% C.L) with a median 90% C.L. lower limit sensitivity for $T^{0\nu}_{1/2}$ of 7.6×10^{24} yr.

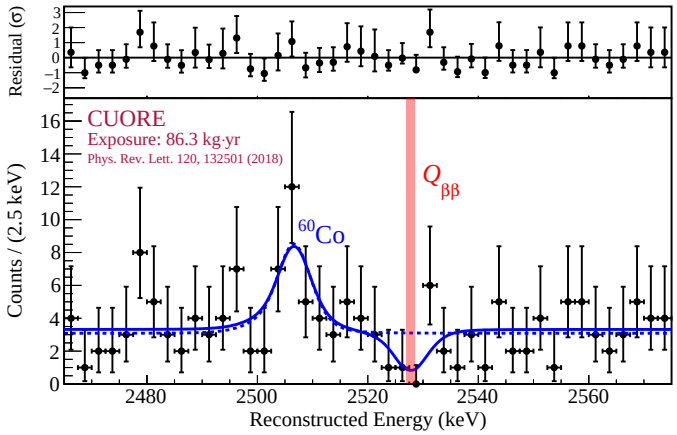

FIGURE 6.3: Spectrum of $0\nu\beta\beta$ decay candidates observed in CUORE and best-fit model result (solid line) overlaid. [34]

The CUORE result (24.0 kg · yr ^{130}Te exposure) is combined with the CUORE-0 (9.8 kg · yr ^{130}Te exposure) [107], [125] and Cuoricino (19.75 kg · yr ^{130}Te exposure)

[2]The position of the $Q_{\beta\beta}$ posited peak is fixed at the Q-value of $0\nu\beta\beta$ process, given the assumption that the $0\nu\beta\beta$ decay peak (sum of the energy of two electrons) should not have a different quenching factor from the single γ lines used in calibration.

[82] results. The combined profile NLL curve for the decay rate $\Gamma_{0\nu}$ is shown in Fig.6.4. A new (bayesian) half-life limit for $0\nu\beta\beta$ decay in ^{130}Te is obtained:

$$T^{0\nu}_{1/2}(^{130}Te) > 1.5 \times 10^{25}\ yr \text{ (at 90\% C.L.)}$$

A combined limit of CUORE, CUORE-0 and Cuoricino, can be also obtained following the Rolke frequentist technique: $T^{0\nu}_{1/2} > 2.2 \times 10^{25}$ yr (90% C.L).

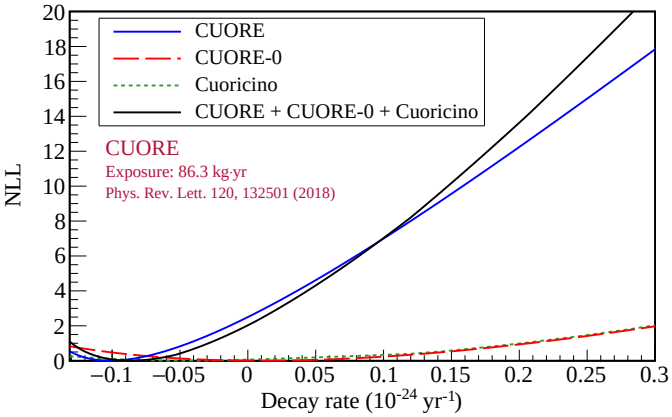

FIGURE 6.4: Profile negative-log-likelihood curves for CUORE, CUORE-0, Cuoricino, and their combination. [34]

The half-life limits can be used to extract a limit on the effective Majorana neutrino mass ($m_{\beta\beta}$) in $0\nu\beta\beta$ decay models mediated by a light Majorana neutrino exchange, via Eq.1.14. To this end the phase-space factor $G(Q_{\beta\beta}, Z)$ and the nuclear matrix elements $M_{0\nu\beta\beta}$, from a broad range of recent calculations , were used. The corresponding limit on the effective Majorana neutrino mass, for $T^{0\nu}_{1/2} > 1.5 \times 10^{25}$ yr, depending on the nuclear matrix element estimates utilized (Fig.1.9) is:

$$m_{\beta\beta} < 110 - 520 \text{ meV (at 90\% C.L)}$$

6.2 $2\nu\beta\beta$ half-life measurement and background model

Given the physics data acquired in 2017, the analysis to reconstruct the observed CUORE background and extract the ^{130}Te $2\nu\beta\beta$ half-life was also performed.

As anticipated in Chap.5.4.3, the physics data were splitted into four types of spectra: M1L0, M1L1, M2 and M2Sum. MC simulated spectra for the several sources compatible with the expected CUORE background, as described in Chap.5.4, were produced. These were fitted to the observed data simultaneously across the four spectra using the JAGS software. A set of 60 sources was sufficient to describe the CUORE physics spectra. Many contaminations were identified and located, others were still utilized by the fit but only a limit on their activity was obtained.

In general, the result of the fit shows an agreement within 1 σ between the model for the background sources and the data; indeed the model is able to reproduce nearly all the major features of the observed spectra, see Fig.6.5. Nevertheless a slight disagreement was found in the reconstruction of several α and γ peaks. For example, the ^{210}Po α peak at 5.4 MeV had its reconstructed intensity and position off by $\sim$ 3-4 σ in all the four spectra.

In the future, increasing the statistics, it would be possible to disentangle the origins of the contaminations leading to these backgrounds and this will improve the goodness of the fit also on the peaks reconstruction.

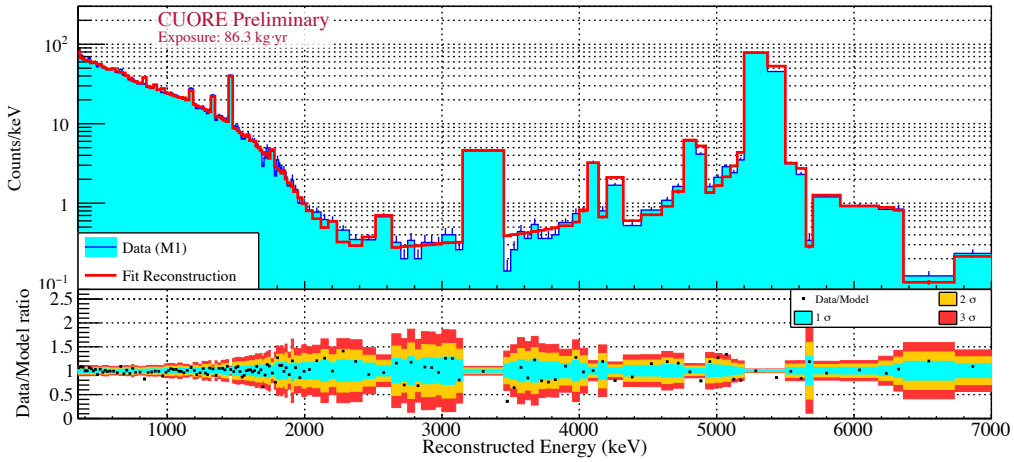

FIGURE 6.5: [Top] Measured M1L0 spectrum (cyan) and its reconstruction (red). The spectra are binned with an adaptive binning to contain peaks into a single bin, while also achieving good resolution of the continuum shape. [Bottom] Ratio of the data to the reconstructed model with 1 σ, 2 σ and 3 σ error bars. [11]

Despite the limited statistics, the systematic uncertainties were improved and a stable estimate of the $2\nu\beta\beta$ half-life was extracted. The $2\nu\beta\beta$ decay is the dominant component of the observed M1 spectrum between ~ 1 to ~ 2 MeV (see Fig.6.6), due to the increased ^{130}Te mass in CUORE and the reduced γ backgrounds. To prevent any bias while tuning the data quality cuts and the fitting procedure, the MC normalization constant for the $2\nu\beta\beta$ component was kept blinded; therefore the extracted half-life was expressed in terms of an unphysical ratio that could not be compared to previous results. After the fit procedure was finalized, the correct normalization[3] was unblinded and a measurement of the $2\nu\beta\beta$ half-life of ^{130}Te was obtained, utilizing Eq.5.37.

$$T^{2\nu}_{1/2}(^{130}Te) = [7.9 \pm 0.1\ (\text{stat})\ \pm 0.2\ (\text{syst})\ ] \times 10^{20}\ \text{yr}$$

The result is consistent with previous measurements of the same half-life [118], [126]. It represents the most precise measurement of the $2\nu\beta\beta$ half-life of ^{130}Te and one of the most precise measurements of a $2\nu\beta\beta$ decay half-life to date.

The only component of the reconstructed model which is strongly correlated with the $2\nu\beta\beta$ decay rate is the contamination level of ^{40}K in the TeO_2 crystal bulk (see Fig.6.6); the β^- decay of ^{40}K has an endpoint at 1310.9 keV and its spectrum becomes correlated with the broad $2\nu\beta\beta$ spectrum. This introduces only a small ($\sim$ 1 %) statistical uncertainty of the final $2\nu\beta\beta$ measured decay rate, given the CUORE large statistic and low γ background in the 1-2 MeV region.

For this result an improved evaluation of the signal acceptance efficiency was utilized. The efficiency of the pulse shape cuts was evaluated utilizing the M2 spectrum. Due to the very low event rate of CUORE in the physics runs, accidental M2

[3] The $2\nu\beta\beta$ decay normalization factor obtained with the fit of the physics data with the background model was: $f^{ref}_{2\nu\_std} = (1.862 \pm 0.016) \times 10^{-3}$

events are rare (< 1% [4]); the M2 spectrum constitutes a clean sample of events, at every energy. The statistics on single gamma lines in the M2 spectrum is increased compared to the M1 spectrum, which was used for calculating the PSA efficiency for the $0\nu\beta\beta$ result. This resulted in lowering the uncertainty on the PSA efficiency from $\sim$ 2.4 % to 0.2%.

The actual leading contribution to the systematic uncertainty on the measurement of $T^{2\nu}_{1/2}$ is related to the geometrical splitting of the data in subgroups. The different splittings of the data by geometry allow to probe the uncertainty caused by the present ignorance of the exact origin of localized contaminations.

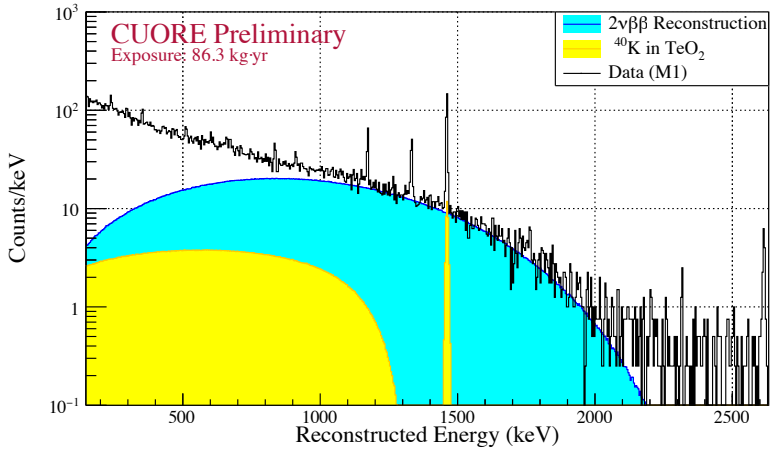

FIGURE 6.6: The observed M1L0 spectrum (black) with a reconstruction of the $2\nu\beta\beta$ component (cyan) of the background as well as the ^{40}K background (yellow). Note: The observed spectra has been converted back to the 1 keV binning and the $2\nu\beta\beta$ and ^{40}K to smooth continua for illustrative purposes. [11]

[4] A general estimate of the rate of accidental coincidences on the detector can be derived with probability laws. Given an event on channel i, the probability of another event happening on another detector within a time window Δt is:

$$P_{acc,i} = 1 - e^{-(N_{ch}-1)R_{ch}\Delta t}$$

where the exponential is the Poisson probability of no event happening within Δt, R_{ch} is the event rate on channel i and N_{ch} is the total number of channels. In case of CUORE, N_{ch} is the total number of channels used for the analysis, Δt is 10 ms (the coincidence window). R_{ch} is the (average) rate of events on the single channel, which is evaluated by considering the rate of 1461 keV ^{40}K decay in the physics spectrum, which is a single γ line. Considering all the other analysis factors, such as the effect of some event-based cuts and the energy threshold for the coincidence calculation, the probability of accidentals coincidences filling the M2 spectrum is < 1 % for the CUORE data.

Summary

The CUORE first physics results on $0\nu\beta\beta$ of ^{130}Te after $\sim$2 months of data taking in 2017 were released: $T^{0\nu}_{1/2}(^{130}Te) > 1.3 \times 10^{25}$ yr (90% C.L including systematics). An improved limit of $T^{0\nu}_{1/2}(^{130}Te) > 1.5 \times 10^{25}$ yr (90% C.L including systematics) has been obtained when combining the results of the precursor experiments Cuoricino and CUORE-0 [34]. The analysis of the same CUORE data for the background reconstruction, lead to a new precise measurement of the $2\nu\beta\beta$ decay half-life of ^{130}Te , $T^{2\nu}_{1/2}(^{130}Te) = [7.9 \pm 0.1\ (\text{stat}) \ \pm 0.2\ (\text{syst})\ ] \times 10^{20}$ yr [11] .
The CUORE first physics data were characterized by excellent performances of the cryostat and the detectors. Moreover important informations on the detectors performance, noise, resolutions and background levels have been collected. The background index is slightly higher than the CUORE background goal of 0.01 $counts/(keV \cdot kg \cdot yr)$, in part because all of the data quality cuts and software tuning at disposal were not implemented for this initial analysis. The energy resolution is also larger than the goal of 5 keV FWHM in the ROI. However, there is a ongoing work to continue to improve the energy resolution by developing better algorithms as well as by better understanding of the CUORE cryostat.

Chapter 7

The Lorentz violating two-neutrino double beta decay

7.1 Statistical analysis method

A global model that describes the CUORE background spectrum is obtained by fitting the simulated spectra of different contributions to the measured energy spectrum using a Bayesian fit with JAGS (see Chap.6.2). The possible presence of other sources contributing to the physics spectrum can be investigated by adding them in the background model fit.

In case of the search for a possible CPT violation signature in the $2\nu\beta\beta$ decay, the statistical method for the analysis consists in including the $2\nu\beta\beta$ decay CPT violating term in the background model fit. The CPT violating term in the $2\nu\beta\beta$ decay differs from the standard one, by having a spectral index[1] of order 4 instead of 5 in the differential decay rate, see Eq.1.25. More details about the model predicting the CPT violation and its effect on the $2\nu\beta\beta$ decay are in Chap.1.2.3.
The fit result of the $2\nu\beta\beta$ CPTV component will allow to set a limit for the $\dot{a}^{(3)}_{of}$ parameter, which quantifies the neutrino coupling with the SME countershaded operator which breaks CPT.
The $\dot{a}^{(3)}_{of}$ parameter can be obtained from the ratio of the $2\nu\beta\beta$ standard and CPTV rates, as it is described below.

The differential decay rates in Eqs.1.25 and 1.27 can be rewritten in terms of the sum of kinetic energies $K = (T_1 + T_2)/m_e$ for the two electrons, after a suitable change of integration variables [2].

$$\frac{d\Gamma_0}{dK} \approx \zeta'(K^5 + 10K^4 + 40K^3 + 60K^2 + 30K)(Q_{\beta\beta} - K)^5 \tag{7.1}$$

$$\frac{d\delta\Gamma}{dK} \approx \zeta'(K^5 + 10K^4 + 40K^3 + 60K^2 + 30K)10\dot{a}^{(3)}_{of}(Q_{\beta\beta} - K)^4 \tag{7.2}$$

$$\frac{d\Gamma}{dK} = \frac{d\Gamma_0}{dK} + \frac{d\delta\Gamma}{dK} \tag{7.3}$$

[1] We define as 'spectral index' the n^{th} power order of the $(Q_{\beta\beta} - T_1 - T_2)$ term in the differential rate of the $\beta\beta$ process of interest.

[2] All the energies are here expressed in units of electron mass: $K = (T_1 + T_2)/m_e$, $Q_{\beta\beta} = Q_{\beta\beta}/m_e$. The variables are expressed in natural units.

The total rates can then be expressed as integrals over all the electrons energies of the differential rates:

$$\Gamma^{mis}_{std} = \int_0^{Q_{\beta\beta}} \frac{d\Gamma_0}{dK} dK = \zeta' \Gamma_1 \tag{7.4}$$

$$\Gamma^{mis}_{CPTV} = \int_0^{Q_{\beta\beta}} \frac{d\delta\Gamma}{dK} dK = 10 \dot{a}^{(3)}_{of} \zeta' \Gamma_2 \tag{7.5}$$

$$\tag{7.6}$$

The values of Γ_1 and Γ_2 can be easily calculated for ^{130}Te [3]:

$$\Gamma_1 = \int_0^{Q_{\beta\beta}} (K^5 + 10K^4 + 40K^3 + 60K^2 + 30K)(Q_{\beta\beta} - K)^5 dK = 4.05 \times 10^5 \tag{7.7}$$

$$\Gamma_2 = \int_0^{Q_{\beta\beta}} (K^5 + 10K^4 + 40K^3 + 60K^2 + 30K)(Q_{\beta\beta} - K)^4 dK = 1.42 \times 10^5 \tag{7.8}$$

From the (adimensional) ratio of the decay rates, the $\dot{a}^{(3)}_{of}$ parameter can thus be obtained, considering the measured values of Γ^{std}_{CPTV} and Γ^{mis}_{CPTV}.

$$\frac{\Gamma^{mis}_{CPTV}}{\Gamma^{mis}_{std}} = \frac{10 \dot{a}^{(3)}_{of} \Gamma_2}{\Gamma_1} \tag{7.9}$$

The $\dot{a}^{(3)}_{of}$ parameter is then:

$$\dot{a}^{(3)}_{of} = \frac{\Gamma^{mis}_{CPTV}}{\Gamma^{mis}_{std}} \frac{\Gamma_1}{10\Gamma_2} [eV/m_e] \tag{7.10}$$

The Bayesian fit of the physics data will provide two normalization factors[4] for the two double beta processes in ^{130}Te, $f_{2\nu\_std}$ ($2\nu\beta\beta$ standard) and $f_{2\nu\_CPTV}$ ($2\nu\beta\beta$ CPTV). The decay rates ($\Gamma = \frac{1}{\tau} = \frac{ln(2)}{T_{1/2}}$) will be proportional to these values. From Eqs. 5.32, 5.33 and 5.35:

$$\Gamma^{mis}_{std} = \frac{N_{decays,2\nu\_std}}{N^{130} T_{live}} = \frac{f_{2\nu\_std}\, N^{MC}_{chain,2\nu\_std}}{N^{130} T_{live} \epsilon} \tag{7.11}$$

$$\Gamma^{mis}_{CPTV} = \frac{N_{decays,2\nu\_CPTV}}{N^{130} T_{live}} = \frac{f_{2\nu\_CPTV}\, N^{MC}_{chain,2\nu\_CPTV}}{N^{130} T_{live} \epsilon} \tag{7.12}$$

$$\tag{7.13}$$

where $N_{decays,2\nu\_j} = \frac{f_{2\nu\_j} \times N^{MC}_{chain,2\nu\_j}}{\epsilon}$ (with $j = std, CPTV$) is the number of decays (chains) of ^{130}Te observed in the data for both the $2\nu\beta\beta$ channels. N^{130} is the number of ^{130}Te source atoms (see Eq.5.36).
In case the decay rates for the standard and the CPTV $2\nu\beta\beta$ terms are obtained from

[3] Here Γ_1 and Γ_2 have been calculated with a non-relativistic approximation which reduces the computational time for the integrals calculation. Despite the shape of the energy spectrum is a bit different for the relativistic and the non-relativistic cases, the difference between the integrals should be negligible considering the statistical uncertainties.

[4] The normalization factor for a given source or process corresponds to the ratio between the number of events in the physics and in the MC spectra, which are associated to that process by the fit procedure. See Chap.5.4.3, for a detailed description of the Bayesian fit procedure and extraction of the normalization factors for all the sources.

the fit of the same set of data, with a given T_{live}, and considering to have produced the same number of MC chains for both the processes in the simulations ($N^{MC}_{chain,2\nu\_std}$ = $N^{CPTV}_{chain,2\nu\_std}$), the ratio of the rates in Eq.7.10 can be expressed in terms of a ratio of the normalization factors of the Bayesian fit:

$$\dot{a}^{(3)}_{of} = \frac{f_{2\nu\_CPTV}}{f_{2\nu\_std}} \frac{\Gamma_1}{10\Gamma_2} [eV/m_e] \tag{7.14}$$

7.2 CUORE MC simulations of the $2\nu\beta\beta$ CPTV component

The decay rate spectral distribution for the $2\nu\beta\beta$ CPT violating component was added to the CUORE Monte Carlo generator code (qshields) according to Eq.7.2.
After a proper validation of the new code section, a number of events corresponding to Monte Carlo samples for the ^{130}Te $2\nu\beta\beta$ CPT violating component were uniformly produced in the volume of the CUORE detectors.
The Monte Carlo sample of $2\nu\beta\beta$ CPT violating component was generated with the same statistics as the MC sample for the standard $2\nu\beta\beta$ generated and used for the CUORE background model analysis. In Fig.7.1, the two electron sum energy simulated spectra for $2\nu\beta\beta$ decay of ^{130}Te are compared. The CPT violating operator produces a distortion of the conventional electron sum spectrum; the energy at which the residual spectrum reaches its maximum, is slightly shifted at higher energies (from $\sim$ 850 keV to 1.05 MeV). The best chance to observe the effect is therefore at energies higher than that value, where the CPT violating component is dominant.

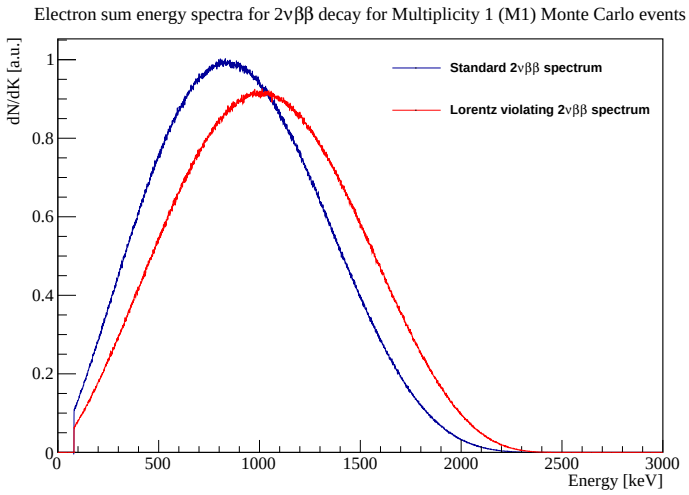

FIGURE 7.1: The electron sum spectra for $2\nu\beta\beta$ decay of ^{130}Te (Multiplicity 1 events): SM $2\nu\beta\beta$ process (blue line) and perturbation due to Lorentz-violating effects, LV (red line). Both spectra are obtained with MC simulations within the CUORE geometry.

7.3 Sensitivity study

A study of the CUORE sensitivity to the CPT violating component in the $2\nu\beta\beta$ decay of ^{130}Te was performed using a bayesian analysis based on a toy Monte Carlo (MC) approach.

7.3.1 Exclusion sensitivity: the method

The computation of the exclusion sensitivity can be summarized as follows:

- H_0: null hypothesis, including only the known physics processes needed to explain the experimental data. H_0 is implemented as the CUORE background model, which contains the 59 sources related to the contaminations (radioactive contaminations of the setup materials plus the environmental and cosmic contribution) and the $2\nu\beta\beta$ decay of ^{130}Te.
- H_1: alternative hypothesis, obtained by adding to H_0 the $2\nu\beta\beta$ CPT violating component.
- $\vec{\mathbf{E}}$: data (physics spectrum)
- Γ_{CPTV} is the parameter describing the CPTV decay rate for H_1 and from this value $\dot{a}^{(3)}_{of}$ can be obtained
- $\vec{\mathbf{\Theta}}$ are the nuisance parameters describing the background processes in H_0 and H_1

Given the Bayes theorem, the probability distribution for the parameter set [Γ_{CPTV},$\vec{\mathbf{\Theta}}$] is: P(Γ_{CPTV},$\vec{\mathbf{\Theta}}$ | $\vec{\mathbf{E}}$, H_1). This is proportional to the the conditional probability of finding the measured data given the model H_1 for a set of parameters [Γ_{CPTV},$\vec{\mathbf{\Theta}}$] (likelihood), times the prior probability for each of the considered parameters (see Eq.5.28). The prior probability has to be chosen according to the knowledge available before the analysis of the current data.
The posterior probability distribution for Γ_{CPTV}, P(Γ_{CPTV} | H_1,$\vec{\mathbf{E}}$) is obtained after marginalization, which means integrating P(Γ_{CPTV},$\vec{\mathbf{\Theta}}$ | $\vec{\mathbf{E}}$, H_1) over all nuisance parameters $\vec{\mathbf{\Theta}}$.

The exclusion sensitivity is obtained considering the 90% Credibility Interval (C.I.)[5] limit, which is the value of Γ_{CPTV} corresponding to the 90% quantile of the posterior Γ_{CPTV} distribution.

$$\Gamma_{CPTV}(90\%C.I.) \equiv \Gamma_{CPTV} \quad : \quad \int_0^{\Gamma_{CPTV}} P(\Gamma_{CPTV}|H_1, \vec{\mathbf{E}}) d\Gamma_{CPTV} = 0.9 \tag{7.15}$$

A 90% C.I. limit on Γ_{CPTV} (and thus on $\dot{a}^{(3)}_{of}$, from Eq.7.10) is interpreted as the value below which, given the current knowledge of the backgrounds, the true value of Γ_{CPTV} lies with 90% probability.

In order to compute the exclusion sensitivity, it is generated a toy-MC spectrum[6] according to the background-only hypothesis H_0, for a given exposure. The toy-MC

[5] In Bayesian statistics, a credibility interval is a range of values within which an unobserved parameter value falls with a particular probability. It is an interval in the domain of a posterior probability distribution. For a 90% credible interval, the value of interest (e.g. Γ_{CPTV}) lies with a 90% probability in the interval. The credible interval corresponds exactly to the confidence interval (built with the frequentist approach) if prior probability is 'uninformative'.

[6] The Toy-MC method is a useful tool for determination of statistical uncertainties for complex correlated observables and for sensitivity studies. The toy generation methods start from idealized detector and physics model or from some high-level input from the data. A large number of Monte Carlo samples resembling the geometry, the response and the distribution of sources in the detector are generated. Then the simulated data can be splitted into statistically independent sub-samples that can be treated as single Toy-MCs.

spectrum is then fitted with the background-plus-signal model H_1. The likelihood is marginalized over the nuisance parameters and the posterior for Γ_{CPTV} is obtained. The 90% C.I. limit on Γ_{CPTV} is extracted from the posterior and it is turned in an exclusion sensitivity on the parameter $\dot{a}_{of}^{(3)}$ for the given exposure utilized for producing the toy-MC.

In case N toy-MC are generated for each exposure, the distribution of the limits on Γ_{CPTV} can be built and the median sensitivity on Γ_{CPTV} is evaluated.

7.3.2 Toy-MC production and consistency checks

In order to produce the toy-MC according to the background-only hypothesis, the results of the JAGS fit of the CUORE 2017 physics data with the standard background model (see Chap.6.2) were utilized.

The posteriors of the normalization factors f_i for all the 60 background sources (i) obtained from the fit were collected; it is worth to underline that the normalization factors depend on the exposure of the physics spectra that the model was fit to. In case of the CUORE 2017 physics data, the exposure is 86.3 $kg \cdot yr$ of TeO_2 (corresponding to 24.0 $kg \cdot yr$ of ^{130}Te), corresponding to approximately 7 weeks of live-time[7]. These normalization factors will be referred as $f_{i,7weeks}$.

Only sources with converging and non compatible with zero posteriors were utilized to build the toy-MC for the background. The criterion utilized to select these sources was the mean of the normalization factor posterior to be higher than 2.5 sigmas of the same distribution: ($\overline{f}_{i,7weeks} > 2.5 \times \sigma_{f_{i,7weeks}}$). 36 sources were then selected for the toy-MC for the background.

From the MC simulations (g4cuore output) of each of the selected sources, a number of events equivalent to the number of events expected given the normalization factors for the 7 weeks live-time, had to be sorted to fill the energy spectrum of the toy-MC.
The events to be sorted in for the toy-MC had to satisfy the same selections utilized to build the simulated spectra for the JAGS fit of the data, $N_{MC,i}(sel)$.

$$N_{MC,i}(sel) = (N_{MC,i} \;\&\&\; Included \;\&\&\; E \geq E_{th} \;\&\&\; E \leq E_{max} \;\&\&\; (M1||M2)) \quad (7.16)$$

"Included" means that only MC events from detectors included in the physics analysis have to be considered. Moreover a threshold energy is set E_{th} = 350 keV and a maximum energy of the spectrum that is used for the fit is set E_{max} = 7 MeV. Among these basic selections, also the multiplicity of each event has to be considered; only M1 (considering the splitting in the two layers) and M2 events have to be selected for being used for the toy-MC. Given a source i and an event which passed the previous selections, a random number rnd sorted uniformly in [0,1] interval is generated. If this value is lower than the normalization factor of the given source ($rnd < f_{i,7weeks}$,

[7] In order to evaluate correctly the live-time for the CUORE 2017 data utilized for the described analyses, the quoted exposure has to be divided by dataset and the different number of channels utilized for each dataset has to be considered. For DS3018, 876 channels were used for the analysis and an exposure of 37.6 $kg \cdot yr$ of TeO_2 was acquired; for DS3021 the data from 935 channels were used for the physics analyses, with a collected exposure of 48.7 $kg \cdot yr$ of TeO_2. The total mass of TeO_2 of the CUORE detector $M_{tot}^{TeO_2}$, corresponding to the 988 bolometers installed, is $\sim$ 742 kg. The total live-time corresponding to the data from the two datasets can be calculated as follows:

$$T_{live}[yr]\Big|_{2017} = \frac{1}{742}\left(\frac{48.7}{935/988} + \frac{37.6}{876/988}\right)$$

The total live-time for the CUORE 2017 data release is then $T_{live,2017} \simeq 6.6$ weeks.

where $f_{i,7weeks}$ is the mean of the posterior), the event is taken to fill the toy-MC spectra, otherwise it is rejected. This was done for all the sources. In the end the toy-MC with the 7 weeks equivalent statistics was produced by adding the selected and sorted events from the MC simulations of the background sources. If the seed of the random generator is kept different, N independent toy-MC for each source with 7 weeks statistics can be produced. Given the random sorting of the events for filling the toy-MC, the statistics of the M1L0, M1L1, M2 and M2Sum spectra will be already fluctuating. In Figs.7.2 and 7.3, the energy spectra at different multiplicities of one toy-MC corresponding to 7 weeks live-time are overlapped to the CUORE 2017 physics data, in order to show the match in statistics and shape which is obtained with the procedure described above for generating the toy-MC samples.

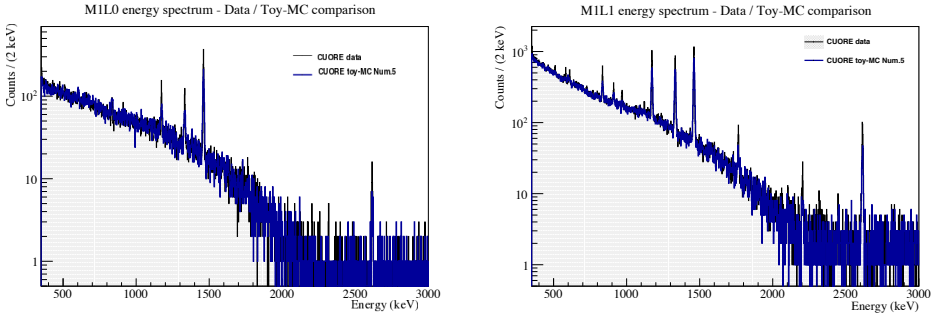

FIGURE 7.2: Comparison of M1L0 [left] and M1L1 [right] energy spectra for CUORE 2017 live-time ($T_{live,2017}$): the blue one is one Toy-MC, produced with the procedure described above, and the black one (filled in shaded grey) are the CUORE physics data.

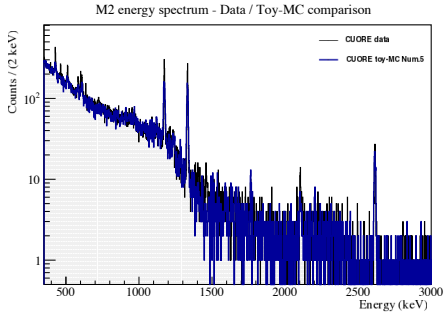

FIGURE 7.3: Comparison of M2 energy spectra for CUORE 2017 live-time ($T_{live,2017}$): the blue one is one Toy-MC, produced with the procedure described above, and the black one (filled in shaded grey) are the CUORE physics data.

This procedure of producing the toy-MC was verified by comparing the energy spectra (M1L0, M1L1, M2 and M2Sum) produced using the toy-MC entries and the scaled spectra obtained summing all the spectra produced using all the statistics of the MC g4cuore simulations and re-weighting the energy bins by the normalization factors for each source. A good agreement was found between the toy-MC spectra and the re-scaled spectra, both in terms of shape and statistics, see Figs.7.4 and 7.5.

A consistency check that was performed to test the goodness of the described procedure in producing a toy-MC resembling the physics data, was to fit the toy-MC with the background only model (H_0) and uniform priors for all the components, in order to check if the obtained values of the normalization factors for converging and

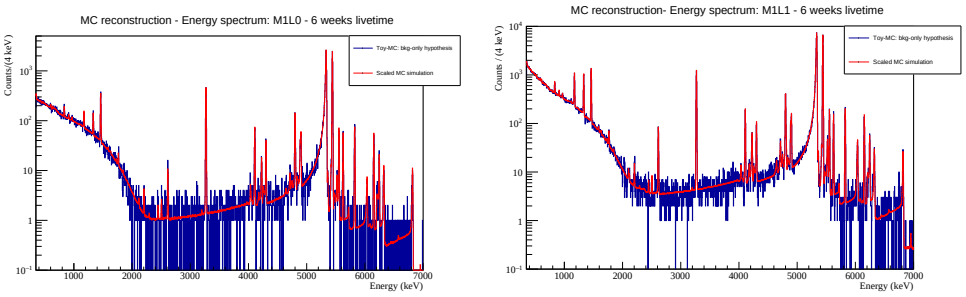

FIGURE 7.4: Comparison of M1L0 [left] and M1L1 [right] energy spectra of 7 weeks of live-time: the blue one is one Toy-MC, produced with the procedure described above, and the red one is the scaled histogram, produced utilizing all the CUORE MC simulated events and re-weighting the spectra od each source by the normalization factor. There is a good agreement in the shape and the statistics of the two spectra. Integrals in [350 keV, 7 MeV]: M1L0 - 6.57 x 10^4 (toy-MC), 6.58 x 10^4 (scaled); M1L1 - 2.30 x 10^5 (toy-MC), 2.31 x 10^5 (scaled).

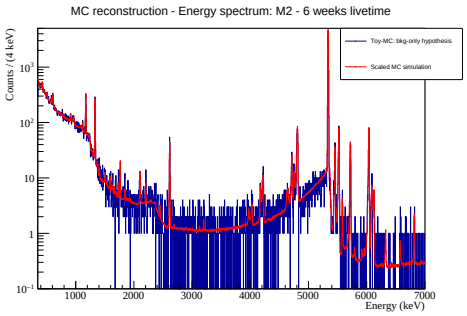

FIGURE 7.5: Comparison of M2 energy spectra of 7 weeks of live-time: the blue one is one Toy-MC, produced with the procedure described above, and the red one is the scaled histogram. Also for this multiplicity, there is a good agreement in the shape and the statistics of the two spectra. Integrals in [350 keV, 7 MeV]: M2 - 6.21 x 10^4 (toy-MC), 6.23 x 10^4 (scaled).

non-converging components were consistent with the reference ones (obtained from the fit of the CUORE data with H_0 hypothesis).
As a most significant example, the $2\nu\beta\beta$ decay normalization factor obtained with the fit of the toy-MC with the background model (H_0) is: $f_{2\nu\_std}$ = (1.805 $\pm$ 0.015) $\times$ 10^{-3}, which is consistent within 3 σ with the reference value for the $2\nu\beta\beta$ decay normalization factor obtained with the fit of the experimental data. Moreover all the normalization factors were consistent within 3 σ with the values obtained from the fit of the data.

The procedure described above allows to produce toy-MC with a statistics equivalent to the one acquired with the CUORE 2017 exposure. In order to produce toy-MC with statistics corresponding to different live-times, the normalization factors used to sample the MC simulations from, had to be re-calculated. The normalization factors were re-weighted:

$$f_{i,Nweeks} = f_{i,7weeks} \times (\frac{Nweeks}{7weeks})$$

where with *7weeks* we mean the CUORE 2017 livetime ($T_{live,2017}$). The new values of the normalization factors $f_{i,Nweeks}$ were utilized as the new probability for sorting events from the MC simulations to create the toy-MC at *Nweeks* exposure. An example of the toy-MC simulated energy spectra for Multiplicity 1 events in layer 0 (M1L0), at several increasing live-times is reported in Fig.7.6.

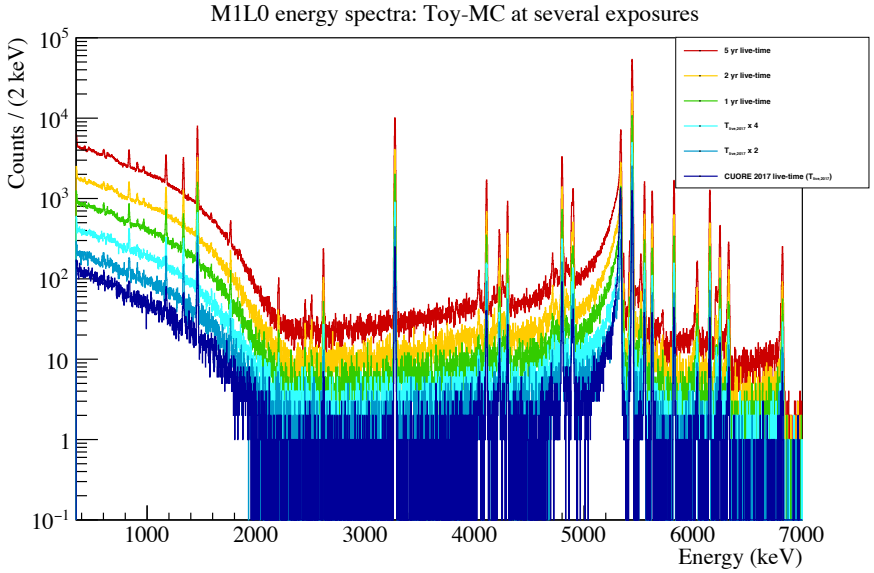

FIGURE 7.6: Comparison of M1L0 toy-MC energy spectra simulated for several increasing exposures: from few weeks to 5 yrs live-time.

7.4 Analysis and results

In order to perform the sensitivity study and, possibly, the assessment of a limit on the CPTV violating component in the $2\nu\beta\beta$ spectrum of ^{130}Te, it is necessary to fix the model and the inputs for the bayesian fit. As for the model, the H_1 hypothesis is utilized, so providing as inputs to the fitter the MC simulation of the $2\nu\beta\beta$ CPTV component and all the other simulations for the sources utilized for the background model (H_0) fit. Same geometry cuts (multiplicities and layers), as it was done in the fit with H_0, are applied both on data and toy-MC, to create several energy spectra to be fitted simultaneously.
Moreover, in case of the bayesian fit with JAGS, the choice of the priors for the several sources can result to be crucial. We identified a subset of the CUORE data, a "blinded sample", on which to test and tune the JAGS fit with the H_1 hypothesis. After having fixed the model, the selections on the spectra and the priors, the sensitivity study on the toy-MC samples and a preliminary fit with H_1 hypothesis on the whole CUORE data sample were performed.

7.4.1 Blinding the data and fixing the priors

The presently most stringent limit on the possible CPTV component from double-beta decay experiments comes from GERDA: $\dot{a}^{(3)}_{of} < 7.5 \times 10^{-8}$ GeV (90% C.I.) [55]. This corresponds to an expected ratio between the $2\nu\beta\beta$ CPTV component and the

standard one (from Eq.7.14):

$$\frac{f_{2\nu\_CPTV}}{f_{2\nu\_std}} < 5 \times 10^{-4} \tag{7.17}$$

The expected ratio between the CPTV and the standard $2\nu\beta\beta$ components is therefore less than 0.1 %.

In order to test the bayesian fit with the $2\nu\beta\beta$ CPTV component added to the standard CUORE background model, a subset of the CUORE available data (from the 2017 data release) was utilized. We define this procedure as "*blinding*".
It was decided to use 10% of the available statistics, corresponding to $\sim 8.6\ kg \cdot yr$ of TeO_2. The events of the CUORE physics data were sorted randomly and kept with 10% probability. An example of the comparison of the CUORE physics spectra with the total statistics and the reduced statistics, is reported in Fig.7.7.

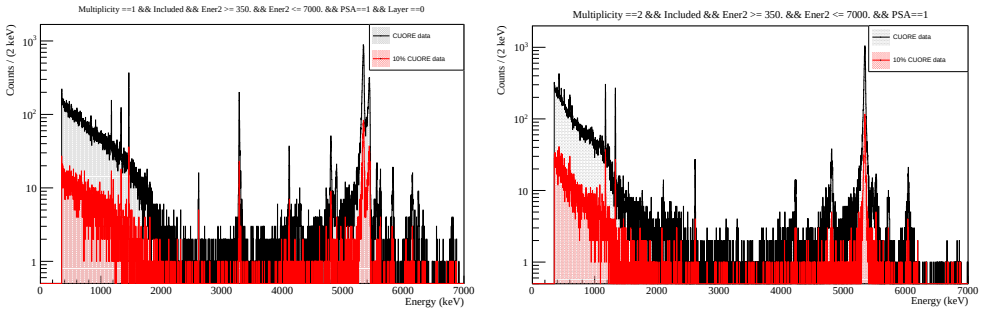

FIGURE 7.7: Comparison of the CUORE physics spectra with the total statistics and the reduced statistics. [Left] M1L0 energy spectra. [Right] M2 energy spectra.

This reduced set of data was fit with the H_1 hypothesis (background model + $2\nu\beta\beta$ CPTV component), utilizing the JAGS bayesian analysis tool. As for the background model analysis (discussed in Chap.6.2), it was performed a simultaneous fit of the M1-L0, M1-L1, M2 and M2sum spectra. Two approaches of the fit were tested:

- *Uniform (non-informative) priors* for all the sources.
  As it was done for the background model fit (H_0), uniform non-informative priors were provided to the fit with H_1 model for all the sources.
  The results for the normalization factors of the $2\nu\beta\beta$ standard and CPTV components are reported:

$$f_{2\nu\_std,10\%} = (1.76 \pm 0.12) \times 10^{-4}$$

$$f_{2\nu\_CPTV,10\%} < 2.47 \times 10^{-5}\ (90\% C.I.)$$

  The ratio between the two normalization factors is:

$$\frac{f_{2\nu\_CPTV,10\%}}{f_{2\nu\_std,10\%}} \approx 1.5 \times 10^{-1}$$

  The uncertainty on the normalization parameters with converging posteriors here is mainly driven by the statistical fluctuations ($\delta N \sim \frac{1}{\sqrt{N}}$), which are higher due to the low statistics.
  The standard $2\nu\beta\beta$ converges, although the shape of the posterior is not perfectly gaussian since it has a truncated tail on the right (Fig.7.8 [left]). The

uncertainty on the $f_{2\nu\_std,10\%}$ evaluation is of the order of $\sim$ 6 %. If the standard $2\nu\beta\beta$ normalization factor is scaled to the total exposure, ($f_{2\nu\_std,10\%} \times 10$) $\sim 1.76 \times 10^{-3}$, this is smaller but consistent within the percentage statistical uncertainty (of the "blinded" sample) with the value obtained with the background model (H_0) of all the CUORE data sample.
The $2\nu\beta\beta$ CPTV component does not converge at a finite value; its posterior has a non-zero mode, but is consistent with zero (Fig.7.8 [center]). Moreover the posteriors of $2\nu\beta\beta$ standard and CPTV components are strongly anti-correlated (Fig.7.8 [right]). This is not surprising since the two contributions have a significant overlap. Their relative contribution is therefore fixed by the constraints coming from the nearby regions. In particular, if the CPTV contribution helps in improving the fit in some of these regions (e.g. 2.0 - 2.5 MeV) we can expect a finite result for the CPTV component and an increased spread of the standard $2\nu\beta\beta$ posterior and a worse convergency.
Given the low statistics of the "blinded" sample used for this test, it is reasonable to expect that using uniform priors for the fit with H_1 hypothesis, makes the CPTV component still not converge to a finite value. However when more statistics will be added, the strong anti-correlation between the two components might lead to a convergence of the standard $2\nu\beta\beta$ posterior to a smaller value than expected from the background model (and maybe not even consistent with that), while favoring the $2\nu\beta\beta$ CPTV component in the fit.

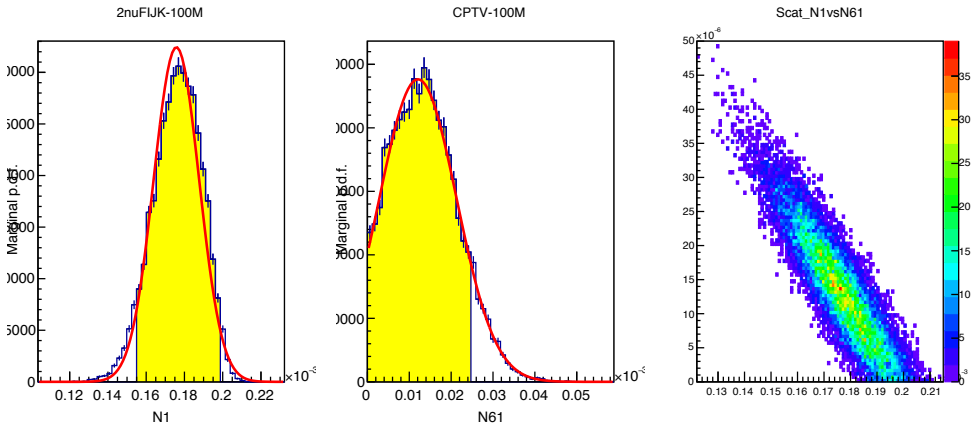

FIGURE 7.8: Posteriors of the $2\nu\beta\beta$ standard and CPTV normalization factors obtained from the fit of the CUORE "blinded" sample (10% of CUORE data), using uniform priors. [Left] Posterior $N1 = f_{2\nu\_std}$. [Middle] Posterior $N61 = f_{2\nu\_CPTV}$ [Right] Correlation plot of the posteriors for $f_{2\nu\_std}$ and $f_{2\nu\_CPTV}$.

- *Priors obtained from re-scaling the posteriors of the H_0 fit of the CUORE data* for all the sources.
  In order to test if non-uniform priors can help the fit convergence without adding a significant bias, a test in which the posteriors of the H_0 fit for the nuisance parameters were used as priors for the H_1 fit (for the same parameters) was carried out. This approach holds within the approximation that the CPTV component in the H_1 hypothesis is not strongly correlated with all the other background components for which the prior is set.
  It was used a gaussian prior for sources with convergent posteriors (from the standard background model fit, H_0) and exponential priors for non-converging ones. Moreover since the H_0 fit was performed over the whole CUORE data

sample (7 weeks), the posteriors had to be rescaled to the correct exposure given the fact that the new fit was performed only on 10% of the data:

- If the source j has a convergent posterior over the 7 weeks: Gauss($f_{j,7weeks}$,$\sigma_{f_{j,7weeks}}$) $\longrightarrow$ Gaussian prior for source j on 10% data sample: Gauss($f_{j,10\%}$,$\sigma_{f_{j,10\%}}$) where $f_{j,10\%} = \frac{f_{j,7weeks}}{10}$ and $\sigma_{f_{j,10\%}} = \sigma_{f_{j,7weeks}}$.
- If the source j has a non-convergent posterior over the 7 weeks: Exp($\lambda_{j,7weeks}$) $\longrightarrow$ Exponential prior for source j on 10% data sample: Exp($\lambda_{j,10\%}$) where $\lambda_{j,10\%} = \frac{\lambda_{j,7weeks}}{10}$

The results for the normalization factors of the $2\nu\beta\beta$ standard and CPTV components are reported:

$$f_{2\nu\_std,10\%,priors} = (1.79 \pm 0.12) \times 10^{-4}$$

$$f_{2\nu\_CPTV,10\%,priors} < 2.42 \times 10^{-5} \ (90\% C.I.)$$

The ratio between the two normalization factors is:

$$\frac{f_{2\nu\_CPTV,10\%,priors}}{f_{2\nu\_std,10\%,priors}} \approx 1.3 \times 10^{-1}$$

The standard $2\nu\beta\beta$ converges although not having a perfect gaussian shape (Fig.7.9 [left]); the mean normalization factor scaled to the total exposure is again smaller but consistent within the percentage statistical uncertainty (of the "blinded" sample) with the value obtained with the background model (H_0) of all the CUORE data sample.
The $2\nu\beta\beta$ CPTV component does not converge at a finite value (Fig.7.9 [center]); its posterior has a mode still compatible with zero although slightly lower than in the case of the fit with uniform priors.
Since the results are compatible and this method is expected to produce more stable results on higher statistics, we will use this method to evaluate the sensitivity and the limit on the full available statistics.

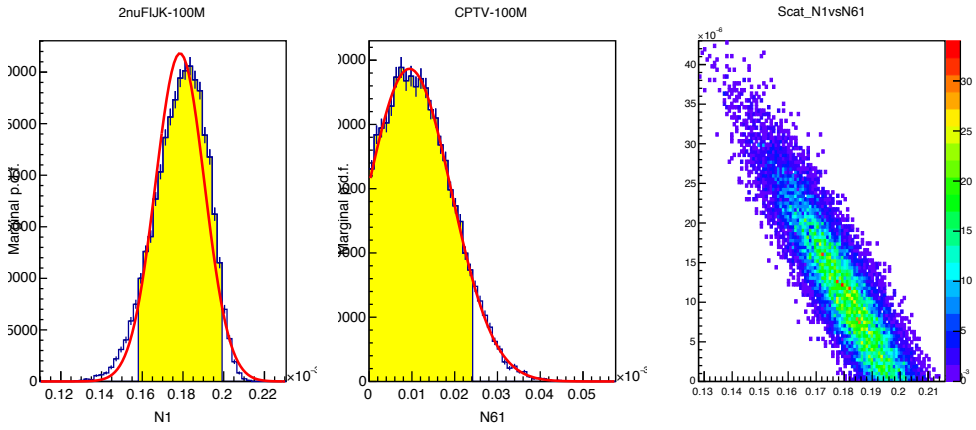

FIGURE 7.9: Posteriors of the $2\nu\beta\beta$ standard and CPTV normalization factors obtained from the fit of the CUORE "blinded" sample (10% of CUORE data), using informative priors. [Left] Posterior $N1 = f_{2\nu\_std}$. [Middle] Posterior $N61 = f_{2\nu\_CPTV}$ [Right] Correlation plot of the posteriors for $f_{2\nu\_std}$ and $f_{2\nu\_CPTV}$.

7.4.2 Sensitivity vs Livetime

As described above, the sensitivity is evaluated by fitting the toy-MC at several exposures with the H_1 model (background model + $2\nu\beta\beta$ CPTV component).
Given the conclusions from the test of the bayesian fit on the "blinded" sample, the priors for the normalization factors for all the sources provided to the the JAGS fitter were taken from the posteriors resulting from the fit with the background-only hypothesis (H_0) of the whole CUORE data sample, which were rescaled for the toy-MC exposure. For the $2\nu\beta\beta$ CPTV normalization factor, uniform non-informative priors were utilized.
Toy-MC at several exposures were produced, from few weeks to 5 years of livetime.
For each exposure, N = 300 toy-MC were produced and fitted with the procedure described above. The posteriors of the $2\nu\beta\beta$ CPTV component were analyzed and a 90% C.I. limit on the $f_{2\nu\_CPTV}$ normalization factor was extracted. From the distribution of the limits, the median value of the limit on $f_{2\nu\_CPTV}$ and the width of the distribution were calculated. The 90% C.I. limit on the $f_{2\nu\_CPTV}$ is converted into a limit of the $\dot{a}^{(3)}_{of}$ coefficient. It is therefore built the plot of the median $\dot{a}^{(3)}_{of}$ limits (at 90% C.I.) for increasing live-times, as shown in Fig.7.10. This plot gives the (exclusion) sensitivity of the CUORE experiment to the $2\nu\beta\beta$ CPTV component, given the present knowledge of the background.

7.4.3 Preliminary analysis of physics data

The CUORE physics data collected in 2017 (DS3018 and DS3021) were used for the bayesian fit, which included the background sources and the standard $2\nu\beta\beta$ decay of ^{130}Te, plus the $2\nu\beta\beta$ CPT violating component. It was performed a simultaneous fit of the M1-L0, M1-L1, M2 and M2sum spectra.
The analysis of the posteriors and the investigation of the correlation between the standard and the CPTV $2\nu\beta\beta$ normalization coefficients was performed.

In the JAGS bayesian fit, for the CPTV $2\nu\beta\beta$ source it was utilized an uniform non-informative prior. For the other background sources, the posteriors obtained from the fit with the H_0 model were used as priors.
The outcome of the fit is an evident anti-correlation of the posteriors of standard and CPTV $2\nu\beta\beta$ normalization factors, as reported in Fig.7.11 [right].
The normalization factor of the standard $2\nu\beta\beta$ is shifted to a value within 2 σ from the reference factor $f^{ref}_{2\nu\_std}$.

$$f_{2\nu\_std} = (1.935 \pm 0.036) \times 10^{-3}$$

The posterior for the CPTV component normalization factor shows a non-zero mode, but is consistent with zero at the 90% C.I. (see Fig.7.11 [left]), thus allowing to set a limit on $f_{2\nu\_CPTV}$. The calculated limit on $\dot{a}^{(3)}_{of}$ is:

$$f_{2\nu\_CPTV} < 6.49 \times 10^{-5} \quad (90\%\ \text{C.I.}) \quad \longrightarrow \quad \dot{a}^{(3)}_{of} < 4.88 \times 10^{-6}\ GeV \quad (90\%\ \text{C.I.})$$

The systematics haven't been calculated and folded yet.
The current limits on the $\dot{a}^{(3)}_{of}$ parameter obtained by CUORE, GERDA and EXO-200 are superimposed to the CUORE sensitivity plot, in Fig.7.10.
In Fig.7.12, the double beta fitted spectra for the CUORE 2017 datasets are reported:

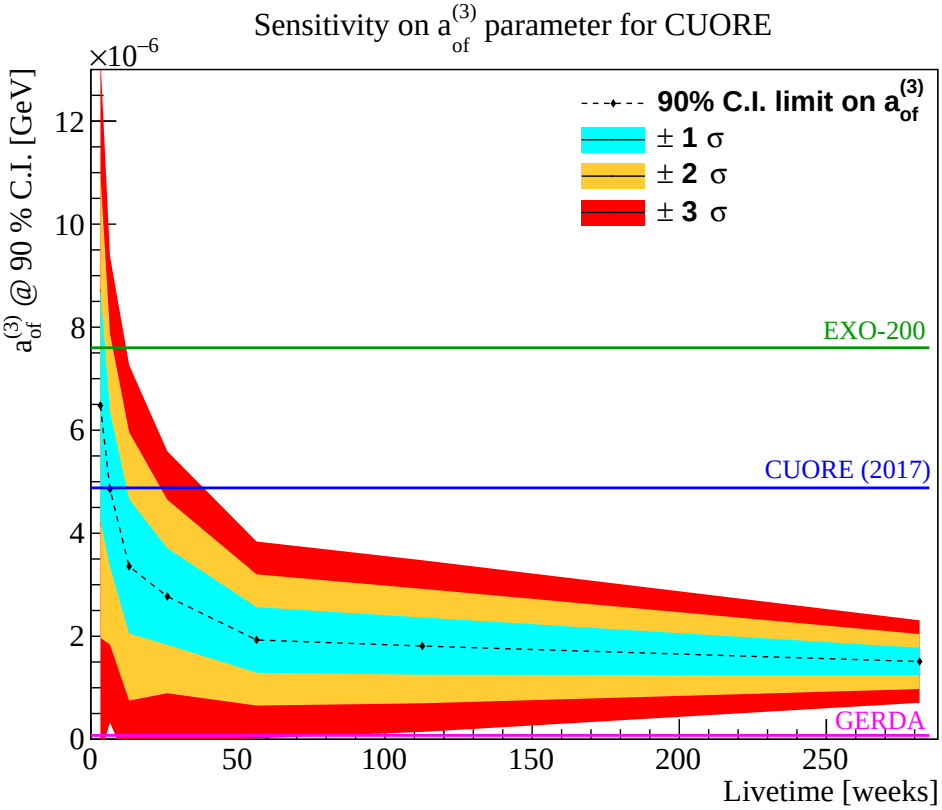

FIGURE 7.10: CUORE sensitivity plot on the $\dot{a}^{(3)}_{of}$ parameter for the CPTV $2\nu\beta\beta$ decay component, for several values of live-time, from few weeks to 5 years live-time. The green-line is the current limit on $\dot{a}^{(3)}_{of}$ set by EXO-200 [54], the magenta one is the limit from GERDA [55]. The blue-line is the preliminary result of the limit on $\dot{a}^{(3)}_{of}$ obtained from the analysis of the CUORE data collected in 2017.

the Standard Model double-beta decay mode and the Lorentz-violating mode spectrum corresponding to the upper limit of the $f_{2\nu\_CPTV}$ normalization factor obtained from the fit.

From a preliminary analysis of the results, it appeared the new fit partially utilizes the CPTV component to fill the region around 2-2.5 MeV which is not perfectly reconstructed in the standard background model.

The preliminary outcome of the fit enlightens the limits of the standard background model fit on the CUORE 2017 data[8]. Some low energy alpha backgrounds, appear to be mis-reconstructed; this can be due to a non-uniform distribution of the contamination know sources in the volume or to some other localized sources not yet introduced in the model. Given the low statistics of the DS3018+DS3021, 24.0 kg (^{130}Te), the uncertainties on the standard fit parameters for reconstructing the data (e.g. $\sigma_{f_{2\nu\_std}} / f_{2\nu\_std} \approx 2$ %) do not make possible to reach the fit precision needed to be sensitive to another exotic component in the physics spectrum, like the CPTV-related distortion in the $2\nu\beta\beta$ decay spectrum.

[8] See Sec.6.2 for details about the background model fit and results on the CUORE 2017 data.

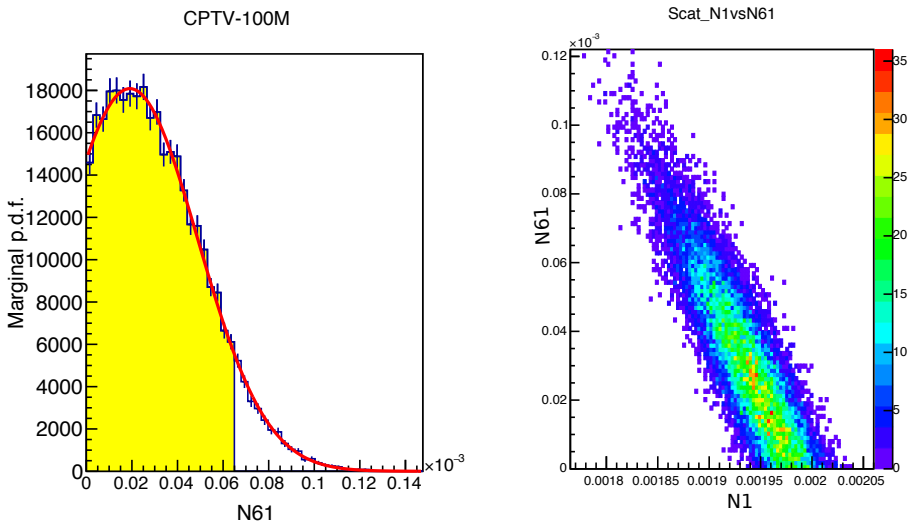

FIGURE 7.11: [Left] Posterior of the distribution of the normalization factor of the CPTV component (N61 = $f_{2\nu\_CPTV}$). [Right] Correlation of the standard and the CPTV $2\nu\beta\beta$ normalization factors (N1 = $f_{2\nu\_std}$, N61 = $f_{2\nu\_CPTV}$).

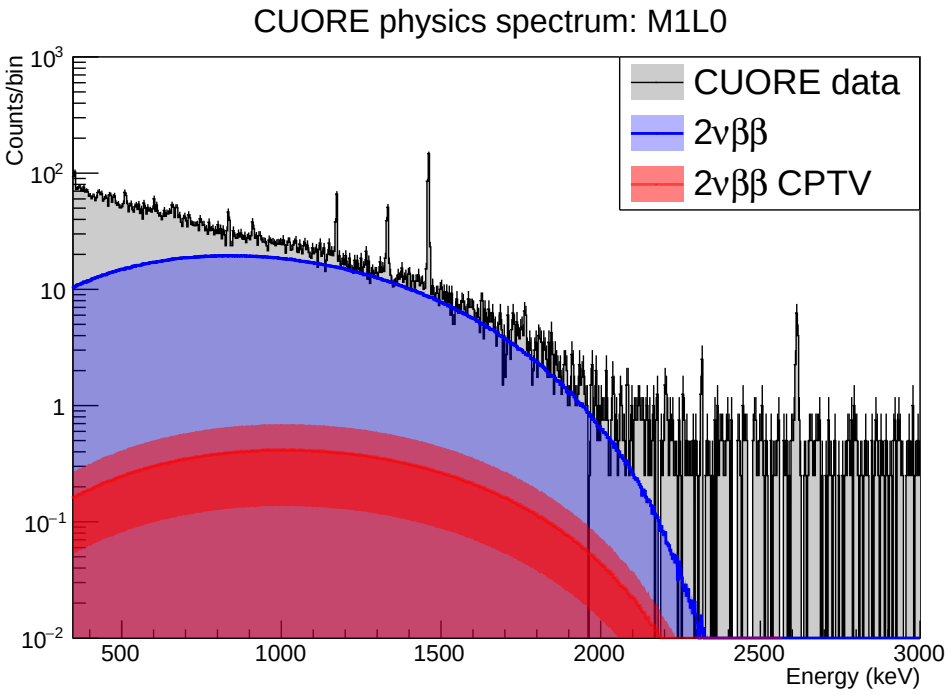

FIGURE 7.12: Double beta fitted spectra for the CUORE 2017 datasets: the black histogram represents the data, the blue shape is the Standard Model double-beta decay mode, the red one is the Lorentz-violating mode.

7.5 Outlook

Given its large mass and low background, the CUORE experiment can perform rare events searches for processes other than the $0\nu\beta\beta$ decay, like the CPT symmetry violation in the $2\nu\beta\beta$ decay.

A bayesian statistical analysis has been developed to study the sensitivity of CUORE to the CPT symmetry violation in the $2\nu\beta\beta$ decay of ^{130}Te.

The CUORE projected sensitivity on the $\dot{a}^{(3)}_{of}$ parameter, related to the CPT violating component in the $2\nu\beta\beta$ decay, was evaluated by fitting toy-MC samples at several increasing live-times (from few weeks to 5 yrs) with a model (H_1) in which the $2\nu\beta\beta$ CPTV component was added to the standard CUORE background model. The present result is constrained by the limited available statistics which influences the actual knowledge of the CUORE backgrounds.

Moreover a preliminary limit on the $\dot{a}^{(3)}_{of}$ parameter (systematics not-included) was extracted from the fit of the whole CUORE 2017 data sample with the H_1 model.

In the following years, CUORE will keep taking data, increasing its exposure and lowering the statistical uncertainties on the background model reconstruction. This will lead to a better knowledge of the background contaminations (localization and effect on the energy spectra).

To this end, it could be possible to either extract a new limit on the $\dot{a}^{(3)}_{of}$ parameter, just by fitting a larger data sample, or to even improve the actual CUORE sensitivity to the CPT symmetry violation in the $2\nu\beta\beta$ decay, by a better reconstruction of the backgrounds.

Conclusion

My PhD thesis work has been carried out within the CUORE experiment at the Gran Sasso National Laboratories (LNGS). Since September 2016 I have been working for the CUORE experiment at LNGS following and contributing to the last phase of the setup commissioning and to the initial phase of the data-taking. My main activities have been related to the CUORE detector operation, characterization and optimization of the bolometers system. Moreover, I developed software tools for CUORE data processing and analysis. In the meantime, I have been investigating the CUORE perspectives of rare events research, for processes other than the $0\nu\beta\beta$ decay, like the CPT symmetry violation in the $2\nu\beta\beta$ decay.

Between September and November 2016, I have been involved in the activities of the commissioning of the CUORE experiment at the LNGS.
During the first CUORE detector cool-down, between December 2016 and January 2017, I have worked on the TeO_2 bolometers thermal model utilizing the data from the CUORE-0 experiment, which was a single-tower CUORE prototype which took data in 2014-2015 at LNGS. The main goal of the analysis has been to study the CUORE-0 thermal pulses, in order to define a fit function and a set of parameters which could describe their shape. I have studied the correlation between fit and physics parameters and the reproducibility of the modeled response to different bolometers. This work set the basis for further studies performed on the CUORE bolometers data.

The CUORE experiment started taking data in late January 2017. The first period of data-taking was devoted to detector characterization and optimization campaigns, in order to set the best operating conditions of the cryogenic system and of the bolometers for the $0\nu\beta\beta$ decay search.
During February 2017, the first campaign to identify the optimal operating temperature for the data-taking was performed, by scanning from 9 mK to 15 mK and by a preliminary characterization of the Signal-to-Noise (SNR). I have been in charge of the analysis of the detectors Load Curves, and I developed an algorithm to identify the voltages for polarizing the NTDs (working points) of the CUORE channels, in order to ensure a linear response of the detectors for small temperature variations and a maximization of the SNR. The identified optimal working temperature, 15 mK, was utilized for the CUORE data-taking in 2017.

To continue, the first CUORE physics datasets were acquired between May and September 2017. The total collected $0\nu\beta\beta$ exposure was then 86.3 kg($^{nat}TeO_2$) $\cdot$ yr, or 24.0 kg(^{130}Te) $\cdot$ yr. The analysis of these data lead to the first CUORE $0\nu\beta\beta$ result [34]: there was no evidence for the decay and a lower limit of $T^{0\nu}_{1/2}(^{130}Te) > 1.3 \times 10^{25}$ yr (90% C.L including syst.) on the half-life $T^{0\nu}_{1/2}$ was extracted. The CUORE result was combined with the CUORE-0 and Cuoricino (CUORE predecessors) results. The new best limit on the half-life for the $0\nu\beta\beta$ decay in ^{130}Te was obtained: $T^{0\nu}_{1/2}(^{130}Te) > 1.5 \times 10^{25}$ yr (90% C.L). Moreover, the analysis of the same CUORE data for the background reconstruction lead to a new precise measurement of the $2\nu\beta\beta$ decay half-life of ^{130}Te , $T^{2\nu}_{1/2}(^{130}Te) = [7.9 \pm 0.1\ (\text{stat})\ \pm 0.2\ (\text{syst})\ ] \times 10^{20}$ yr [11].

I have contributed to the analysis of the first CUORE data, initially as 'analysis shifter' and later as 'analysis expert', by developing and debugging the software for processing and analyzing the CUORE data. Moreover, I have worked on the evaluation of the selection efficiencies for the finalization of the CUORE results.

The CUORE design energy resolution is 5 keV FWHM at the $0\nu\beta\beta$ transition energy. Several optimization activities have been performed aiming to reach this goal. In order to reduce the noise on the bolometers induced by the vibrations of the Pulse Tubes (PTs) system, it has been developed a system of active noise cancellation by stabilizing and controlling the phases of the valves driving each CUORE PT. I have contributed to the development of the software utilized for analyzing the data acquired during the scans of the PT phases. These scans were dedicated procedures aimed to find the best configuration of the PT phases which would minimize the effect of the PT system vibrations on the CUORE bolometers. Moreover I have been involved in other tests to identify further vibrational noise sources, related to the structures sustaining the cryostat and the detector.
After the preliminary results of the first temperature scan campaign, two more scans from 11 mK to 27 mK were performed, utilizing a representative subset of CUORE channels. During the first one in July 2017 also the Load Curves at each temperature were acquired and analyzed to set the working points. In September 2017, the second temperature scan was performed while the calibration sources were also deployed. It was studied with more details, the variation with temperature of the noise and the bolometer response to particle and heater signals. I was in charge of finding the working points for all the channels at each temperature and of analyzing the data to study the energy resolution variation with temperature. The analysis of these data lead to the identification of a new optimal detector working temperature, 11 mK.

For the CUORE data-taking in 2018, the operational temperature was set to 11 mK. I took care of the procedure for the Load Curves measurements for all the CUORE channels and of the analysis of the data for identifying the optimal working points. Eventually I set the selected working points and checked the stability of the channels response before the physics data-taking started. During the CUORE data-taking in 2018, I supported the analysis shifters, who were involved in the preliminary data processing, given the experience gained during the previous year.

Particularly, for my PhD thesis project, I have focused on the study of the possibilities of the CUORE experiment in the search for other rare events and/or for physics beyond the Standard Model. Particularly, I analyzed the sensitivity of the CUORE experiment to the CPT symmetry violation. The violation of this symmetry is described in several Standard Model Extensions (SME); in case of isotopes which can undergo double-beta decay, the CPT violation would induce a deformation in the spectrum of the total energy of the two electrons emitted in the $2\nu\beta\beta$ process. The coefficient utilized to quantify the CPT violation in the SME considered in the PhD thesis work is defined as $\dot{a}^{(3)}_{of}$. I performed a dedicate sensitivity study to the CPT violation in the $2\nu\beta\beta$ decay for several increasing live-times of CUORE, in order to evaluate the perspectives of the experiment for this search of physics beyond the Standard Model. Utilizing the data acquired by CUORE in 2017, it was possible to set the first limit for the CPT violation evaluated by studying the $2\nu\beta\beta$ decay of ^{130}Te. From a bayesian analysis of the CUORE physics spectrum, with the exposure acquired in 2017, a preliminary limit on this parameter was obtained: $\dot{a}^{(3)}_{of} < 4.88 \times 10^{-6}$ GeV (90% C.I.), systematic uncertainties were not yet included and will be the

subject of further analysis.

In parallel with this activity, I have continued the study for modeling the TeO_2 bolometers response, applying the results to the CUORE data, in order to develop a complete (static and dynamic) thermal model of the detectors. During the optimization campaigns, dedicated measurements for these studies were performed. The development of a thermal model, which could describe the CUORE detectors performance, is a topic of high interest. It can contribute to the identification of the physical parameters which are affecting the bolometers energy resolution and which could be possibly better optimized. Given the higher number of detectors, it was possible to study and model more features of the bolometers response: the pulse shape variation with the NTD polarization bias, the correlations in response between bolometers with NTDs belonging to same production and doping batches, the thermal response of TeO_2 crystals with Pt inclusions, ... A model describing the static behavior of the NTD and bolometer system, obtained by the thermal balance of input powers to the system and flowing powers, was studied with the Load Curve data. Moreover, one the preliminary results of the study of signal generation was the identification of a fit function that well describes the pulse shape of the CUORE thermal signals. Actually, we are working in an attempt to correlate the parameters of the models with physics quantities related to the thermal circuit.

The CUORE experiment has demonstrated that it is possible to run a ton-scale bolometric detector operating at temperatures ~ 10 mK. The collection of the CUORE first physics data was made possible by the excellent performance of the cryostat and the detectors. While proceeding with the physics data-taking, CUORE will keep working for improving the energy resolution and for a better understanding of the sources of background. In the upcoming years, CUORE is going to have a leading role among the most sensitive experiments for the search of the $0\nu\beta\beta$ decay and other rare processes.

Appendix A

Static Thermal model on CUORE data

A.1 The model

The static equations of the bolometer thermal model allow to obtain the temperatures of the various components of the detector when it is at the thermal equilibrium.

A minimal thermal model can be built with 3 components. The 3 thermal nodes have finite heat capacities (TeO_2 crystal absorber, NTD thermistor lattice and NTD thermistor electrons) and are connected among them and to the heat bath by means of thermal conductances. The bolometer thermal model is described by a system of differential equations, which are obtained by the thermal balance of input powers to the system and flowing powers. In general, given an element of the circuit at temperature T_A on which some power $P_{in,A}$ is injected, if it is coupled to an element at T_B ($T_B < T_A$) via a thermal conductance G(T), the heat will flow to the element at lower temperature, until a static equilibrium is reached:

$$P_{in,A} = P_{AB} = \int_{T_B}^{T_A} G(T)dT$$

In Fig.A.1, the scheme of the bolometer minimal thermal model with 3 nodes is reported. The thermal equations corresponding to the thermal circuit in the figure are:

$$\begin{cases} P_e = P_J + P_{bkg,e} = P_3 \\ P_2 + P_3 + P_{bkg,l} = P_4 \\ P_1 + P_2 = P_{bkg,a} \end{cases}$$

where P_1 is the power flowing through the PTFE link between the TeO_2 crystal and the heat bath, P_2 is the power flowing through the glue used to couple the NTD to the absorber, P_3 is the power flowing through the electron-phonon conductance and P_4 is the power flowing through the read-out Au wires which link the NTD to the heat sink. $P_{bkg,k}$ with k = a,e,l is a background thermal power contribution, that is mainly due to electromagnetic interferences. In the system of equations, it is also taken into account for the polarization of the NTD, by a Joule-heating power dissipation term P_J on the NTD electrons system.

The energetic balance equations of the model have to be solved in order to find the values of the unknown thermal parameters, such as the conductances, the background powers,... This system of differential equations for the bolometers static thermal model can be solved only with numerical methods. Alternatively, approximated solutions are also possible.

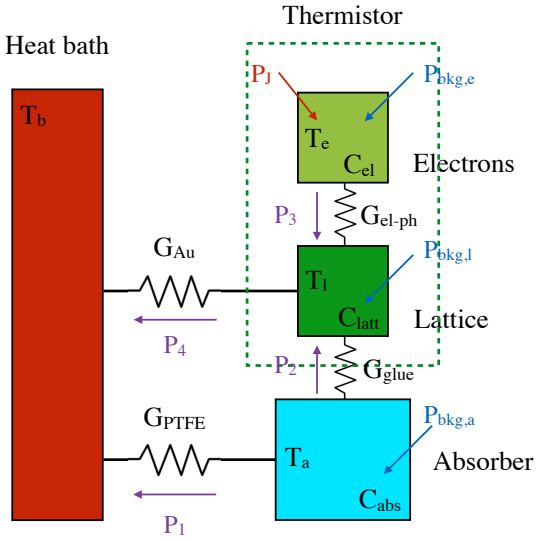

FIGURE A.1: Minimal bolometer thermal model: the thermal capacitances, the thermal conductances and the (input and flowing) powers are identified.

A.1.1 Single stage thermal model

Given the weak thermal link between the TeO_2 crystals and the bath provided by the PTFE holders, the electric power basically flows from the NTD thermistor to the heat sink through the Au-wires; the capacitances and conductances in parallel (glue, absorber,..) are practically negligible. Moreover the coupling between the bolometer-NTD system and the heat bath can be approximated on the first order with a single conductance. These approximations lead to the, so called, **single stage thermal model**.
A single stage model provides a good approximation in describing the static behavior of the NTD and bolometer system, which can be studied with the Load Curve data. However this model is not suited to describe the dynamic behavior of the system, in particular the response to energy depositions and the thermal pulse generation.

In the single stage thermal model (see Fig.A.2), only a single conductance is considered, which connects the bolometer and NTD system to the heat bath. Thus, the temperature of the bath $T_0 = T_b$ is different from the temperature of the NTD, T_1. The "Hot Electron Model" is not considered for the NTD response and no decoupling between NTD lattice and electrons behavior due to the NTD polarization bias, is considered. NTD electrons and lattice are supposed to be at the same temperature, $T_1 = T_e = T_l$. The power dissipated on the NTD P_{in} is composed by the power due to Joule-heating when biasing the NTD, P_J, and a possible background power, P_{bkg}.

$$P_{in} = P_J + P_{bkg} \quad \text{where } P_J = I_{bol} V_{bol} \tag{A.1}$$

Given the power dissipated on it, the NTD sets to a temperature T_1 slightly higher than the one of the bath, T_b. From the principles of thermodynamics, the heat flows through the NTD-bath conductance G(T), from the higher temperature system to the

lower one. The flowing power from the NTD to the bath is:

$$P_{10} = \int_{T_b}^{T_1} G(T)dT \quad \text{where } G(T) = g_{10}T^{\alpha} \tag{A.2}$$

$$P_{10} = \frac{g_{10}}{\alpha+1}[T_1^{\alpha+1} - T_b^{\alpha+1}] \tag{A.3}$$

A dynamic equilibrium is reached when:

$$P_{in} = P_{10}$$

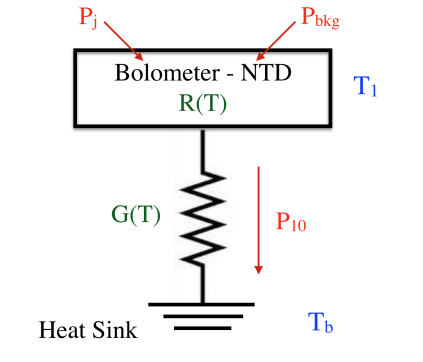

FIGURE A.2: Sketched representation of the single stage bolometer static thermal model.

The thermistor static resistance depends on the temperature of the electrons in the NTD, which is $T_e = T_1$ in the single stage model.

$$R(T_e) = R(T_1) = R_0 exp(\frac{T_0}{T_1})^{\gamma} \tag{A.4}$$

Given the static equilibrium condition, the NTD temperature T_1 can be expressed in terms of the joule heating, background power and conductance parameters.

$$T_1 = \left(\frac{P_J + P_{bkg} + \frac{g_{10}}{\alpha+1}T_b^{\alpha+1}}{\frac{g_{10}}{\alpha+1}}\right)^{\frac{1}{\alpha+1}} \tag{A.5}$$

In CUORE, the actual temperature of the Mixing Chamber plate (T_b) is read by the noise thermometer (T_{NT}). It is reasonable to assume a possible offset (T_{off}) in the measurement of the temperature from the noise thermometer and the actual temperature of the heat bath where the channel is linked to: $T_b = T_{NT} - T_{off}$.

A.2 Load Curves at several temperatures

Dedicated LoadCurve runs were performed at several temperatures from 15 to 27 mK in July 2017. For each run, the collected data were for the 78 active channels of columns 1 and 2 of Towers 8-9-10. In such a way, from these load curves, there would be a sample of 26 channels for each NTD batch: ch 365-390 Tower 8 NTD-41C, ch 417-442 Tower 9 NTD-39C, ch 469-494 Tower 10 NTD-39D.
The list of these acquired Load Curve runs is:

- 301301 - 15 mK: T_{NT} = (15.28 $\pm$ 0.09) mK

- 301302 - 17 mK: T_{NT} = (17.37 $\pm$ 0.12) mK
- 301311 - 19 mK: T_{NT} = (19.06 $\pm$ 0.13) mK
- 301319 - 21 mK: T_{NT} = (21.21 $\pm$ 0.14) mK
- 301322 - 24 mK: T_{NT} = (24.13 $\pm$ 0.16) mK
- 301331 - 27 mK: T_{NT} = (26.89 $\pm$ 0.20) mK

These data were acquired with the same load curve procedure (bipolar load curves), and the ntuples for the analysis were produced with the same algorithm. Among the LC reconstructed points, the static resistance R_{bol} and the NTD Joule-heating power P_{bol} are evaluated for each bias voltage i. R_{bol} and P_{bol} can be expressed in terms of non correlated variables, like the bias voltage V_B, the load resistor R_L and the baseline variation ΔV.

$$R_{bol} = \frac{\Delta V R_L}{G V_B - \Delta V} \tag{A.6}$$

$$P_{bol} = \frac{\Delta V}{G}\left(V_B - \frac{\Delta V}{G}\right)\frac{1}{R_L} \tag{A.7}$$

The errors on R_{bol} and P_{bol} can be obtained by propagating the errors on the former variables.

$$\sigma^2_{R_{bol}} = \left(\frac{V_{bol} R_L}{(V_B - V_{bol})^2}\right)^2 \sigma^2_{V_B} + \left(\frac{V_{bol}}{V_B - V_{bol}}\right)^2 \sigma^2_{R_L} + \left(\frac{R_L G V_B}{(G V_B - \Delta V)^2}\right)^2 \sigma^2_{\Delta V} \tag{A.8}$$

$$\sigma^2_{P_{bol}} = \left(\frac{V_{bol}}{R_L}\right)^2 \sigma^2_{V_B} + \left(\frac{V_{bol}}{R_L^2}(V_B - V_{bol})\right)^2 \sigma^2_{R_L} + \left(\frac{V_B}{R_L G} - 2\frac{\Delta V}{R_L G^2}\right)^2 \sigma^2_{\Delta V} \tag{A.9}$$

The load resistor accuracy is 10% ($\sigma_{R_L} = R_L \times 10\%$). The uncertainty on V_B is related to the accuracy of the electronics in reading-writing the bias values, $\sigma_{V_B} \approx 50$ mV. The error on ΔV is assumed to be the RMS of the baseline, $\sigma_{\Delta V}$ = RMS.

A.3 Load Curves Analysis

A fit of the P_{bol} vs. R_{bol} dependence has been implemented to test the **single stage thermal model** on the load curve data acquired at the different temperatures.
The fit function utilizes the combination of Eq.A.4 and A.5, for each point i of the LC at every measured temperature T_{NT}:

$$R_{bol,i} = R_0 exp\left(\frac{T_0}{T_{1,i}}\right)^\gamma \quad \text{where } T_{1,i} = \left(\frac{P_{bol,i} + P_{bkg} + \frac{g_{10}}{\alpha+1}(T_{NT} - T_{offset})^{\alpha+1}}{\frac{g_{10}}{\alpha+1}}\right)^{\frac{1}{\alpha+1}} \tag{A.10}$$

The fit function has 7 free parameters:

- NTD thermistor: $R_0[\Omega]$, T_0 [mK], γ
- P_{bkg}[pW], the background power injected on the NTD
- Conductance G(T) between the bolometer and the heat bath from Eq.A.2, where α and g_{10} are the actual fit parameters

- Temperature offset: T_{off}[mK], a systematic shift between the real detector temperature and the temperature read with the noise thermometer [1]

An example of P_{bol} vs. R_{bol} NTD curves at several temperatures is reported in Fig.A.3; these curves were constructed utilizing the single stage model (in Eq.A.10) and utilizing reference values for the thermal parameters [2].

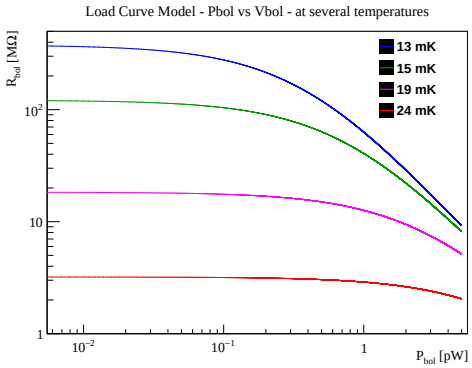

FIGURE A.3: Example of P_{bol} vs. R_{bol} NTD curves at several temperatures (13, 15, 19, 24 mK). The $R_{bol}(P_{bol})$ dependence has been evaluated in the case of a single stage static thermal model for an NTD having reference thermal values of: R_0 = 1.8 Ω, T_0 = 5 K, γ = 0.5, P_{bkg} = 0.1 pW, α = 4.5, g_{10} = 0.05 $W/K^{\alpha+1}$, T_{off} = -0.1 mK.

In case of fitting the data for a given channel at a single temperature, the points of each single load curve would span a small range of NTD temperature variation driven only by the electro-thermal feedback. The value of the conductance G has a strong dependence on the actual temperature of the heat sink. Therefore utilizing data at several temperatures would allow to exploit a wider dynamic range of operation and response of the NTD-bolometer system.

The approach chosen in order to gain the most of the informations for the fit from the given data was to proceed with a **simultaneous fit of the LC data for several temperatures** for each channel. Using a single fit for a set of temperatures, there will be more data to be used and it can be profited of the variation of the thermal response with temperature. It is then possible to have the fit converging and giving reasonable results for all the thermal parameters of interest. In order to perform the fit considering also the uncertainties on each LC point, the minimization function was defined.
Let's assume y_i is the random variable and the model $y(x_i, \vec{\Theta})$ depends on the variable x_i and on the set of parameters $\vec{\Theta}$, for which we search the best estimate. Several functions to be minimized can be implemented in the fit procedure:

- Minimum Least Squares (MLS)

$$MLS_{log} = \sum_{i=1}^{N} (log(y_i) - log(y(x_i, \vec{\Theta})))^2 \tag{A.11}$$

[1] The configuration of the noise thermometer was not modified among the LC runs, therefore it is expected the (possible) temperature offset to be the same among the runs.

[2] For the NTD resistance parameters, reference values from Tab.3.1 were used. For the other thermal parameters, reasonable estimates were utilized: negligible P_{bkg} and T_{offset}, and α as an intermediate value between the coefficient for Au-wires and electron-phonon conductances([60]).

The MLS here is calculated for $log(y_i)$. When y has a complex exponential dependence on x, huge variations of y are expected when x changes; with the $log(y)$ MLS approach, that dependence is transformed into a linear/power law dependence, thus allowing the fit to converge easier. In the MLS approach, the errors on the y_i measurements are not taken into account; in this way, all the data points are weighted equally.
This is a basic approach that can be used to extract some initial values of the fit parameters, that can be then used as an input for the fits which consider also the errors on the measurements.

- Maximum Likelihood estimator - Chi Square (χ^2)
This estimator is appropriate when each data point y_i can be regarded as a Gaussian random variable distributed around the true value. Each random variable y_i is related to another variable x_i, which is assumed to be known without error, and it has a measurement error σ_i (on y_i). The χ^2 estimator is the parameter that has to be minimized in the fit, to find the best values for the model parameters $\vec{\Theta}$.

$$\chi^2 = \sum_{i=1}^{N} \frac{(y_i - y(x_i, \vec{\Theta}))^2}{\sigma_i^2} \tag{A.12}$$

- Robust statistical estimator (*RobEst*):
In case the measurement errors are not normally distributed, different distributions can be used. As a general rule, the best estimate of the parameters can be obtained by minimizing the sum of $\rho(z)$, the logarithm of the assumed distribution. Besides the well known gaussian, two other distributions provide generally a better description when (as in our case) the distribution of the measured points is not gaussian.

$$RobEst = \sum_{i=1}^{N} \rho(z) \quad \text{where } z = \frac{(y_i - y(x_i, \vec{\Theta}))}{\sigma_i} \tag{A.13}$$

- Two-sided exponential: $\rho(z) = |z|$
- Lorentzian distribution: $\rho(z) = log(1 + \frac{1}{2}z^2)$

In our case: $y_i = R_{bol,i}$ is the measured value of the bolometer resistance, $P_{bol,i}$ is the corresponding electrical power dissipated on it and σ_i is the error on y_i, for each LC point i at a given temperature T. Therefore the expression for the NTD resistance to be compared with the measured value in the minimization function, will depend on the measured power, on the measured temperature and on the set of parameters of the model, for which the best estimate is searched for: $R^{exp}_{bol,i}(P_{bol,i}, T, \vec{\Theta})$.

A.3.1 Preliminary results

The preliminary results of the fit performed on different individual detectors are reported. In this analysis, the parameter γ in the $R(T)$ dependence has been fixed to $\gamma = 0.5$. Since the distribution of the uncertainties on P_{bol} and R_{bol} is not perfectly gaussian, a robust fit utilizing a two-sided exponential distribution for describing the errors was performed. The MLS on $log(P_{bol})$ fit was used to extract initial values of the model parameters, which were then used as an input for the robust fit.

In Figs.A.4 and A.5, the fit results for three channels each on a different tower are reported. The LC data (P_{bol} vs. R_{bol}) at the several temperatures are plotted; the solid

lines correspond to the fit model with a robust estimator. A reasonable agreement between the data and the model can be observed.
The median values of the fit parameters for the different towers are reported in Tables A.1 and A.2. The results for the (R_0,T_0) NTD parameters are close to the values measured on spare NTDs belonging to the same production Ge-batches (see Tab.3.1). The obtained values for the exponent α of G(T) can give some hint on which is the dominant contribution to the effective thermal conductance in the system. The NTD-bath thermal coupling by the Au-wires seems not sufficient to describe the system (α_{Au} = 2.37 [60]); the electron-phonon conductance inside the thermistor itself (α_{el-ph} = 4.37 [60]) seems then to give the driving contribution. We expect the Au-wires and electron-phonon conductances to be in series (see Fig.3.7):

$$G(T) = \frac{1}{(\frac{1}{G_{Au}}) + (\frac{1}{G_{el-ph}})} \longrightarrow G(T) \sim G_{el-ph} \text{ if } G_{Au} \gg G_{el-ph}$$

The fit convergence was found to depend strictly on the input values given for the fit parameters. Moreover the uncertainties on many of the obtained parameters' best fit are quite large.

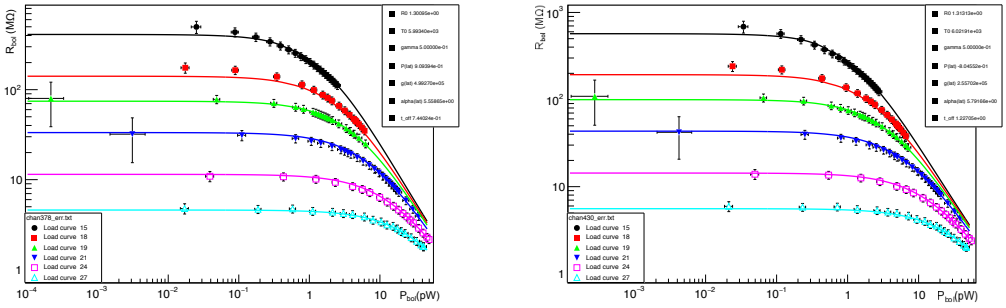

FIGURE A.4: [Left] LC fit for channel 378 - Tower 8. [Right] LC fit for channel 430 - Tower 9.

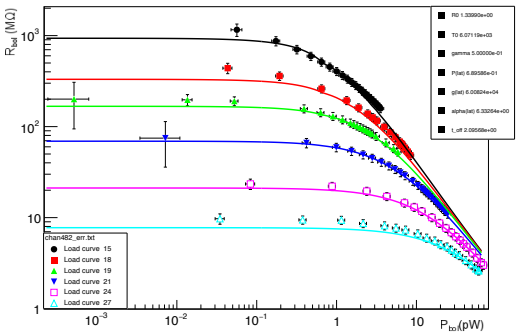

FIGURE A.5: LC fit for channel 482 - Tower 10

	R_0 [Ω]	T_0 [K]
Tower 8 - NTD 41C	(1.31 $\pm$ 0.13)	(5.98 $\pm$ 0.06)
Tower 9 - NTD 39C	(1.18 $\pm$ 0.17)	(5.98 $\pm$ 0.07)
Tower 10 - NTD 39D	(1.32 $\pm$ 0.25)	(6.00 $\pm$ 0.06)

TABLE A.1: Median values of the NTD parameters (R_0, T_0) from the fits of the detectors belonging to the 3 different towers.

	P_{bkg} [pW]	g_{10} [$W/K^{\alpha+1}$]	α	T_{off} [mK]
Tower 8 - NTD 41C	(0.81 $\pm$ 0.13)	(0.13 $\pm$ 0.07)	(4.56 $\pm$ 0.19)	(0.93 $\pm$ 0.23)
Tower 9 - NTD 39C	(0.96 $\pm$ 0.19)	(0.19 $\pm$ 0.08)	(4.59 $\pm$ 0.27)	(1.14 $\pm$ 0.19)
Tower 10 - NTD 39D	(0.76 $\pm$ 0.15)	(1.5 $\pm$ 1.0)	(5.11 $\pm$ 0.24)	(1.86 $\pm$ 0.36)

TABLE A.2: Median values of the static thermal model LC fit parameters for the three towers: background power, conductance parameters and temperature offset.

A.3.2 Outlook

Given the preliminary result, further upgrades on the static thermal model development and analysis could be:
- add more LC data at other (lower) temperatures;
- perform a global fit at tower level, grouping together the data of the 26 channels of each tower and fixing most of the thermal parameters to be the same values for all the channels;
- perform a global fit, including all the channels at the same time, fixing the T_{off} fit parameter to be the same value for all the channels/towers (the systematic shift between the actual base temperature and the value read by the NT should be the same) while leaving the other parameters to be channel/tower dependent;
- utilize a two stage static thermal model to fit the data, separating the NTD-bath thermal coupling by the Au-wires and the electron-phonon conductance inside the thermistor.

Appendix B

Pulse shape analysis on CUORE data

A complete understanding of the pulse shape of the signals produced by CUORE bolometers hasn't yet been obtained. The several thermal elements contributing to the signal generation and transmission in the TeO_2 crystals coupled with the NTDs make the modellization of the pulses quite complex.

Making use of previous pulse shape studies on CUORE-like bolometers ([60], [102], [103]), we are trying to develop a more accurate dynamic thermal model to describe the CUORE signals. The idea is to identify a sufficiently accurate template to fit the pulse shape of the CUORE signals and then to correlate the result with thermal parameters. We successfully developed a fit function that is able to reproduce TeO_2 pulses with good accuracy. This template was tested on signals at several temperatures and on particle and heater signals. We are presently working on the identification of correlations among the fit parameters and physical properties of CUORE detectors.

B.1 The dynamic thermal model

Modeling the bolometer response consists in accounting for all the steps starting from the energy release into the crystal that contribute to shape the signal eventually sampled by the ADC. Thermal processes in bolometers involve many elements like the capacitance of the crystal, the conductance of the glue that attaches the thermistor to the crystal, the capacitance of the crystal supports and their conductance to the main bath, the capacitance of the thermistor and the conductance of its wires to the main bath, as described in Chap.3.

An effective thermal model that could describe the pulse shape of the signals $r(t)$ can be built following the theory of the bolometer working principles. The pulse function would be the convolution of $i(t)$, that is the thermal energy release due to phonons thermalization, and the thermal circuit transfer function $f(t)$, which describes the effect of the several thermal elements in shaping the signal. See Eq.B.1.

$$r(t) = i(t) \otimes f(t) \tag{B.1}$$

B.1.1 Solving thermal circuits

A thermal circuit can be schematized and solved as an electrical circuit if we consider the following equivalences:

- Thermal capacitance C [J/K] $\rightarrow$ Electric capacitance C [Farad= A s/V]
- Thermal conductance G [W/K] $\rightarrow$ Electric conductance G [Ω^{-1}]

- Temperature T [K] $\rightarrow$ Voltage V [V]
- Power dissipation P [W] $\rightarrow$ Current I [A]

Using the Laplace transform method it is possible to analytically solve a circuit replacing

$$\text{G=1/R} \rightarrow \text{G} \qquad \text{C} \rightarrow 1/\text{sC}$$

The response of a circuit $r(t)$ to an input signal $i(t)$ can be calculated multiplying the Laplace transform of the input signal for the function $F(s)$, and then applying the Laplace anti-transform.

$$I(s) = \mathcal{L}[i(t)] \tag{B.2}$$
$$R(s) = I(s) \times F(s) \tag{B.3}$$
$$r(t) = \mathcal{L}^{-1}[R(s)] \tag{B.4}$$

In case we assume the input function is a delta $i(t) = \delta(t)$, which is equivalent to assuming that the release of energy inside the crystal is instantaneous (much faster than the circuit response), its Laplace transform is equal to 1. Therefore the response of a circuit to a delta-function input is equal to the Laplace anti-transform of the transfer function only.

It is possible to build a generic transfer function for the thermal circuit, without specifying in advance all the thermal components, just following the general approach that is used for analyzing circuits in the Laplace domain.
In the Laplace domain the general transfer function of a circuit $F(s)$ has the form of a ratio of polynomials, as in Eq.B.5.

$$F(s) = \frac{b_0 + b_1 s + ... + b_{m-1}s^{m-1} + b_m s^m}{a_0 + a_1 s + ... + a_{n-1}s^{n-1} + a_n s^n} \tag{B.5}$$

where $R = n - m$ is the degree of the function $F(s)$.
The $F(s)$ function can then be written as:

$$F(s) = K \cdot \frac{(s - z_0)(s - z_1)...(s - z_{m-1})(s - z_m)}{(s - p_0)(s - p_1)...(s - p_{m-1})(s - p_n)} \tag{B.6}$$

where the p_i and the z_i are the poles and the zeros of the F(s) function, respectively. The zeros are the roots of the numerator and represent the values in which $F(s) = 0$. The poles are the roots of the denominator of and represent the values in which the $F(s) \rightarrow \infty$

If $R \geq 1$, then the transfer function F(s) can undergo partial fraction decomposition

$$F(s) = \frac{N(s)}{D(s)} = \frac{N(s)}{(s - p_1)(s - p_2)...(s - p_n)} = \sum_{i=1}^{n} \frac{k_i}{s - p_i} \tag{B.7}$$

The inverse Laplace transform of the transfer function is then the sum of exponentials (if the poles are all different)

$$\mathcal{L}^{-1}[F(s)] = \sum_{i=1}^{n} k_i e^{p_i \cdot t} \tag{B.8}$$

The amplitude of the i-th exponential contribution, k_i, is called the *residuals of F(s) in the p_i pole*. It is given by:

$$k_i = \left[(s - p_i) \cdot \frac{N(s)}{D(s)} \right]_{s \to p_i} \tag{B.9}$$

Moreover

$$\sum_{i=1}^{n} k_i = 0 \qquad \text{if} \quad R \geq 2 \tag{B.10}$$

Otherwise

$$\sum_{i=1}^{n} k_i = \frac{b_m}{a_n} \qquad \text{if} \quad R < 2 \tag{B.11}$$

The response of the circuit integrated over time is given by

$$Q = \sum_{i=1}^{n} A_i p_i \tag{B.12}$$

and it's proportional to the dissipated energy.

If all the a_i and b_j coefficients in Eq.B.5 are real, then the poles and the zeros can only be real or complex coniugate. A necessary condition for a polynomial to have only solutions with negative real part, is that all the coefficients are real.
In case of modeling a electrical/thermal system, the a_i e b_j coefficients are related to physical quantities (C,R,...) which are real and positive by definition. Therefore only negative real and not-coincident poles are expected for a circuit in which the thermal components don't change their values. To each real pole then corresponds a time constant $\tau_i = -p_i^{-1}$. The number of poles is equal to the number of independent capacitances (and inductances) present in the circuit.
In case an electro-thermal feedback is applied to the circuit, see Eq. B.13, this can affect the position of the poles; there can be roots of the denominator which have negative discriminant, therefore leading to complex conjugate poles (with negative real part).

$$F'(s) = \frac{N(s)}{D(s) + GN(s)} \tag{B.13}$$

In Fig.B.1 there is a schematic representation of the time response of circuits, given the position of the poles. Poles with negative real part have exponential attenuation. Complex poles generate dumped oscillations. Poles with positive real part generate divergent systems.

B.1.2 Thermal elements in CUORE

A general representation of the CUORE bolometer thermal circuit should account for the heat capacities of the various components and the thermal conductances between them and towards the heat bath. Indeed it is a complex system to be considered in order to model the thermal response to energy depositions by particles. Experimentally, it has been observed that the thermal pulses from the CUORE-like crystals are characterized by 3-4 dominant time constants. Several works aimed to develop a thermal model which would reproduce the pulses from the CUORE predecessor experiments ([102], [103]) and correlate the time constants of the pulses to the thermal and electrical properties of the crystals and the NTDs. Given the high number of active channels in CUORE, we are trying to develop a comprehensive

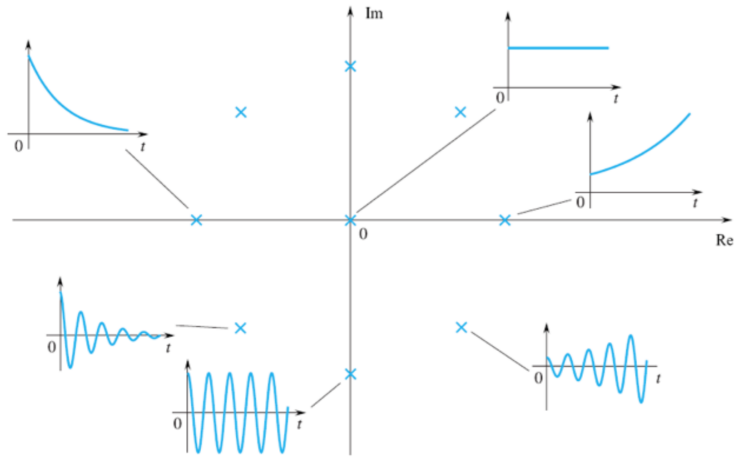

FIGURE B.1: Schematics of the time response of circuits, given the position of the poles.

model of the thermal response, starting from the study of the shape of the pulses for different bolometers, at different energies and for particle/heater energy depositions.

B.1.3 The signal template for CUORE bolometers

In order to find a model that could describe the CUORE pulse shape, the approach of building transfer functions for the thermal circuit for fitting the signals was utilized.

Case1: 3 real poles and 1 zero

The majority of the CUORE-like bolometers (from Cuoricino and CUORE-0 experiments) show pulses with one rise time and two decay times. The detector response can then be written in terms of a transfer function F(s) with 3 real negative poles and 1 zero:

$$F(s) = \frac{(s - z_1)}{(s - p_1)(s - p_2)(s - p_3)} \qquad \text{with} \qquad p_3 < p_2 < z_1 < p_1 < 0 \tag{B.14}$$

The bolometer response would be then a pulse given by the sum of three exponentials:

$$f(t) = \underbrace{\frac{p_1 - z_1}{(p_1 - p_2)(p_1 - p_3)} e^{-\frac{t}{\tau_1}}}_{=k_1>0} + \underbrace{\frac{p_2 - z_1}{(p_2 - p_1)(p_2 - p_3)} e^{-\frac{t}{\tau_2}}}_{=k_2>0} + \underbrace{\frac{p_3 - z_1}{(p_3 - p_1)(p_3 - p_2)} e^{-\frac{t}{\tau_3}}}_{=k_3<0} \tag{B.15}$$

where $\tau_3 = -1/p_3$ corresponds to the rise time, $\tau_1 = -1/p_1$ and $\tau_2 = -1/p_2$ are the two components of the fall time.

In Figs.B.2 and B.3, the position of the model poles in the complex plane is shown and the comparison between a CUORE-0 sample pulse and a pulse built with the fit function described before are shown.

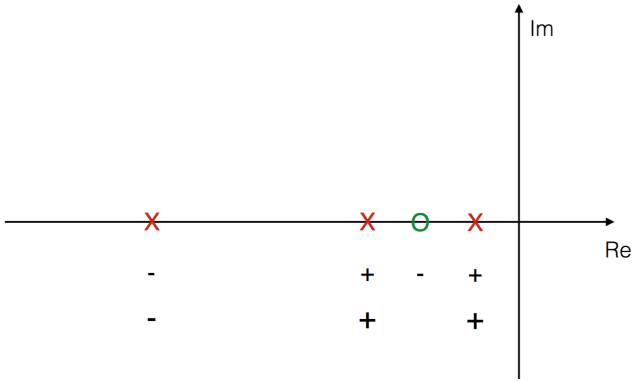

FIGURE B.2: Position of the poles (red crosses) and of the zeros (green circle) on the complex plane of a transfer function with 3 poles and 1 zero. The "+" and "-" symbols represents the sign of the poles, so that "+" stands for a decay time constant and "-" stands for a rise time constant.

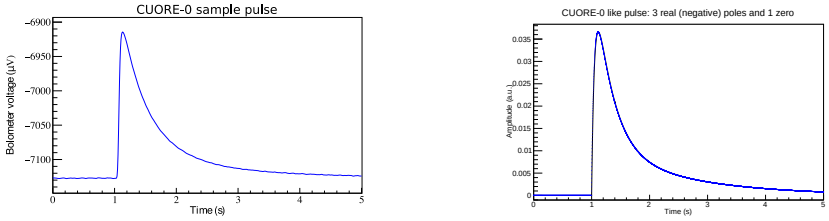

FIGURE B.3: CUORE-0 Sample pulse (left) and its analytic reproduction, following Eq.B.15 (right).

Case 2: 2 real poles, 2 complex conjugate poles and 1 zero

The CUORE pulses appeared, since the very beginning, a bit different from the CUORE-0 ones.

The primary reason for this is that the working point resistances of the CUORE NTDs are higher ($R_{wp} \approx$ 0.3-1 $G\Omega$) than the CUORE-0 ones ($R_{wp} \approx$ 30-100 $M\Omega$), because they belong to different NTD production sets. Therefore the RC-coupling between the NTD resistance and the parasitic capacitance of the copper bundles driving the signal out from the NTD to the Junction Boxes and above ($C_{par} \approx 500$ pF), cannot be neglected. This fact introduces an additional time constant that was found in our study of the CUORE detectors pulse shape while it was absent in CUORE-0.

The bolometers are coupled with the NTD thermistors. The NTD thermistor is polarized; this introduces a feedback due to the Joule heating induced by the current of the biasing circuit. The **electrothermal feedback** is in fact the modification of the behavior of a device with a temperature-dependent electrical resistance, due to the temperature variation due to the current flow.The heat induced by the bias current (Joule effect) leads to a temperature increase. This reduces the resistance (and consequently the power) until an equilibrium is reached. The effect of the feedback is to change the position of the poles, leading also to complex conjugate ones (see Eq.B.13).

Making use of all these considerations, we built a transfer function F(s) with 4 poles (all with negative real part; 2 real poles and 2 complex conjugate poles) ed 1 zero:

$$F(s) = \frac{(s - z_1)}{(s - p_1)(s - p_2)(s - p_3)(s - p_4)} \qquad \text{with} \qquad p_2 < z_1 < p_1 < 0 \tag{B.16}$$

$$p_3 = p_4^\star : \qquad p_3 = \sigma + i\omega \, , \, p_4 = \sigma - i\omega \, , \qquad \sigma < 0 \tag{B.17}$$

The bolometer response in the time domain would be then a pulse given by:

$$f(t) = f_1(t) + f_2(t) \tag{B.18}$$

$$f_1(t) = k_1 e^{tp_1} + k_2 e^{tp_2} \tag{B.19}$$

$$f_2(t) = k_3 e^{t\sigma} cos(wt + atan(\phi)) \tag{B.20}$$

$$\phi = -i \frac{(p_3 - z_1)}{(p_3 - p_1)(p_3 - p_2)(2\omega)} \tag{B.21}$$

where $f_1(t)$ corresponds to the real poles (p_1, p_2) contribution, $f_2(t)$ to the complex conjugate poles (p_3, p_4).
The residuals at the poles (k_1 at p_1, k_2 at p_2, k_3 for the complex conjugate poles) are:

$$k_1 = \frac{(p_1 - z_1)}{[(p_1 - \sigma)^2 + \omega^2](p_1 - p_2)} \tag{B.22}$$

$$k_2 = \frac{(p_2 - z_1)}{[(p_2 - \sigma)^2 + \omega^2](p_2 - p_1)} \tag{B.23}$$

$$k_3 = \sqrt{\frac{(\sigma - z_1)^2 + \omega^2}{\omega^2[(\sigma - p_1)^2 + \omega^2][(\sigma - p_2)^2 + \omega^2]}} \tag{B.24}$$

In Figs.B.4 and B.5, the position of the model poles in the complex plane is shown and the comparison between a CUORE sample pulse and a pulse built with the fit function described before are shown.

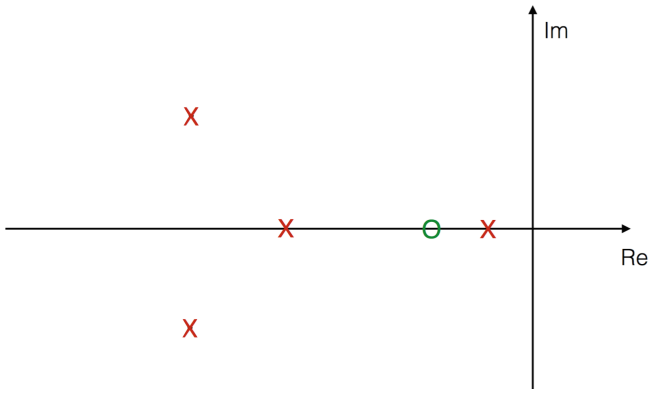

FIGURE B.4: Position of the poles (red crosses) and of the zeros (green circle) on the complex plane of a transfer function with 4 poles (2 real poles and 2 complex conjugates poles) and 1 zero.

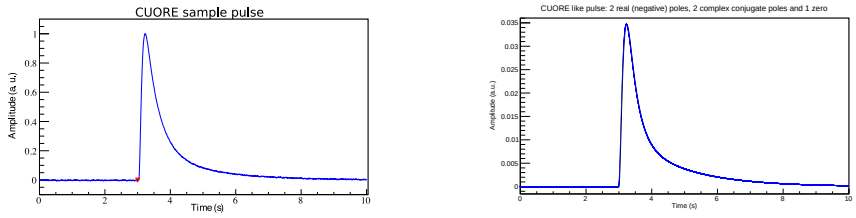

FIGURE B.5: CUORE Sample pulse (left) and its analytic reproduction, following Eq.B.18 (right).

B.2 Analysis and preliminary results

B.2.1 Load curve data and pulse shape variation with the NTD bias

The **heater pulses** for each bias configuration of a Load Curve measurement[1] were fitted with the signal template with 2 real poles, 2 complex conjugate poles and 1 zero.
The fit was implemented for the analysis of the Load Curve data acquired at 11 mK. Examples of the fitted pulses at different bias voltages for a CUORE channel are reported in Figs.B.6, B.7 and B.8. As it can be clearly seen in the figures, the fit is able to reproduce the pulse shape at different bias voltages. Moreover the variation of the real and imaginary parts of the complex conjugate poles in the model, can describe very well the deformation of the pulses which is seen at high bias. As reported on the fit results on the pulse plots and as it is shown in Fig.B.16, the values of the real and the imaginary part of the complex conjugate poles vary with the applied bias. For low bias values, the imaginary part is negligible compared to the real one. When the real part is dominant, the pulse shape is well-described by one time constant on the rising edge and two time constants on the falling edge. Increasing the applied bias, the imaginary part grows faster than the real part in absolute value. When the imaginary part starts to dominate, this corresponds to the condition in which the channel operation gets unstable and the pulse starts showing a dumped-oscillation shape.

These fit results and considerations were utilized in the procedure for finding the optimal working points for the NTD polarization bias at 11 mK.
However this model for the thermal pulse reproduction can be applied also to data acquired at other temperatures (both LC and physics data).

[1] See Chap.4.2.2 for details about the Load Curves procedure and analysis in CUORE.

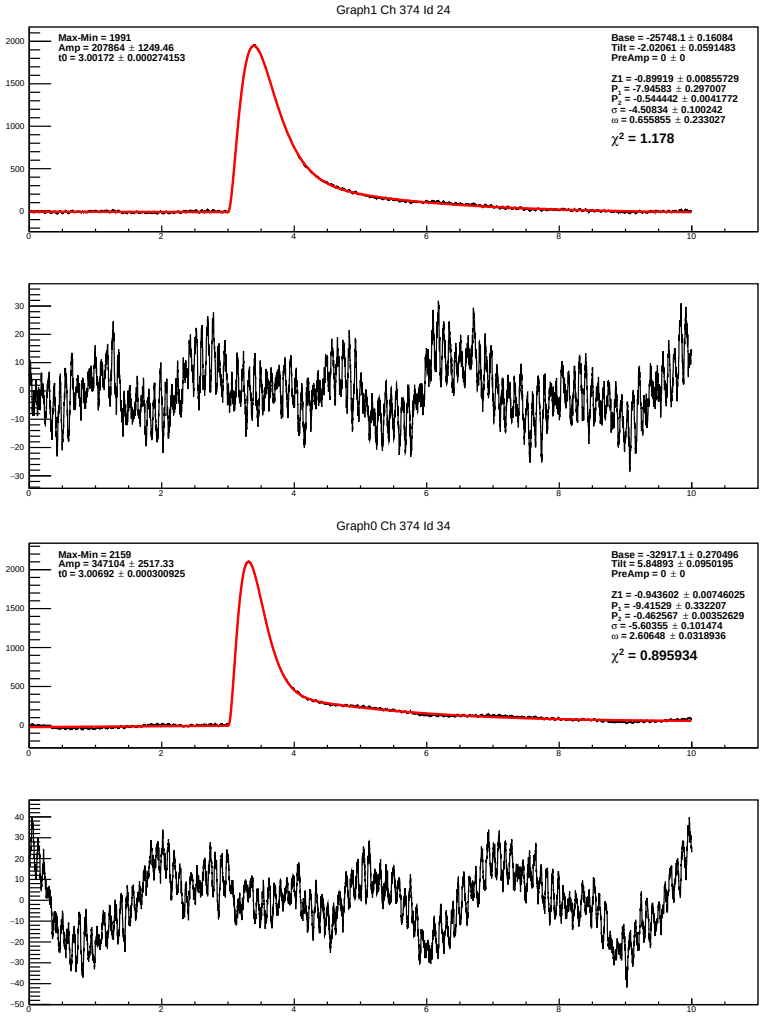

FIGURE B.6: Channel 374 - 11 mK LC: fits of the heater pulses at Id24 = 0.97 V and Id34 = 1.42 V

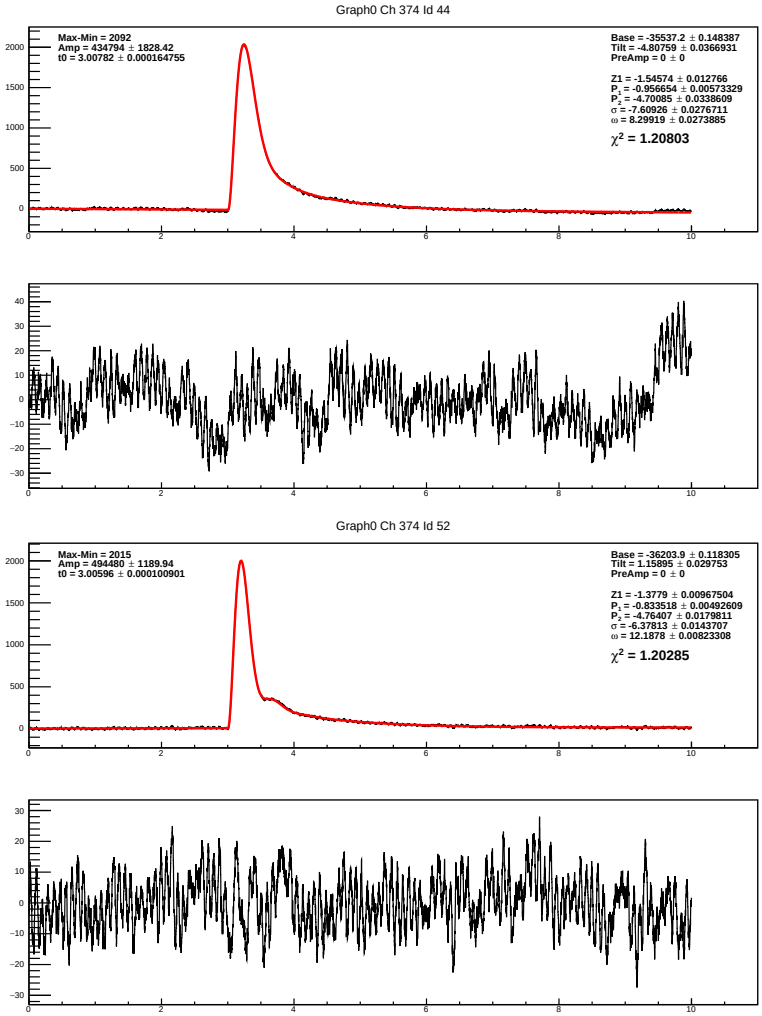

FIGURE B.7: Channel 374 - 11 mK LC: fits of the heater pulses at Id44 = 1.87 V and Id52 = 2.23 V

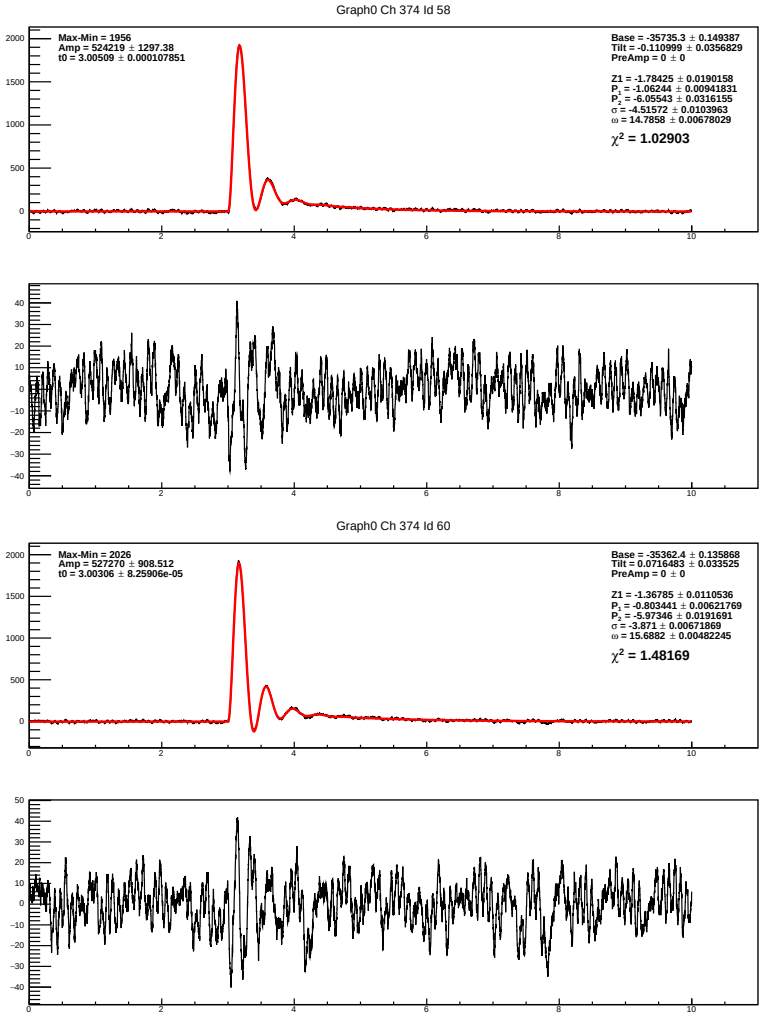

FIGURE B.8: Channel 374 - 11 mK LC: fits of the heater pulses at Id58 = 2.50 V and Id60 = 2.60 V

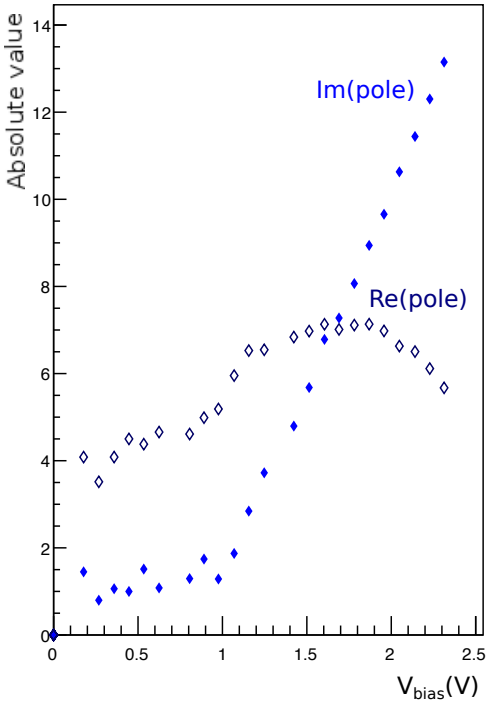

FIGURE B.9: Channel 374 - 11 mK LC: absolute value of the real and imaginary parts of the complex conjugate poles ($Re(pole) = \sigma$, $Im(pole) = \omega$) obtained from the fit of the heater pulses at the different bias voltages along the LC.

B.2.2 Pulse shape reconstruction of the physics data

The signal template with 2 real poles, 2 complex conjugate poles and 1 zero was utilized also to fit the physics data acquired by CUORE in 2017 (DS3021) at 15 mK, both **particle and heater pulses**. This study was performed in order to check the consistency of the model when fitting pulses in a broad energy range and induced by different physics processes.

Fits of 2615 keV Tl pulses for different channels

Examples of pulses corresponding to 2615 keV energy deposition from ^{208}Tl decay, recorded during the calibration runs of DS3021, are reported in Figs.B.10, B.11 and B.12. The fit with the pulse template is overlaid to the waveforms and on the bottom of the figures there are the residuals calculated between the real pulse and the pulse reconstructed with the best fit parameters.

The figures report example pulses for different CUORE channels, in order to show the capability of the model to reproduce the response of different systems and the goodness of the fits. In fact, the fit parameters slightly differ among the channels. The larger pole p_1 appear to be the one which is more similar among the several channels, thus it is possibly related to a thermal quantity which is approximately the same for all the bolometers, which could be the thermal capacitance of the TeO_2 absorber. The pole p_2 varies for each single channel. The zero z_1 sits in between p_1 and p_2. The absolute values of the poles p_1 and p_2 appear to be smaller than the value of the real part of p_3 and p_4, when the channel is operated at its optimal working point.

Moreover, it is worth to note that the fit model is able to well reconstruct also the pulses for very noisy channels (eg. ch 463, ch 374); in that case the shape of the thermal pulse is identified and the plot of the residuals just shows the tracing of the high-frequency noise that was superimposed to the signal pulse in the recorded waveform.

Energy dependence of the fit parameters

Analyzing the trend of the thermal model fit parameters with the deposited energy, would allow to study the linearity of the response of the channels and the possibile limits and constraints of the fitting technique.

An example of the results of the fit when applied on particle pulses in a wide range of energies is reported in Figs.B.13, B.14 and B.15 for one of the CUORE channels. Pulses corresponding to the six γ lines used for calibration are reported: 239 keV, 338 keV, 583 keV, 911 keV, 969 keV, 2615 keV. The quality of the fit does not change with energy ($\chi^2_{dof} \sim 1$).
All the poles and the zero of the model appear slightly vary with the deposited energy. The distribution of the real and imaginary parts of the complex conjugate poles (σ, ω) for all the calibration pulses for the reference channel, is reported in Fig.B.16. The variation of the average values for σ and ω for different energy regions is quite small (e.g. $\sigma_{2615keV} \sim$ -20 s^{-1}, $\sigma_{511keV} \sim$ -18 s^{-1}, for the channel in Fig.B.16). However the variation of the pulse shape parameters with the energy can be different for each channel, depending on their conditions of operation and the linearity of the response.
The spread of the parameters for lower energies is due to the fit precision limits; small pulses will be harder to reconstruct due to the superimposed noise.

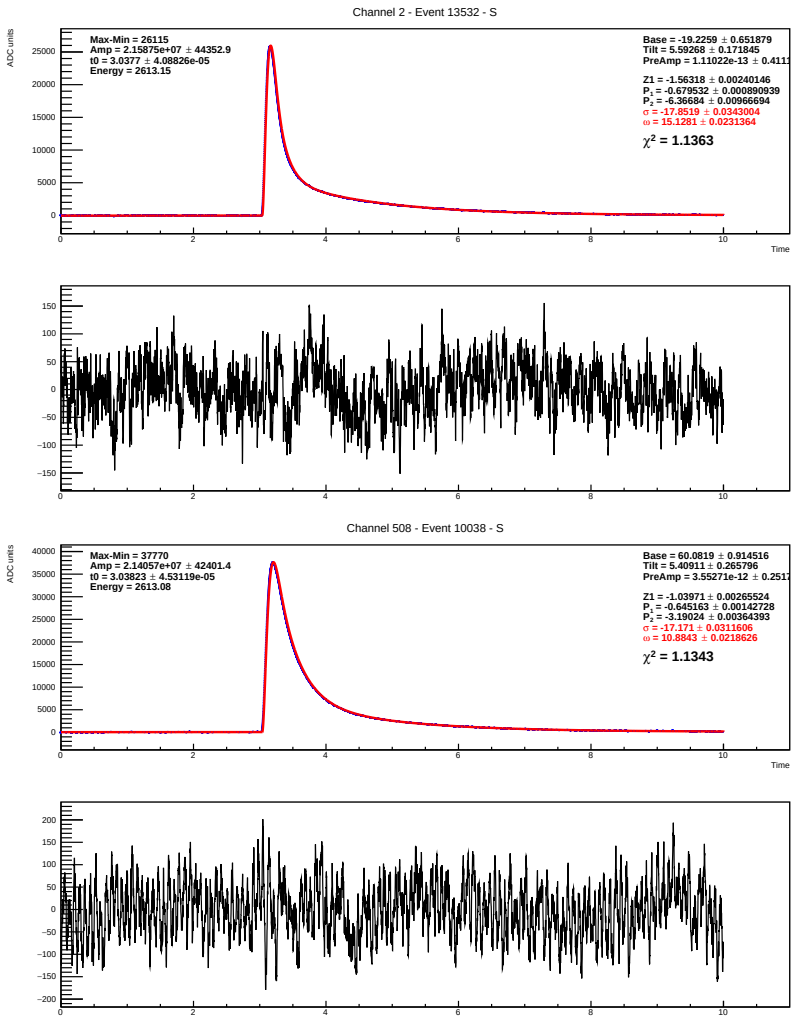

FIGURE B.10: Fit of ^{208}Tl 2615 keV pulses. NTD-type 39D: ch 2 and ch 508.

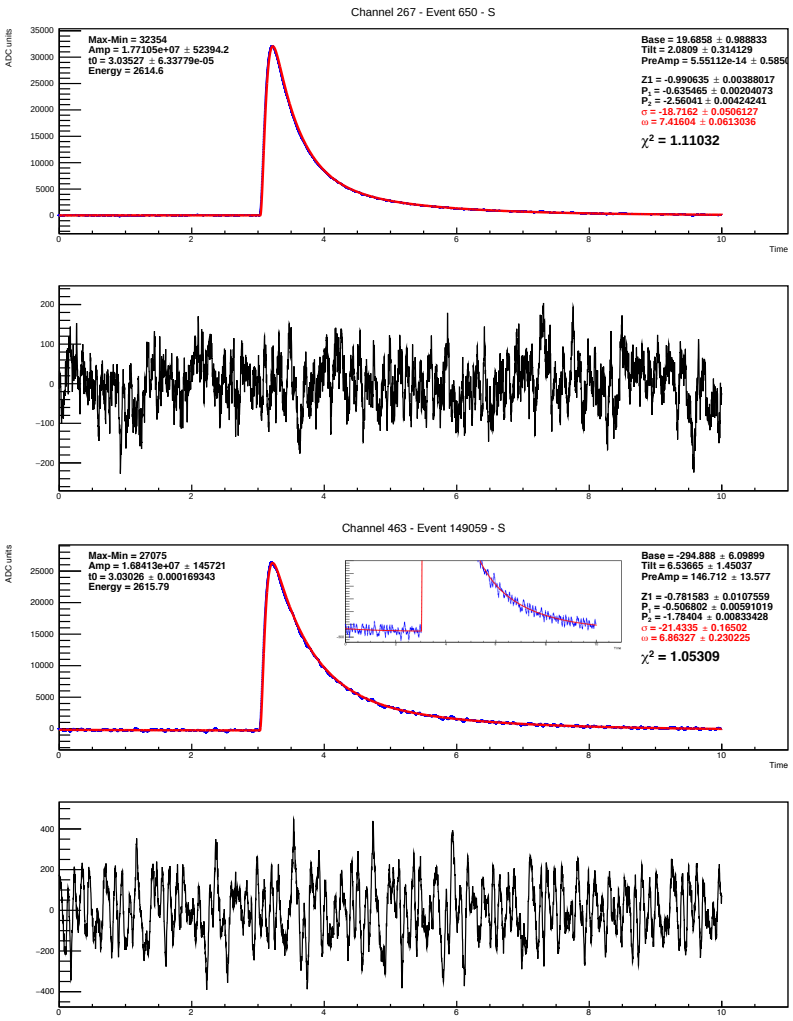

FIGURE B.11: Fit of ^{208}Tl 2615 keV pulses. NTD-type 39C: ch 267 and ch 463.

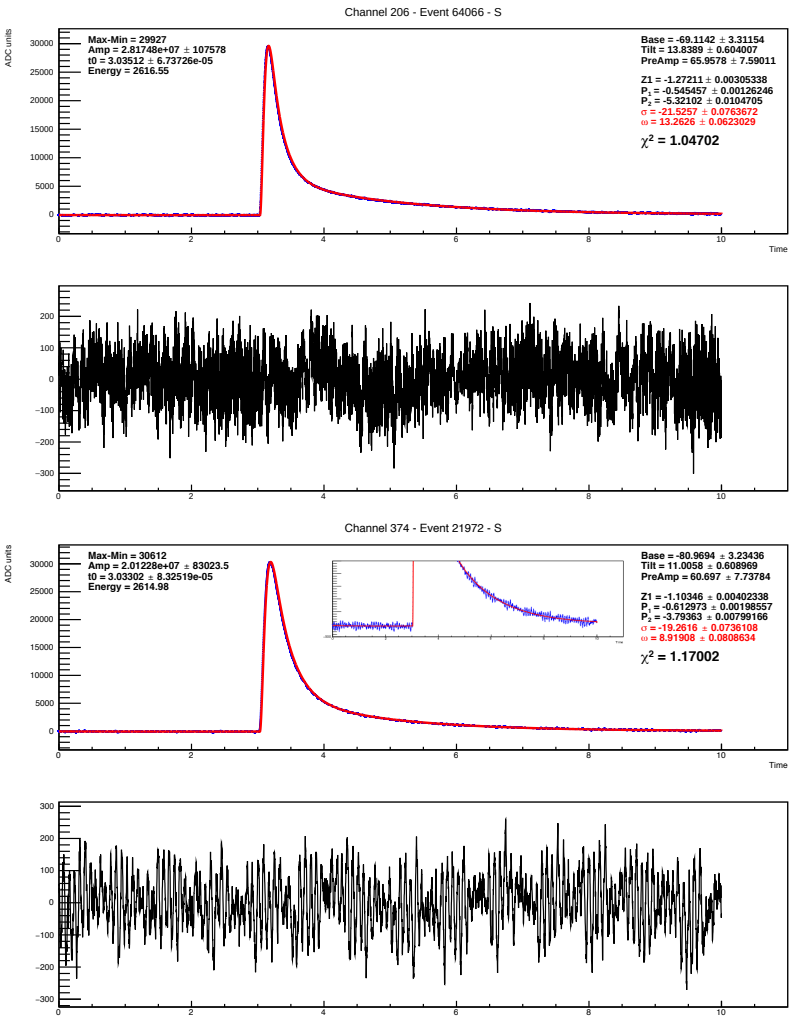

FIGURE B.12: Fit of ^{208}Tl 2615 keV pulses. NTD-type 41C: ch 207 and ch 374.

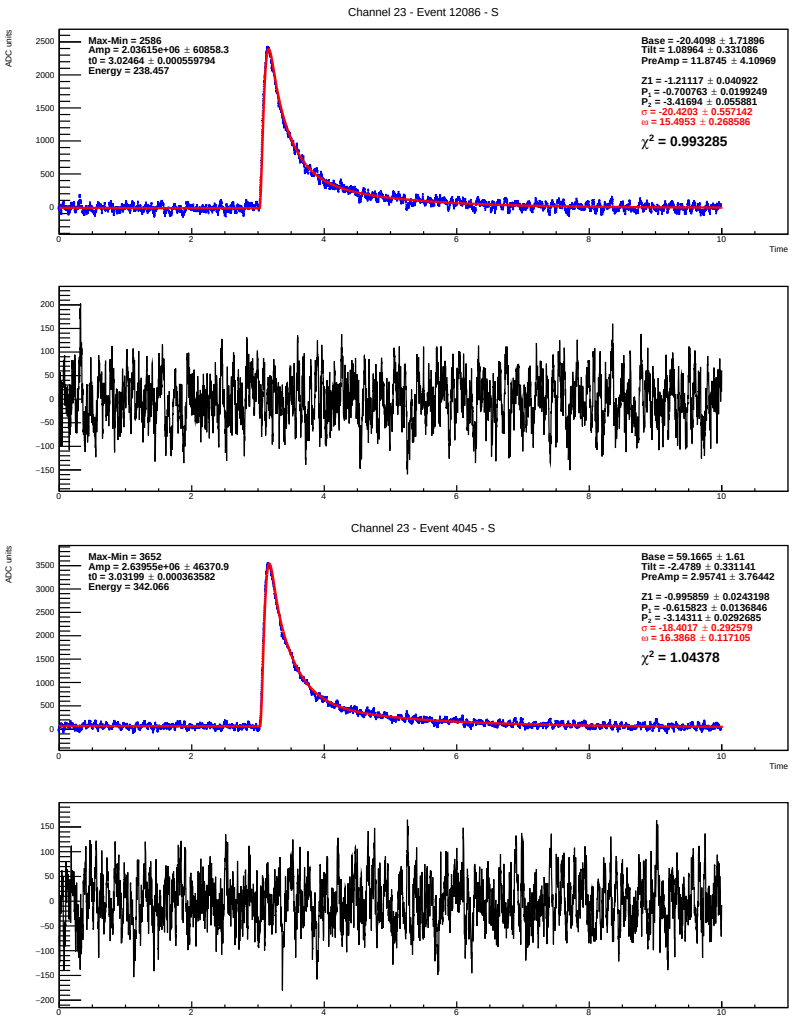

FIGURE B.13: Fit of 239 and 338 keV pulses in calibration data (DS3021) for channel 23.

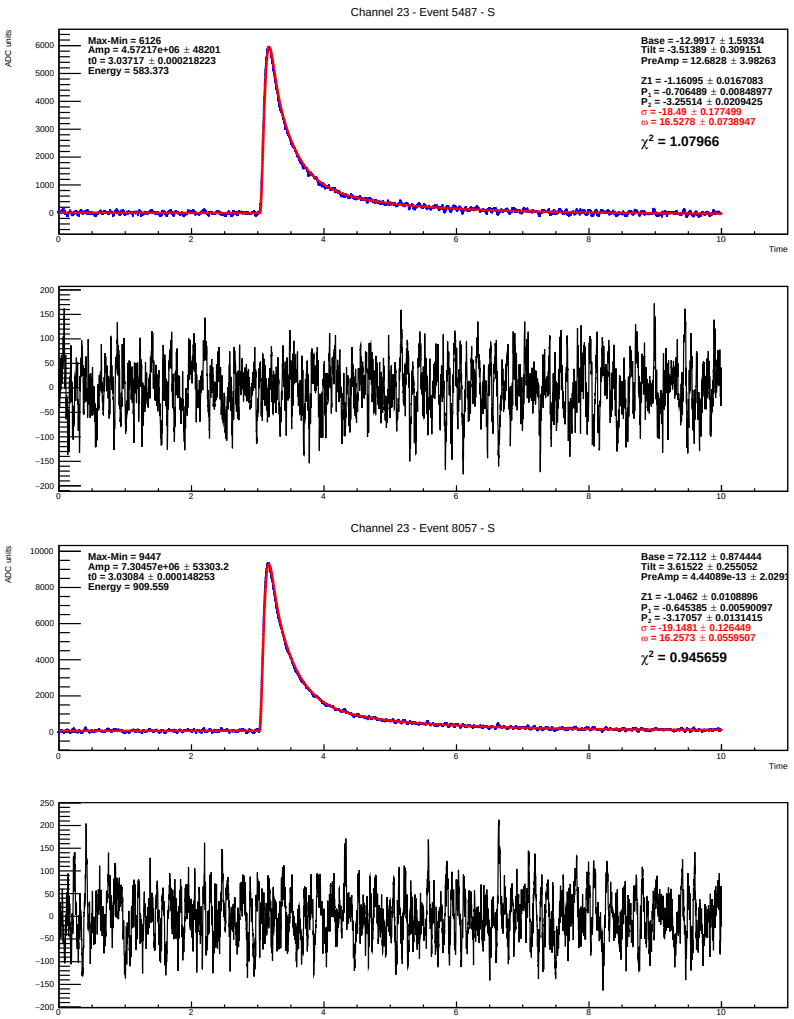

FIGURE B.14: Fit of 583 and 911 keV pulses in calibration data (DS3021) for channel 23.

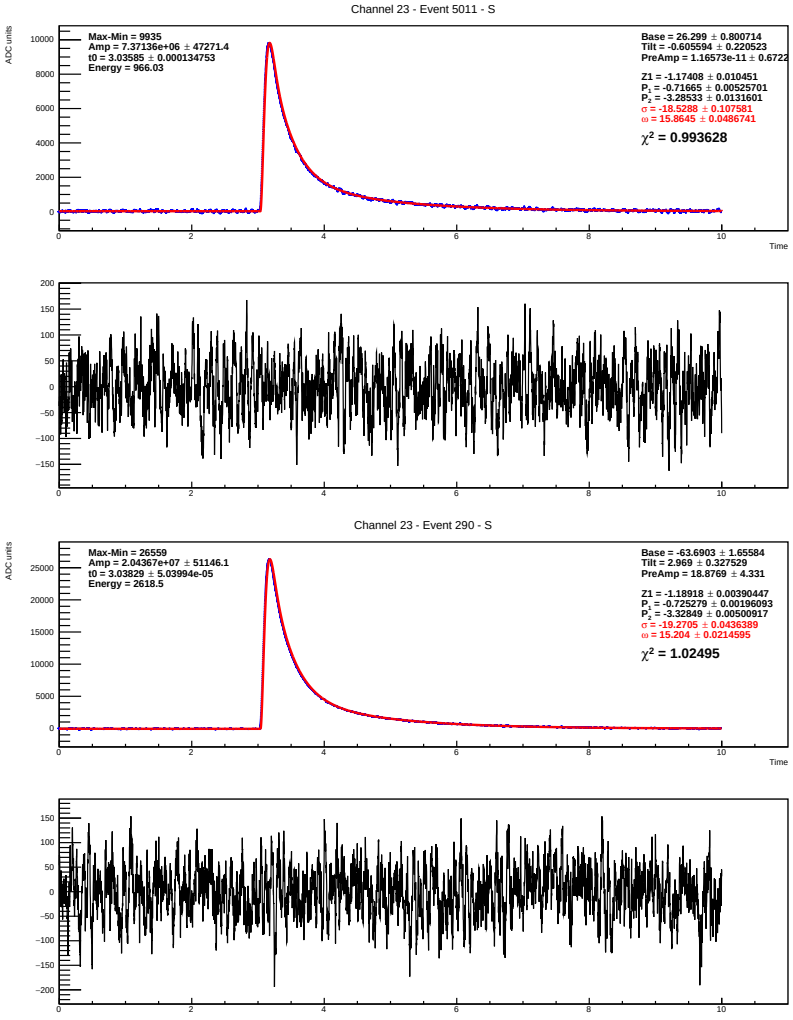

FIGURE B.15: Fit of 969 and 2615 keV pulses in calibration data (DS3021) for channel 23.

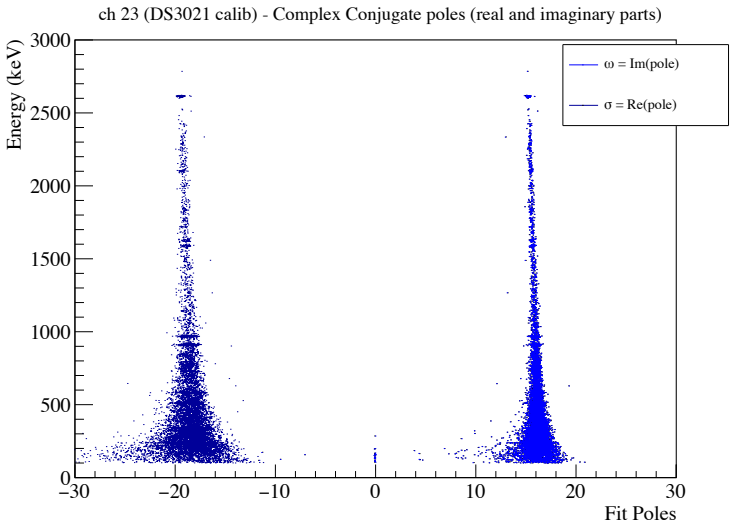

FIGURE B.16: Channel 23 - DS3021 calibration data: real and imaginary parts of the complex conjugate poles ($Re(pole) = \sigma$, $Im(pole) = \omega$) obtained from the fit of the pulses at the several energies.

B.2.3 Outlook

The main result of this preliminary analysis is having identified a fit function that well describes the pulse shape of the CUORE thermal signals. The fit function with 2 real poles, 2 complex conjugate poles and one zero, appears to be able to reproduce the thermal pulses for different channels and for particle/heater energy depositions. Actually, we are working on correlating the poles and zeros of the model with physics quantities related to the thermal circuit.

Moreover, given the preliminary results, further developments and upgrades on the thermal model analysis are planned:
- Assess the effects of the *fit precision* in the thermal pulses reconstruction. It is important to take into account the fit precision determining the model parameters. If we assume for a fixed channel the values of poles and zeros do not change with signal amplitude, it can be possible to quantify the limits of fit precision on simulated pulses when superimposing different noise windows. For any given channel, it can be produced a simulated signal with fixed poles and zero (values from fit on real pulses of that channel) and amplitude. Real noise from that channel is added to the simulated waveform and the new simulated signal is fitted. The spread of the fit parameters corresponding to fixed input signal quantities can be studied, in order to investigate its dependency on noise amplitude and on the event time window.
- Utilize the reconstructed pulse from the average fit parameters as the *'signal-template' for the Optimum Filter (OF)* sequence for the CUORE standard data processing. Utilizing an analytical template in place of the Average Pulse (AP) would have several advantages: it does not depend on the statistics of the calibration data, it is not possibly biased by the selection criteria for selecting the pulses for the AP sequence and it does not have any residual noise frequency in its power spectrum. This might allow to improve the overall resolution of the OF technique. On a longer term, in case the non-linearity of the response over a wide energy range becomes a limiting factor for the analyses, it could be possible to develop an OF sequence that would make use of energy dependent analytical pulse templates.

List of Figures

List of Tables

List of Abbreviations

SM	Standard Model
NH	Normal Hierarchy
IH	Inverted Hierarchy
QD	Quasi Degenerate
NME	Nuclear Matrix Element
QRPA	Quasiparticle Random Phase Approximation
ISM	Interacting Shell Model
IBM-II	Interacting Boson Model
CUORE	Cryogenic Underground Observatory for Rare Events
CUPID	CUORE Upgrade with Particle IDentification
LNGS	Laboratori Nazionali del Gran Sasso
PT	Pulse Tube
PTs	Pulse Tubes
LD	Linear Drive
LDs	Linear Drives
FCS	Fast Cooling System
DU	Dilution Unit
DR	Dilution Refrigerator
OVC	Outer Vacuum Chamber
IVC	Inner Vacuum Chamber
OFE	Oxygen-Free Electrolytic
HEX	Heat EXchangers
MC	Mixing Chamber
TSP	Tower Support Plate
ETP1	Electronic Tough Pitch
DS	Detector Suspension
MSP	Main Support Plate
CR	Clean Room
PTFE	PolyTetraFluoroEthylene
DCS	Detector Calibration System
NTD	Neutron Trasmutation Doped
ST	Semiconductor Thermistors
MIT	Metal-Insulator Transition
VRH	Variable Range Hopping
DAQ	Data AQuisition
FE	Front End
CMRR	Common Mode Rejection Ratio
PGA	Programmable Gain Amplifier
NI	National Instrument
ADC	Analog to Digital Converter
RDCF	Raw Data Continuous Flow
OF	Optimum Filter
AP	Average Pulse

ANPS	Average Noise Power Spectrum
NPS	Noise Power Spectrum
PS	Power Spectrum
DFT	Discrete Furier Transform
OT	Optimum Trigger
PSA	Pulse Shape Analysis
TVL	Test Variable Left
TVR	Test Variable Right
SNR	Signal to Noise Ratio
FWHM	Full Width at Half Maximum
MAD	Median Absolute Deviation
ROI	Region of Interest
UEML	Unbinned Extended Maximum Likelihood
PDF	Probability Density Function
NLL	Negative Log-Likelihood
C.L.	Confidence Level
C.I.	Credibility Interval

Bibliography

[1] W. E. Pauli, "Open letter to the group of radioactive people at the gauverein meeting in tubingen (in german)", December, 4 1930, (unpublished).

[2] F. L. Wilson, "Fermi's theory of beta decay", *Am. J. Phys.*, vol. 36, no. 12, pp. 1150–1160, 1968. DOI: 10.1119/1.1974382.

[3] C. L. Cowan, F. Reines, F. B. Harrison, H. W. Kruse, and A. D. McGuire, "Detection of the free neutrino: a confirmation", *Science*, vol. 124, pp. 103–104, 1956. DOI: 10.1126/science.124.3212.103.

[4] G. Danby, J. M. Gaillard, K. A. Goulianos, L. M. Lederman, N. B. Mistry, M. Schwartz, and J. Steinberger, "Observation of high-energy neutrino reactions and the existence of two kinds of neutrinos", *Phys. Rev. Lett.*, vol. 9, pp. 36–44, 1962. DOI: 10.1103/PhysRevLett.9.36.

[5] K. Kodama *et al.*, "Observation of tau neutrino interactions", *Phys. Lett. B*, vol. 504, pp. 218–224, 2001. DOI: 10.1016/S0370-2693(01)00307-0.

[6] B. Pontecorvo, "Mesonium and anti-mesonium", *Sov. Phys. JETP*, vol. 6, p. 429, 1957, [Zh. Eksp. Teor. Fiz. **33**, 549 (1957)].

[7] Z. Maki, M. Nakagawa, and S. Sakata, "Remarks on the unified model of elementary particles", *Prog. Theor. Phys.*, vol. 28, pp. 870–880, 1962. DOI: 10.1143/PTP.28.870.

[8] M. Tanabashi *et al.*, "Review of particle physics", *Phys. Rev. D*, vol. 98, p. 030 001, 3 2018. DOI: 10.1103/PhysRevD.98.030001.

[9] M. Goeppert-Mayer, "Double beta-disintegration", *Phys. Rev.*, vol. 48, pp. 512–516, 1935. DOI: 10.1103/PhysRev.48.512.

[10] R. Arnold *et al.*, "Measurement of the double-beta decay half-life and search for the neutrinoless double-beta decay of 48ca with the nemo-3 detector", *Phys. Rev.*, vol. D93, no. 11, p. 112 008, 2016. DOI: 10.1103/PhysRevD.93.112008.

[11] D. Q. Adams *et al.*, "Update on the recent progress of the CUORE experiment", 2018. arXiv: 1808.10342 [nucl-ex].

[12] P. A. M. Dirac, "Quantum theory of emission and absorption of radiation", *Proc. Roy. Soc. Lond.*, vol. A114, p. 243, 1927. DOI: 10.1098/rspa.1927.0039.

[13] J. Orear and E. Fermi, *Nuclear Physics: A Course Given by Enrico Fermi at the University of Chicago*. University of Chicago Press, 1950. [Online]. Available: https://books.google.it/books?id=B9gmAAAAMAAJ.

[14] W. C. Haxton and G. J. Stephenson, "Double beta decay", *Prog. Part. Nucl. Phys.*, vol. 12, pp. 409–479, 1984. DOI: 10.1016/0146-6410(84)90006-1.

[15] M. Doi, T. Kotani, and E. Takasugi, "Double beta decay and Majorana neutrino", *Prog. Theor. Phys. Suppl.*, vol. 83, p. 1, 1985. DOI: 10.1143/PTPS.83.1.

[16] J. Kotila and F. Iachello, "Phase space factors for double-β decay", *Phys. Rev. C*, vol. 85, p. 034 316, 2012. DOI: 10.1103/PhysRevC.85.034316.

[17] J. Barea, J. Kotila, and F. Iachello, "$0\nu\beta\beta$ and $2\nu\beta\beta$ nuclear matrix elements in the interacting boson model with isospin restoration", *Phys. Rev. C*, vol. 91, no. 3, p. 034 304, 2015. DOI: 10.1103/PhysRevC.91.034304.

[18] G. Racah, "On the symmetry of particle and antiparticle (in italian)", *Nuovo Cim.*, vol. 14, pp. 322–328, 1937. DOI: 10.1007/BF02961321.

[19] W. H. Furry, "On transition probabilities in double beta-disintegration", *Phys. Rev.*, vol. 56, pp. 1184–1193, 1939. DOI: 10.1103/PhysRev.56.1184.

[20] B. Pontecorvo, "Superweak interactions and double beta decay", *Phys. Lett. B*, vol. 26, pp. 630–632, 1968. DOI: 10.1016/0370-2693(68)90437-1.

[21] J. Schechter and J. W. F. Valle, "Neutrinoless double beta decay in $SU(2) \times U(1)$ theories", *Phys. Rev. D*, vol. 25, p. 2951, 1982. DOI: 10.1103/PhysRevD.25.2951.

[22] S. Dell'Oro, M. Marcocci S.and Viel, and F. Vissani, "Neutrinoless double beta decay: 2015 review", *Adv. High Energy Phys.*, vol. 2016, p. 2 162 659, 2016. DOI: 10.1155/2016/2162659.

[23] M. Duerr, M. Lindner, and A. Merle, "On the quantitative impact of the Schechter-Valle Theorem", *J. High Energy Phys.*, vol. 1106, p. 091, 2011. DOI: 10.1007/JHEP06(2011)091.

[24] F. Šimkovic, V. Rodin, A. Faessler, and P. Vogel, "$0\nu\beta\beta$ and $2\nu\beta\beta$ nuclear matrix elements, quasiparticle random-phase approximation, and isospin symmetry restoration", *Phys. Rev. C*, vol. 87, no. 4, p. 045 501, 2013. DOI: 10.1103/PhysRevC.87.045501.

[25] J. Hyvarinen and J. Suhonen, "Nuclear matrix elements for $0\nu\beta\beta$ decays with light or heavy Majorana-neutrino exchange", *Phys. Rev. C*, vol. 91, no. 2, p. 024 613, 2015. DOI: 10.1103/PhysRevC.91.024613.

[26] J. Menéndez, A. Poves, E. Caurier, and F. Nowacki, "Disassembling the nuclear matrix elements of the neutrinoless beta beta decay", *Nucl. Phys. A*, vol. 818, pp. 139–151, 2009. DOI: 10.1016/j.nuclphysa.2008.12.005.

[27] T. R. Rodriguez and G. Martinez-Pinedo, "Energy density functional study of nuclear matrix elements for neutrinoless $\beta\beta$ decay", *Phys. Rev. Lett.*, vol. 105, p. 252 503, 2010. DOI: 10.1103/PhysRevLett.105.252503.

[28] F. Šimkovic, G. Pantis, J. D. Vergados, and A. Faessler, "Additional nucleon current contributions to neutrinoless double beta decay", *Phys. Rev. C*, vol. 60, p. 055 502, 1999. DOI: 10.1103/PhysRevC.60.055502.

[29] J. Barea, J. Kotila, and F. Iachello, "Nuclear matrix elements for double-β decay", *Phys. Rev. C*, vol. 87, no. 1, p. 014 315, 2013. DOI: 10.1103/PhysRevC.87.014315.

[30] A. Faessler, G. L. Fogli, E. Lisi, V. Rodin, A. M. Rotunno, and F. Šimkovic, "Overconstrained estimates of neutrinoless double beta decay within the qrpa", *J. Phys. G*, vol. 35, p. 075 104, 2008. DOI: 10.1088/0954-3899/35/7/075104.

[31] J. Suhonen and O. Civitarese, "Probing the quenching of g_a by single and double beta decays", *Phys. Lett. B*, vol. 725, pp. 153–157, 2013. DOI: 10.1016/j.physletb.2013.06.042.

[32] J. Engel and J. Menéndez, "Status and future of nuclear matrix elements for neutrinoless double-beta decay: a review", *Rep. Prog. Phys.*, vol. 80, no. 4, p. 046 301, 2017. DOI: 10.1088/1361-6633/aa5bc5.

[33] M. Agostini *et al.*, "Improved limit on neutrinoless double-β decay of 76ge from gerda phase ii", *Phys. Rev. Lett.*, vol. 120, no. 13, p. 132 503, 2018. DOI: 10.1103/PhysRevLett.120.132503.

[34] C. Alduino *et al.*, "First results from CUORE: a search for lepton number violation via $0\nu\beta\beta$ decay of ^{130}Te", *Phys. Rev. Lett.*, vol. 120, no. 13, p. 132 501, 2018. DOI: 10.1103/PhysRevLett.120.132501.

[35] K. Asakura *et al.*, "Search for double-beta decay of 136xe to excited states of 136ba with the kamland-zen experiment", *Nucl. Phys.*, vol. A946, pp. 171–181, 2016. DOI: 10.1016/j.nuclphysa.2015.11.011.

[36] O. Azzolini *et al.*, "First result on the neutrinoless double-β decay of 82*se* with cupid-0", *Phys. Rev. Lett.*, vol. 120, no. 23, p. 232 502, 2018. DOI: 10.1103/PhysRevLett.120.232502.

[37] R. Arnold *et al.*, "Result of the search for neutrinoless double-β decay in 100mo with the nemo-3 experiment", *Phys. Rev. D*, vol. 92, no. 7, p. 072 011, 2015. DOI: 10.1103/PhysRevD.92.072011.

[38] V. A. Kostelecky and S. Samuel, "Spontaneous breaking of Lorentz symmetry in string theory", *Phys. Rev.*, vol. D39, p. 683, 1989. DOI: 10.1103/PhysRevD.39.683.

[39] V. A. Kostelecky and R. Potting, "CPT, strings, and meson factories", *Phys. Rev.*, vol. D51, pp. 3923–3935, 1995. DOI: 10.1103/PhysRevD.51.3923.

[40] R. Lehnert, "CPT and Lorentz-symmetry breaking: a review", *Frascati Phys. Ser.*, vol. 43, pp. 131–154, 2007.

[41] S. J. Diaz, A. Kostelecky, and R. Lehnert, "Relativity violations and beta decay", *Phys. Rev.*, vol. D88, no. 7, p. 071 902, 2013. DOI: 10.1103/PhysRevD.88.071902.

[42] D. Colladay and V. A. Kostelecky, "CPT violation and the standard model", *Phys. Rev.*, vol. D55, pp. 6760–6774, 1997. DOI: 10.1103/PhysRevD.55.6760.

[43] ——, "Lorentz violating extension of the standard model", *Phys. Rev.*, vol. D58, p. 116 002, 1998. DOI: 10.1103/PhysRevD.58.116002.

[44] V. A. Kostelecky, "Gravity, Lorentz violation, and the standard model", *Phys. Rev.*, vol. D69, p. 105 009, 2004. DOI: 10.1103/PhysRevD.69.105009.

[45] V. A. Kostelecky and N. Russell, "Data tables for Lorentz and CPT violation", *Rev. Mod. Phys.*, vol. 83, pp. 11–31, 2011. DOI: 10.1103/RevModPhys.83.11.

[46] V. A. Kostelecky and M. Mewes, "Lorentz and CPT violation in neutrinos", *Phys. Rev.*, vol. D69, p. 016 005, 2004. DOI: 10.1103/PhysRevD.69.016005.

[47] S. J. Diaz, "Lorentz and CPT violation in the neutrino sector", in *Proceedings, 6th Meeting on CPT and Lorentz Symmetry (CPT 13): Bloomington, Indiana, USA, June 17-21, 2013*, 2014, pp. 53–56. DOI: 10.1142/9789814566438_0014.

[48] ——, "Neutrinos as probes of Lorentz invariance", *Adv. High Energy Phys.*, vol. 2014, p. 962 410, 2014. DOI: 10.1155/2014/962410.

[49] ——, "Testing Lorentz and CPT invariance with neutrinos", *Symmetry*, vol. 8, no. 10, p. 105, 2016. DOI: 10.3390/sym8100105.

[50] S. J. Diaz and A. Kostelecky, "Lorentz- and CPT-violating models for neutrino oscillations", *Phys. Rev.*, vol. D85, p. 016 013, 2012. DOI: 10.1103/PhysRevD.85.016013.

[51] T. Katori, V. A. Kostelecky, and R. Tayloe, "Global three-parameter model for neutrino oscillations using Lorentz violation", *Phys. Rev.*, vol. D74, p. 105 009, 2006. DOI: 10.1103/PhysRevD.74.105009.

[52] A. Kostelecky and M. Mewes, "Neutrinos with Lorentz-violating operators of arbitrary dimension", *Phys. Rev.*, vol. D85, p. 096 005, 2012. DOI: 10.1103/PhysRevD.85.096005.

[53] S. J. Diaz, "Limits on Lorentz and CPT violation from double beta decay", *Phys. Rev.*, vol. D89, p. 036 002, 2014. DOI: 10.1103/PhysRevD.89.036002.

[54] J. B. Albert *et al.*, "First search for Lorentz and CPT violation in double beta decay with EXO-200", *Phys. Rev.*, vol. D93, no. 7, p. 072 001, 2016. DOI: 10.1103/PhysRevD.93.072001.

[55] L. Pertoldi, "Search for Lorentz and CPT symmetries violation in double-beta decay using data from the GERDA experiment", 2017, [Master thesis, University of Padua].

[56] D. R. Artusa *et al.*, "Searching for neutrinoless double-beta decay of ^{130}Te with CUORE", *Adv. High Energy Phys.*, vol. 2015, p. 879 871, 2015. DOI: 10.1155/2015/879871.

[57] C. Alduino *et al.*, "CUORE sensitivity to $0\nu\beta\beta$ decay", *Eur. Phys. J. C*, vol. 77, no. 8, p. 532, 2017. DOI: 10.1140/epjc/s10052-017-5098-9.

[58] ——, "The projected background for the CUORE experiment", *Eur. Phys. J. C*, vol. 77, no. 8, p. 543, 2017. DOI: 10.1140/epjc/s10052-017-5080-6.

[59] E. Fiorini and T. O. Niinikoski, "Low temperature calorimetry for rare decays", *Nucl. Instrum. Meth. A*, vol. 224, p. 83, 1984. DOI: 10.1016/0167-5087(84)90449-6.

[60] M. Barucci, C. Brofferio, A. Giuliani, E. Gottardi, I. Peroni, and G. Ventura, "Measurement of low temperature specific heat of crystalline TeO_2 for the optimization of bolometric detectors", *J. Low Temp. Phys.*, vol. 123, no. 5-6, pp. 303–314, 2001. DOI: 10.1023/A:1017555615150.

[61] R. A. H. El-Mallawany, *Tellurite Glasses Handbook: Physical Properties and Data*. CRC Press, 2002. [Online]. Available: https://www.crcpress.com/Tellurite-Glasses-Handbook-Physical-Properties%-and-Data-Second-Edition/ElMallawany/9781439849835.

[62] Y. Chu, Y. Li, Z. Ge, G. Wu, and H. Wang, "Growth of the high quality and large size paratellurite single crystals", *J. Cryst. Growth*, vol. 295, no. 2, pp. 158–161, 2006. DOI: 10.1016/j.jcrysgro.2006.08.009.

[63] C. Arnaboldi *et al.*, "Production of high purity TeO_2 single crystals for the study of neutrinoless double beta decay", *J. Cryst. Growth*, vol. 312, no. 20, pp. 2999–3008, 2010. DOI: 10.1016/j.jcrysgro.2010.06.034.

[64] C. Arnaboldi, C. Brofferio, C. Bucci, P. Gorla, G. Pessina, and S. Pirro, "1.3 kg bolometers to search for rare events", *Nucl. Instrum. Meth. A*, vol. 554, pp. 300–305, 2005. DOI: 10.1016/j.nima.2005.07.060.

[65] L. Cardani, L. Gironi, J. W. Beeman, I. Dafinei, Z. Ge, G. Pessina, S. Pirro, and Y. Zhu, "Performance of a large TeO_2 crystal as a cryogenic bolometer in searching for neutrinoless double beta decay", *J. Instrum.*, vol. 7, P01020, 2012. DOI: 10.1088/1748-0221/7/01/P01020.

[66] C. Alduino *et al.*, "CUORE-0 detector: design, construction and operation", *J. Instrum.*, vol. 11, no. 07, P07009, 2016. DOI: 10.1088/1748-0221/11/07/P07009.

[67] C. Enss and D. McCammon, "Physical principles of low temperature detectors: ultimate performance limits and current detector capabilities", *Journal of Low Temperature Physics*, vol. 151, no. 1, pp. 5–24, 2008. DOI: 10.1007/s10909-007-9611-7.

[68] K. Alfonso, L. Cassina, A. Giachero, C. Gotti, G. Pessina, and P. Carniti, "A high precision pulse generation and stabilization system for bolometric experiments", *JINST*, vol. 13, no. 02, P02029, 2018. DOI: 10.1088/1748-0221/13/02/P02029.

[69] A. Alessandrello, C. Brofferio, D. V. Camin, O. Cremonesi, E. Fiorini, A. Giuliani, G. Pessina, and E. Previtali, "The first underground low radioactivity bolometric system", *Proc. 3rd Int. Workshop on Low Temp. Det. for Neutrinos and Dark Matter*, pp. 253–262, 1989.

[70] P. G. Catalano, G. Cavinato, F. Salvini, and M. Tozzi, "Structural analysis of the Gran Sasso Laboratories of INFN (in italian)", *Mem. Soc. Geol. It.*, vol. 35, pp. 647–655, 1986.

[71] M. Ambrosio *et al.*, "Vertical muon intensity measured with MACRO at the Gran Sasso Laboratory", *Phys. Rev. D*, vol. 52, pp. 3793–3802, 1995. DOI: 10.1103/PhysRevD.52.3793.

[72] H. Wulandari, J. Jochum, W. Rau, and F. von Feilitzsch, "Neutron flux at the Gran Sasso underground laboratory revisited", *Astropart. Phys.*, vol. 22, pp. 313–322, 2004. DOI: 10.1016/j.astropartphys.2004.07.005.

[73] A. D'Addabbo, C. Alduino, A. Bersani, M. Biassoni, C. Bucci, A. Caminata, L. Canonica, L. Cappelli, G. Ceruti, N. Chott, S. Copello, O. Cremonesi, J. S. Cushman, D. D'Aguanno, C. J. Davis, S. Dell'Oro, S. Di Domizio, A. Drobizhev, M. Faverzani, E. Ferri, M. A. Franceschi, L. Gladstone, P. Gorla, C. Ligi, L. Marini, T. Napolitano, A. Nucciotti, I. Nutini, J. L. Ouellet, C. E. Pagliarone, L. Pattavina, C. Rusconi, D. Santone, B. Schmidt, V. Singh, D. Speller, L. Taffarello, F. Terranova, J. Wallig, B. Welliver, and T. Wise, "The CUORE cryostat", *Journal of Low Temperature Physics*, 2018. DOI: 10.1007/s10909-018-2054-5.

[74] F. Alessandria *et al.*, "The 4K outer cryostat for the CUORE experiment: construction and quality control", *Nucl. Instrum. Meth. A*, vol. 727, pp. 65–72, 2013. DOI: 10.1016/j.nima.2013.06.015.

[75] C. Pagliarone, L. Cappelli, C. Bucci, P. Gorla, D. D'Aguanno, F. Marignetti, G. Erme, and S. Kartal, "The CUORE fast cooling system", *PoS*, vol. EPS-HEP2017, p. 634, 2018. DOI: 10.22323/1.314.0634.

[76] F. Pobell, *Matter and Methods at Low Temperatures*. Springer, 2007. DOI: 10.1007\%2F978-3-540-46360-3.

[77] A. D'Addabbo, C. Bucci, L. Canonica, S. Di Domizio, P. Gorla, L. Marini, A. Nucciotti, I. Nutini, C. Rusconi, and B. Welliver, "An active noise cancellation technique for the CUORE pulse tube cryocoolers", *Cryogenics*, vol. 93, pp. 56–65, 2018. DOI: 10.1016/j.cryogenics.2018.05.001.

[78] Cryomech, Inc, *PT415-RM supporting documentation*. [Online]. Available: http://www.cryomech.com/specificationsheet/.

[79] A. Alessandrello *et al.*, "A new search for neutrinoless beta beta decay with a thermal detector", *Phys. Lett. B*, vol. 335, pp. 519–525, 1994. DOI: 10.1016/0370-2693(94)90388-3.

[80] ——, "Preliminary results on double beta decay of ^{130}Te with an array of twenty cryogenic detectors", *Phys. Lett. B*, vol. 433, pp. 156–162, 1998. DOI: 10.1016/S0370-2693(98)00645-5.

[81] C. Arnaboldi *et al.*, "A calorimetric search on double beta decay of ^{130}Te", *Phys. Lett. B*, vol. 557, pp. 167–175, 2003. DOI: 10.1016/S0370-2693(03)00212-0.

[82] E. Andreotti *et al.*, "^{130}Te neutrinoless double-beta decay with Cuoricino", *Astropart. Phys.*, vol. 34, pp. 822–831, 2011. DOI: 10.1016/j.astropartphys.2011.02.002.

[83] S. Dell'Oro, "Optimization of the CUORE detector during the commissioning phase", 2017, [Ph. D. thesis, Gran Sasso Science Insitute].

[84] E. Buccheri, M. Capodiferro, S. Morganti, F. Orio, A. Pelosi, and V. Pettinacci, "An assembly line for the construction of ultra-radio-pure detectors", *Nucl. Instrum. Meth. A*, vol. 768, pp. 130–140, 2014. DOI: 10.1016/j.nima.2014.09.046.

[85] G. Benato *et al.*, "Radon mitigation during the installation of the CUORE $0\nu\beta\beta$ decay detector", *JINST*, vol. 13, no. 01, P01010, 2018. DOI: 10.1088/1748-0221/13/01/P01010.

[86] C. Arnaboldi, P. Carniti, L. Cassina, C. Gotti, X. Liu, M. Maino, G. Pessina, C. Rosenfeld, and B. X. Zhu, "A front-end electronic system for large arrays of bolometers", *JINST*, vol. 13, no. 02, P02026, 2018. DOI: 10.1088/1748-0221/13/02/P02026.

[87] A. Bersani *et al.*, "Detector suspension system for the CUORE detector ", (in preparation), 2018.

[88] A. Alessandrello *et al.*, "Measurements of internal radioactive contamination in samples of roman lead to be used in experiments on rare events", *Nucl. Instrum. Meth. B*, vol. 142, pp. 163–172, 1998. DOI: 10.1016/S0168-583X(98)00279-1.

[89] J. S. Cushman *et al.*, "The detector calibration system for the CUORE cryogenic bolometer array", *Nucl. Instrum. Meth. A*, vol. 844, pp. 32–44, 2017. DOI: 10.1016/j.nima.2016.11.020.

[90] S. Di Domizio, A. Branca, A. Caminata, L. Canonica, S. Copello, A. Giachero, E. Guardincerri, L. Marini, M. Pallavicini, and M. Vignati, "A data acquisition and control system for large mass bolometer arrays", 2018.

[91] C. Alduino *et al.*, "Low energy analysis techniques for CUORE", *Eur. Phys. J.*, vol. C77, no. 12, p. 857, 2017. DOI: 10.1140/epjc/s10052-017-5433-1.

[92] F. Simon, "Application of low temperature calorimetry to radioactive measurements", *Nature*, vol. 135, p. 763, 1935. DOI: 10.1038/135763a0.

[93] C. Enss and H. Siegfried, *Low-Temperature Physics*. Springer, 2005. DOI: 10.1007/b137878.

[94] A. Alessandrello, J. W. Beeman, C. Brofferio, O. Cremonesi, E. Fiorini, A. Giuliani, E. E. Haller, A. Monfardini, A. Nucciotti, M. Pavan, G. Pessina, E. Previtali, and L. Zanotti, "High energy resolution bolometers for nuclear physics and x-ray spectroscopy", *Phys. Rev. Lett.*, vol. 82, pp. 513–515, 3 1999. DOI: 10.1103/PhysRevLett.82.513.

[95] Y. B. Levinson, "Propagation of nonequilibrium phonons with frequency down-conversion (anthracene)", *Mol. Cryst. Liq. Cryst.*, vol. 57, pp. 23–38, 1980. DOI: 10.1080/00268948008069816.

[96] W. Eisenmenger and A. Kaplianskiĭ, *Nonequilibrium Phonons in Nonmetallic Crystals*. North-Holland Publ., 1986, [Phonon propagation with frequency down-conversion in Chap. 3, pp. 91-143]. [Online]. Available: https://books.google.it/books?id=T0wsAAAAYAAJ.

[97] J. C. Mather, "Bolometer noise: Nonequilibrium theory", *Appl. Opt.*, vol. 21, no. 6, pp. 1125–1129, 1982. DOI: 10.1364/AO.21.001125.

[98] S. H. Moseley, J. C. Mather, and D. McCammon, "Thermal detectors as x-ray spectrometers", *J. Appl. Phys.*, vol. 56, p. 1257, 1984. DOI: 10.1063/1.334129.

[99] N. F. Mott and J. H. Davies, "Metal-insulator transition in doped semiconductors", *Philos. Mag. B*, vol. 42, no. 6, pp. 845–858, 1980. DOI: 10.1080/01418638008222332.

[100] A. Miller and E. Abrahams, "Impurity conduction at low concentrations", *Phys. Rev.*, vol. 120, pp. 745–755, 32 1960. DOI: 10.1103/PhysRev.120.7452.

[101] E. E. Haller, N. P. Palaio, M. Rodder, W. L. Hansen, and E. Kreysa, "Ntd germanium: A novel material for low temperature bolometers", in *Neutron Transmutation Doping of Semiconductor Materials*, R. D. Larrabee, Ed., Springer US, 1984, pp. 21–36, ISBN: 978-1-4612-9675-1. DOI: 10.1007/978-1-4613-2695-3_2. [Online]. Available: http://dx.doi.org/10.1007/978-1-4613-2695-3_2.

[102] M. Vignati, "Model of the response function of CUORE bolometers", 2010, [Ph. D. thesis, University of Rome - La Sapienza].

[103] M. Pedretti, "The single module for Cuoricino and CUORE detectors: tests, construction and modelling", 2004, [Ph. D. thesis, University of Insubria].

[104] F. Alessandria *et al.*, "CUORE cryostat commissioning", (in preparation), 2018.

[105] L. Canonica, L. Marini, and I. Nutini, "Setting detector working points and thresholds", [CUORE Internal Note (preliminary)], 2017.

[106] G. Wang *et al.*, "CUPID: CUORE (Cryogenic Underground Observatory for Rare Events) Upgrade with Particle IDentification", 2015. arXiv: 1504.03599 [physics.ins-det].

[107] C. Alduino *et al.*, "Analysis techniques for the evaluation of the neutrinoless double-β decay lifetime in ^{130}Te with the CUORE-0 detector", *Phys. Rev. C*, vol. 93, p. 045 503, 2016. DOI: 10.1103/PhysRevC.93.045503.

[108] M. Biassoni, A. Branca, I. Nutini, S. Pozzi, B. Schmidt, V. Singh, D. Speller, and C. Tomei, "Data production for the PRL 2017 data release", [CUORE Internal Note 127D], 2018.

[109] *ROOT- an object oriented data analysis framework*, For the CUORE first data analysis it was used ROOT version 5.34. [Online]. Available: https://root.cern.ch/.

[110] E. Gatti and P. F. Manfredi, "Processing the signals from solid state detectors in elementary particle physics", *Riv. Nuovo Cim.*, vol. 9, pp. 1–146, 1986. DOI: 10.1007/BF02822156.

[111] S. Pozzi, "Search for double-beta decay of ^{130}Te to the excited states of ^{130}Xe in CUORE-0", 2017, [Ph. D. thesis, University of Milano-Bicocca].

[112] P. C. Mahalanobis, "On the generalized distance in statistics", *Proceedings of the National Institute of Sciences (Calcutta)*, vol. 2, pp. 49–55, 1936.

[113] G. Cowan, K. Cranmer, E. Gross, and O. Vitells, "Asymptotic formulae for likelihood-based tests of new physics", *Eur. Phys. J.*, vol. C71, p. 1554, 2011, [Erratum: Eur. Phys. J.C73,2501(2013)]. DOI: 10.1140/epjc/s10052-011-1554-0,10.1140/epjc/s10052-013-2501-z.

[114] A. Caminata and I. Nutini, "CUORE PRL analysis efficiency evaluation", [CUORE Internal Note 126D], 2018.

[115] C. J. CLOPPER and E. S. PEARSON, "The use of confidence or fiducial limits illustrated in the case of the binomial", *Biometrika*, vol. 26, pp. 404–413, 1934. DOI: 10.1093/biomet/26.4.404.

[116] S. Agostinelli *et al.*, "Geant4: a simulation toolkit", *Nucl. Instrum. Meth.*, vol. A506, pp. 250–303, 2003. DOI: 10.1016/S0168-9002(03)01368-8.

[117] M. Doi, T. Kotani, H. Nishiura, and E. Takasugi, "Double beta decay", *Prog. Theor. Phys.*, vol. 69, p. 602, 1983. DOI: 10.1143/PTP.69.602.

[118] C. Alduino *et al.*, "Measurement of the two-neutrino double beta decay half-life of ^{130}Te with the CUORE-0 experiment", *Eur. Phys. J. C*, vol. 77, no. 1, p. 13, 2017. DOI: 10.1140/epjc/s10052-016-4498-6.

[119] M. Aglietta *et al.*, "Muon 'depth intensity' relation measured by LVD underground experiment and cosmic ray muon spectrum at sea level", *Phys. Rev.*, vol. D58, p. 092 005, 1998. DOI: 10.1103/PhysRevD.58.092005.

[120] S. P. Ahlen *et al.*, "Muon astronomy with the MACRO detector", *Astrophys. J.*, vol. 412, pp. 301–311, 1993. DOI: 10.1086/172921.

[121] G. Cowan, *Statistical Data Analysis*, ser. Oxford science publications. Clarendon Press, 1998. [Online]. Available: https://books.google.it/books?id=ff8ZyW0nlJAC.

[122] Plummer, M., *JAGS version 4.3.0 user manual*. [Online]. Available: http://web.sgh.waw.pl/~atoroj/ekonometria_bayesowska/jags_user_manual.pdf.

[123] A. Drobizhev and L. Marini, "Lineshape analysis for the first PRL results", [CUORE Internal Note 125D], 2018.

[124] W. A. Rolke, A. M. Lopez, and J. Conrad, "Limits and confidence intervals in the presence of nuisance parameters", *Nucl. Instrum. Meth.*, vol. A551, pp. 493–503, 2005. DOI: 10.1016/j.nima.2005.05.068.

[125] K. Alfonso *et al.*, "Search for neutrinoless double-beta decay of ^{130}Tewith CUORE-0", *Phys. Rev. Lett.*, vol. 115, no. 10, p. 102 502, 2015. DOI: 10.1103/PhysRevLett.115.102502.

[126] R. Arnold *et al.*, "Measurement of the double beta decay half-life of ^{130}Te with the NEMO-3 detector", *Phys. Rev. Lett.*, vol. 107, p. 062 504, 2011. DOI: 10.1103/PhysRevLett.107.062504.

Acknowledgements

I take this opportunity to express gratitude to my advisors Dr. Carlo Bucci and Dr. Oliviero Cremonesi for sharing expertise, for encouraging me during each step of the PhD thesis experience and for their sincere and valuable guidance. I came to CUORE with little knowledge of the bolometric technology and, thanks to their patience and support, I learnt a lot and I hope I gave a contribution to the CUORE data-taking and analyses during the PhD project.

I place on record a thank you to Gran Sasso Science Institute - GSSI, which endorses the growth of the PhD students to become independent researchers with critical minds and gives them the opportunity to be involved in thesis projects in international institutions and collaborations.
I wish to express my gratitude to Laboratori Nazionali del Gran Sasso - INFN LNGS, for hosting me for the thesis project and for providing me with all the necessary facilities for the research.
I would like also to thank the PhD thesis referees for having read the work and for their valuable comments.

My sincere thanks go to the CUORE collaboration especially, for trusting young and new students, giving them the opportunity to be an active part of the experiment and making them feel a completing part of the collaboration.
I want to place a special thank you to the CUORE group at LNGS. I am grateful to Paolo and Lucia, together with Carlo, for their everyday help and their suggestions in doing my first steps in CUORE. Nello, Laura and Luigi explained me a lot about CUORE and they supported me (and all the 11 nutinis) during the PhD work. My CUORE office mates at LNGS had a strong role in making every day full of interesting discussions and exchange of ideas: the oldies, Stefano D. and Daria, and the newbies, Valentina and Guido. I would like to thank also Claudia R., Chiara, Nic and all the CUORE people who shared with me expertise about bolometers and cryogenics. I feel I have been lucky for having stayed at LNGS during these first years of CUORE in operation, since I got the chance to meet people with different expertise and I learnt everyday something new from all of them.
I would like to thank the CUORE analysis team; I got the chance to be part of that group working hard for a common purpose: analyzing the very first CUORE data! Matteo, Stefano P. and Antonio were guides into the deep secrets of the CUORE data processing. Sergio guided me into the world of the CUORE data acquisition. There are many more people I want to thank: Jon, Tommy, Alice, Alessio, Simone, Claudia T., Marco, Brad, Ben, Sachi, Vivek ...
I really had a great experience working with all of the CUORE people.

Besides the CUORE people, I wish to express my gratitude to Dr. Francesco Vissani; his enthusiasm for science, his wise advices and the interesting exchange of ideas helped me grow as a scientist. I would like also to thank my Master's thesis advisor, Dr. Flavio Cavanna; thanks to his warm suggestion I came to apply to GSSI,

and now I am about to conclude this experience, even if working on a different technology than the LArTPCs.

I want to thank the GSSI family. Wherever we will end up for our research after the PhD at the GSSI, we will never really leave "the LA bubble". Alena, Giovanni, Daniele, Gialex, Ding, Lorenzo, Akshat, Silvia, Valerio, Andrea, Imran, Seva, Myrto, Maurizio, Wolfgang, Sabina, Paola, Miriam, Vanessa, Stefano, Carlo, Odysse, Enrico, Ambra, ... Thanks my friends, just for being you.
I would like also to thank all the other nice people I met and I spent time with at GSSI and at LNGS.

I would like to thank my close old-time friends at home and my physics-friends spread around the world, for their support during these three years of experiences and challenges.

Lastly, I want to state that I am extremely grateful to my parents, Andrea and Tiziana, for the unceasing encouragement through this venture. I want to thank my sisters, Noemi and Olivia, who cheered on me in my effort for pursuing my thesis goal at GSSI. And, anyways, we got the opportunity to discover the hidden beauties of Abruzzo... and arrosticini!
I am grateful to all of my family too, my aunts Cristina and Vanna, my uncle Enrico and all the close relatives who strongly supported my choice to come to GSSI for my PhD.
My PhD thesis is dedicated to my grandparents, Giulietta, Augusto, Vasco and Gemma; I hope that from the bright sky above Gran Sasso you can see me achieving this goal and you are proud of me.